The Sulfur, Argon, and Calcium Isotopic Composition of the Galactic Cosmic Ray Source

Thesis by

Ryan Christopher Ogliore

In Partial Fulfillment of the Requirements

for the Degree of

Doctor of Philosophy

California Institute of Technology

Pasadena, California

2007

(Defended December 18, 2006)

For my grandfather, Harold Meyer

Acknowledgements

> *My fantasy was also wrong. Because I started the last lap - Boom! And I started to sprint, and they were twice as fast as me! Until 300 meters, Chataway, Schade, Mimoun, all three in front, ohh oh. And you see, gold medal, silver medal, bronze medal; and for me, potato. What to do? But to give up? Never! Nah, no, no! I must run and ARH! I must run, AHH!*
>
> – Emil Zatopek

I am indebted to many individuals who aided me in the creation of this thesis. Throughout my education I have been exceptionally fortunate to have kind, intelligent, and extraordinary people as my mentors. These years at Caltech have been rewarding thanks to the many people who have helped me through the tribulations of grad school.

My adviser, Ed Stone, has been a lucid teacher, a relentless motivator, and my scientific idol during my graduate school years. When I encounter a difficult problem, my first thought is usually, “How would Ed look at this?” and I’ll probably carry that with me the rest of my career. I am very grateful for his willingness to patiently discuss problems with me. Our discussions have greatly aided in my education and the development of this thesis.

Richard Mewaldt was my mentor through my early years in graduate school and the Space Radiation Laboratory. He guided me through those initial treacherous journeys through space physics and data analysis, and I am thankful for his willingness to first take me on as a student.

Mark Wiedenbeck provided me with invaluable assistance with this thesis. I strive to write IDL code as elegantly as he does. In addition, Mark was a fantastic teacher during my hardware work on STEREO. His patience with my endless questions over the last few years is greatly appreciated.

Whenever I had a probing curiosity about an instrument, or a random programming question, or a tenuous thought about a space physics phenomenon, Rick Leske was always there with an answer, just one door away. His knowledge of our particle detection instruments is astounding, and his willingness to educate me on many matters over my graduate school experience has been invaluable.

Luke Sollitt, graduate student the elder, was the source of sage advice and good company in room 219. Hubert Chen has been my only company in the upstairs grad student office during the thesis-writing process, and I thank him for putting up with me.

The guidance of Jim Higdon through my undergraduate years was indispensable. He is the reason I first became interested in astrophysics and cosmic rays, and Jim's advice has assisted me in the theoretical components of this work.

Many others have been helpful during my time at Caltech: Alan Cummings, Christina Cohen, Allan Labrador, Sven Geier, Hiromasa Miyasaka. Good times were had during the ISOMAX balloon campaign in Lynn Lake, Manitoba. The SRL crew of Georgia de Nolfo, Jill Burnham, Steve Schindler, and Glen Albritton, made the experience memorable, and eased the rigor of seventeen-hour work days and an entirely tuber-based diet.

Whenever I mention SRL to someone who has experience working with our group, they mention what a nice bunch of people they are. This has helped make my experience here a pleasant one.

Graduate school, especially graduate school at Caltech, would not have been survivable without the frenetic antics of my friends. The adventures have been many: from running around the Caltech track for 24 hours, to running up to the top of Mt. Wilson in a snowstorm, to running from Pasadena to Compton on a Sunday morning, and various other indiscretions that probably involved running in some form. My housemates, Jesse Bloom, Alex Gagnon, and Kenji Sasaki, were indispensable sources of entertaining anecdotes and pointless discussions these past few years. Hansel, the rat-eating python slash snake-model, has been sitting idly by as vermin have infested our living quarters. But all is forgiven. Scott Jung, the coach of the Caltech Cross Country team, has graciously let me be involved in the college athletic experience of some great kids. Jason Rogers, Ian Shapiro, Mark Eichenlaub, Chris Raub, Steve Alves, Megumi Abe, Pat McGrail, and Dan Feldman have been great running buddies and the oft unwitting outlet for my competitive impulses. I wish I had met Talia Starkey sooner, but her companionship has been precious to me these last couple years, as has her cooking and her willingness to accompany me on the occasional ill-planned enterprise.

Though they're a thousand miles away, my family has supported me so much through these years that I feel I never really left Seattle. My mother has been asking me for six years: When are you coming home? My father sends postal packages filled with Rice Krispie treats and fudge. My brother asks me if I've figured out the Pythagorean Theorem or blown up any asteroids yet. My aunt sends me pictures of dogs in costumes, daily. My family's presence in my everyday life has been critical to my happiness in graduate school, a fact that becomes painfully apparent only when someone is no longer there.

These years have been the best of my life so far, but also the most challenging. Sometimes I've felt like Emil Zatopek at the end of the Helsinki Olympic 5000 meters. But through the support, friendship, and inspiration of others, I never settled for potato.

Abstract

Galactic cosmic ray measurements of the sulfur, argon, and calcium isotopes made by the Cosmic Ray Isotope Spectrometer on the NASA Advanced Composition Explorer are reported over the energy range from 100 to 400 MeV/nucleon. The propagation of cosmic rays through the Galaxy and heliosphere is modeled with observational constraints imposed by measurements. Source abundance ratios of the sulfur, argon, and calcium isotopes are deduced from this model. Cosmic rays are thought to originate in the cores of superbubbles which contain stellar ejecta mixed with the surrounding interstellar medium. The composition of the superbubble core should reflect the composition of the cosmic rays at their source. Based on the derived isotopic source ratios of sulfur, argon, and calcium, the superbubble material at the cosmic ray source is constrained to be $18\%^{+26\%}_{-14\%}$ supernova and wind ejecta, with the remainder interstellar medium material. This mix of metal-rich ejecta and interstellar medium in the superbubble core corresponds to a cosmic ray source metallicity of $2.7^{+3.9}_{-2.1}$ times solar metallicity.

Contents

List of Figures

List of Tables

Chapter 1

Introduction

Galactic cosmic rays (GCRs) are energetic charged particles that propagate through the Galaxy. They are detected near Earth, making them the only high-energy particles of cosmic origin that can be directly sampled. Therefore, the study of cosmic rays, their energies and composition, provide a unique insight into extreme astrophysical environments.

Galactic cosmic rays consist of $\sim$98% atomic nuclei, $\sim$2% electrons and positrons, and a very small fraction anti-protons. Of the atomic nuclei, protons make up the majority (87%) of GCRs, 12% are helium nuclei, and $\sim$1% are elements with atomic number (Z) greater than two (Simpson, 1983). They range in energy from $\sim 10^8$ eV to $\sim 10^{18}$ eV, with particles of extragalactic origin extending the spectra up to $\sim 10^{20}$eV. The relative abundances of GCRs and their spectra at Earth are shown in Figure 1.1. The cosmic ray flux is isotropic; there is no preferred arrival direction. This is because the motion of GCRs during their propagation through the Galaxy is diffusive, due to scattering off of the irregular interstellar magnetic fields.

Measurements of the composition of extraterrestrial material has immensely contributed to our understanding of the astrophysical environment in which that material was synthesized. The Sun, Earth, stars, meteorites, and comets have all been better understood through isotopic, elemental, and mineralogical measurements. The GCRs provide an excit-

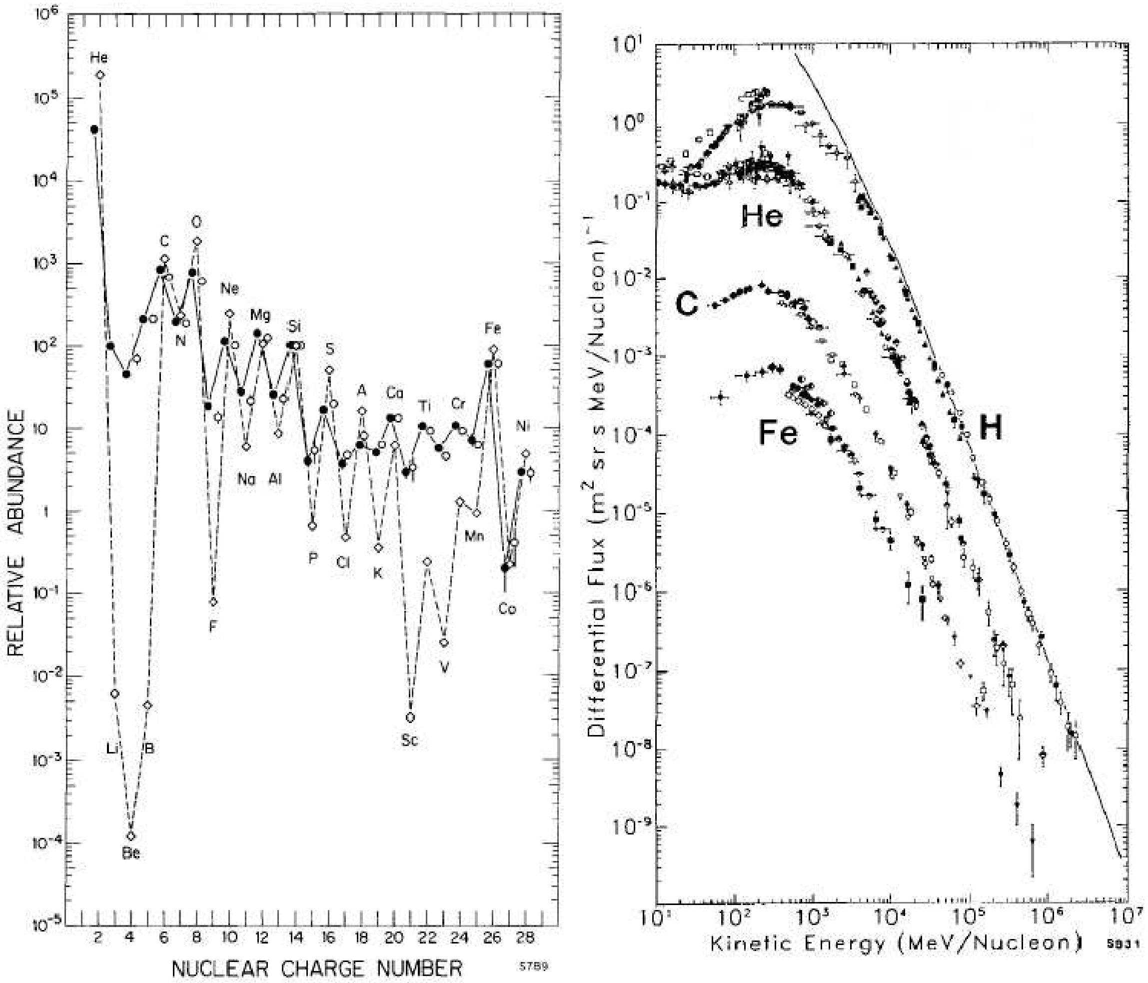

Figure 1.1: The relative abundance and energy spectra of GCRs, reproduced from (Simpson, 1983). The left plot shows GCR abundances measured at Earth, relative to silicon. The solid circles are low-energy data (70-280 MeV/nucleon), open circles are high-energy data (1000-2000 MeV/nucleon). Compared to solar system abundances (diamonds), the GCRs are enhanced in Li, Be, B and Sc, V, Mn. This is because "secondary" cosmic rays are produced by the breakup, or spallation, of heavier species during propagation. The right plot shows the observed energy spectra of H, He, C, and Fe at Earth. The curves roll over below a few hundred MeV per nucleon due to the effects of solar modulation (Section 1.3). The spectrum of hydrogen in interstellar space (removing solar modulation) is shown by the solid curve. The helium turn-up below ~60 MeV/nucleon is due to anomalous cosmic rays: interstellar neutral particles drift into the solar system, become ionized, and are swept out to be accelerated at the termination shock (where the solar wind slows to subsonic speeds).

ing opportunity to probe an exotic astrophysical environment by means of a direct sample of high-energy extra-solar material.

1.1 Source and acceleration

Based on the Galactic cosmic ray confinement time ($\sim$15 Myr, Yanasak *et al.* (2001)), and the energy density of cosmic rays in the Galaxy (1 eV/cm^3), the power required to maintain the GCRs is $\sim$10^{41} ergs/s (Maran, 1991). Supernova (SN) shocks are one of the few Galactic sites that can satisfy this power budget and have been shown to be capable of accelerating GCRs up to $\sim$10^{15}eV by Fermi acceleration (Axford, 1981; Blandford & Ostriker, 1980). The supernova rate is about three per century per Galaxy (van den Bergh & McClure, 1994). Core-collapse events from young stars of spectral types O and B make up 80%-90% of the supernova, with the other 10%-20% being thermonuclear explosions of older accreting white dwarfs. With one supernova occuring every $\sim$10^9 seconds in the Galaxy, it is necessary to have 10^{41}ergs/s $\cdot$ 10^9 seconds $= 10^{50}$ ergs be available per supernova to accelerate cosmic rays. The ejecta kinetic energy of core-collapse supernova is consistently about 10^{51} ergs (Nomoto *et al.*, 1997; Woosley & Weaver, 1995), meaning a cosmic ray acceleration efficiency of $\sim$10% is required (Ptuskin, 2001).

Though supernova explosions can supply the energetics necessary to accelerate cosmic rays, the actual source of the particles that they accelerate is not known with certainty. Clues to this issue can be found in the composition of the cosmic rays measured near Earth. The isotope ^{59}Ni decays to ^{59}Co by electron-capture. After cosmic ray ^{59}Ni is accelerated to high energies and its orbital electrons are stripped off, it can no longer decay by electron-capture and becomes stable. Therefore, the amount of ^{59}Ni compared to ^{59}Co seen in GCRs provides a measure of the time delay between the nucleosynthesis and acceleration of cosmic rays. The bulk of the ^{59}Ni was observed to have decayed, meaning that at least 100,000 years had to pass between its creation in the supernova and the acceleration of the GCR material (Wiedenbeck *et al.*, 1999). A supernova explosion ejects many solar masses of material processed by nucleosynthesis during the quiescent phase during its lifetime and explosive nucleosynthesis that occurs during the supernova explosion. This material is ejected into the surrounding interstellar medium, but the ^{59}Ni observations rule out the possibility that a supernova shock accelerates its own ejecta.

Since GCRs are likely accelerated in the region of supernova shocks, the composition of this region should give information regarding the composition of the cosmic rays. As stated earlier, the progenitor stars for most core-collapse supernova are massive O and B stars. Most of these stars are born in the molecular clouds of OB associations (Garmany, 1994), and consequently O and B stars are seen in clusters tens of parsecs in diameter. The non-uniformity of O and B stars in the sky has been observed for many years (Kapteyn, 1914). The OB associations are gravitationally unbound, but the stars in the associations do not stray far from their birthplace during their lifetimes before they explode as supernova. This is because these stars are short lived, 3-30 Myr (Schaller *et al.*, 1992), and have low average velocities ($\sim$4 km/s, Lada & Kylafis (1991)), meaning they can traverse at most 120 parsecs before they explode. The resulting supernova from a progenitor O or B star sweeps out material around it, leaving a region of hot, low-density gas. The most massive and short-lived stars in the association, Wolf-Rayet stars, initiate the formation of a tenuous region around the association by the action of their intense wind. The wind ejecta material is enriched in elements heavier than helium. Other supernovae occurring in the association around the same time and place (McCray & Snow, 1979), evacuate their own bubbles, resulting in merger and the formation of a superbubble hundreds of parsecs in diameter

(Tenorio-Tagle & Bodenheimer, 1988).

The material inside a superbubble consists of supernovae and Wolf-Rayet wind ejecta, mixed with evaporated molecular clouds and material from the interstellar medium (ISM) that is swept up during the expansion of the superbubble. Since 90%±10% of core-collapse supernovae occur inside superbubbles (Higdon *et al.*, 1998), the GCR-accelerating shocks accelerate the material inside the superbubble. As stated earlier, time delay between supernova and acceleration of the GCR material must be greater than 100,000 years, based on the ^{59}Ni observations. Supernovae occur in the superbubble once every ~300,000 years, so this requirement is satisfied. The superbubble origin of Galactic cosmic rays is discussed in detail by Higdon *et al.* (1998).

Astronomical observations should confirm the correlation between cosmic ray acceleration and OB associations if the bulk of GCRs originate in superbubbles. Inverse Compton scattering of 2.7K cosmic background photons by high-energy cosmic ray electrons in the acceleration region generates TeV gamma rays (Tanimori *et al.*, 1998). Discoveries of TeV γ-ray sources by the High Energy Gamma-Ray Astronomy telescope (HEGRA) as well as the High Energy Stereoscopic System (HESS) have shown three sources spatially coincident with OB associations (HEGRA Collaboration: F. Aharonian, 2005; Aharonian *et al.*, 2005b,a). These observations strengthen the link between OB associations and the acceleration of high-energy particles.

The composition of the material inside the superbubbles is not well known. Superbubble cores must be enriched with the high-metallicity (fraction of elements heavier than helium) contribution of Wolf-Rayet stellar winds and ejecta of core-collapse supernovae. The amount of mixing of this ejecta with older ISM material of lower metallicity is not precisely determined. If Galactic cosmic rays are accelerated from superbubble interiors, then their composition should reflect the superbubble composition. However, the acceleration mechanism is not equally efficient for all species of GCRs.

The elemental composition of GCRs shows an enhancement in those elements that have high condensation temperatures and therefore more easily condense into grains (Meyer *et al.*, 1997). The process that is responsible for this is as follows: Interstellar dust grains near stars obtain a small positive charge, due to UV ionization of their surface. They undergo efficient preliminary acceleration because of their high rigidity (mass-to-charge ratio). A supernova shock then sputters and accelerates individual atoms from the dust grains to cosmic ray energies (Meyer *et al.*, 1997).

Isotopes of the same element have very similar condensation temperatures, so there should be little difference in the efficiency of accelerating one isotope compared to another of the same element. Therefore, abundances of isotopes are indicative of the nuclear processes that lead to their creation. A way to probe the environment of the superbubble interior is to look at ratios of GCR isotopes traced back to their source.

The abundance of isotopes and elements in the solar system has historically been used as a benchmark with which to compare other samples of extraterrestrial material. The solar system composition is derived from meteorites, spectroscopic studies of the Sun, and the solar wind (Lodders, 2003). Most elements and isotopes are relatively well known and are assumed to be the same abundances present in the presolar nebula.

It has long been known that the ^{22}Ne/^{20}Ne ratio in the Galactic cosmic ray source is substantially larger than that observed in the solar wind (Maehl *et al.*, 1975). Binns *et al.* (2005) found this enhancement factor to be 5.3±0.3. The winds of Wolf-Rayet stars are rich in ^{22}Ne, and did not contribute material to the presolar nebula. It was first postulated by Casse & Paul (1982) that this was the source of the excess ^{22}Ne. Higdon & Lingenfelter

(2003b) calculated the contributions to the abundances of neon isotopes in the superbubble core, taking into account supernova ejecta and Wolf-Rayet winds mixing with the interstellar medium. They found that the observed GCR source ^{22}Ne/^{20}Ne ratio is a consequence of GCRs being accelerated in a superbubble core, assuming that the material from which the cosmic rays are accelerated consists of 18%±5% ejecta+wind material, with the remainder ISM. Binns *et al.* (2005) demonstrated that a ~20% Wolf-Rayet wind component in the ISM-mixed superbubble core material accounts for the observed enhancement in the ^{12}C/^{16}O (corrected for the different acceleration efficiency of O and C) and ^{58}Fe/^{56}Fe ratios compared to the solar system, as well as the ^{22}Ne anomaly.

Other GCR isotope source ratios should reflect the superbubble core composition derived from the ^{22}Ne/^{20}Ne ratio. The amount of ISM mixing in the superbubble core was calculated based on an isotope ratio that is dominated by the Wolf-Rayet component of the superbubble core material. Isotopes that are not dominantly Wolf-Rayet produced in the superbubble core can better probe the supernova ejecta component. The amount of ISM mixing can be independently determined using other GCR isotopes, providing constraints on the superbubble origin of Galactic cosmic rays. Since the supernova ejecta and Wolf-Rayet wind material has enriched metallicity compared to the ISM, the amount of mixing also determines the metallicity of the GCR source material in the superbubble core. These are the issues that will be addressed in the following chapters by determining the GCR isotopic source abundances of sulfur, argon, and calcium.

1.2 Propagation

Once they are accelerated, the cosmic ray nuclei propagate through the interstellar medium. As charged particles, they spiral around Galactic magnetic fields with gyroradii determined by their energy and charge Z. However, Galactic magnetic fields are not smooth, but are thought to have irregularities like those measured in the interplanetary medium. These irregularities cause large deviations in the trajectory of a cosmic ray particle. For this reason the GCRs can be considered to diffuse from their sources through the interstellar medium.

The ISM contains ambient hydrogen gas of average density 0.34±0.04 atoms/cm^3 (Yanasak *et al.*, 2001) and helium atoms at about 10% of this density. The interaction of cosmic rays with this gas significantly affects their composition and energy spectra. A cosmic ray can lose energy to ionization of the interstellar H and He atoms, or it can collide with an atom and break apart. The fragmentation of a primary particle from the cosmic ray source produces a lighter nucleus, called a secondary. The presence of rare solar system elements like Li, Be, B, Sc, Ti, and V in the cosmic rays is explained by the spallation of the more common heavier elements C, N, O, and Fe into these lighter nuclei. If an unstable secondary nucleus is created, it will decay to another species. Nuclides that decay by electron-capture are effectively stable during propagation at high energies, though there is a small probability that the particle will attach an electron at lower energy.

Not all primary particles fragment, or spallate, into lighter nuclei during propagation. By measuring the ratio of primary nuclei to their secondary spallation products, combined with cross-section information for these spallation reactions, it is possible to determine how much matter the cosmic rays traverse before being observed at Earth. The radionuclide ^{10}Be is produced as a cosmic ray secondary during propagation, and has a halflife of 3.9 million years. The β-decay daughter, ^{10}B, is also present in the cosmic rays. The confinement time for cosmic rays in the Galaxy can be inferred from the amount of ^{10}Be that has decayed to ^{10}B, combined with an estimate of the average amount of material traversed (derived from the secondary/primary ratios). The ^{10}Be results, along with other radionuclides ^{26}Al, ^{36}Cl, and ^{54}Mn, yield a mean confinement time for cosmic rays of 15.0±1.6 Myr (Yanasak *et al.*, 2001). Assuming a typical dimension of 1-10 kpc for the Galaxy, high-energy particles traveling unimpeded close to the speed of light would escape the Galaxy in 3×10^3 to 3×10^4 years. This suggests that cosmic rays take a much more torturous path through the Galaxy, and the assumption that their propagation is essentially diffusion is a valid one.

The flux of Galactic cosmic rays is known to be constant to within a factor of two over the past billion years, based on measurements of cosmic-ray-produced ("cosmogenic") ^{40}K in iron meteorites (Lal, D. & Elliot, H., 1975) and other measurements of cosmogenic isotopes in ice cores, deep sea sediments, and other types of meteorites. Therefore the losses of cosmic rays due to escape from the Galaxy, energy loss due to ionization of the ISM, and destruction due to spallation and radioactive decay is balanced by their production at the source. Cosmic ray propagation is modeled for the source abundances derived in this work, and is described in Section 4.1.

1.3 Solar modulation

The preceding section described the propagation of cosmic rays through the Galaxy. During their journey from the cosmic ray source to detection at Earth, they must pass through the region of the Sun's influence, the heliosphere. The dynamics of charged particles in this region is heavily influenced by the outward expanding solar wind plasma. A cosmic ray entering the heliosphere from interstellar space will be convected outward by the momentum outflow of the solar wind, and will also undergo adiabatic deceleration due to the outward expansion of magnetic fields (Parker, 1966; Potgieter & Ferreira, 2001). The magnetic irregularities in the solar wind effectively scatter charged particles (Parker, 1965), making their propagation a diffusive process. Owing to these effects, a particle with an energy of 500 MeV per nucleon in interstellar space can lose more than a third of its energy by the time it reaches Earth. The cosmic ray spectrum measured at Earth are thus said to be "modulated" from spectrum in the interstellar medium. The rollover in the cosmic ray proton spectrum at ~250 MeV/nucleon seen in Figure 1.1 is a result of solar modulation.

The magnetohydrodynamical characteristics of the solar wind plasma vary as solar activity varies. It has been known for many years that sunspot number varies from a minimum number to a maximum over an ~11 year cycle. During the time period when the sunspot count is high, solar maximum, the structure of solar magnetic fields is more complex. High speed solar wind streams emanate from the Sun, creating an increase of turbulence in the solar wind. The change in the nature of the solar wind plasma responsible for solar modulation means that the effective modulation will vary from solar minimum to solar maximum. The energy loss of cosmic rays diffusing through the heliosphere is larger during solar maximum compared to during solar minimum as seen by measurements (Niebur *et al.*, 2003; Mewaldt *et al.*, 2004), though the detailed changes in the physics between these two situations is not entirely certain. The model for solar modulation used in this work is discussed in Section 4.2.2.

1.4 Detection

Cosmic rays were first detected by Victor Hess during a balloon flight in 1912. He used an electroscope to observe that the intensity of ionizing radiation increased with altitude, and concluded that the source of the radiation was extraterrestrial. Hess was awarded the Nobel Prize in physics for this discovery in 1936.

The detection of cosmic rays has progressed greatly in the past hundred years. It is now possible to measure the abundances and energy spectra of rare isotopes with high accuracy. The same fundamental principles of measuring the energy, mass, and charge of a particle are used today as were used in the early years of cosmic ray physics. A charged nucleus incident on a medium loses energy by ionization through inelastic collisions with atoms of the material. The Bethe-Bloch formula gives the energy deposited per unit length by the incident charged particle

$$-\frac{dE}{dx} = \frac{4\pi}{m_e c^2} \cdot \frac{n_e Z^2}{\beta^2} \cdot \left(\frac{e^2}{4\pi\epsilon_0}\right)^2 \cdot \left[ln\left(\frac{2m_e c^2 \beta^2}{I \cdot (1-\beta^2)}\right) - \beta^2\right], \tag{1.1}$$

where Z is the incident particle's charge, β is its velocity in units of the speed of light c, and γ is its Lorentz factor. The electron number density of the medium is n_e, and I is the mean excitation potential of the target (usually approximated as $I = 16\,eV \cdot Z^{0.9}$). By measuring the energy deposited in the medium, it is possible to use the Bethe-Bloch formula to deduce the incident particle's charge, mass, and energy. This property is exploited by most GCR detectors, and is further discussed for a modern charged particle telescope in Section 2.1.

The space age made it possible to measure cosmic rays outside of the Earth's atmosphere and magnetosphere. The atmosphere causes incoming cosmic rays to fragment, and the Earth's magnetic field shields charged particles of lower rigidities incident at lower latitudes (see, e.g., Ogliore *et al.* (2001)). Cosmic ray detectors aboard spacecraft are used to measure the lowest energy GCRs, from tens to hundreds of MeV/nucleon. Balloon-borne detectors are used to measure cosmic rays from a few hundred up to 10^{15} MeV/nucleon, because thick detectors with large surface areas are required to measure these rare, energetic particles. Such detectors would be prohibitively expensive to launch into space. Cosmic rays with energies greater than 10^{16} eV are extremely rare, meaning that a large-surface-area detector is needed to detect any particles on a reasonable time scale. At high energies, incident cosmic rays hit the top of the atmosphere and precipitate large showers of secondary particles. These showers are detected on the ground by looking for the Cherenkov radiation or fluorescence created by secondary charged particles in the atmosphere.

1.4.1 Advanced Composition Explorer

NASA's Advanced Composition Explorer (*ACE*) was launched August 25th, 1997, on a Delta II rocket from the Kennedy Space Center in Florida. The spacecraft carries a suite of nine instruments to measure the interplanetary magnetic field, and the ionic charge state, elemental, and isotopic composition of particle populations ranging in energy from low-speed solar wind ($\sim$400 km/sec) to low-energy cosmic rays (several hundred MeV/nucleon). *ACE* is in a halo orbit around the first Lagrangian point between the Sun and the Earth (L1, about a million miles sunward of Earth) and thus is not affected by the Earth's magnetic field. The Cosmic Ray Isotope Spectrometer is the highest-energy instrument aboard *ACE*, and is discussed in more detail in the next chapter. Cosmic ray measurements by the CRIS telescope will be used in this work to deduce the source composition of the sulfur, argon, and calcium isotopes.

Chapter 2

The Cosmic Ray Isotope Spectrometer

The Cosmic Ray Isotope Spectrometer (CRIS) aboard *ACE* measures the energy, mass, and charge of Galactic cosmic rays from helium through zinc at energies from about 50 to 600 MeV/nucleon. The collecting power of this instrument is fifty times larger than any previous instrument of its kind; the CRIS geometry factor is 250 $\mathrm{cm}^2\,\mathrm{sr}$. An incoming particle passes through scintillating optical fibers for trajectory determination and stops in one of four identical stacks of silicon solid-state detectors. As of this writing, the CRIS instrument has been functioning splendidly for nearly nine years, well beyond its proposed two-year mission length. A comprehensive description of the CRIS instrument is given in Stone *et al.* (1998).

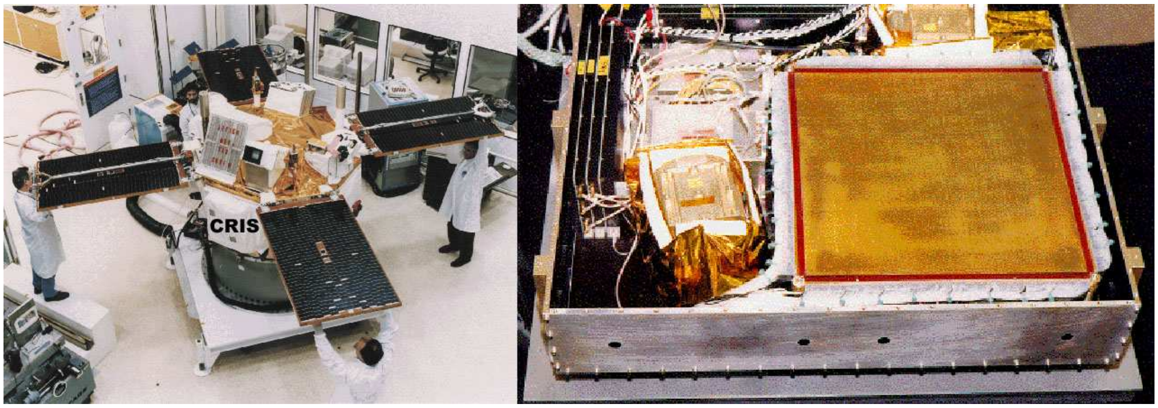

Figure 2.1: The CRIS instrument on the *ACE* spacecraft

2.1 The ΔE vs. E' technique

The method that CRIS uses to identify particles using silicon detectors has been used for many years, though its implementation in CRIS is unparalleled in terms of collecting power and mass resolution.

As a particle of charge Z, mass M, and kinetic energy E penetrates material, it loses energy according to the Bethe-Bloch formula (Equation 1.1). This formula can be integrated to express the particle's total range R after depositing all of its energy E into the material. The relationship between E and R depends upon the nature of the material (its mean excitation potential I), but it is possible, for example, to express the particle's range R in silicon as a function of its charge, mass, and energy per nucleon:

$$R = R_{Z,M}(E/M) \tag{2.1}$$

Equation 2.1 is known as a range-energy relation.

If the particle passes through a silicon detector of thickness L and emerges with kinetic energy E', one can say that the difference in range between the particle at energy E and the same particle at E' is just the thickness of the silicon material it penetrated:

$$R_{Z,M}(E/M) - R_{Z,M}(E'/M) = L \tag{2.2}$$

Consider two detectors and the particle incident at an angle θ as shown in Figure 2.2. The particle loses energy ΔE in the first detector and loses the remainder of its energy E' in the second detector, such that $E = \Delta E + E'$. The pathlength of the particle in the first

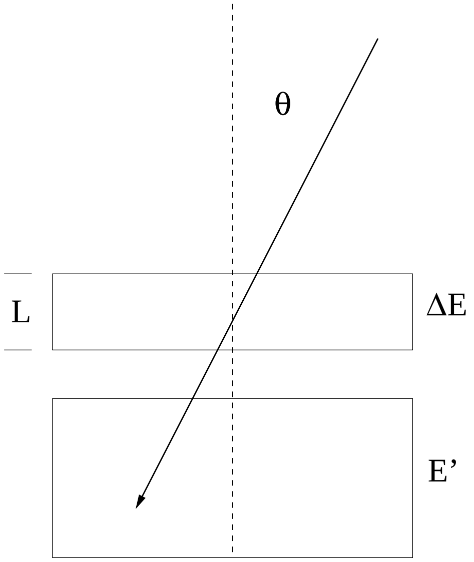

Figure 2.2: Schematic of the ΔE vs. E' method

detector is $L/cos(\theta)$ or $Lsec(\theta)$, so Equation 2.2 becomes:

$$R_{Z,M}((\Delta E + E')/M) - R_{Z,M}(E'/M) = Lsec(\theta). \tag{2.3}$$

If one assumes a range-energy relation of the form (Stone *et al.*, 1998):

$$R_{Z,M}(E/M) \approx \frac{kM}{Z^2}\left(\frac{E}{M}\right)^{\alpha}, \tag{2.4}$$

it is possible to use Equation 2.3 to derive an expression for mass:

$$M \approx \left(\frac{k}{Z^2 Lsec(\theta)}\right)^{\frac{1}{\alpha-1}} ((\Delta E + E')^{\alpha} - E'^{\alpha})^{\frac{1}{\alpha+1}}. \tag{2.5}$$

For the cosmic ray particles that CRIS is detecting, $M/Z = 2+\epsilon$ with $\epsilon \leq 0.4$; isotopes with M/Z outside this range have half-lives that are too short to be found in Galactic cosmic rays. With this assumption, the pseudo-charge of the particle can be derived:

$$Z_* \approx \left(\frac{k}{Lsec(\theta)(2+\epsilon)^{\alpha-1}} \right)^{\frac{1}{\alpha+1}} ((\Delta E + E') - E'^{\alpha})^{\frac{1}{\alpha-1}} \tag{2.6}$$

The elements separate themselves neatly into bands when ΔE is plotted against E' as in Figure 2.3. The isotopes are separated into sub-bands, with spacing $(2+\epsilon)(a+1)/(a-1) \approx 8$ times less than the spacing between elements. In the practical analysis of CRIS data, charge is first calculated from Equation 2.6, and the resulting histogrammed data shows well-separated element peaks. From these peaks, an integer Z value is assigned, and mass is calculated from Equation 2.5.

Uncertainties in the measured quantities ΔE, E', and L affect the final calculation of a particle's mass M (Equation 2.5). The uncertainty of M, called the mass resolution (σ_M), determines how well one can identify individual isotopes. The CRIS instrument achieves outstanding mass resolution: $\sigma_M \leq 0.25$ amu. A discussion of the important contributions to mass resolution is given in Section 3.1.

2.2 The Scintillating Optical Fiber Trajectory system

After an incident particle passes through the CRIS window, it traverses the Scintillating Optical Fiber Trajectory hodoscope system (SOFT). The SOFT system (Stone *et al.*, 1998; Klarmann *et al.*, 1998) is used to measure the particle's trajectory, and consists of three xy scintillating fiber planes and a trigger plane. The fibers are polystyrene doped with scintillation dyes. They measure 180 μm square, plus 10 μm of acrylic cladding on each side; SOFT uses nearly ten thousand of these fibers. A black ink coating on each fiber cladding prevents optical coupling between neighbors. Individual fibers are laid parallel to

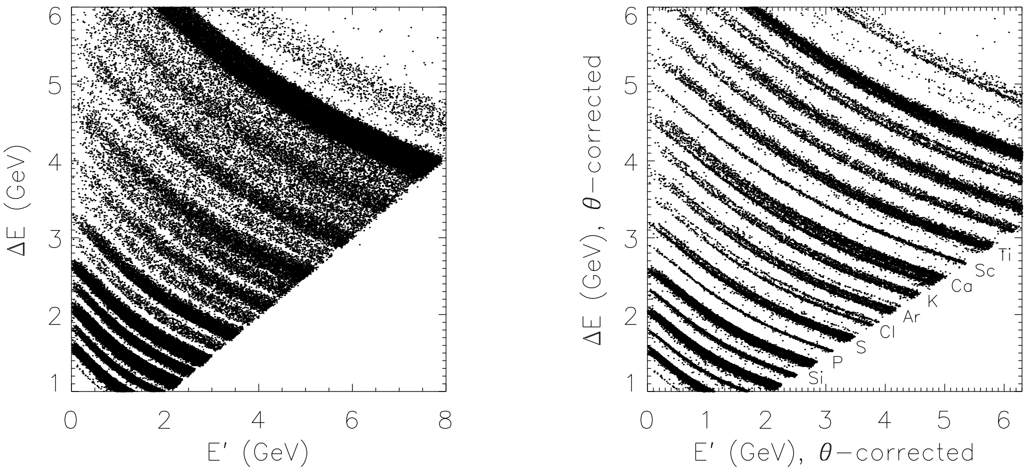

Figure 2.3: The left plot shows ΔE vs. E' flight data for two consecutive CRIS detectors without angular information from the hodoscope; the right plot shows the element bands corrected for angle. The elements separate themselves into bands and the isotopes into sub-bands once the angle correction is made. For both plots, the particle incident angle is restricted to be less than 25° , the ΔE detector is Range 3, and the E' detector is Range 4.

each other to form a layer, with the next layer mounted orthogonal to the first, forming an xy plane. The SOFT fiber planes form an active region 26×26 cm. The photons generated by a penetrating particle are lightpiped to two (for redundancy) image intensifier assemblies. The intensified image of the 3×24 mm fiber bundle is read out by a 244×550 pixel CCD.

2.3 Silicon detector telescopes

After passing through the SOFT hodoscope, an incoming particle next penetrates one of four CRIS telescopes, consisting of fifteen stacked silicon detectors. These detectors measure the energy loss of the particle, and consequently determine its charge and mass by the process described in Section 2.1. Each silicon detector is 3 mm thick, cylindrical in shape with a 10 cm diameter, and made of nearly pure silicon using the lithium compensation technique (Allbritton *et al.*, 1996). The detectors are single-grooved or double-grooved; the single-grooved detectors have an inner active region separated from an outer annulus

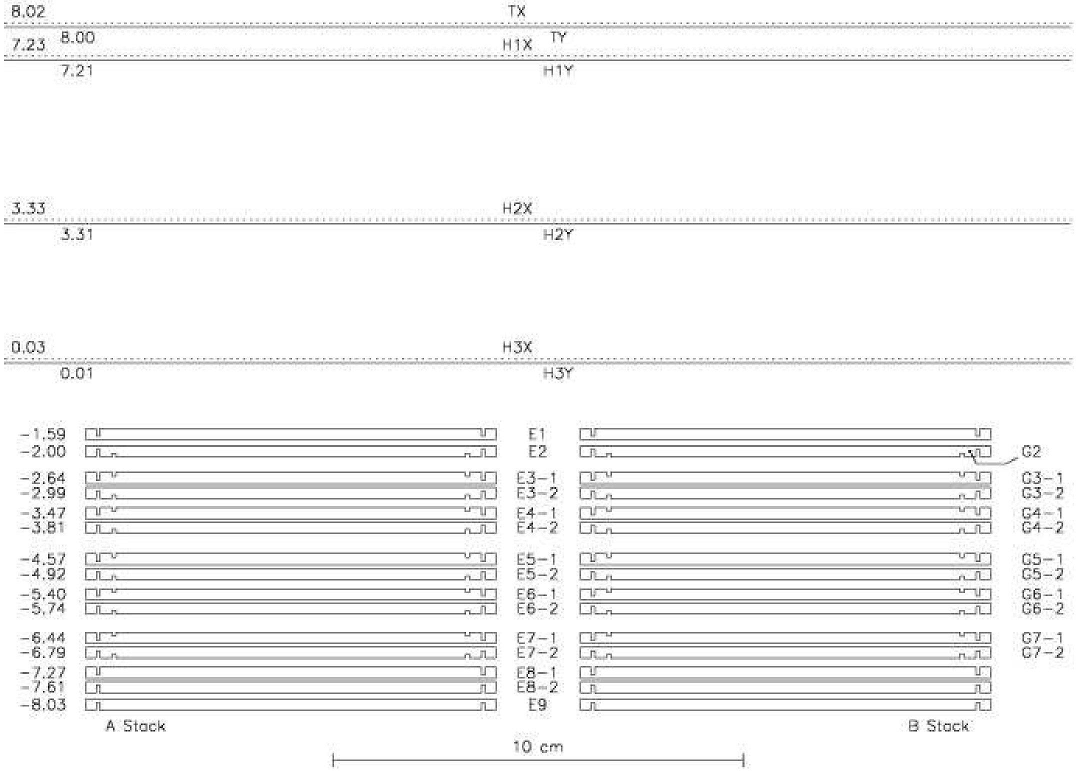

Figure 2.4: Side view schematic of SOFT and the CRIS stack, two of the four telescopes are visible. The dimensions on the left indicate the position (in cm) of the top surface of each sensor relative to the bottom of the SOFT system. TX and TY are the SOFT trigger planes, the SOFT hodoscope planes are labeled H1X through H3Y, E1 through E9 are the inner active regions of the silicon detectors, and G2 through G7-2 are the guard rings of the double-grooved detectors.

used for mounting the detector, the double-grooved design creates an active guard ring that is read out separately from the detector's inner area. The ΔE vs. E' technique requires a measurement of the particle's total energy, so a particle not stopping in the telescope will not be identified accurately. These guard rings, together with the E9 detector at the bottom of the stack (see Figure 2.4), provide an active anticoincidence to discard particles that penetrate the sides and back of the telescope.

Figure 2.4 shows a cross-section of the CRIS instrument. Detectors labeled E1, E2, and E9 are single wafers, and E3 through E8 are paired. Detectors E1, E8, and E9 are single-grooved; the others are double-grooved. A particle stopping in E2 is called a "Range

2" particle, a "Range 3" particle stops in E3, and likewise down to the deepest penetrating valid event: a "Range 8" particle.

2.4 CRIS event data

A valid CRIS event must create a signal in the trigger plane of SOFT and detectors E1 and E2, with no signal in any of the guard rings or E9. An onboard microprocessor reads a 12-bit signal from a subset of the 32 pulse-height analyzers connected to the system of silicon detectors. A CRIS event consists of the pulse-height analyzer values with signals above threshold, along with the position and intensity of the two brightest centroids (clusters of bright adjacent pixels) of the SOFT CCD. The events, varying in length from 31 bytes to 162 bytes, are compressed and, along with event rates, trigger rates, housekeeping data (temperatures, current readings, etc.), and livetimes for each 256-second cycle, are stored in the onboard Solid State Data Recorder. The CRIS data are downloaded from *ACE* to Earth in an eleven-minute window each day by the NASA Deep Space Network. The data are sent to the *ACE* Integrated Mission Operations Center at the Goddard Space Flight Center and, after some processing, a publicly available data set is released by the *ACE* Science Center (Garrard *et al.*, 1998). Data sets and plots from CRIS and the other *ACE* instruments are available online at: http://www.srl.caltech.edu/ACE/ASC/.

This work uses event data read in by the `xpick` routine, developed at Caltech in the IDL programming language. Some preliminary analysis and data cuts (as described in Table 3.1) are done by `xpick`.

Chapter 3

Data Analysis

The CRIS instrument has compiled a high quality data set of Galactic cosmic rays since it detected its first particle on August 28, 1997. The large geometry factor, excellent mass resolution, and several years of collecting time make it possible to study the abundances of isotopes with unprecedented precision.

To achieve the most accurate possible measurements, certain cuts are made on the data to distinguish a valid particle event from one that will give an incorrect mass value. Applying further corrections yields a data set that shows clearly defined mass peaks. A maximum-likelihood estimation is employed to calculate the abundance of a given isotope. After further corrections due to instrumental effects and the spectral shape of each isotope are made, isotopic abundances of Galactic cosmic rays arriving in the vicinity of Earth are derived.

3.1 Calculation of particle mass

The charge Z and mass M of a particle are calculated using the $\Delta E - E'$ technique described in Section 2.1. For a particle passing through more than two detectors, it is possible to calculate its mass multiple ways, using different combinations of ΔE and E' detectors. For example, the mass of a particle that stops in Range 5 (R5) of the CRIS instrument can be calculated using R4 as the ΔE detector and R5 as E', or the sum of the energies measured in the second and third detector, R2+R3, as ΔE and R4+R5 for E', etc. The optimal way to calculate M is whatever method results in the best mass resolution. A detailed analysis of this problem is given in Appendix A. The following method turns out to result in the best mass resolution: for a particle stopping in detector R, calculate its mass R-1 different ways by using individual detectors as the ΔE detector and the sum of all subsequent detectors as E'. For a Range 5 particle, the mass is calculated as the weighted average of the following $\Delta E \cdot E'$ combinations: R1·(R2+R3+R4+R5), R2·(R3+R4+R5), R3·(R4+R5), R4·R5. Each weight is the inverse square of the mass resolution for that $\Delta E \cdot E'$ combination. Therefore, to properly compute a particle's mass from a series of $\Delta E \cdot E'$ measurements, it is necessary to know the mass resolution for this detector combination and particle species. The dominating contributions to mass resolution are well known and can be computed analytically.

3.1.1 Contributions to mass resolution

From Section 2.1:

$$M(L, \theta, \Delta E, E'; \alpha, k, Z) = \left(\frac{k}{L_0 sec(\theta) Z^2} [(\Delta E + E')^\alpha - E'^\alpha] \right)^{\alpha - 1} . \tag{3.1}$$

Contributions to mass resolution will arise from uncertainties in the measured quantities L, θ, ΔE, and E'. Taking partial derivatives of Equation 3.1 with respect to each measured quantity tells us how the mass resolution depends on measurement uncertainties:

$$\sigma_M^2 = \left(\frac{\partial M}{\partial L} \right)^2 \sigma_L^2 + \left(\frac{\partial M}{\partial \theta} \right)^2 \sigma_\theta^2 + \left(\frac{\partial M}{\partial E'} \right)^2 \sigma_{E'}^2 + \left(\frac{\partial M}{\partial \Delta E} \right)^2 \sigma_{\Delta E}^2 . \tag{3.2}$$

Each partial derivative of M is proportional to M, so mass resolution is proportional to mass.

3.1.1.1 Landau fluctuations

The energy deposited by an incoming particle in the ΔE detector is due to a large number of independent ion-electron collisions in the silicon. Particles of the same species and of the same energy do not lose exactly the same amount of energy traveling through a given thickness in the CRIS stack. These fluctuations in energy loss are called Landau fluctuations. Since this is an inherent property of the energy-loss process in silicon detectors, the measurement uncertainties due to Landau fluctuations provide a lower bound on the mass resolution of the instrument.

For particles of atomic number and energies relevant to CRIS, the energy loss in a thin detector (where energy loss in the detector is a small fraction of the particle's initial energy) of thickness x is Gaussian (Stone *et al.*, 1998; Rossi, 1952). The r.m.s. spread is given by $\sqrt{(d\sigma^2_{\Delta E}/dx)_{\text{Landau}}x}$ where:

$$\left(\frac{d\sigma^2_{\Delta E}}{dx}\right)_{\text{Landau}} = Z^2\frac{(0.396\ \text{MeV})^2}{\text{g cm}^{-2}}\frac{Z_m}{A_m}\frac{\gamma^2+1}{2} \tag{3.3}$$

is the derivative of the energy loss variance with respect to the length of material the incident particle has traversed (Stone *et al.*, 1998). Here, Z is the particle's charge, Z_m and A_m are the charge and mass number of the target medium (silicon, in the case of CRIS detectors), and γ is the Lorentz factor of the particle.

For a thicker detector, one must take into account the fact that particles at different energies lose energy at different rates (Payne, 1969). That is to say, dE/dx for a given element (the function $\chi_{\rm Z}(E)$ in the following equation) is not constant. The Landau contribution to $\sigma_{\Delta E}$ in Equation 3.2 can then be calculated:

$$\sigma^2_{\Delta E(\text{Landau})} = M \int_{E'/M}^{E/M} \frac{\chi^2_{\rm Z}(E'/M)}{\chi^3_{\rm Z}(\epsilon)} \left(\frac{d\sigma^2_{\Delta E}}{dx}\right)_{\text{Landau}} d\epsilon, \tag{3.4}$$

where E is the incident energy of the particle, and E' is its energy after the particle passes through the ΔE detector.

Since total energy of the particle is conserved, the amount of energy fluctuation in the ΔE detector is simply the opposite of the energy fluctuation in the E' detector. The total contribution to the mass resolution due to Landau fluctuations is the total of these two effects:

$$\sigma_{\text{M, Landau in L}} = \left(\frac{\partial M}{\partial \Delta E} - -\frac{\partial M}{\partial E'}\right) \sigma_{\Delta E(\text{Landau})}. \tag{3.5}$$

3.1.1.2 Multiple Coulomb scattering

When the incident charged particle passes in the neighborhood of a nucleus of the detector material, Coulomb interactions cause a small deflection in the particle's trajectory (the radiation emitted during this process can be neglected). The total of many such scatterings in the ΔE detector causes the pathlength to differ from the assumed line. As detailed in Payne (1969), the distribution of trajectories after passing through a scattering plane of thickness x is approximately Gaussian, when projected on a plane centered on the incoming trajectory. The r.m.s. angular width of the Gaussian is given by $\sqrt{(d\sigma^2_{\delta\theta}/dx)x}$, where the derivative of the angular distribution's variance with respect to path length is given by:

$$\frac{d\sigma^2_{\delta\theta}}{dx} \simeq \left(\frac{Z}{M}\frac{0.0146}{\beta^2\gamma^2}\right)^2 \frac{1}{X_0}. \tag{3.6}$$

Here, β is the particle's velocity divided by the speed of light, and X_0 is the radiation length of the medium (21.82 g/cm^2 for silicon). The r.m.s. path-length error due to multiple scattering is (Stone *et al.*, 1998):

$$\sigma_{\mathrm{L\ (scatt)}} = Ltan(\theta)\sqrt{M\int_{E'/M}^{E/M}\left(\frac{\mathcal{R}(E/M)-\mathcal{R}(\epsilon)}{L}\right)^2\left(\frac{d\sigma_{\delta\theta}^2}{dx}\right)_\epsilon\frac{d\epsilon}{\chi_{\mathrm{Z}}(\epsilon)}}, \tag{3.7}$$

where $\mathcal{R}(\mathcal{E})$ is the projected range of a particle as a function of its energy, L is the angle-corrected distance traversed in the ΔE detector (equal to $L_0 sec(\theta)$ where L_0 is the detector thickness), and θ is the incoming particle's angle from the normal to the detector plane.

The contribution to mass resolution from multiple Coulomb scattering is:

$$\sigma_{\mathrm{M,\ scatt}} = \frac{\partial M}{\partial L}\sigma_{\mathrm{L\ (scatt)}}. \tag{3.8}$$

3.1.1.3 Other contributions

Additional contributions to mass resolution include trajectory measurement errors (uncertainties in the trajectory slope and intercept as calculated by SOFT), mapping errors (inaccuracies in the thickness maps of the CRIS detectors), and energy measurement errors (due to the finite channel width of the pulse height analyzer and noise in the electronics). All of these contributions are insignificant compared to Landau fluctuations and multiple scattering. Trajectory measurement errors were calculated to be less than 0.05 amu r.m.s., and mapping errors were found to be approximately 0.02 amu. Energy measurement errors are less than 0.01 amu, due to the low noise in the CRIS electronics and twelve-bit digitization of the pulse height analyzers.

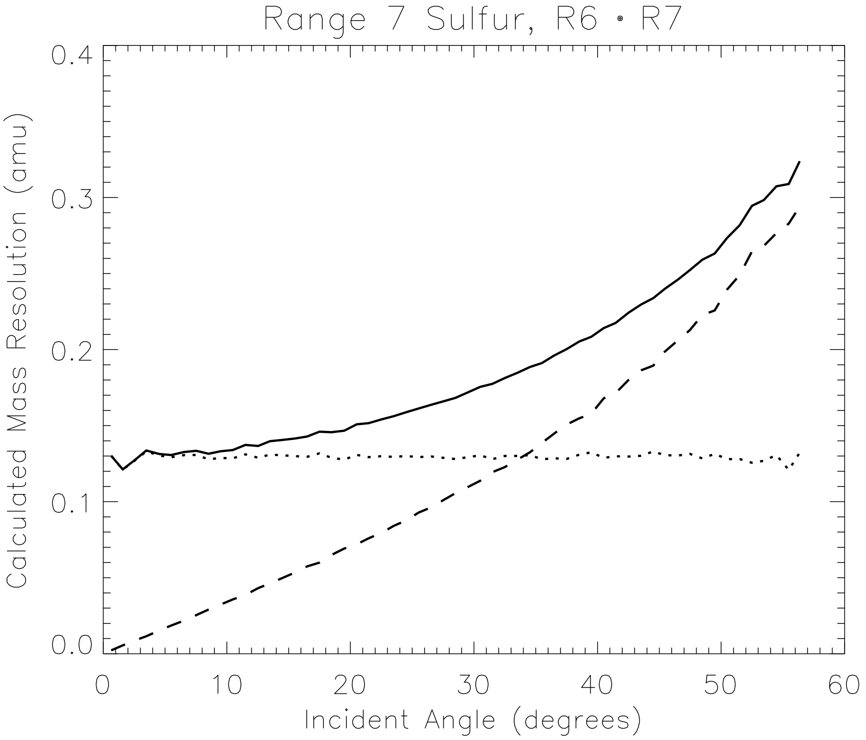

Figure 3.1: Mass resolution as a function of incident angle for range 7 sulfur, using R6 as the ΔE detector and R7 as the E'. The dashed line is the multiple scattering contribution, the dotted line represents Landau fluctuations, and the solid line is their quadrature sum.

3.1.2 Mass resolution as a function of incident angle

As described in Section 3.1, to calculate the correctly weighted mass values for each particle detected by CRIS, it is necessary to know the mass resolution for each $\Delta E \cdot E'$ combination. The above analysis of the dominant contributors to mass resolution, Landau fluctuations and multiple scattering, will provide a good estimation for this quantity. Equations 3.1 – 3.8 show that mass resolution will depend on such quantities as the particle species (Z and M), the particle energy (γ and β), the detector thickness (L), and the incident angle of the incoming particle (θ). For a given particle species and $\Delta E \cdot E'$ combination, the relationship between mass resolution and incident angle can be established, as is shown in Figure 3.1.

For a range R particle, the single detector $\Delta E \cdot E'$ combination that yields the best calculated mass resolution is R-1 $\cdot$ R. As shown in Figure 3.2, the mass resolution gets

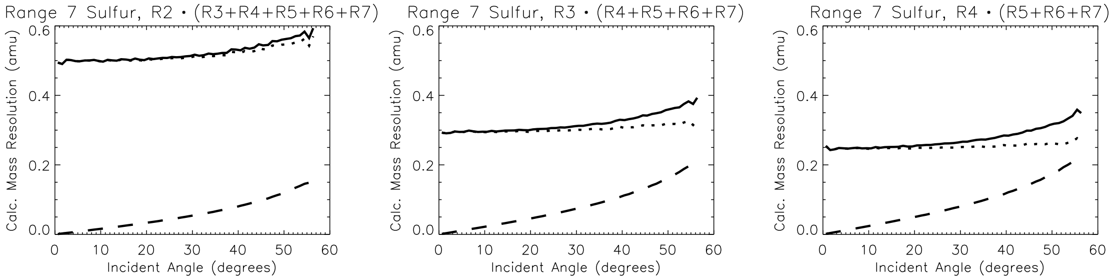

Figure 3.2: Calculated mass resolution as a function of incident angle for three different $\Delta E \cdot E'$ combinations. The Landau fluctuations are larger when the ΔE detector is thin relative to E'. Also contributing to better mass resolution in the right panel, the ΔE energy loss in R4 is larger than in R3 and R2, meaning the energy fluctuations are a smaller fraction of the total deposited energy in ΔE.

worse as the ΔE detector gets thinner compared to the E' detector.

The multiple scattering contributions for different $\Delta E \cdot E'$ combinations changes only slightly in Figure 3.2 because this is a phenomenon occurring in the ΔE detector, the thickness of which does not vary much across the different detector combinations considered here. Conversely, the Landau fluctuations change significantly across Figure 3.2. These statistical energy fluctuations are a larger fraction of the total energy deposited by the incident ion when the number of ion-electron collisions is small. Therefore, Landau fluctuations are more significant when the ΔE detector is thin relative to the E' detector.

3.1.3 Weighting $\Delta E \cdot E'$ combinations for average mass calculation

A particle stopping in range R has R-1 different calculated masses. Since each ΔE measurement is independent of the others, each of the R-1 different masses are mostly uncorrelated. For further discussion, see Appendix A. Taking a properly weighted average of the R-1 different masses will therefore yield a better mass estimate than just using one of these measurements. The SOFT hodoscope determines each particle's incident angle θ. Therefore, using the analytic calculations from Section 3.1.2 it is possible to analytically model the mass resolution $\sigma_{M_R}(\theta)$ for each of the R-1 calculated masses. For each particle, the average mass is calculated using weights equal to the inverse square of $\sigma_{M_R}(\theta)$:

$$M_{avg} = \frac{\frac{M_1}{\sigma_{M_1}(\theta)^2} + \frac{M_2}{\sigma_{M_2}(\theta)^2} + ... + \frac{M_{R-1}}{\sigma_{M_{R-1}}(\theta)^2}}{\frac{1}{\sigma_{M_1}(\theta)^2} + \frac{1}{\sigma_{M_2}(\theta)^2} + ... + \frac{1}{\sigma_{M_{R-1}}(\theta)^2}}. \tag{3.9}$$

3.2 Data selection

3.2.1 Initial data whittling

Certain physical processes, geometries, and accidental coincidences of incident Galactic cosmic ray nuclei in the CRIS instrument can cause an inaccurate calculation of the energy or species of the incident particle. Cuts on the data can be made to exclude some of these events and improve overall mass resolution. These cuts are shown in Table 3.1 for sulfur particles in the CRIS data set.

3.2.2 Residual range correction and dead-layer cuts

The fabrication of the lithium-drifted silicon detectors produces a 55-70 μm thick "dead-layer" on one side of the wafer. In this region, a significant fraction of the ionization charge created by the incident particle is not collected in the output signal. The region of the wafer near the dead-layer is also not 100% efficient in ionization charge collection. For particles stopping in the dead-layer or close to it, the E' energy measured will be too low, moving the particle to the left on the ΔE vs. E' plot and causing it to be assigned a too-small mass (as seen in the right side of the plots in Figure 3.3). Therefore, care must be taken to remove particles that stop in the vicinity of the dead-layer. Dead-layer cuts were made to the data set based on the particle's depth in the stopping detector for each range and telescope combination, as given in Scott (2005).

CRIS Data Exclusions		
Exclusion	Description	Percentage Remaining
Hazard	Exclude events recorded less than 130ms after another event.	98%
Trajectory	Discard events without valid trajectories.	74%
Range	Only particles that stop in ranges 2 through 8 are valid, also eliminate particles that deposit energy in the range 9 (anticoincidence) detector.	26%
SOFT deviation	Reject particles that lie outside 5σ of the trajectory defined by a straight line joining hodoscope fiber hits.	26%
Guard ring	Particles must be 500 μm away from guard rings in all hit detectors.	25%
SOFT trigger	Exclude particles that pass less than 500 μm from the edge of the SOFT active area.	24%
Charge Consistency	Calculate Z of the particle using different detector combinations for dE and E' and only accept particles with a consistent calculated Z. This eliminates heavy nuclei that fragment into lighter nuclei in the silicon detector stack.	22%

Table 3.1: Cuts applied to the CRIS data set to improve mass resolution

The calculation of a particle's mass requires a function that relates a particle's energy and species with its range in silicon. These functions (Anderson & Ziegler, 1977) claim uncertainties of about 5%, but are more inaccurate at the end of a particle's range, where complicated physical processes such as charge pickup become important. If calculated mass is plotted against the residual range in the stop detector, one sees a mass dependence on residual range as shown in Figure 3.3. This effect is due to inaccurate range-energy functions and is not a physical property of the telescope. The shape of the trend varies with the particle's range and the CRIS detector stack hit. Also, the mass dependence on

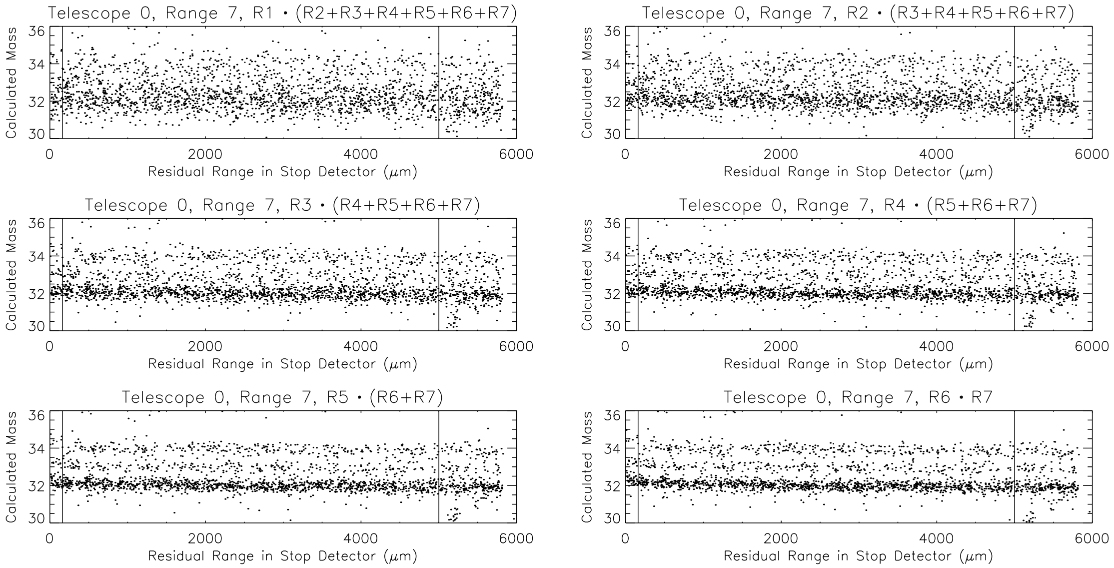

Figure 3.3: Calculated mass vs. residual range for range 7 sulfur isotopes detected in telescope 0. Vertical lines are the dead-layer cuts: the high cutoff is to remove particles that stop near the dead-layer in the stop detector, the low cutoff is to remove particles stopping near the dead-layer in the backside of the previous detector. The improving mass resolution from R1·(R2+R3+R4+R5+R6+R7) to R6·R7 is obvious in these plots, and is explained in Section 3.1.2

residual range changes as the $\Delta E \cdot E'$ combination changes.

To correct for the dependence on residual range, the calculated mass of the dominant isotope of the element of interest was assumed to vary linearly at higher values of residual range, and as a power-law at lower values. Continuity was forced at the boundary between the linear and power-law fits, typically ~1000 μm. After iteratively defining the dominant isotope to be the particles in the band defined by the fits, the dependence of the calculated mass on residual range was found. All particles of an element were then adjusted by subtracting off this dependence.

After the residual range dependence was removed, the average mass per particle was calculated using the method described in Section 3.1.

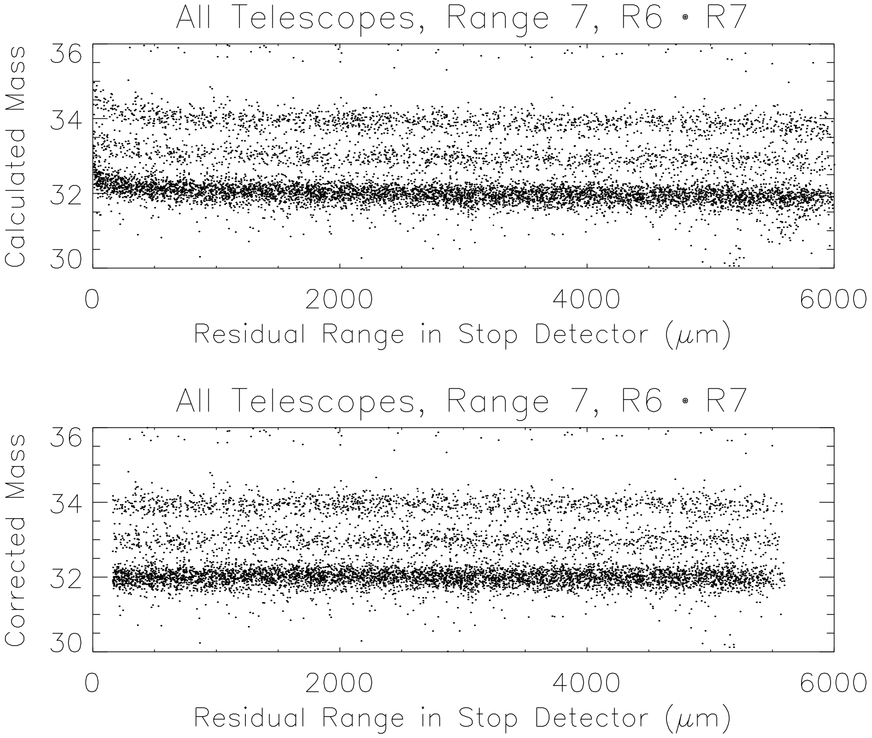

Figure 3.4: The calculated mass is shown in the top plot for sulfur isotopes of range 7, all telescopes, and the R6·R7 mass calculation. The bottom plot shows the data with dead-layer cuts and the residual range dependence removed.

3.3 The data set

3.3.1 Solar minimum and solar maximum

The level of solar modulation affects the spectra of Galactic cosmic rays arriving at Earth as described in Section 1.3. Energy-dependent abundances of isotopes will also be affected by solar modulation, so it is necessary to calculate abundances during time periods when the solar modulation level is relatively constant. The solar modulation parameter ϕ as calculated by Wiedenbeck (2006), described in Section 4.2.2, and shown in Figure 3.5, serves as a measure of the modulation level. The data will be divided into two sets based on this parameter: August 28, 1997, through August 17, 1999, will be referred to as solar minimum, with ϕ between 300 MV and 500 MV; and data recorded from February 1, 2000, to April 1, 2004, (700 MV $\leq \phi \leq$ 1200 MV) will be called solar maximum.

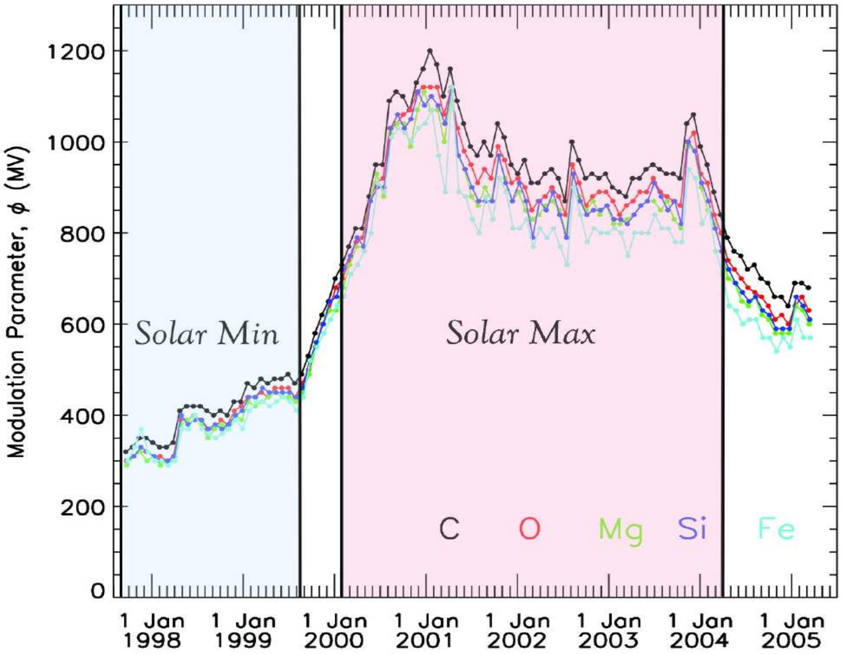

Figure 3.5: The solar modulation parameter ϕ, as calculated by Wiedenbeck (2006), for the five different elements listed. The solar minimum time period is in blue, solar maximum is in red.

3.3.2 Small angles and large angles

Particles detected by CRIS can enter the telescope over an incident angle range from 0° to ~70° . Mass resolution decreases as the incident particle angle increases: particles entering the telescope at 50° will have broader isotope peaks than particles entering at 10° . This effect is studied analytically in Appendix A and can be clearly seen in the CRIS data, as shown in Figure 3.6.

The higher-resolution low-angle data, $\theta < 25°$, is separated from the lower-resolution high-angle data, $25° < \theta < 50°$. Above 50° , the rarer peaks, like ^{33}S, are not resolvable (the inflection point between peaks is lost) so these data are ignored. Separating out the high-resolution data will provide a check on the abundances calculated from the low-resolution

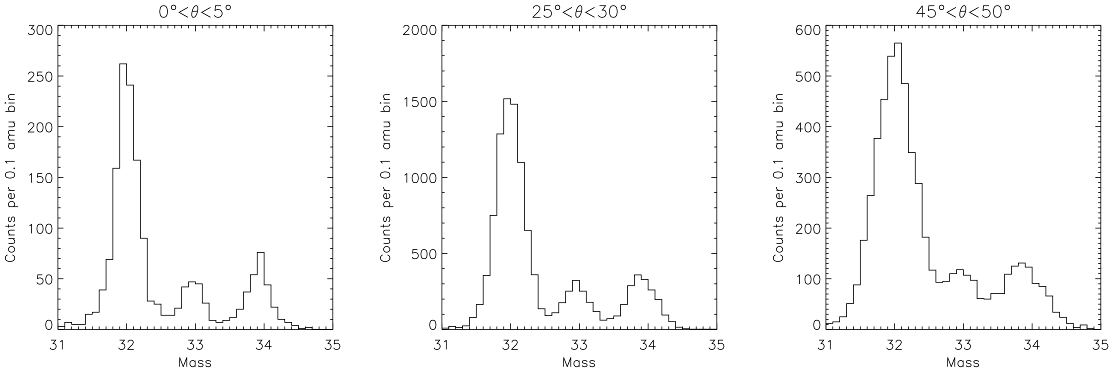

Figure 3.6: Histograms of the three most abundant sulfur isotopes for a five-degree-wide angle acceptance shown for three different angle ranges. The decreasing mass resolution (due to multiple scattering), seen as broadening of the peaks, is evident as the angle acceptance bin increases from 0° – 5° to 45° – 50° .

data set. Inclusion of $25° < \theta < 50°$ increases the size of the data set by 122%.

Solar Modulation and Angle Divisions		
Modulation	Angle Range	Percentage of Data Set
Solar Min	0° - 25°	24%
Solar Min	25° - 50°	30%
Solar Max	0° - 25°	21%
Solar Max	25° - 50°	25%

Table 3.2: The size of the four modulation/angle data sets as a percentage of the total

3.3.3 Range separation

For each element of interest, the data are further divided into ranges 2 through 8. Each CRIS detector range for the species of interest has a median energy as listed in Table 3.3.

CRIS Median Energy				
Element	Range	Median Energy (MeV/nucleon)		
		$0° < \theta < 25°$	$25° < \theta < 50°$	$0° < \theta < 50°$
Phosphorus	2	109	121	117
	3	149	164	157
	4	191	211	201
	5	229	250	238
	6	262	286	270
	7	293	317	303
	8	324	349	332
Sulfur	2	115	127	122
	3	155	172	165
	4	200	221	211
	5	240	263	250
	6	275	301	285
	7	309	336	318
	8	340	369	349
Argon	2	123	135	130
	3	165	183	176
	4	212	236	224
	5	255	280	267
	6	293	320	305
	7	330	358	341
	8	362	396	373
Calcium	2	129	143	137
	3	174	193	185
	4	225	249	236
	5	269	296	281
	6	310	341	323
	7	349	379	360
	8	385	418	396

Table 3.3: Median energies for the elements of interest in CRIS ranges 2-8

3.4 Maximum-likelihood estimation of isotope abundances

3.4.1 Standard deviation as a function of θ

The angle-divided data sets still contain particles incident from a broad range of angles: $0^\circ - 25^\circ$ and $25^\circ - 50^\circ$. As shown in Section 3.1.2, the standard deviation of the mass distribution depends on the incident angle. Therefore, the mass distribution of a mix of N particles coming into the telescope at different angles will not be a simple Gaussian, but rather a sum of N Gaussians with different standard deviations.

A relationship between the incident angle θ of the particle and the associated standard deviation $\sigma(\theta)$ is needed to characterize the distribution of the data sets. Dividing the data into angle bins and fitting Gaussians to the mass histograms yields σ values for various θs (see Figure 3.7).

Figure 3.1 suggests that σ varies as an exponential function of θ plus an offset. The Gaussian fit σs from different-sized angle bins over $0^\circ < \theta < 50^\circ$ are fit with the function $\sigma(\theta) = Ae^{B\theta} + C$, weighted by the errors on the σs calculated from the maximum-likelihood Gaussian fitting algorithm to each bin.

3.4.2 The maximum-likelihood technique

An unbinned maximum-likelihood technique is employed to determine isotope abundances. Another technique that is used in similar problems is the χ^2 method, but this procedure does not work well with low statistics (as is seen between isotope peaks), and can give a different answer depending on how the data are binned. Using $\sigma(\theta)$ for the Gaussian standard deviation precludes the possibility of binning the data by mass: each particle must be looked at individually because it has a unique σ and therefore a unique Gaussian

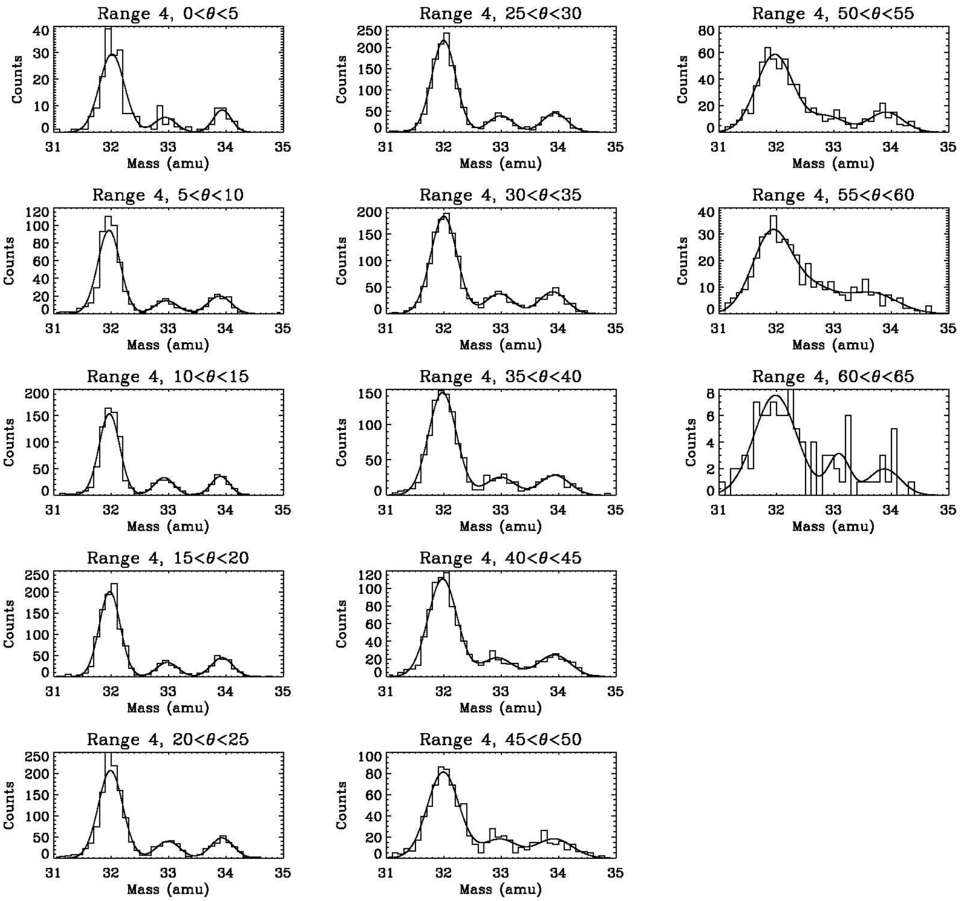
Range 4, 0<θ<5

Range 4, 5<θ<10

Range 4, 10<θ<15

Range 4, 15<θ<20

Range 4, 20<θ<25

Range 4, 25<θ<30

Range 4, 30<θ<35

Range 4, 35<θ<40

Range 4, 40<θ<45

Range 4, 45<θ<50

Range 4, 50<θ<55

Range 4, 55<θ<60

Range 4, 60<θ<65

Figure 3.7: Five-degree-angle bins for range 4 sulfur. The mass resolution of the middle isotope, ^{33}S, is fixed to be the average of the mass resolution of neighboring isotopes, ^{32}S and ^{34}S, because mass resolution should increase approximately linearly with mass (see Section 3.1.1).

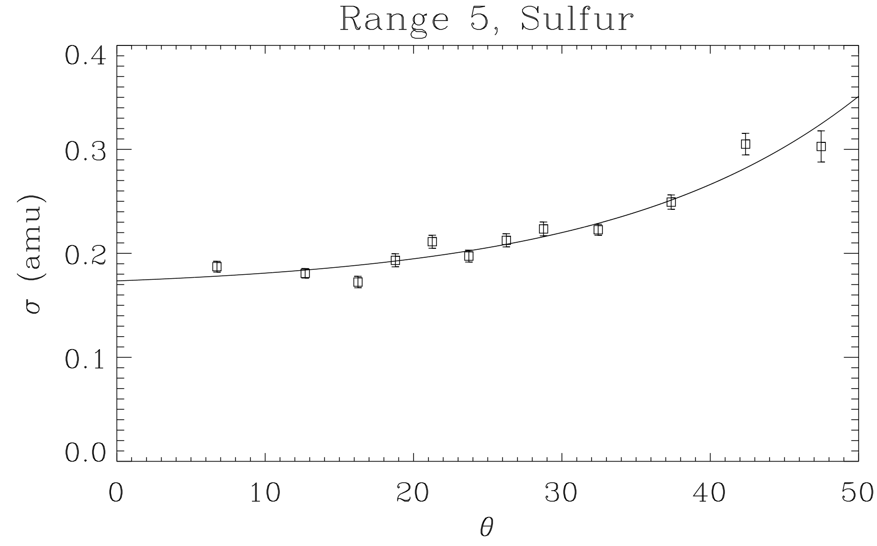

Figure 3.8: Mass resolution as a function of incident angle θ for range 5 ^{32}S. The data are fit with an exponential to get a smooth and continuous function $\sigma(\theta)$.

probability distribution; all particles of similar mass cannot be simply thrown together into one bin.

The technique used here will assume a multiple Gaussian probability distribution for each particle of a given element, with the width of the Gaussians dependent on the angle the particle entered the telescope. The likelihood function describes the joint probability that all the particles in the data set are described by a set of parameters. Changing the parameters to maximize this likelihood will yield the optimal description of the probability distribution function of the data set and the isotope abundances of each element.

For a single particle of element Z and incident angle θ, the probability distribution over n isotopes is:

$$p(A,\mu;m) = \sum_{i=1}^{n} A_i e^{\frac{-(m-\mu_i)^2}{2(\sigma_i(\theta))^2}}. \tag{3.10}$$

The joint probability distribution of N particles is the likelihood function:

$$L(A,\mu)=\prod_{j=1}^{N}p(A,\mu;m_j). \tag{3.11}$$

Taking the natural logarithm of the likelihood function simplifies the calculations. Also, normalization is enforced by an additional term, so that the sum of the distribution is equal to the total number of particles in the data set. The likelihood function to be maximized is:

$$W=\sum_{j=1}^{N}\left(\sum_{i=1}^{n}\frac{-\sqrt{2\pi}}{N}A_i\sigma_{ij}(\theta)+ln\left(\sum_{i=1}^{n}A_ie^{\frac{-(m_j-\mu_i)^2}{2(\sigma_{ij}(\theta))^2}}\right)\right), \tag{3.12}$$

where the σ_{ij}s were calculated in Section 3.4.1 , and therefore are not a parameter to be fit here.

When the log likelihood function (W) is plotted against one of the parameters being determined (a), the uncertainty (σ_a) in the fit parameter can be visualized as the spread of a about the value that maximizes W, a^*. By applying the Central Limit Theorem it is possible to show (Orear, 1982) that for a large number of events, the likelihood function approaches a Gaussian distribution and since $W=ln(L(a))$:

$$\frac{\partial^2W}{\partial a^2}=-\frac{1}{\sigma_a^2} \tag{3.13}$$

and

$$\sigma_a=\frac{1}{\sqrt{-\frac{\partial^2W}{\partial a^2}}}. \tag{3.14}$$

3.5 Instrumental corrections to abundances

3.5.1 Spallation corrections

A particle entering the CRIS instrument has a certain probability of fragmenting as it traverses the windows, hodoscope, and silicon stack. By calculating the charge of the nuclei at various levels in the telescope and requiring that the calculation yields the same value for Z, the spallating nuclei are cut out of the data set (see Table 3.1). The probability for a given nucleus to fragment is different for different species. Therefore, it is necessary to correct for this difference when comparing abundances of isotopes.

Calling $\Lambda(A_i)$ the mean free path against spallation for a particle of mass number A_i, charge Z_i and mean energy $\overline{E}$, the survival probability of this particle passing through a range R of silicon is:

$$\eta_{\mathrm{spall}}(\overline{E}, Z_i, A_i) = exp\left(-\frac{R(\overline{E}, Z_i, A_i)}{\Lambda(A_i)}\right). \tag{3.15}$$

The spallation mean free path can be expressed as:

$$\Lambda(A_i) = \frac{A_T}{N_A \sigma(A_i, A_T)}, \tag{3.16}$$

where A_T is the mass number of the target material (28 for silicon) and N_A is Avogadro's number. To estimate the cross-section interaction between the incident particle of mass A_i and a target nucleus of mass A_T, Bradt & Peters (1950) made the assumption that the effective collision radius is equal to the geometrical radius ($R_{\mathrm{geom}} = r_0 A^{1/3}$), minus a decrement that is of the order of the range of nuclear forces. Westfall *et al.* (1979) proved that this was a good approximation to experimental data using $r_0 = 1.47$ fm and $b = 1.12$:

$$\sigma(A_i, A_T) = \pi r_0^2 (A_i^{1/3} + A_T^{1/3} - b)^2. \tag{3.17}$$

Calculated survival probabilities take into account the material above the detector stack (Stone *et al.*, 1998) and the silicon detectors themselves, with survival probabilities for species of interest in this study varying from 89% for range 2 ^{31}P, to 55% for range 8 ^{46}Ca (see "Spallation Correction", equal to $1/\eta_{\mathrm{spall}}$, in Tables B.1 – B.4).

The error in the spallation correction is predominantly due to uncertainty in the cross-section estimation (Equation 3.17). Due to the exponential form of Equation 3.15, even with large cross-section errors near 10%, the error in the correction will be small. A conservative error estimate of 3% has been assigned to the spallation corrections, as was done in George *et al.* (2006) and Scott (2005).

3.5.2 SOFT efficiency corrections

The detection efficiency of the SOFT hodoscope is nearly 100%. There is a small chance an incident particle will pass between fibers, exciting only knock-on electrons in the cladding instead of a stronger signal from the nucleus depositing energy into the fiber.

To calculate the SOFT efficiency, the charge Z of particles depositing a signal in ranges 4 through 8 was determined without information from the hodoscope. For each Z, it was possible to determine what fraction of these events had well-defined trajectories in SOFT. For elements of Z≥17, SOFT efficiency was better than 99%, falling to around 86% for boron. The systematic uncertainty in this method is small; a 2% error is assigned to the SOFT efficiency corrections (George *et al.*, 2006).

3.6 Mass histograms and derived isotope abundances

A downhill simplex method is used iteratively to maximize the log likelihood function as described by Equation 3.12. The maximum-likelihood parameters A_i and μ_i, along with the $\sigma_{ij}(\theta)$ values from Section 3.4.1, form the functional fit to the data plotted as a curve on the histograms in Figures 3.9 – 3.24.

The number of particles detected of the isotope centered at μ_i is:

$$\mathcal{N}_i = \sum_{j=1}^{N} \frac{\sqrt{2\pi}}{N} \sigma_{ij}(\theta) A_i. \tag{3.18}$$

The abundances for each isotope, CRIS range, time period, and angle bin are given in Appendix B, along with the correction factors and corrected abundances. The mass histograms for phosphorus, sulfur, argon, and calcium are shown in Sections 3.6.1 – 3.6.4.

3.6.1 Phosphorus

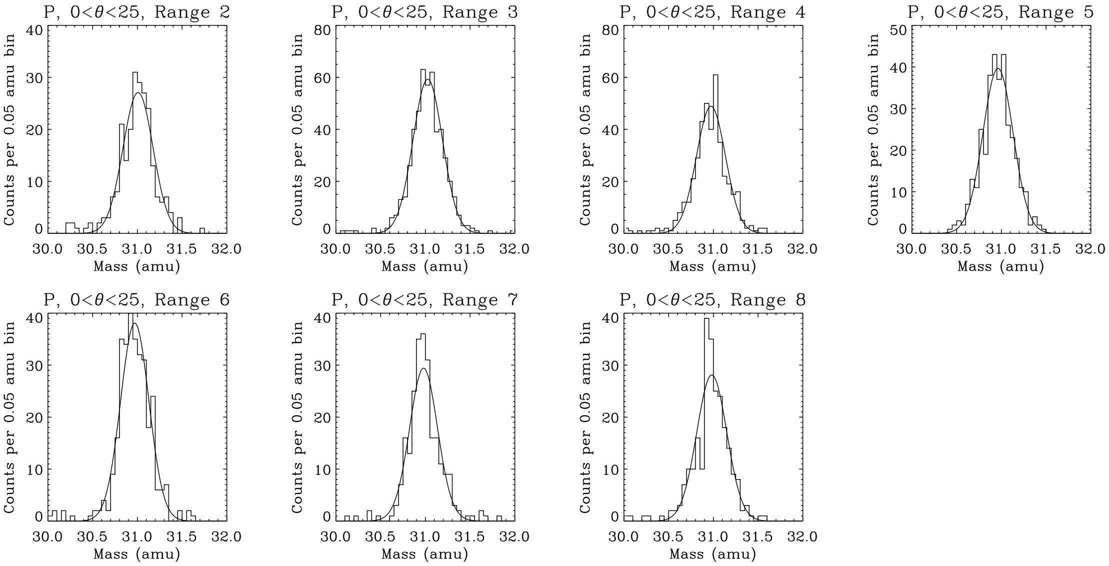
P, 0<θ<25, Range 2
P, 0<θ<25, Range 3
P, 0<θ<25, Range 4
P, 0<θ<25, Range 5
P, 0<θ<25, Range 6
P, 0<θ<25, Range 7
P, 0<θ<25, Range 8

Figure 3.9: Phosphorus histograms for Solar Minimum

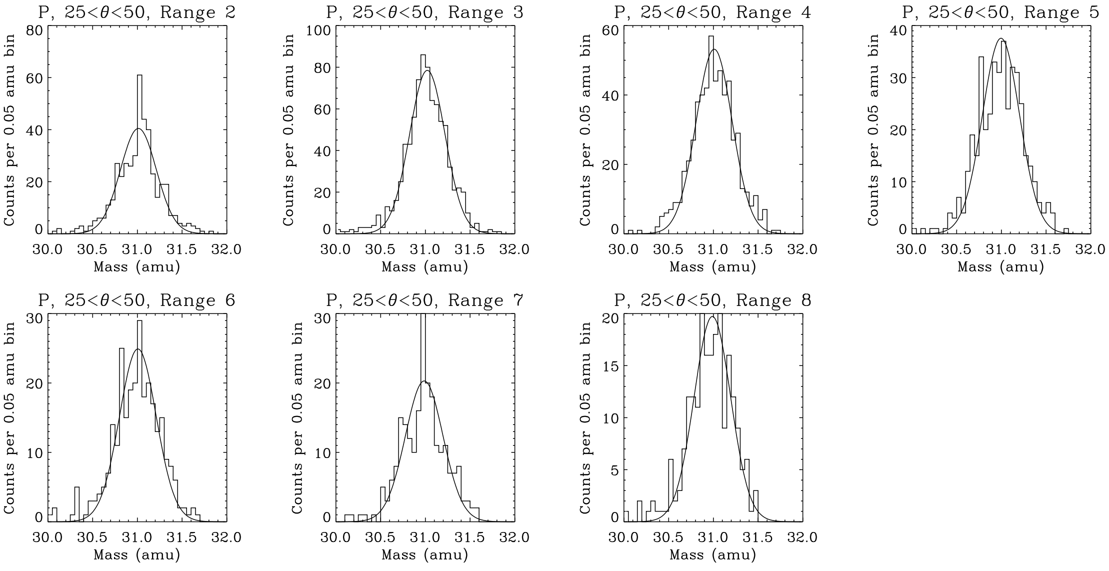
P, 25<θ<50, Range 2
P, 25<θ<50, Range 3
P, 25<θ<50, Range 4
P, 25<θ<50, Range 5
P, 25<θ<50, Range 6
P, 25<θ<50, Range 7
P, 25<θ<50, Range 8

Figure 3.10: Phosphorus histograms for Solar Minimum

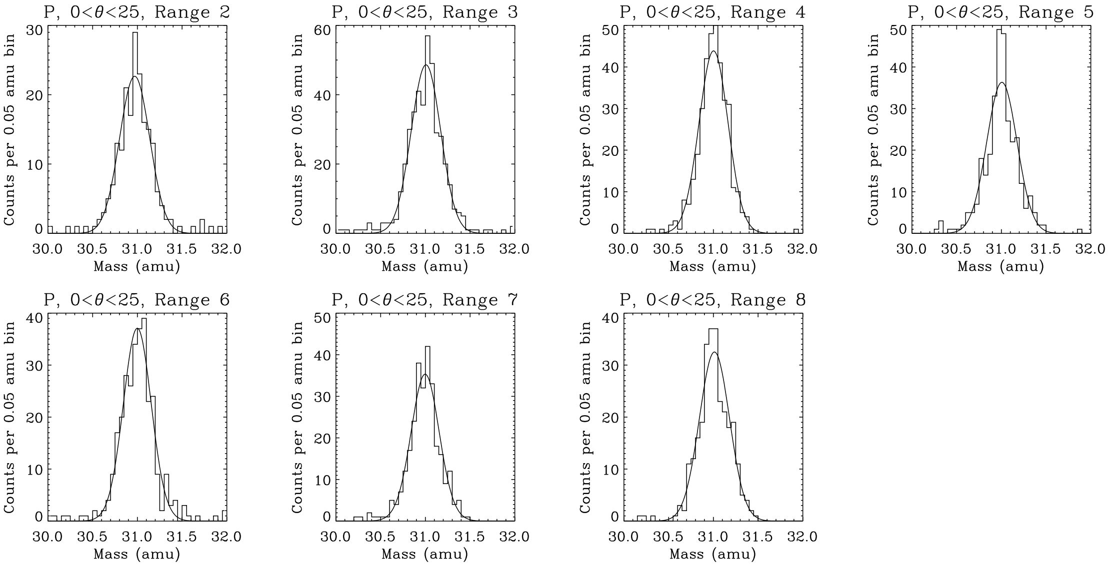

Figure 3.11: Phosphorus histograms for Solar Maximum

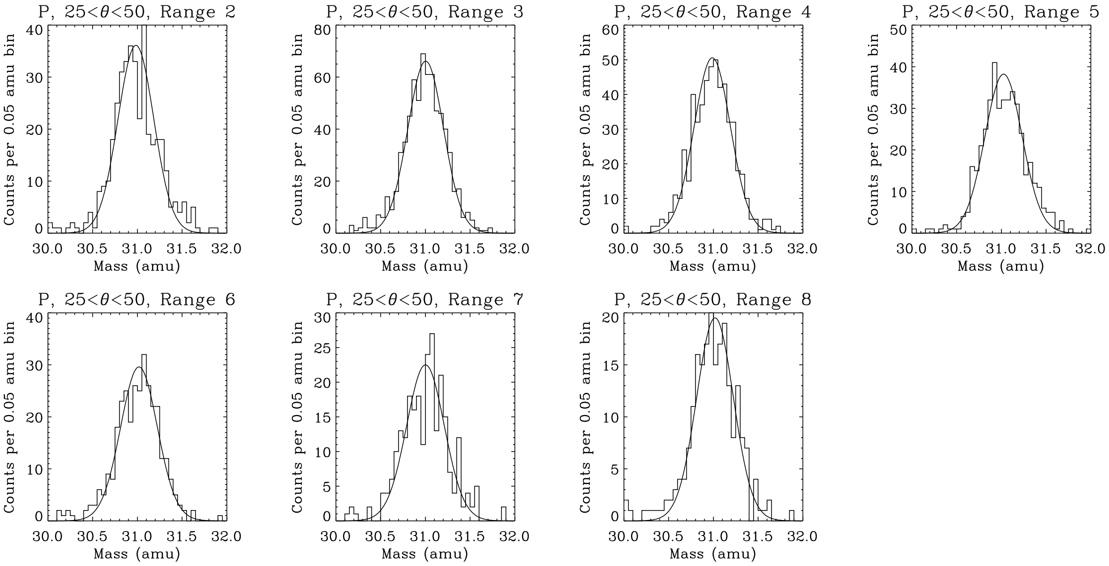

Figure 3.12: Phosphorus histograms for Solar Maximum

3.6.2 Sulfur

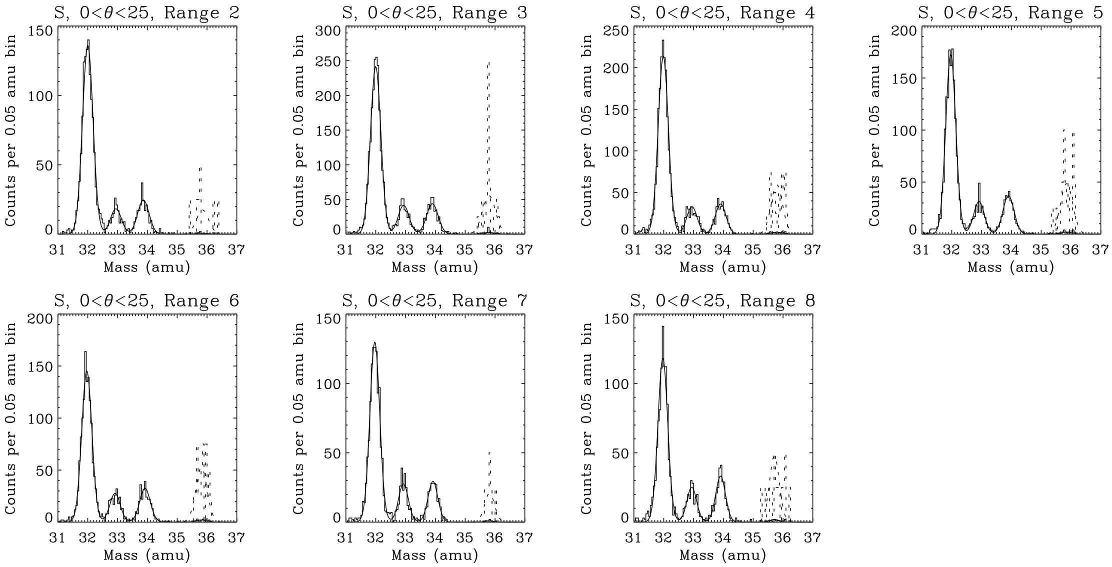

Figure 3.13: Sulfur histograms for Solar Minimum. The ^{36}S histogram and fit are ×25.

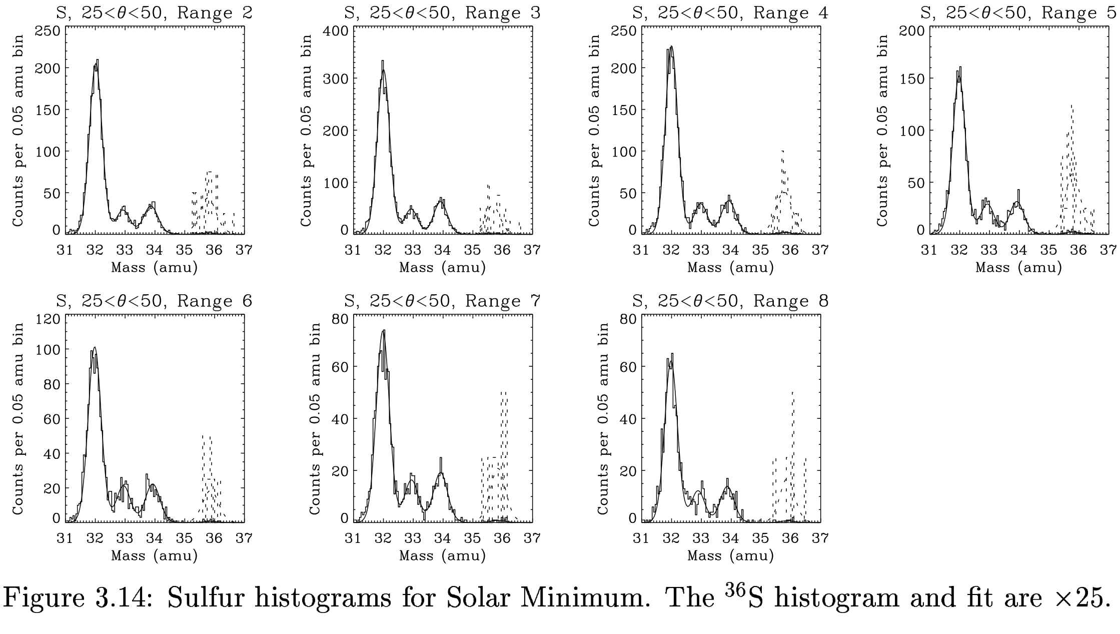

Figure 3.14: Sulfur histograms for Solar Minimum. The ^{36}S histogram and fit are ×25.

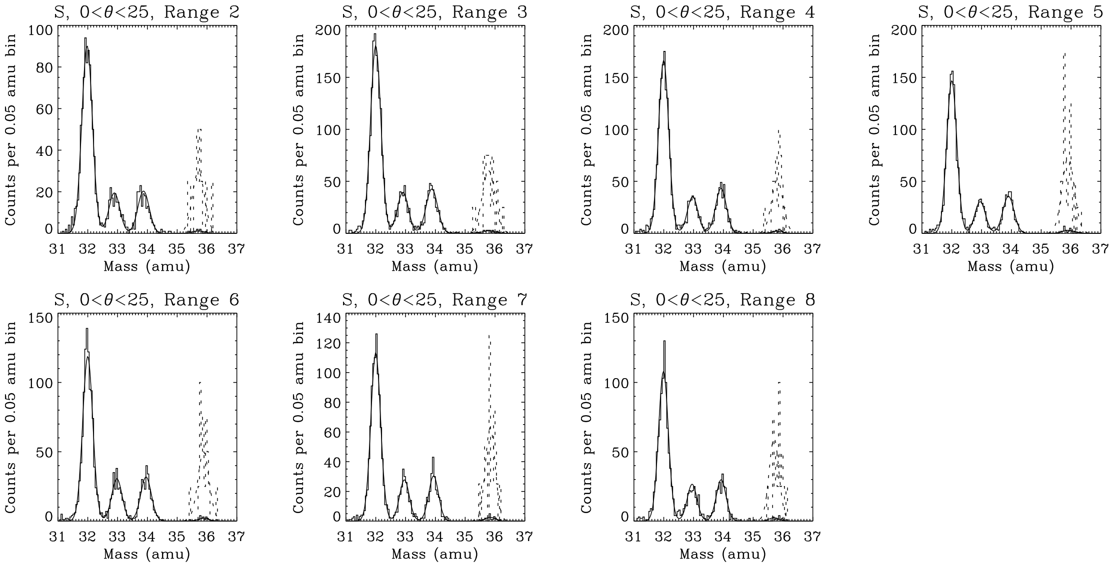

Figure 3.15: Sulfur histograms for Solar Maximum. The ^{36}S histogram and fit are ×25.

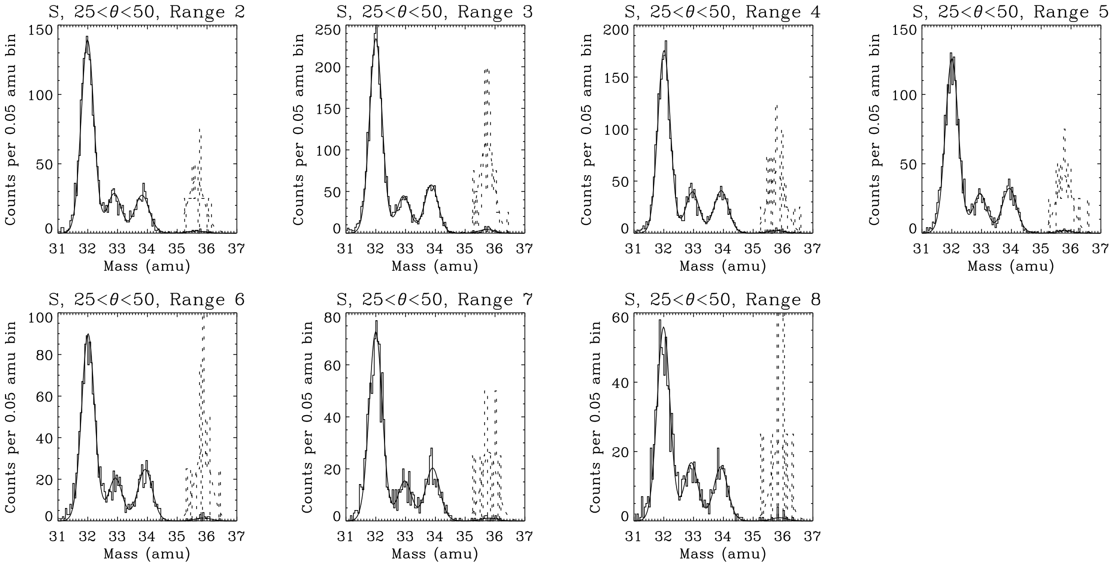

Figure 3.16: Sulfur histograms for Solar Maximum. The ^{36}S histogram and fit are ×25.

3.6.3 Argon

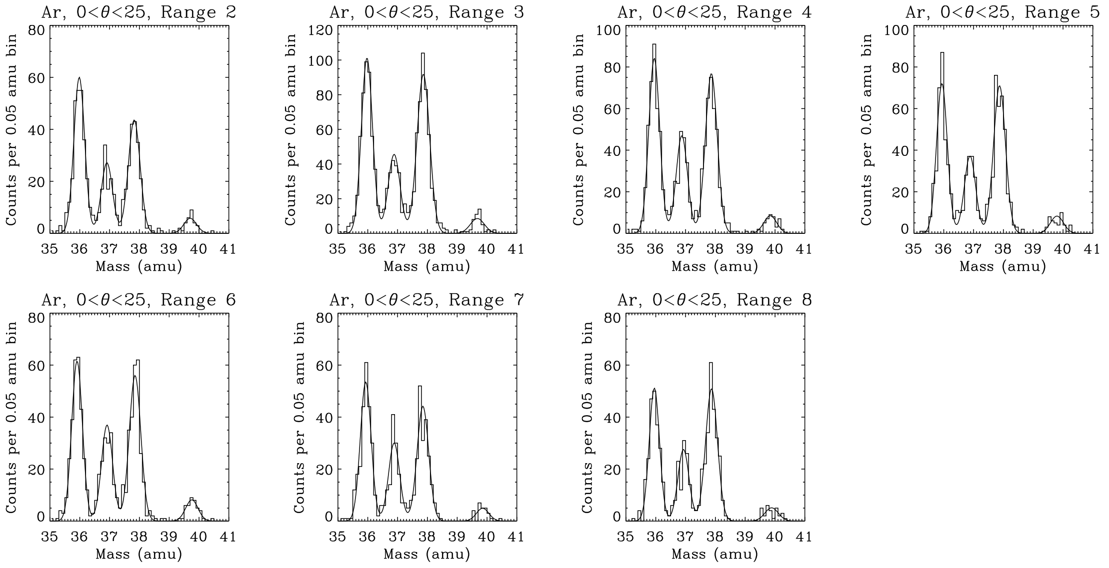
Ar, 0<θ<25, Range 2
Ar, 0<θ<25, Range 3
Ar, 0<θ<25, Range 4
Ar, 0<θ<25, Range 5
Ar, 0<θ<25, Range 6
Ar, 0<θ<25, Range 7
Ar, 0<θ<25, Range 8

Figure 3.17: Argon histograms for Solar Minimum

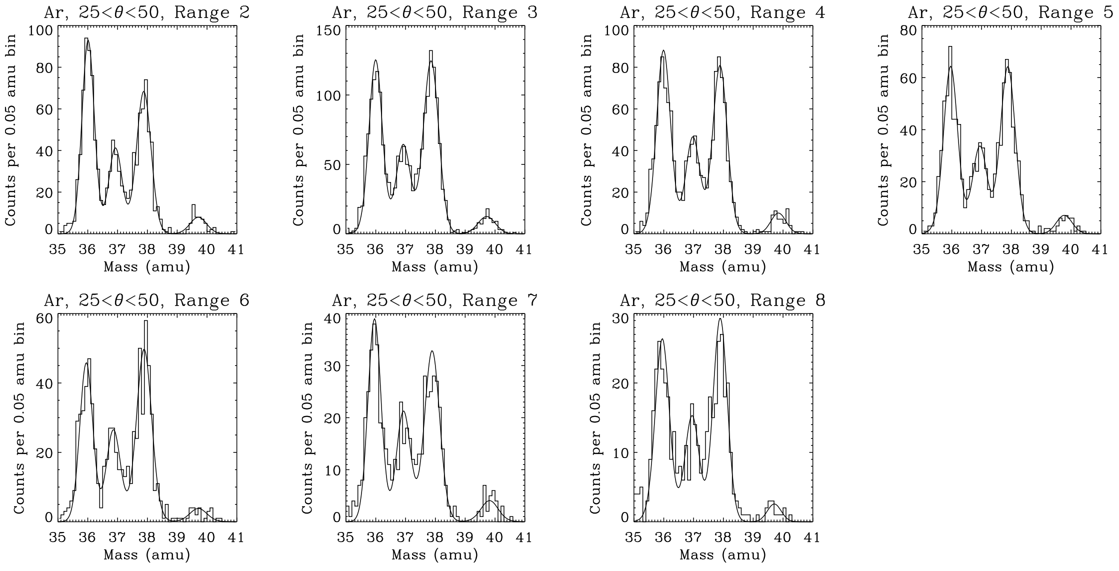
Ar, 25<θ<50, Range 2
Ar, 25<θ<50, Range 3
Ar, 25<θ<50, Range 4
Ar, 25<θ<50, Range 5
Ar, 25<θ<50, Range 6
Ar, 25<θ<50, Range 7
Ar, 25<θ<50, Range 8

Figure 3.18: Argon histograms for Solar Minimum

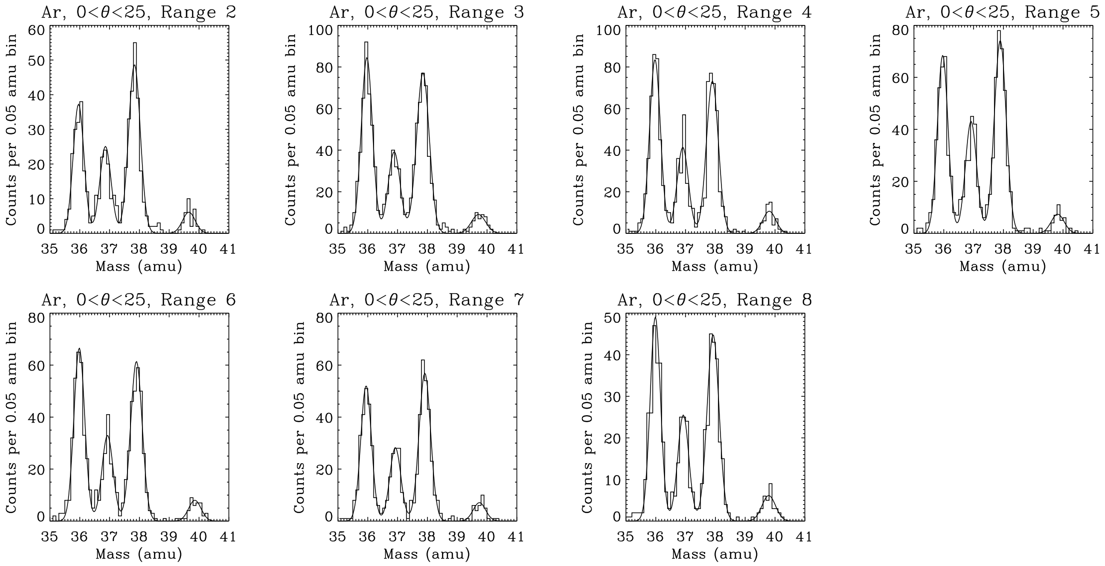

Figure 3.19: Argon histograms for Solar Maximum

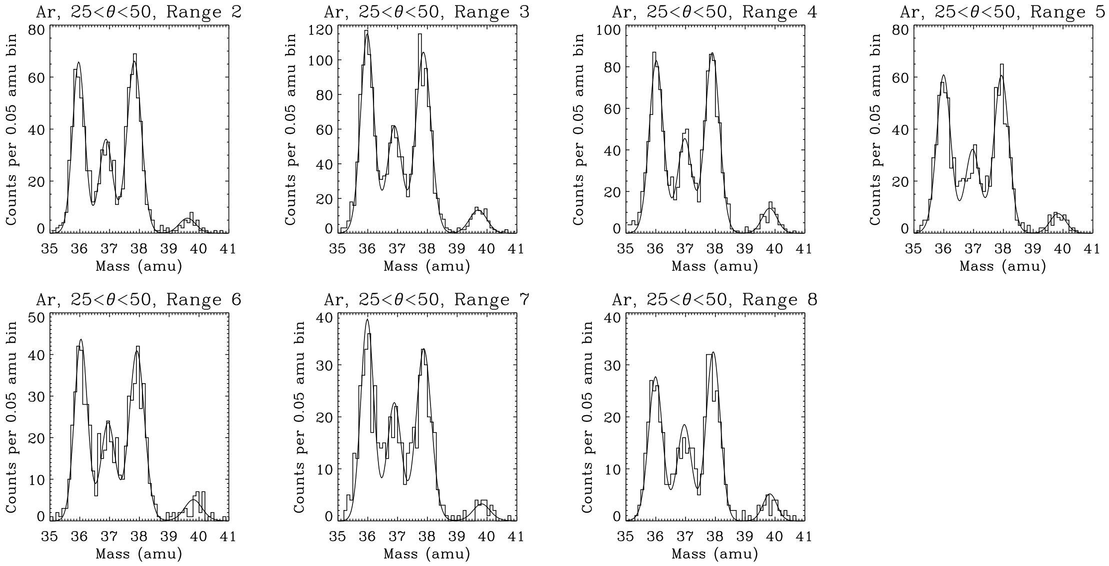

Figure 3.20: Argon histograms for Solar Maximum

3.6.4 Calcium

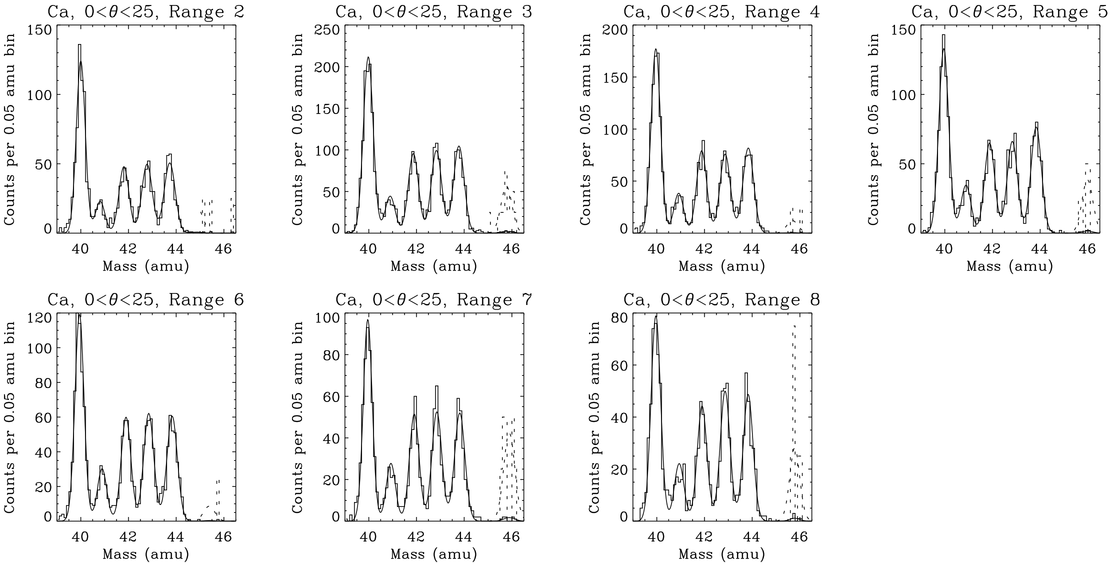

Figure 3.21: Calcium histograms for Solar Minimum. The ^{46}Ca histogram and fit are ×25.

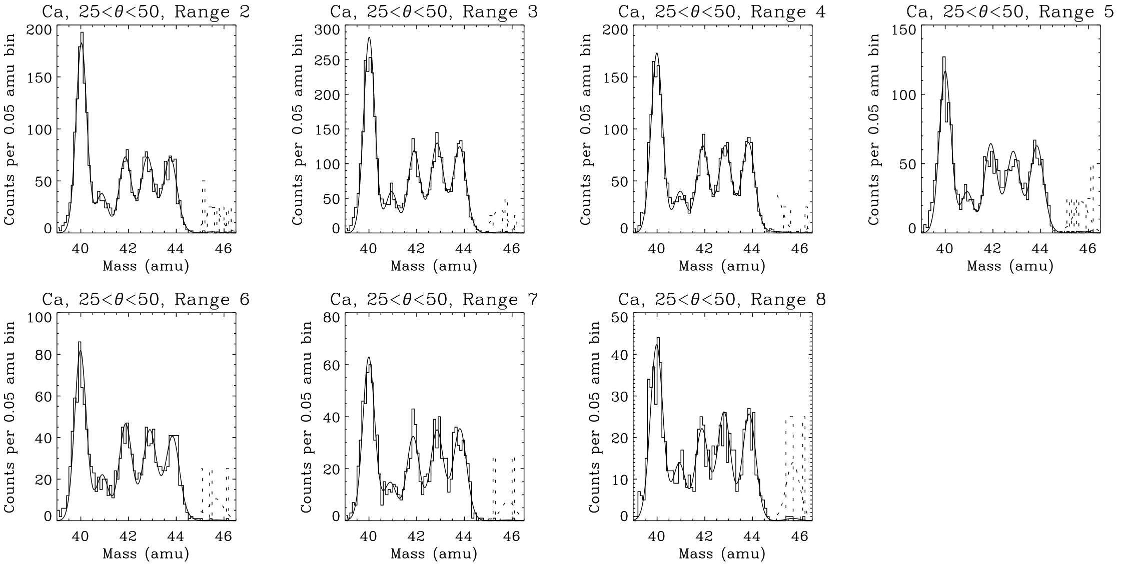

Figure 3.22: Calcium histograms for Solar Minimum. The ^{46}Ca histogram and fit are ×25.

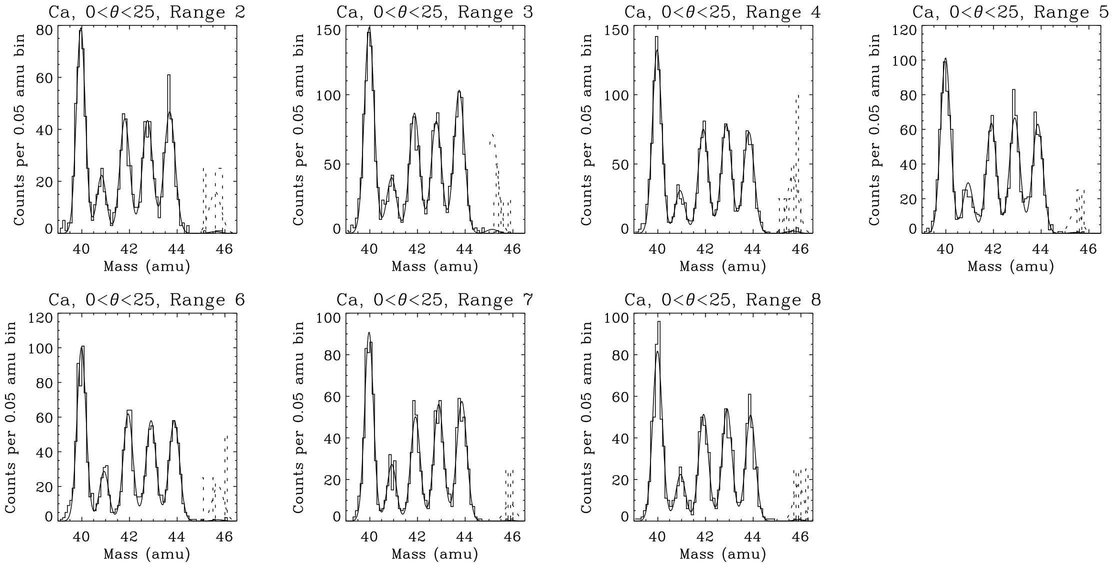

Figure 3.23: Calcium histograms for Solar Maximum. The ^{46}Ca histogram and fit are ×25.

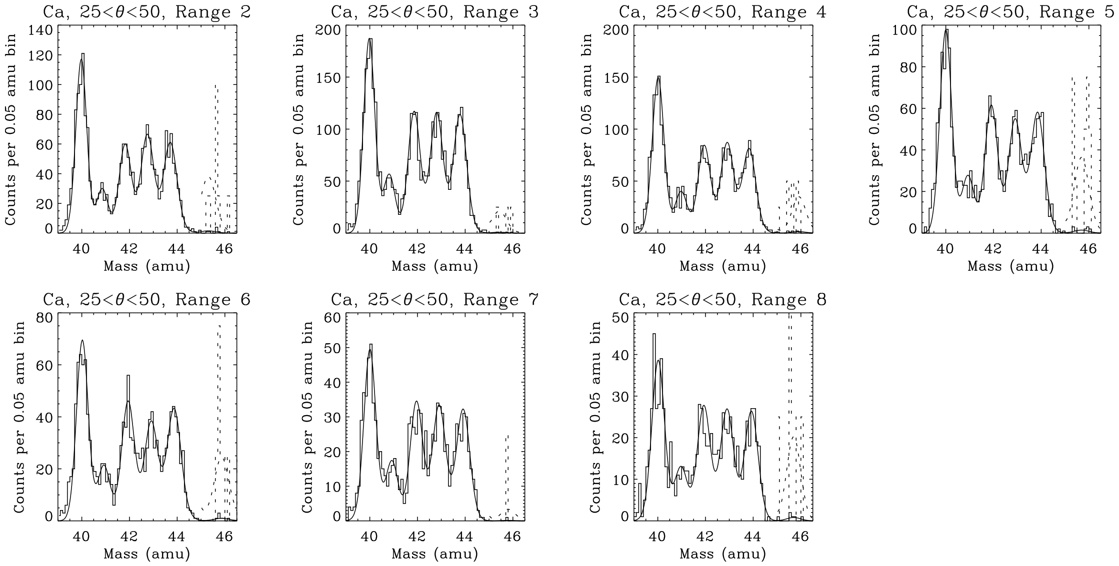

Figure 3.24: Calcium histograms for Solar Maximum. The ^{46}Ca histogram and fit are ×25.

3.7 Isotope ratios

3.7.1 Spectral corrections

The isotope abundances derived in Section 3.6 are calculated by range in the CRIS instrument. As Table 3.3 shows, a given range corresponds to a different energy interval for each species of particle. This is because the energy E of a particle (with mass M and charge Z) can be related to its range in silicon:

$$R = \frac{kM}{Z^2} E^{\alpha}. \tag{3.19}$$

Comparing abundances over the same energy interval is more physically meaningful than comparing over the same range, so before ratios are calculated it is necessary to adjust the isotope abundances to the same energy range. If the intensities of two particle species were independent of energy, this correction factor would simply be the ratio of the two energy intervals. However, the cosmic rays arriving at CRIS do not show a flat spectrum, but exhibit a spectral shape that can be fit by:

$$\frac{dJ}{dE} \propto E^{\beta(E)}, \tag{3.20}$$

where $\beta(E) = b + a[ln(E)]$ and dJ/dE is the differential particle intensity in units of $cm^{-2} sr^{-1} s^{-1} (MeV/nuc)^{-1}$.

If N_2 is the abundance of isotope 2 measured in range R, the relevant isotope ratio to calculate is N_1'/N_2, where N_1' is the abundance of isotope 1 if it was measured in the energy range of isotope 2. The energy interval of isotope 2 in range R, $[E2_{min}, E2_{max}]$, is different from the energy interval of isotope 1 in the same range, $[E1_{min}, E1_{max}]$. Knowing

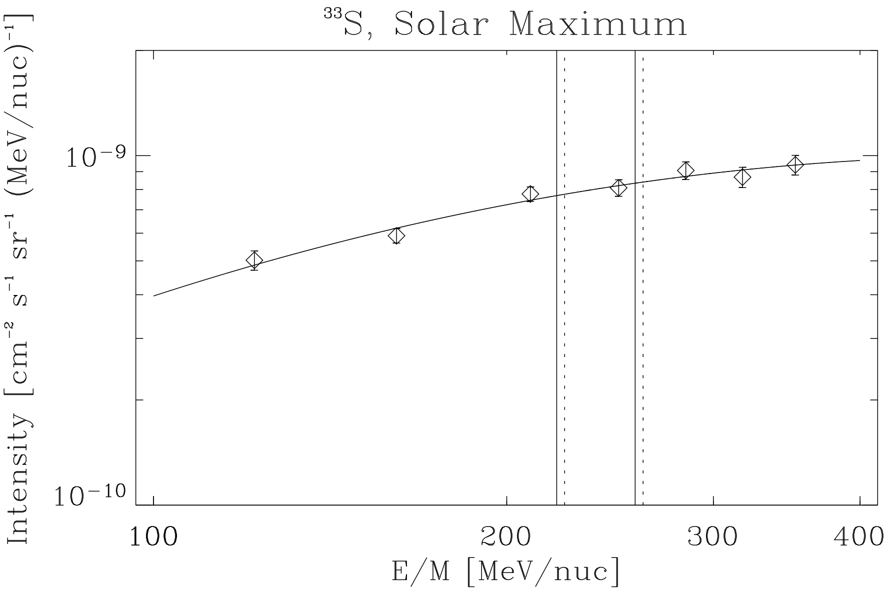

Figure 3.25: The solar maximum ^{33}S spectrum. Vertical solid lines show the energy interval for range 5 ^{33}S; vertical dotted lines are for range 5 ^{32}S. The correction factor to calculate the ratio ^{33}S/^{32}S in the ^{32}S energy range is equal to the area under the curve between the dotted lines, divided by the area under the curve between the solid lines.

the spectral shape, β_1, of isotope 1 makes it possible to adjust its abundance in range R, N_1, to match the energy range of N_2:

$$N_1' = N_1 \frac{\int_{E2_{min}}^{E2_{max}} E^{\beta_1(E)} dE}{\int_{E1_{min}}^{E1_{max}} E^{\beta_1(E)} dE}. \tag{3.21}$$

Applying these corrections, the isotope ratios for phosphorus, sulfur, argon, and calcium are calculated. In all ratios, the isotope in the numerator is spectrally corrected to the energy range of the isotope in the denominator.

3.7.2 Combining high- and low-angle data sets

The data were combined by summing the counts in the high- and low-angle data sets, and reducing the statistical errors accordingly. In Figure 3.26 – 3.29, the ▲ symbol is the ratio from the low-angle data set, ▼ is derived from the high-angle data, and ● is the ratio over

$0° < \theta < 50°$. The ratios are plotted as a function of median energy as given in Table 3.3; the three ratios corresponding to different angle bins for a given range are connected by a line. The overall 1σ statistical uncertainty is plotted for the $0° < \theta < 50°$ ratio.

Isotope ratios for sulfur, argon, and calcium are given in Section 3.7.3 – 3.7.5. All ratios and spectral correction are given in Appendix C.

3.7.3 Sulfur ratios

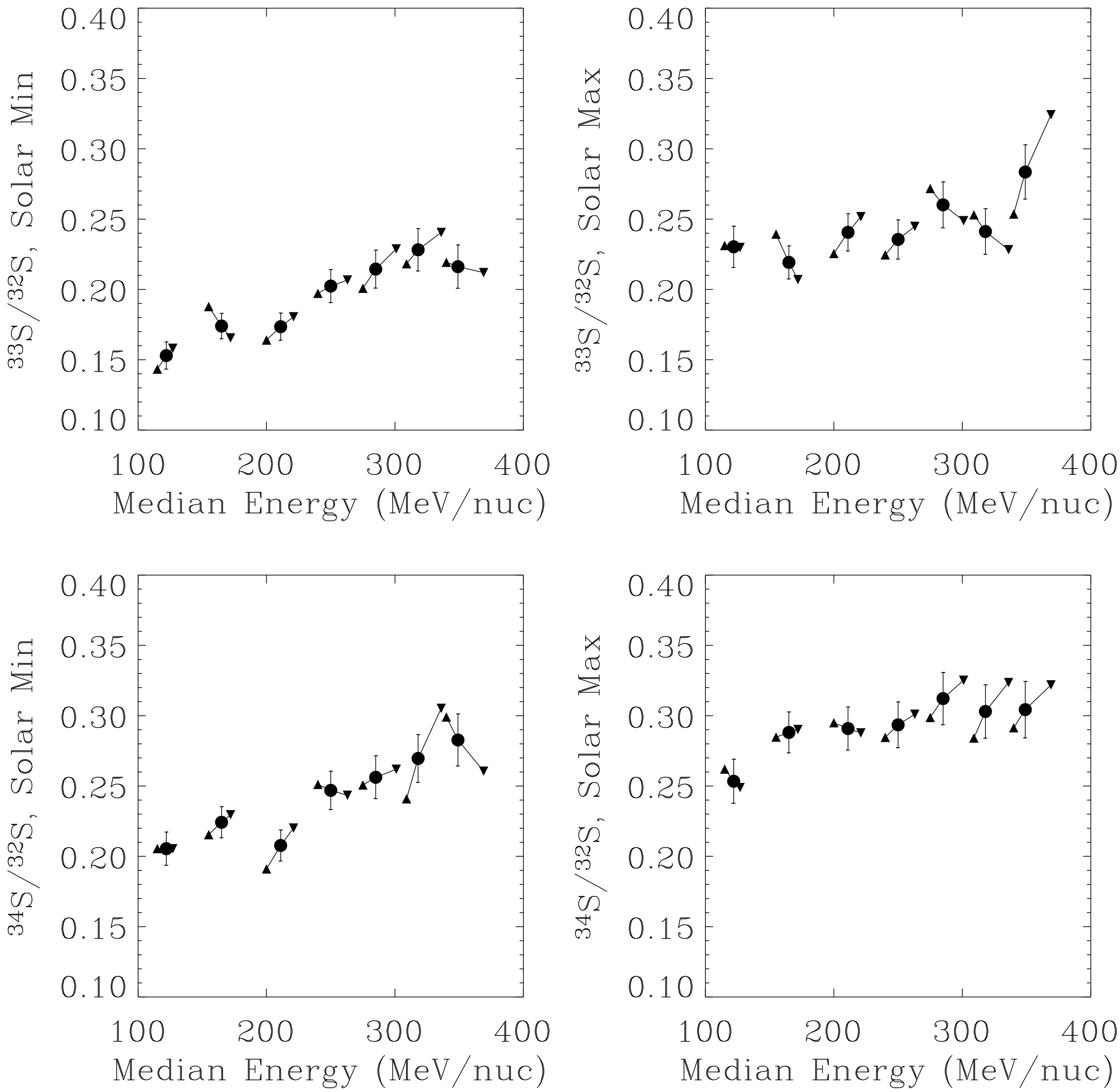

Figure 3.26: The ^{33}S/^{32}S and ^{34}S/^{32}S isotope ratios as a function of median energy for solar minimum and solar maximum. Upward triangles represent the 0° – 25° data set, downward triangles are 25° – 50° , and circles represent the combined data set, 0° – 50° , with associated statistical error bars.

3.7.4 Argon ratios

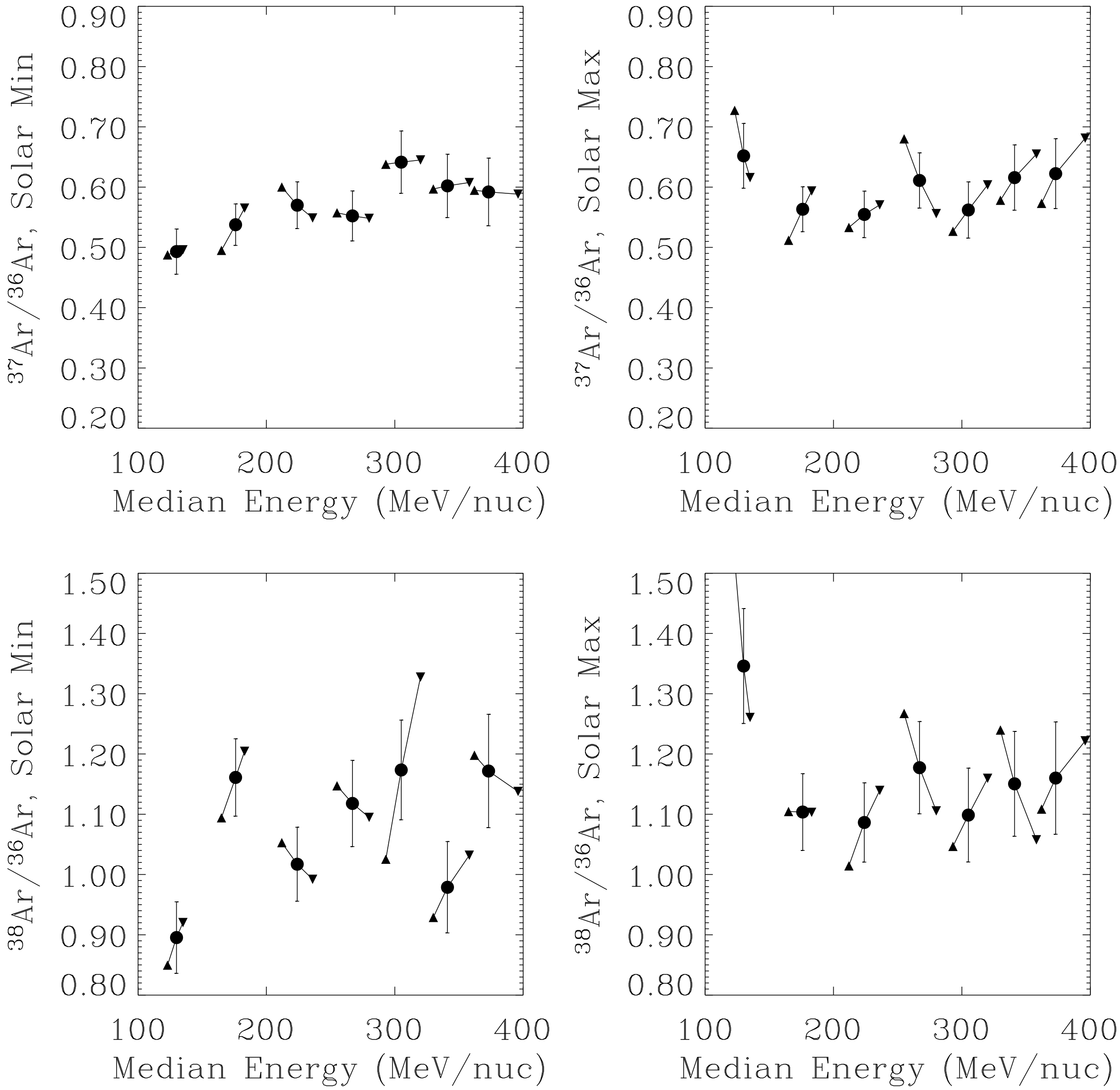

Figure 3.27: The ^{37}Ar/^{36}Ar and ^{38}Ar/^{36}Ar isotope ratios as a function of median energy for solar minimum and solar maximum. Upward triangles represent the 0° – 25° data set, downward triangles are 25° – 50° and circles represent the combined data set, 0° – 50° , with associated statistical error bars.

3.7.5 Calcium ratios

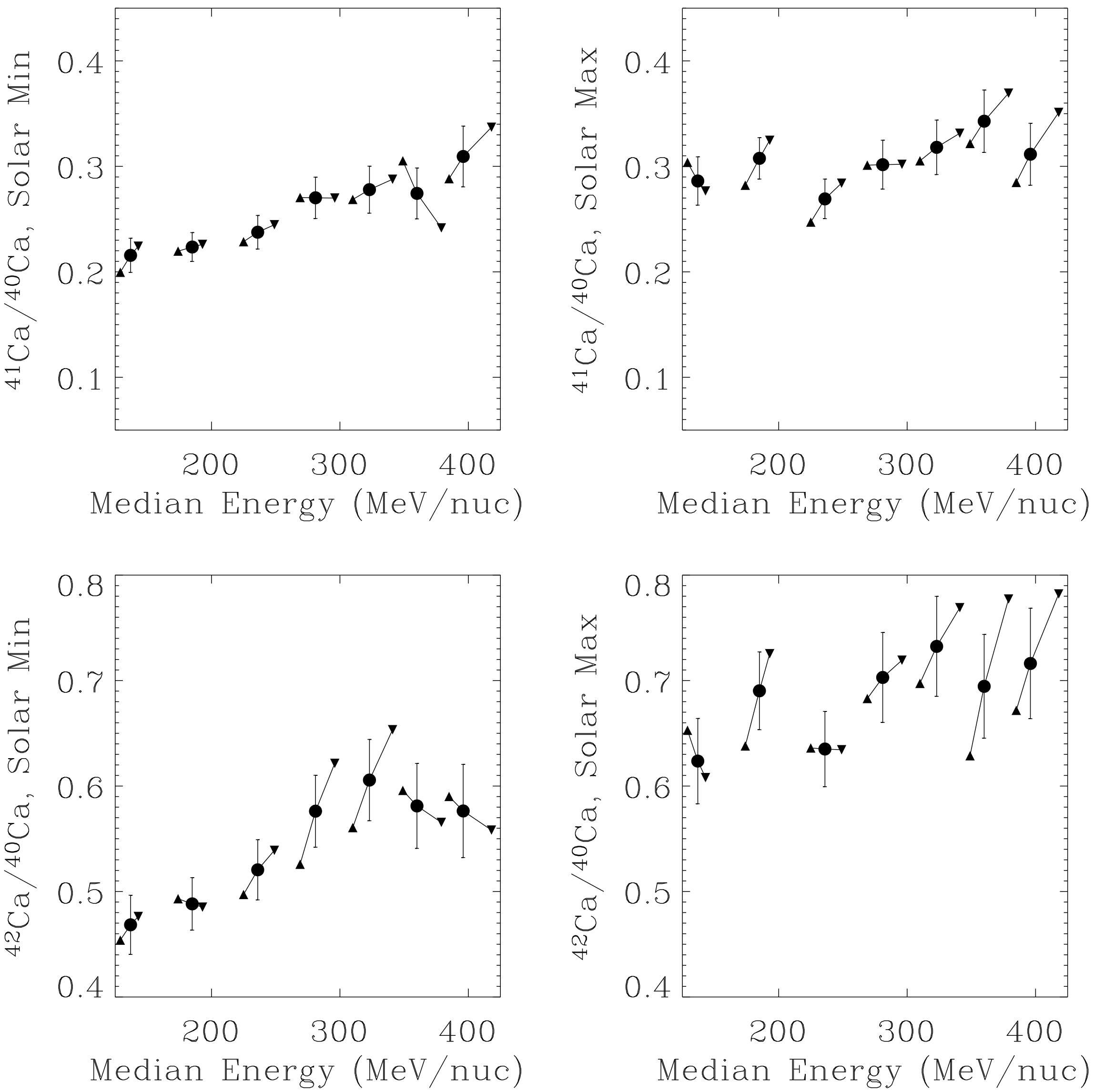

Figure 3.28: The ^{41}Ca/^{40}Ca and ^{42}Ca/^{40}Ca isotope ratios as a function of median energy for solar minimum and solar maximum. Upward triangles represent the 0° – 25° data set, downward triangles are 25° – 50° and circles represent the combined data set, 0° – 50° , with associated statistical error bars.

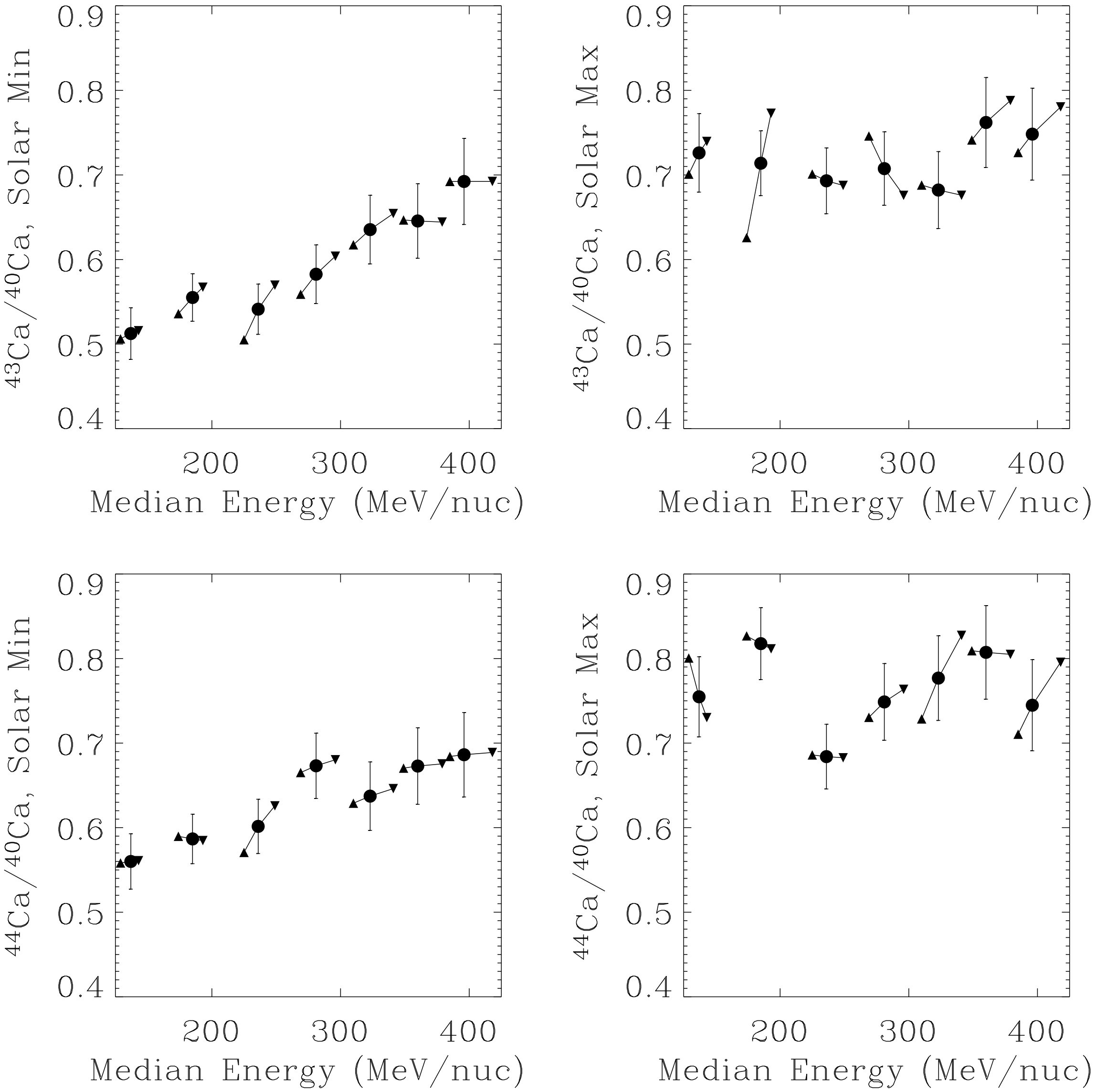

Figure 3.29: The ^{43}Ca/^{40}Ca and ^{44}Ca/^{40}Ca isotope ratios as a function of median energy for solar minimum and solar maximum. Upward triangles represent the 0° – 25° data set, downward triangles are 25° – 50° and circles represent the combined data set, 0° – 50° , with associated statistical error bars.

3.8 Isotope spectra

The tracer method used to derive source abundances (Section 4) requires isotope spectra as measured by *ACE*/CRIS. The isotope spectra $\varphi_{Z,M}$ of element Z and atomic number M is derived using the isotope abundance N as calculated in the previous section, together with the elemental spectra of Z in the publicly available *ACE* Level 2 data set:

$$\varphi_{Z,M} = \frac{N_M}{\sum\limits_{i \in Z} N_i} \varphi_Z. \tag{3.22}$$

The *ACE* Level 2 spectra are calculated using particles entering the telescope from 0° – 30° , where the isotope abundances calculated here use 0° – 50° . Therefore it is necessary to calculate a value of the elemental spectra interpolated to a different energy than what was measured. Also, it is reasonable to assume that the Galactic cosmic ray spectrum arriving at CRIS is smoothly varying. By fitting the seven measured elemental intensities with a smoothly varying function, interpolation will be straight-forward, and the uncertainty in the fit intensity at a given energy point will be smaller than the uncertainty at the nearby measured intensity.

The spectra of elements measured by CRIS can be reasonably fit by a parabola (Scott, 2005):

$$ln\left(\frac{dJ}{dE}\right) = a[ln(E)]^2 + b[ln(E)] + c, \tag{3.23}$$

which is equivalent to:

$$\frac{dJ}{dE} \propto E^{\beta(E)}, \tag{3.24}$$

with $\beta(E) = b + a[ln(E)]$.

Applying standard propagation of errors yields the uncertainty in the measured intensity:

$$\begin{aligned}\sigma^2_{\frac{dJ}{dE}} = \sigma^2_a\left(\frac{\partial\frac{dJ}{dE}}{\partial a}\right)^2 + \sigma^2_b\left(\frac{\partial\frac{dJ}{dE}}{\partial b}\right)^2 + \sigma^2_c\left(\frac{\partial\frac{dJ}{dE}}{\partial c}\right)^2 \qquad (3.25)\\ +2\sigma^2_{ab}\left(\frac{\partial\frac{dJ}{dE}}{\partial a}\right)\left(\frac{\partial\frac{dJ}{dE}}{\partial b}\right) + 2\sigma^2_{bc}\left(\frac{\partial\frac{dJ}{dE}}{\partial b}\right)\left(\frac{\partial\frac{dJ}{dE}}{\partial c}\right) + 2\sigma^2_{ac}\left(\frac{\partial\frac{dJ}{dE}}{\partial a}\right)\left(\frac{\partial\frac{dJ}{dE}}{\partial c}\right),\end{aligned}$$

where $\frac{dJ}{dE}$ is given by Equation 3.23 and the σs are the elements of the covariance matrix returned by `MPFIT`, an IDL implementation of the Levenberg-Marquardt technique to solve the least-squares problem, written by Craig Markwardt (Markwardt, 2006).

The Level 2 data was downloaded and adjusted to coincide with the time periods used in deriving the isotope abundances: that is, excluding the times when instrument livetime is below 80%. This criteria effectively excludes the times when CRIS is measuring an unusually high flux of particles, attributable to a solar energetic particle event. With this requirement, the particles measured by CRIS are ensured to be a sample of Galactic cosmic rays uncontaminated by solar energetic particles.

The elemental spectra and associated fits are shown in Figures 3.30 – 3.31.

From the elemental spectral fits and Equation 3.22, the isotope spectra are calculated (Figures 3.33 - 3.38). The errors on the isotope fluxes are the quadrature sum of the statistical errors associated with the isotope abundances and the error on the elemental flux given by Equation 3.25.

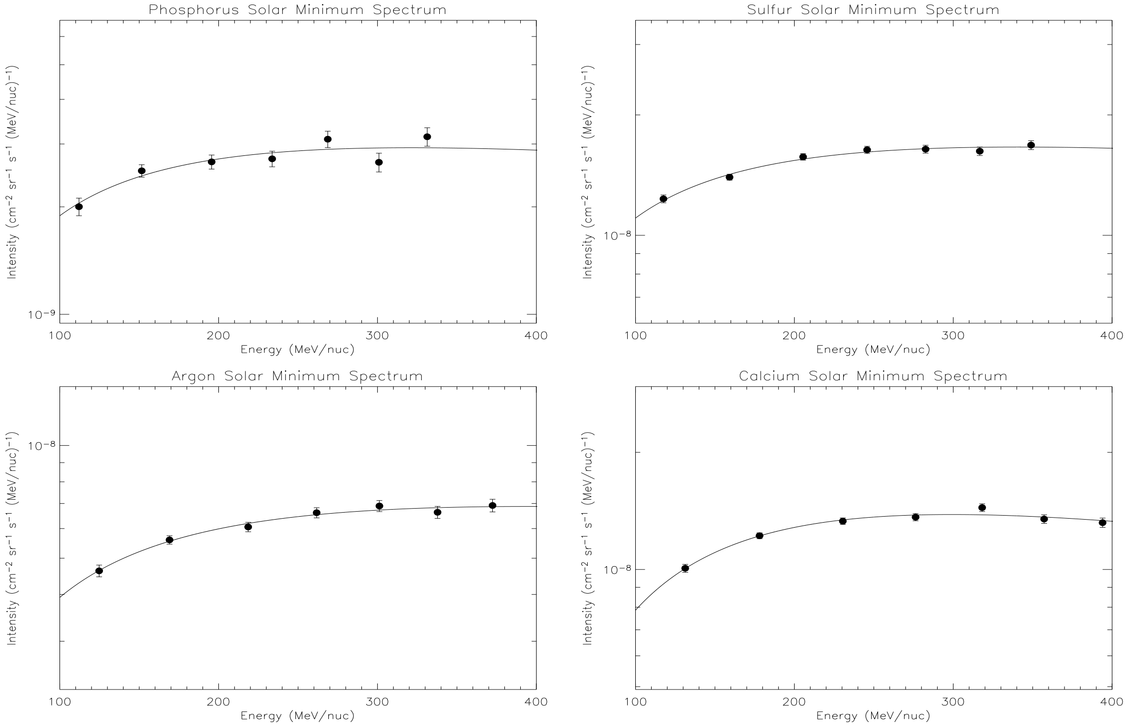

Figure 3.30: Elemental spectra for phosphorus, sulfur, argon, and calcium, as measured by CRIS for the solar minimum time period

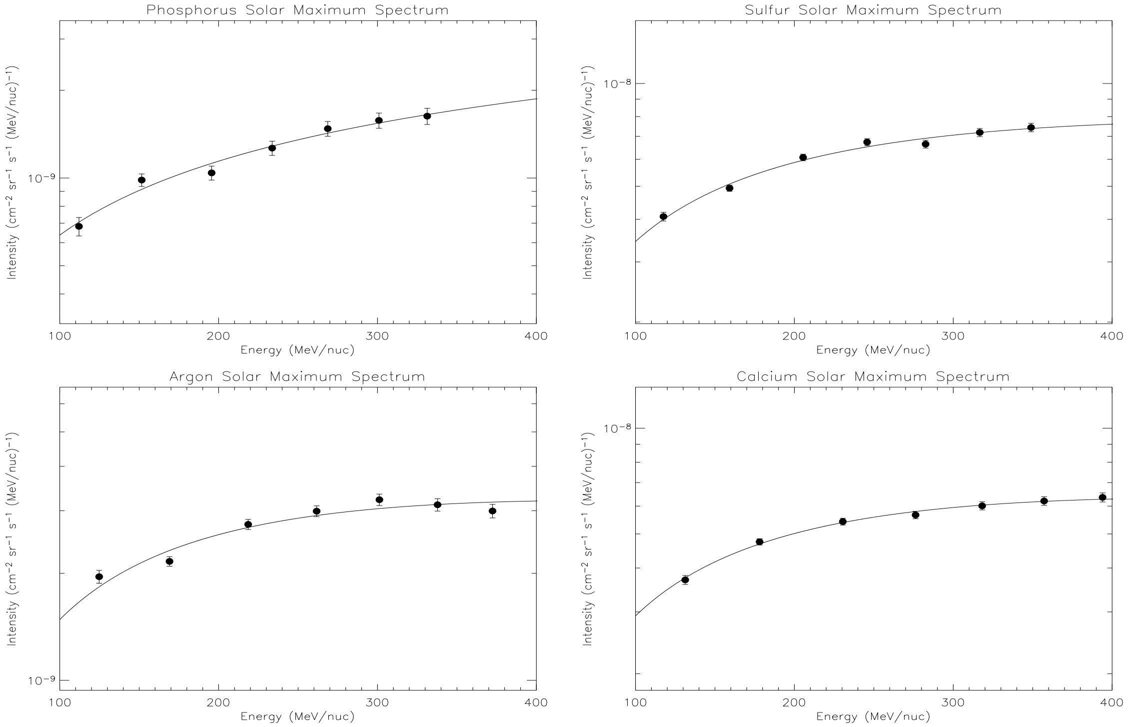

Figure 3.31: Elemental spectra for phosphorus, sulfur, argon, and calcium, as measured by CRIS for the solar maximum time period

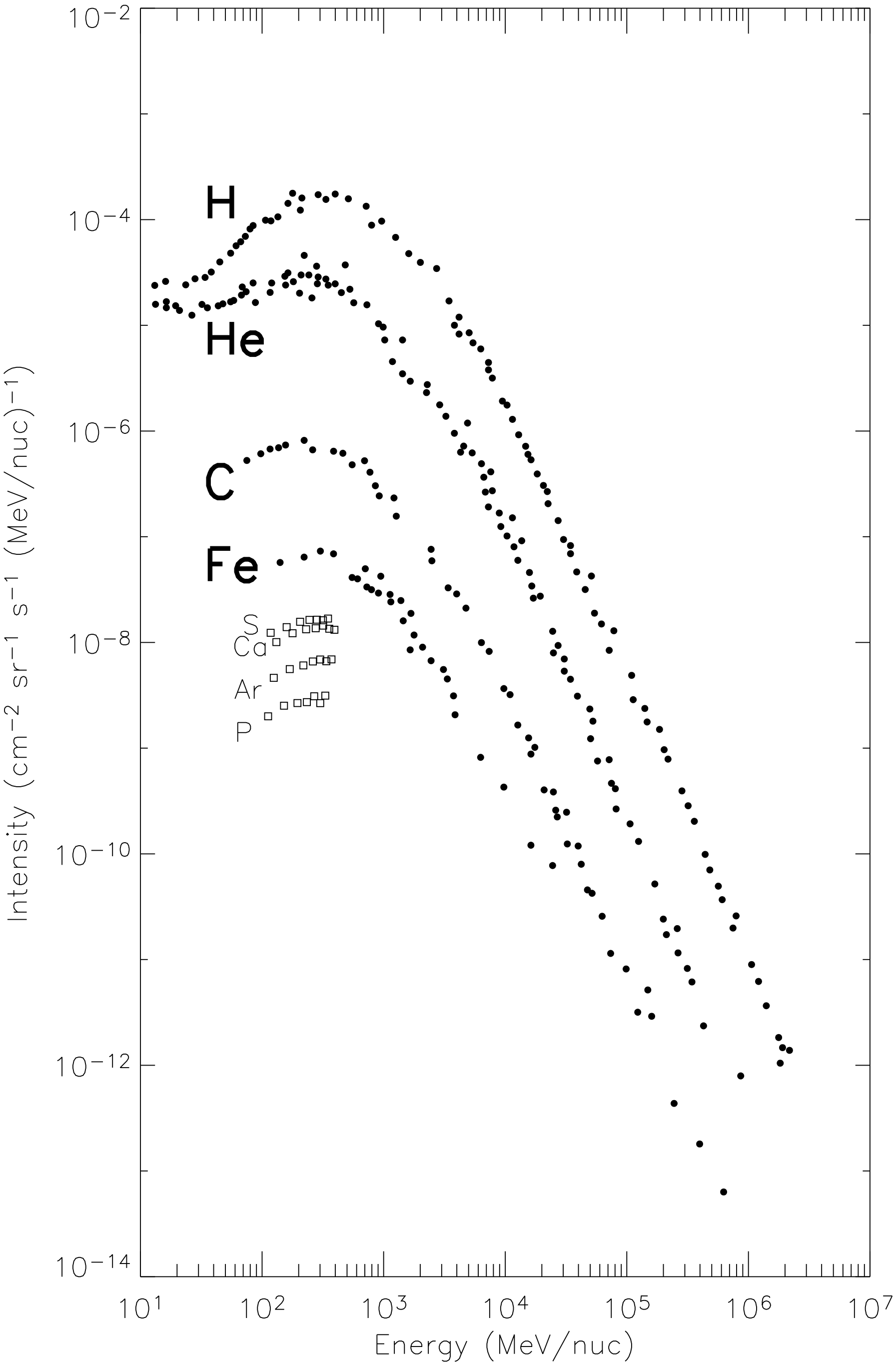

Figure 3.32: The CRIS observed solar minimum elemental spectra for phosphorus, sulfur, argon, and calcium (open squares), plotted with hydrogen, helium, carbon, and iron GCR spectra from Figure 1.1 (filled circles)

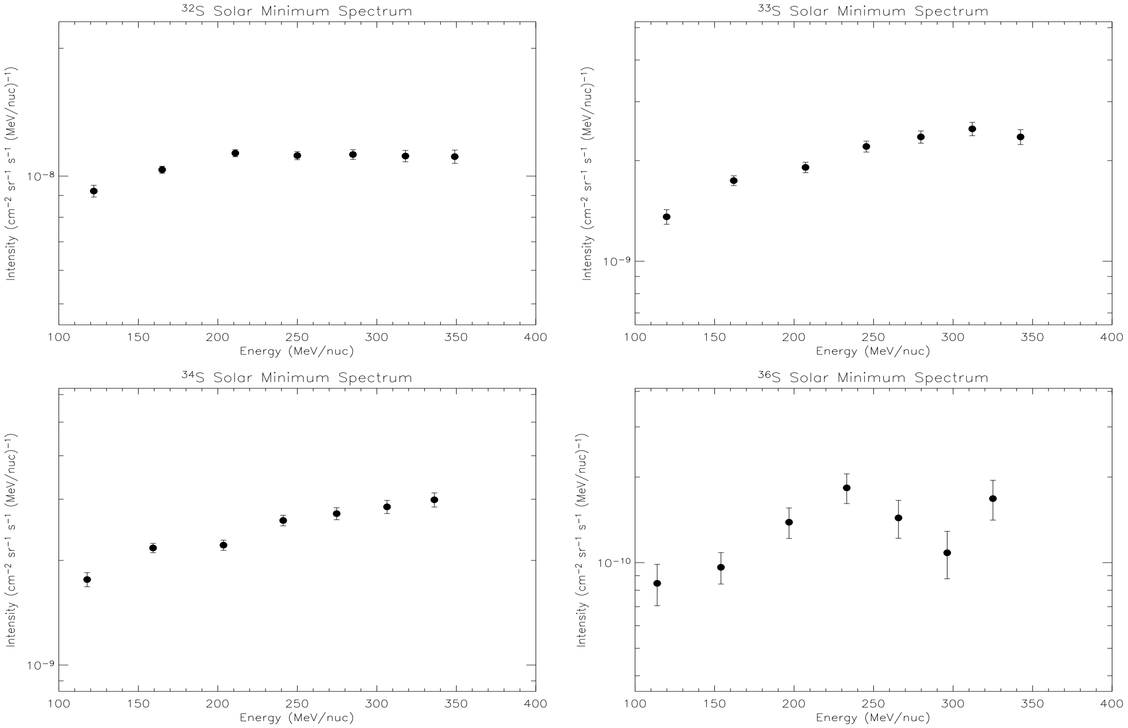

Figure 3.33: Sulfur isotope spectra for solar minimum

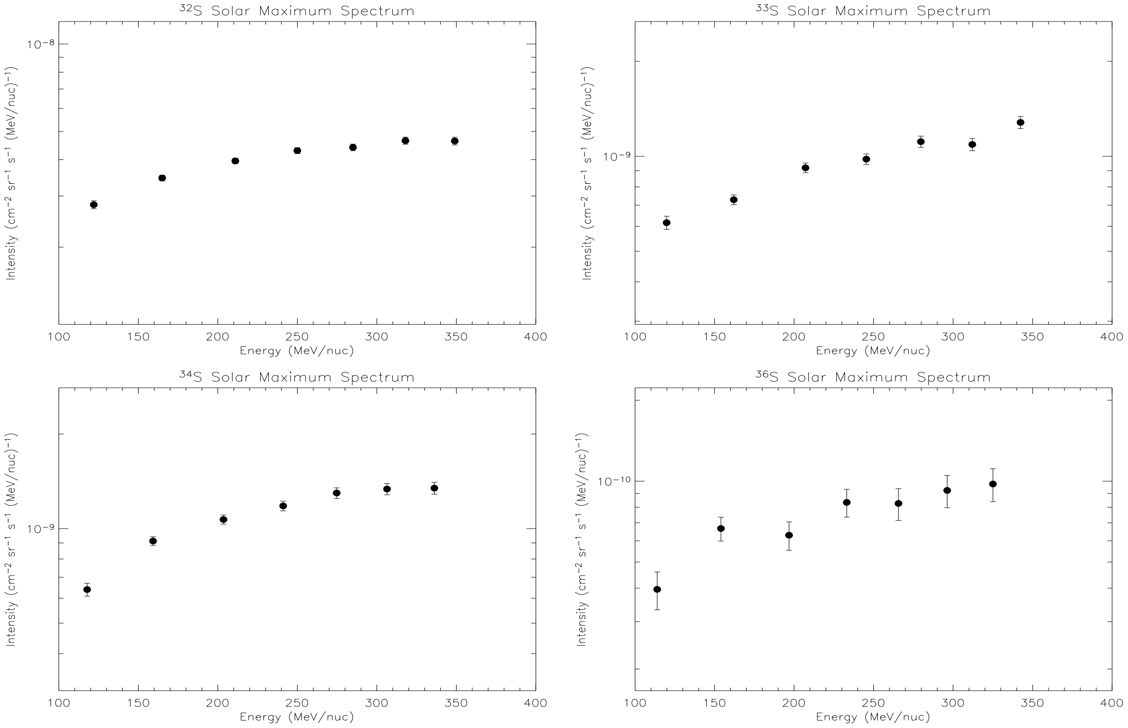

Figure 3.34: Sulfur isotope spectra for solar maximum

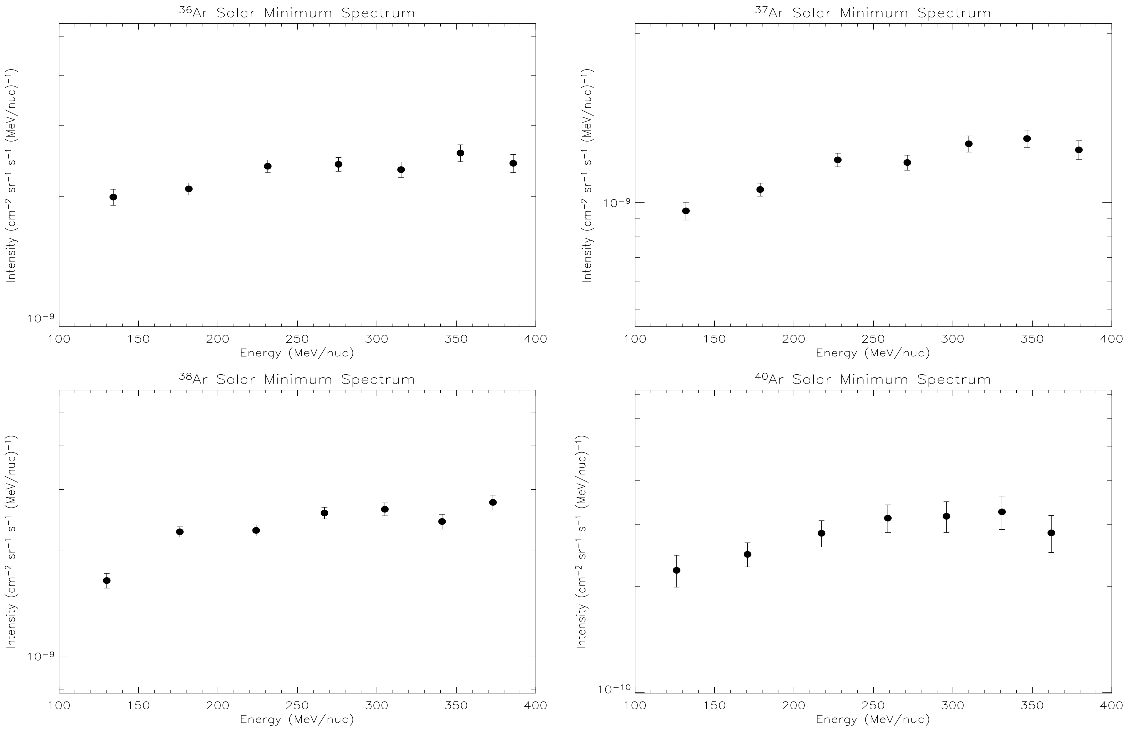

Figure 3.35: Argon isotope spectra for solar minimum

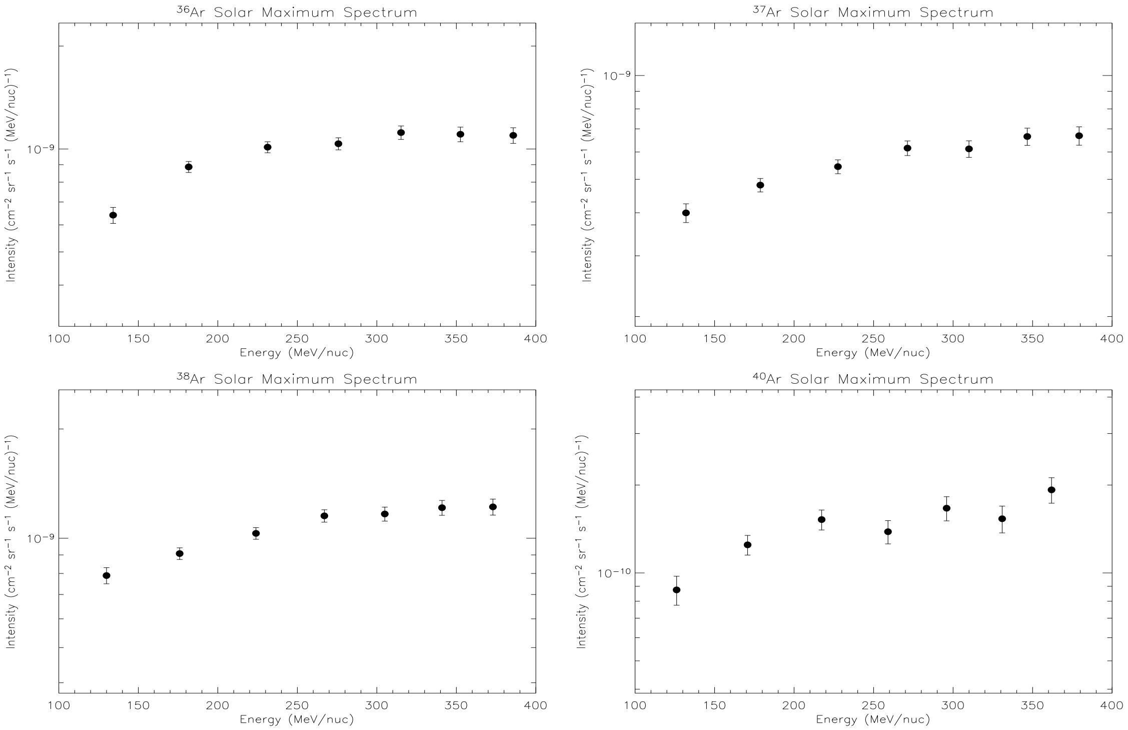

Figure 3.36: Argon isotope spectra for solar maximum

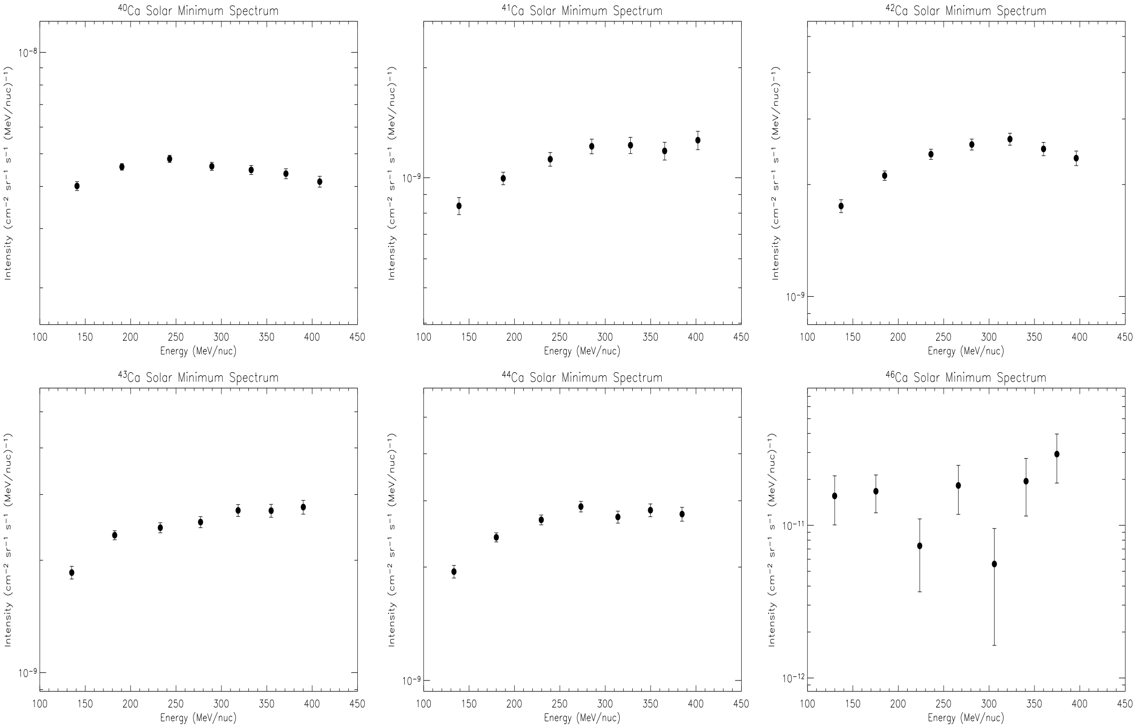

Figure 3.37: Calcium isotope spectra for solar minimum

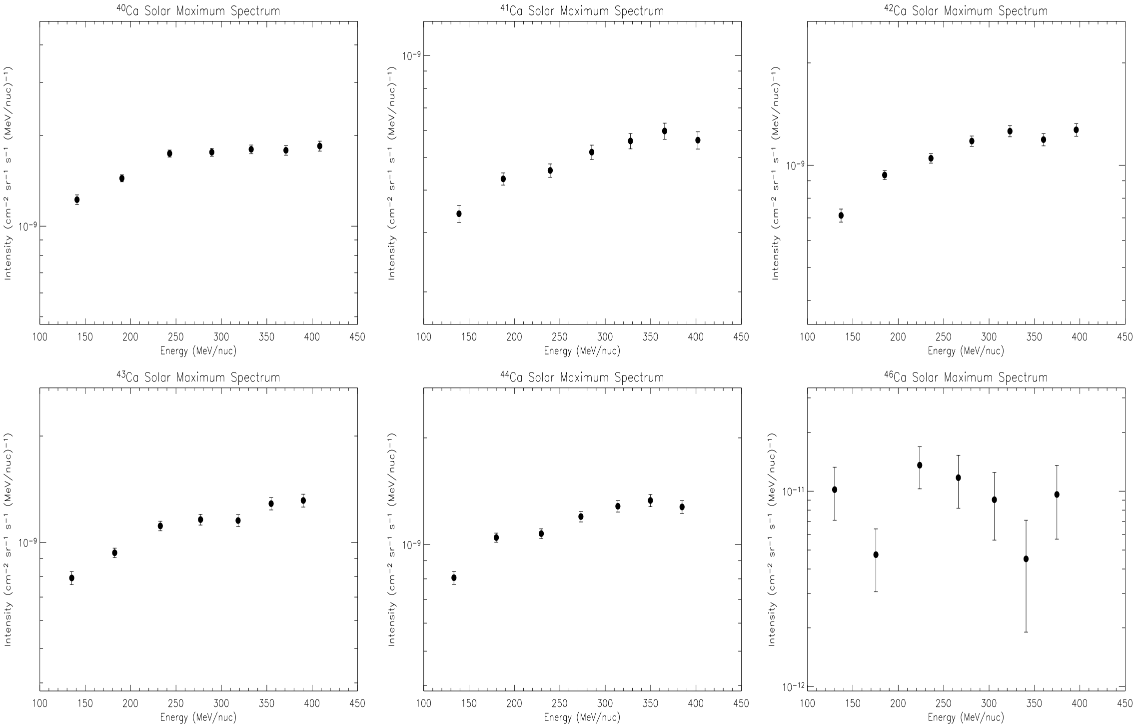

Figure 3.38: Calcium isotope spectra for solar maximum

Chapter 4

Derivation of Source Abundances

The isotopic abundances of cosmic ray sulfur, argon, and calcium arriving at the *ACE* spacecraft were calculated in Chapter 3. The abundances of these isotopes at their astronomical source are desired for this study. During propagation from the cosmic ray source to detection at Earth (as described in Section 1.2), the nuclei undergo physical processes such as energy loss and spallation. These processes must be taken into account when adjusting the isotope ratios calculated in Sections 3.7.3 – 3.7.5 to determine the ratios at the cosmic ray source.

4.1 The leaky-box model

The propagation of cosmic rays in the Galaxy, as described in Section 1.2, would most accurately be modeled as a number of point sources distributed within a large volume, emitting particles with a time-dependent energy spectrum. The cosmic rays then propagate throughout the volume diffusively and have a certain probability of escape when they encounter the boundary. The leaky-box model (first proposed by Cowsik *et al.* (1967)) that is considered here takes a more simplistic view of the situation to ease computation without sacrificing prediction precision for certain types of propagation problems. In particular, this simplified model has been successfully employed to reproduce observed spectra of cosmic rays at Earth (Yanasak *et al.* (2001), Connell (1998)).

Instead of discrete point sources, the leaky-box model assumes a uniform distribution of cosmic ray accelerating sources in a homogeneous medium. The cosmic rays are emitted with a time-independent spectrum, and a shape that is assumed to be the same for all species when expressed in terms of energy per nucleon.

The steady-state leaky-box transport equation, where particle fluxes have reached an equilibrium between injection, deceleration, production, and loss, for a given species i with interstellar spectra φ_i is given by:

$$0 = q_i f_i(\epsilon) - \frac{\varphi_i}{\Lambda_i} + \sum_{j \geq i} \frac{\varphi_j}{\Lambda_{ji}} + \frac{\partial}{\partial \epsilon}(w_i \varphi_i), \tag{4.1}$$

where q_i is the source abundance of species i with source spectral shape $f_i(\epsilon)$, ϵ is the energy per nucleon, and w_i is the ionization energy loss rate of species i. The terms on the right-hand side of Equation 4.1 represent production of i by the source, destruction of i by fragmentation during propagation through the Galaxy, production of i from the fragmentation of heavier nuclei j during propagation, and changes in the spectral shape due to ionization energy loss. The cosmic rays that come from the source $q_i f_i(\epsilon)$ are primary cosmic rays; those produced by fragmentation of heavier nuclei are secondary cosmic rays. Equation 4.1 contains the mean free paths for production (Λ_{ji}) and for loss (Λ_i), which themselves represent different physical processes:

$$\frac{1}{\Lambda_{ji}} = \frac{\sigma_{ji}^{H} + (n_{\mathrm{He}}/n_{\mathrm{H}})\sigma_{ji}^{He}}{M_H + (n_{\mathrm{He}}/n_{\mathrm{H}})M_{He}} + \frac{1}{\rho v \tau_{ji} \gamma} \tag{4.2}$$

$$\frac{1}{\Lambda_i} = \frac{1}{\Lambda_i^{esc}} + \frac{\sigma_i^{H} + (n_{\mathrm{He}}/n_{\mathrm{H}})\sigma_i^{He}}{M_H + (n_{\mathrm{He}}/n_{\mathrm{H}})M_{He}} + \frac{1}{\rho v \tau_i \gamma}. \tag{4.3}$$

The escape-probability boundary condition of the leaky-box model is manifested in Equation 4.3 as Λ_i^{esc}, the escape mean free path of i from the Galaxy. The total destruction cross sections of the nucleus i by interstellar hydrogen and helium are σ_i^H and σ_i^{He} respectively, n_{H} and n_{He} are the number densities of hydrogen and helium in the interstellar medium, M_{H} and M_{He} are the masses of hydrogen and helium atoms, σ_{ji}^H and σ_{ji}^{He} are the cross sections for production of the nucleus i from the spallation of nucleus j by hydrogen and helium respectively, and the mass density of the interstellar medium is $\rho = n_{\mathrm{H}}M_H + n_{\mathrm{He}}M_{He}$. The decay of radioactive isotopes with lifetimes comparable to the fifteen-million-year residence time of cosmic rays in the Galaxy is accounted for by the last term in the above equations, with v representing the particle's velocity, τ_i the mean lifetime for the decay of i, and τ_{ji} the mean lifetime for the decay of isotope j to isotope i.

4.2 Implementation of the leaky-box model

The equations in Section 4.1 are solved numerically in IDL computer code written and maintained by Mark Wiedenbeck. The implementation of the leaky-box model to derive source abundances, as described in the following sections, requires computational algorithms developed specifically for this work.

4.2.1 Propagation parameters

The following parameters were used in this investigation to model the leaky-box propagation of cosmic rays.

4.2.1.1 Escape mean free path

The escape mean free path in Equation 4.3 is chosen to take the form given in Davis *et al.* (2000) and Wiedenbeck *et al.* (2001):

$$\Lambda^{esc} = \frac{\Lambda_0 \beta}{\left(\frac{\beta R}{1.0\,\mathrm{GV}}\right)^{0.6} + \left(\frac{\beta R}{1.3\,\mathrm{GV}}\right)^{-2.0}} \tag{4.4}$$

This expression for Λ^{esc} is modified from Soutoul (1999) and provides a good fit to cosmic ray secondary/primary abundance ratios as a function of energy. If the escape mean free path is short, primary nuclei have less material to traverse before they exit the Galaxy, and thus less of an opportunity to spall into secondary nuclei. The value of Λ_0 is chosen to fit measured secondary/primary ratios and will be taken as a free parameter in the calculation of source ratios.

4.2.1.2 Interstellar medium composition

The number density of hydrogen, n_{H}, is set as 0.34 cm^{-3} (Yanasak *et al.*, 2001), and the ISM is assumed to be 90% hydrogen and 10% helium by number.

4.2.1.3 Shape of the source spectrum

The HEAO-3-C2 instrument measured cosmic rays at energies from 0.6 – 35 GeV/nuc, where solar modulation does not greatly alter the spectral shape of the nuclei (Figure 1.1). Leaky-box calculations by Engelmann *et al.* (1990) showed that source spectra proportional to a power law in momentum per nucleon fit these measurements well. For this work, we will assume the spectral shape to be:

$$f_i(\epsilon) \propto P^{-2.35}. \tag{4.5}$$

4.2.2 Solar modulation

The cosmic ray spectra φ in Equation 4.1 are interstellar spectra, but CRIS measures nuclei at Earth. In order to compare the measured spectra (Section 3.8) with the leaky-box calculations, it is necessary to take into account the diffusion of cosmic rays in the heliosphere (described in Section 1.3). A spherically-symmetric solar modulation model is employed that includes convection, diffusion, and adiabatic energy loss to accurately model the change in spectral shapes due to solar modulation (Gleeson & Axford, 1968). The numerical solution for this model is described by Fisk *et al.* (1971). The interstellar diffusion coefficient of cosmic rays is assumed to be:

$$\kappa(r, R) = \kappa_0 \beta g(r, R), \tag{4.6}$$

where β is equal to the particle's speed divided by the speed of light, r is the radial distance from the Sun, R is the magnetic rigidity of the particle, and the function $g(r, R)$ embodies the rigidity and spatial dependence of the diffusion coefficient κ. The factor, κ_0, has units of $\mathrm{cm^2 s^{-1} MV^{-1}}$ and varies with the solar cycle. The solar modulation model for this work assumes that the interstellar diffusion coefficient is simply proportional to rigidity: $\kappa = \kappa_0 \beta R$. The validity of this assumption is discussed in Section 4.3.5. The quantity κ_0 and the ϕ parameter plotted in Figure 3.5 are related by the equation:

$$\phi = \int_{1\ \mathrm{AU}}^{r_B} \frac{V_{\mathrm{SW}}}{3\kappa_0} dr = \frac{V_{\mathrm{SW}}}{3\kappa_0} \left(r_B - 1\ \mathrm{AU} \right), \tag{4.7}$$

where V_{SW} is the velocity of the solar wind and r_B is the outer boundary of the modulation region.

The ϕ parameter for a particular time period is calculated by choosing the κ_0 value that best fits the observed spectra (Davis *et al.*, 2001; Wiedenbeck, 2005). The time evolution of ϕ, as calculated with CRIS data, is shown in Figure 3.5. The solar minimum time period is described approximately by ϕ_{min} = 380 MV, and solar maximum by ϕ_{max} = 900 MV. The appropriate ϕ that is to be used in the final calculations should be chosen as to fit the spectra of the species of interest, and so the solar minimum value may differ from 380 MV. This process is described in Section 4.3.1.

4.2.3 Spallation cross sections

The production and loss mean free paths, Λ_{ji} and Λ_i, depend on the spallation cross sections for production and loss, σ_{ji} and σ_i, for collisions with interstellar hydrogen and helium nuclei, as given in Equation 4.1. The total destruction cross section of isotope i, σ_i, is assumed to be of the form given by Webber *et al.* (1990), with energy dependence from Letaw *et al.* (1983) and a small renormalization based on Tripathi *et al.* (1997). The production of secondaries will depend on the σ_{ji}s from all of the nuclides j that are heavier than i. The accuracy of the leaky-box in modeling the local abundances of mostly, or totally, secondary nuclides (Section 4.2.4.2) depends most sensitively on the uncertainties of production cross-sections. Some proton-nucleus reactions have been measured in the lab, others have not been measured over the energies relevant to the cosmic ray propagation problem. For unmeasured reactions, cross-section values can be obtained from a semi-empirical formula for proton-nucleus reactions. Solving Equation 4.1 requires energy-dependent cross-section values for a large number of reactions. The set of necessary proton-nucleus cross-sections was compiled in the following manner.

First, a list of all known direct cross-section measurements (where the daughter particle hasn't decayed) was accumulated, based on past work done on the cosmic ray propagation problem by Mark Wiedenbeck (Binns *et al.*, 2005) and Igor Moskalenko (Strong & Moskalenko, 2001), in addition to recent spallation reaction measurements of ^{56}Fe nuclei accelerated into a liquid hydrogen target (Villagrasa-Canton, 2003). The list contains the parent and daughter nucleus, cross-section measurement, and uncertainty for each reaction. The semi-empirical formulas of Webber (Webber *et al.*, 1990) were calculated for each reaction; the Silberberg (Silberberg *et al.*, 1998) formulas were used for the reactions where the Webber formulas did not predict cross-sections. The Webber formulas were chosen instead of Silberberg, due to the presence of low energy peaks in the Silberberg cross-sections that were not seen in the compiled list of cross section measurements. A description of the Webber semi-empirical cross-section formula used in this work is given in Appendix D. The Webber formula for a given reaction was multiplied by a scaling factor to fit the data for the reactions with measurements, and the reduced χ^2 was calculated for the fit if there are two or more data points. If $\chi^2_{\text{reduced}} < 1$, to avoid the scaling factor being determined by measurements with very small reported uncertainties, each uncertainty was increased by adding a constant in quadrature to the reported uncertainty. The constant was varied until $\chi^2_{\text{reduced}} = 1$, and the scaling factor was recalculated with the broadened uncertainties. Four cross-section reactions with associated measurements, uncertainties, and Webber formula fits are shown in Figure 4.1.

The production cross-sections for collisions with interstellar helium are scaled from the proton-nucleus reactions by a factor of $(A^{3/8} + 0.682)^2$ (Orth & Buffington, 1976; Dermer, 1986), where A is the atomic number of the fragmenting nucleus. The abundance of interstellar helium is only ~10% that of hydrogen, so the contribution of these spallation reactions is comparatively small.

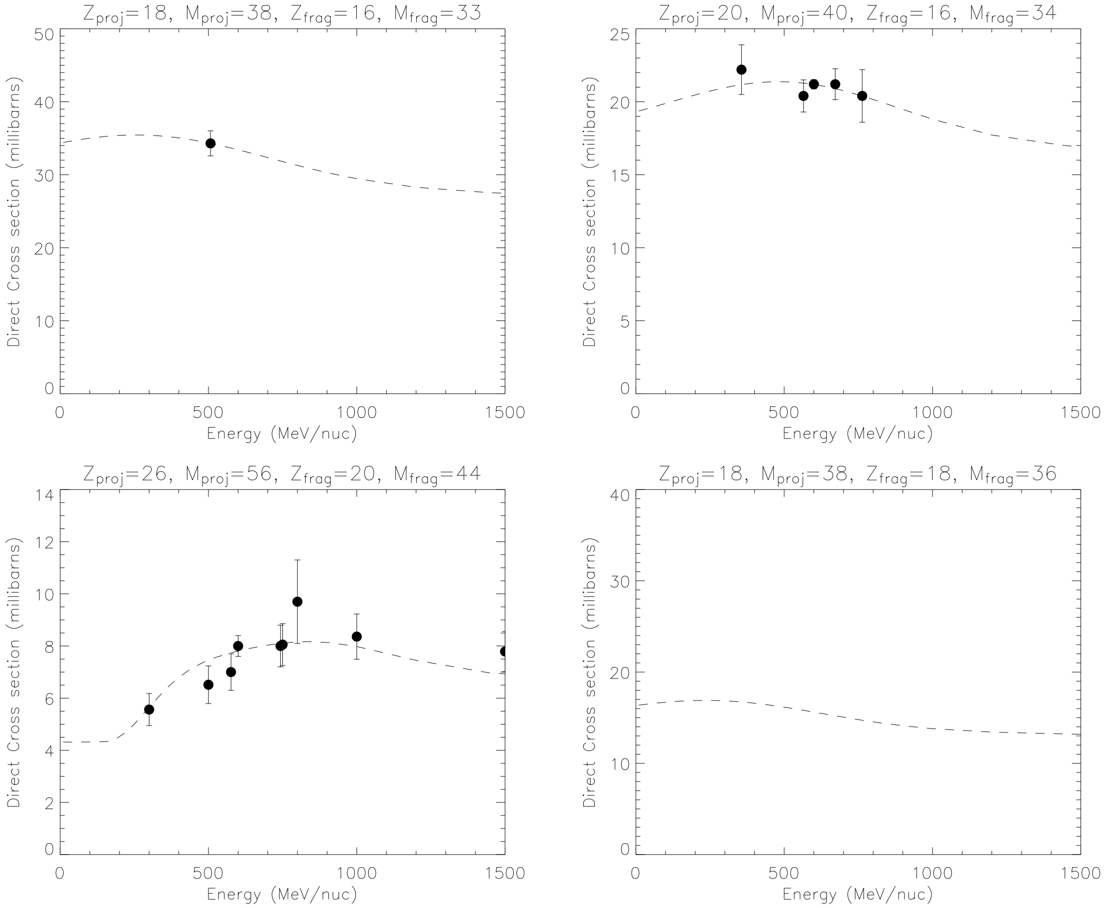

Figure 4.1: Direct cross-section measurements and reported uncertainties for (clockwise from top-left) $^{38}\mathrm{Ar} \rightarrow {}^{33}\mathrm{S}$, $^{40}\mathrm{Ca} \rightarrow {}^{34}\mathrm{S}$, $^{38}\mathrm{Ar} \rightarrow {}^{36}\mathrm{Ar}$, $^{56}\mathrm{Fe} \rightarrow {}^{44}\mathrm{Ca}$. The Webber formula scaled to the data (when available) by the method described in Section 4.2.3, is plotted as a dashed line.

For the leaky-box calculation, nuclei that decay by β^+ (positron emission) or β^- (electron emission) with lifetimes less than 8000 years are treated as decaying immediately after they are produced. Using the most recent branching ratios for these decays from Firestone & Shirley (1998), the direct cross-sections are combined to form a compilation of decayed cross-sections for use in the leaky-box calculation. Decays by $\beta^\pm$ longer than 8000 years are handled explicitly in the leaky-box code. Electron-capture decay is also handled explicitly, as fully stripped cosmic rays are essentially stable to electron-capture at high energies but have some probability of attaching an electron at low energies (Soutoul *et al.*, 1978).

The spallation cross-sections, σ_{ji} and σ_i in Equation 4.1, deduced from the method described above, are an important part of the leaky-box model used to determine source abundances, as they determine how many secondary cosmic rays are produced during the propagation of cosmic rays through the Galaxy. Consequently, uncertainties in these values will be important in assigning uncertainties in the derived source abundances. The Webber and Silberberg formulas claim uncertainties of ~10% and ~15% respectively (Webber *et al.*, 1990; Tsao *et al.*, 1993), though hindsight analysis of predicted cross-sections yielded larger errors (~35%) for the older Silberberg and Tsao formulae (Raisbeck, 1979). An uncertainty value of 25% is adopted for the 1993 version of the Webber cross-section formulae. This is the uncertainty that will be assigned to the direct cross-sections without measurements. The error on the measured reactions is taken to be the error on the scaling factor associated with the rescaled uncertainties as described above. These values vary from 5%-12%. If there is only one data point, the uncertainty on the cross-section values is assigned as 15%. The uncertainties on the direct cross-sections are weighted by the branching ratios and summed in quadrature to derive the uncertainty on decayed cross-sections. The accuracy of these uncertainties is reexamined in Section 4.3.3.1.

4.2.4 Observational constraints

The leaky-box model has been used to determine cosmic ray source abundances for many years (Silberberg *et al.*, 1976). It is conventionally solved by assuming a form for $f_i(\epsilon)$ and Λ^{esc}, as in Equation 4.4. Equation 4.1 is then solved for some set of source abundances q_i, first solving for the heaviest nuclide and then continuing to lighter nuclides, as spallation produces lower mass secondaries. Modulating the interstellar spectra yields the spectra of nuclei observed at Earth. To improve the accuracy of the leaky-box model, it is important to use observational data whenever possible to refine the parameters of the model. Comparing the model-predicted abundance ratios of a species that is thought to be purely secondary and the primary nuclide responsible for its production, like B/C, will yield a better determination of the escape mean free path, Λ^{esc}. As mentioned earlier, cosmic ray data at high energies help in the determination of $f_i(\epsilon)$. The source abundances q_i are altered until the modulated spectra from the leaky-box model become consistent with those measured at Earth.

Deriving source abundances in this manner leads to discrepancies when comparing with high-precision measurements like those obtained by CRIS. The problems with the leaky-box model are evident when looking at nuclides that are mostly secondary. It is sometimes necessary to have an unrealistically large (compared to the solar system value) source abundance of a nuclide in order to match observations, or the leaky-box model may require a negative source abundance for a species thought to be absent from the source. These kind of problems are mostly attributable to errors in the cross-sections as described above. It is possible to circumvent some of the dependence on uncertain cross-sections by constraining model-calculated quantities to observations whenever possible, and still take advantage of the model's predictive capabilities using relatively few free parameters.

4.2.4.1 Scaling to observed spectra

To calculate the interstellar spectrum of a nuclide, φ_i, Equation 4.1 states that it is necessary to know the interstellar spectra of all the nuclides heavier than, or equal in mass to, isotope i. The set of φ_js are responsible for the secondary production of i. The "top-down" approach of first calculating the heavier nuclides using Equation 4.1 will yield errors in these spectra due to uncertainties in cross-sections. However, if these spectra were known, they would not need to be calculated using the leaky-box equation, and uncertainties in the cross-sections for producing isotope j would not enter into the evaluation of the spectra of isotope i. The only cross-sections needed for the determination of φ_i would be the cross-sections for the production and destruction of isotope i directly. Also, the determination of source abundances of heavier nuclides would not be required to calculate φ_i. The CRIS instrument does not measure the interstellar spectra; it measures solar modulated spectra observed at Earth. It is still possible to use these measurements to constrain the interstellar spectra through the scaling procedure described below.

Using the forms discussed earlier for leaky-box parameters Λ^{esc} and $f_i(\epsilon)$, as well as nominal cosmic ray source abundances (source abundance calculations where available, as in Wiedenbeck *et al.* (2001), and solar system composition with fractionation effects included for other nuclides), the leaky-box model is solved in the conventional manner as described above. The resulting interstellar spectra are modulated and then compared to the CRIS observations made at Earth. The leaky-box propagation and solar modulation models should produce approximately the right shape of the spectra observed at Earth, though the overall magnitude of the modeled spectra may differ from the observations, due to cross-section errors. Multiplying each modeled spectrum by a constant k_i brings the model predictions into agreement with the data, as seen in Figure 4.2.

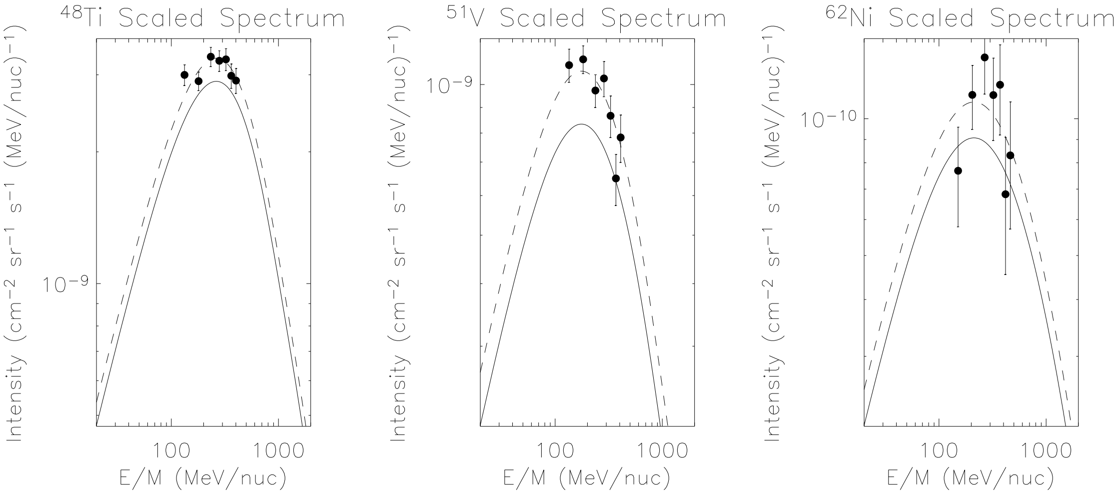

Figure 4.2: The modulated model spectra (solid lines) are multiplied by a constant to fit CRIS measurements (circles) to obtain scaled spectra at Earth (dotted lines). Shown here are three examples of scaled spectra. The predicted spectral shape of the models is reasonably close to the observations, so only the overall magnitude needs to be adjusted to fit the data.

The solar modulation equation is linear in the cosmic ray intensity, so the k_i factors calculated to make the observed spectra agree with the modulated spectra can be used instead to scale the interstellar spectra. Defining scaled interstellar spectra, $\varphi_i' \equiv k_i \varphi_i$, and substituting φ_i' into Equation 4.1, forces agreement to data with the leaky-box parameters used in calculating k_i. Scaling the heavier nuclides in this manner allows for the calculation of the source abundance of a nuclide q_i without requiring the leaky-box to correctly determine the source abundance of all the heavier nuclides.

4.2.4.2 Tracers

A purely secondary cosmic ray isotope k (produced entirely by spallation during cosmic ray propagation) will have no source abundance, $q_k = 0$, and Equation 4.1 becomes:

$$0 = -\frac{\varphi_k}{\Lambda_k} + \sum_{j \geq k} \frac{\varphi_j}{\Lambda_{jk}} + \frac{\partial}{\partial \epsilon}(w_k \varphi_k). \tag{4.8}$$

The solution to the leaky-box calculation (with heaver nuclides scaled as described in Section 4.2.4.1) for k depends on the choice of Λ^{esc} and the destruction and production cross-sections for producing k. Therefore, it is possible in this case to calculate Λ^{esc} in terms of measurable quantities (Reames, 1974). The secondary component of isotopes nearby in mass to k will be produced by similar spallation parents during propagation. Therefore k can be thought of as a probe of the secondary production; a solution to an important part of the propagation problem for nearby isotopes that are mostly secondary with a primary component. These purely secondary isotopes are called "tracers". The tracer method to derive source abundances is described in Stone & Wiedenbeck (1979), and has been used recently to derive the source abundances of neon isotopes in Binns *et al.* (2005).

4.2.5 Determining source abundances of sulfur, argon, and calcium isotopes

4.2.5.1 Choice of tracer isotopes

Based on solar system abundances (Lodders, 2003) and stellar nucleosynthesis systematics (Woosley & Weaver, 1995), the candidate tracer isotopes in the element range $14 \leq Z \leq 22$ were identified to be: ^{33}S, ^{36}S, ^{37}Ar, ^{40}Ar, ^{41}Ca, ^{42}Ca, ^{43}Ca. Of these seven, ^{37}Ar and ^{41}Ca decay by electron-capture. This process is accounted for in the leaky-box model, but it involves electron-attachment cross-sections, which is a source of additional uncertainty in calculating interstellar spectra. Therefore ^{41}Ca and ^{37}Ar are removed from the set of tracer isotopes. Cross-section data for the production of ^{40}Ar is not available, except for spallation from ^{56}Fe. The other candidate tracers have at least a few measurements for parents lighter than ^{56}Fe, even the rare isotope ^{36}S. This disqualifies ^{40}Ar, leaving for the tracer set: ^{33}S, ^{36}S, ^{42}Ca, and ^{43}Ca.

4.2.5.2 The minimization problem

The leaky-box model is employed (Equations 4.1 – 4.3) to calculate interstellar spectra, assuming an escape mean free path of the form in Equation 4.4. The source abundances of the nuclei of interest q_i and the overall constant in the escape mean free path Λ_0 are taken as free parameters in the model. The heavier nuclides are scaled to observations as described in Section 4.2.4. After the nuclei are propagated through the leaky-box, the spectra at Earth $J_i(\epsilon)$ are derived by modulating the interstellar spectra. The modeled spectra are then compared with the CRIS-observed spectra at seven energy values corresponding to CRIS ranges 2-8 (Section 3.8). A χ^2 between the model and observations is calculated for isotope i:

$$\chi_i^2 = \sum_m \left(\frac{J^i(\epsilon = \epsilon_m^i) - I_m^i}{\delta_{total}^i} \right)^2 , \tag{4.9}$$

where the sum m runs over the seven CRIS ranges, and I_m^i is the measured CRIS intensity of isotope i at range m. The total uncertainty δ_{total}^i in Equation 4.9 is the quadrature sum of the statistical uncertainty of the CRIS observations, δ_I^i, and the uncertainty of the secondary production of isotope i, $\delta_{secondary}^i$. The secondary contribution to the interstellar spectra of nuclei i is uncertain, due to uncertainties in the individual decayed cross-sections (described in Section 4.2.3). A total uncertainty on the secondary contribution is calculated by summing in quadrature all the uncertainties on the production cross-sections σ_{ji} for isotopes j heavier than i, and weighting by the interstellar abundance of the parent.

Derivation of source abundances can now be phrased in terms of a minimization problem. It is convenient to express source abundances as ratios of isotopes of the same element, like $^{34}S/^{32}S$. It is valid to assume these isotopes are not fractionated with regards to one another during the acceleration process, because they have similar refractory/volatile characteristics and first ionization potentials (see Section 1.1). Therefore the ratio can be seen as a representative description of the composition of the cosmic ray source, and can be easily compared with other samples of matter. To calculate the source abundance of a given ratio, it is necessary to model two isotopes plus the four tracers. The total χ^2 to be minimized is the sum of six individual χ^2s given in Equation 4.9. The free parameters in the leaky-box model are the source abundances of the two isotopes q_i and q_k (for the tracers, $q = 0$), along with the escape mean free path parameter, Λ_0. The values of q_i, q_k, and Λ_0 that minimize χ^2 will represent the source abundances of i and k and the mean free path required to produce the observed cosmic ray secondaries. The function minimization is performed by a truncated-Newton method algorithm, `TNMIN`, written in the IDL programming language by Craig Markwardt (Markwardt, 2006).

4.3 Results

4.3.1 Determination of modulation parameter for solar minimum

The modulation parameter derived in Figure 3.5 may not be the optimal value for the modulation parameter to be used in the calculation of source abundances for this work. The escape mean free path used in Figure 3.5 takes the form of Equation 4.4, with $\Lambda_0 = 29.5$ g cm^{-2} as described earlier. The Λ_0 parameter used in the calculation of source abundances will differ from this value, which can also contribute to the inaccuracy of using the mean ϕ previously derived for the solar minimum time period.

To derive the appropriate ϕ to be used for this calculation, the minimization algorithm is employed for various ϕs with Λ_0, q_i, and q_j as the free parameters to be solved for. From Figure 3.5, a ϕ of around 380 MV is expected to characterize solar minimum modulation, but a larger ϕ fit the spectra better, resulting in a smaller χ^2. The calculation was run for four different ϕ values: 380 MV, 433 MV, 486 MV, and 538 MV. From these results, it is possible to construct a curve relating χ^2 as a function of ϕ. The optimal ϕ is that value corresponding to the minimum χ^2. A different curve is generated for each source ratio, as shown in Figure 4.3. The minimum of the sum of these three curves is the optimal ϕ to be used in the derivation of source abundances, calculated to be 494 MV $\pm$ 34 MV. The uncertainty in the ϕ parameter chosen is another source of error in the final calculations of source abundances, and is handled in Section 4.3.4.

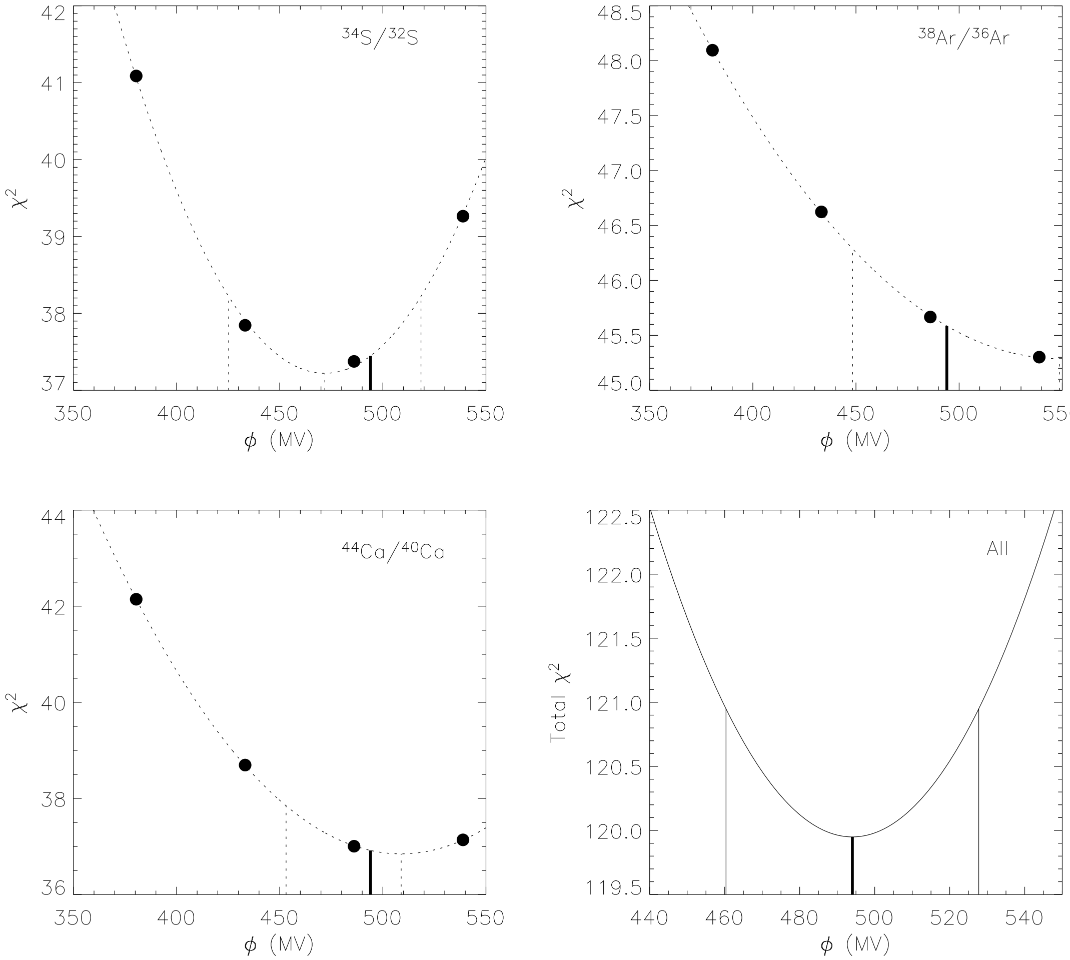

Figure 4.3: The optimal ϕ parameter is derived for all three source ratios. The minimization algorithm employing the leaky-box is used to obtain a χ^2 as described in the text for four different values of the modulation parameter. The calculation for each ratio yields a slightly different optimal ϕ, but the 494 MV optimal value for the set (solid line, shown in the lower right) is consistent with each ratio's derived ϕ to within 1σ uncertainties (bracketing dotted lines). The optimal value for the set, 494 MV, has a 1σ uncertainty of ±34 MV. This is shown in the lower right plot as the ϕ value corresponding to $\chi^2=\chi^2_{min}+1$.

4.3.2 Source abundances

The GCR source abundances for [^{34}S,^{32}S], [^{38}Ar,^{36}Ar], and [^{44}Ca,^{40}Ca] are calculated for the solar modulation parameter ϕ=494 MV over a set of Λ_0 values ranging from 18.6 g/cm^2 to 22.6 g/cm^2. The minimization algorithm solves for the optimal source abundances q_i and q_j, and the mean free path, Λ_0, that minimize χ^2. The algorithm was employed simultaneously for a pair of primary isotopes of the same element, along with the four tracers. The optimal source abundances and cross-section uncertainties for the isotopes of interest are given in Table 4.1, in arbitrary units. For [^{34}S,^{32}S] the minimum value of χ^2_{reduced} was 1.00, for [^{38}Ar,^{36}Ar] it was 1.17, and for [^{44}Ca,^{40}Ca], χ^2_{reduced}=1.03. Seven measured intensities (corresponding to the seven ranges of CRIS events) for six isotopes were fit with three free parameters resulting in 39 degrees of freedom. The optimal Λ_0 for the ensemble was calculated to be 20.32 g/cm^2; the loss mean free path Λ_k varies with species, and is given in Table 4.2. For the optimal source abundances and Λ_0, the set of leaky-box modeled spectra and observations are shown in Figures 4.4, 4.6, and 4.8. Figures 4.5, 4.7, and 4.9 show the source and interstellar spectra calculated by the model.

Isotope	Source Abundance	Cross Sec Err
^{32}S	133.	3.2%
^{33}S	0.0	3.7%
^{34}S	5.25	3.6%
^{36}S	0.0	4.8%
^{36}Ar	15.9	2.9%
^{38}Ar	2.49	4.0%
^{40}Ca	70.8	4.9%
^{42}Ca	0.0	3.2%
^{43}Ca	0.0	3.1%
^{44}Ca	1.35	3.0%

Table 4.1: The derived GCR Source abundances and cross-section errors for the isotopes of sulfur, argon, and calcium. The cross-section error can be thought of as an uncertainty on the secondary production of an isotope.

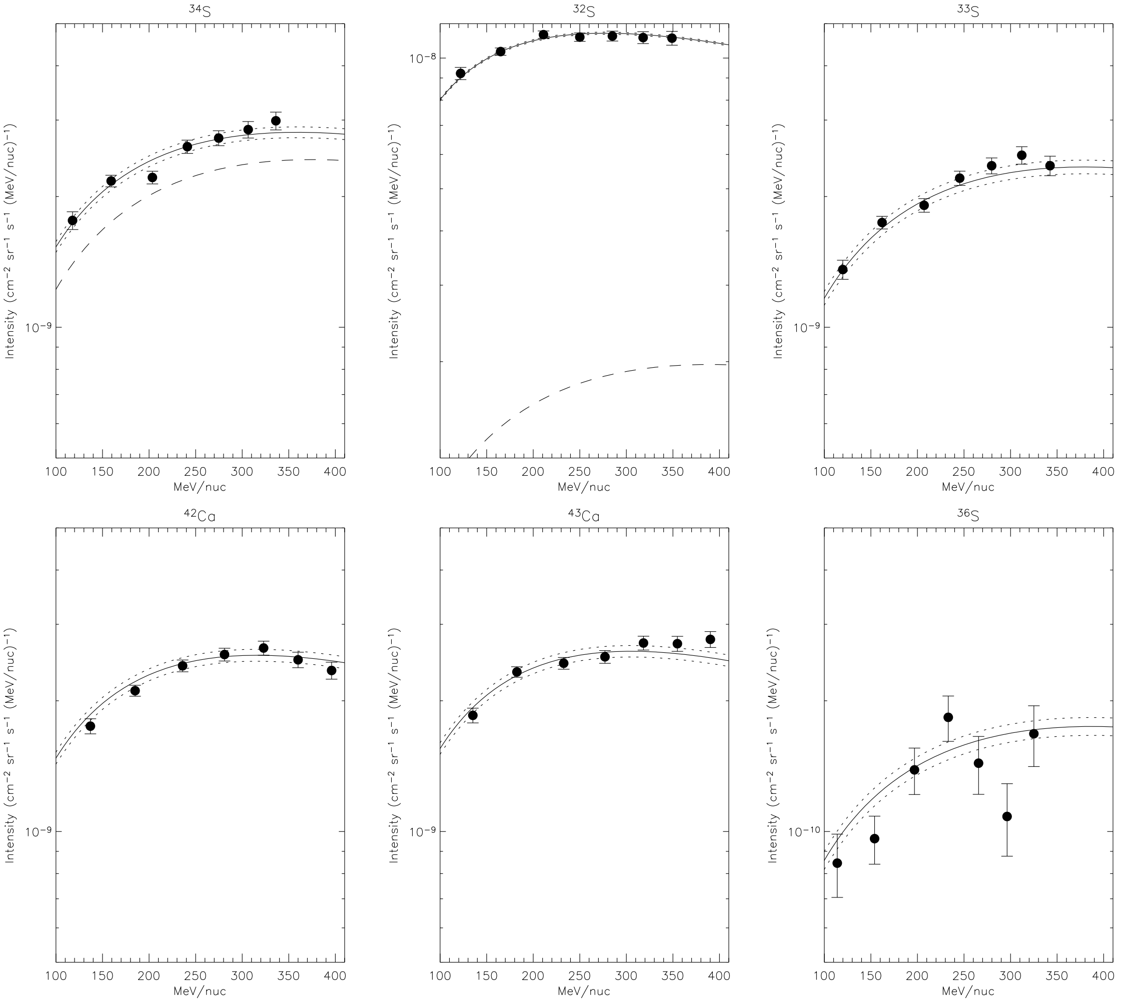

Figure 4.4: The CRIS solar minimum observations (circles, with 1σ statistical uncertainties) are plotted with the model spectra (solid lines) for ^{34}S/^{32}S=0.0394 at the GCR source. The dashed lines show the secondary contribution to ^{34}S and ^{32}S (the tracer isotopes ^{33}S, ^{42}Ca, ^{43}Ca, ^{36}S are all secondary). The dotted lines show the model uncertainty as a result of uncertainties in spallation cross-sections (Section 4.2.3).

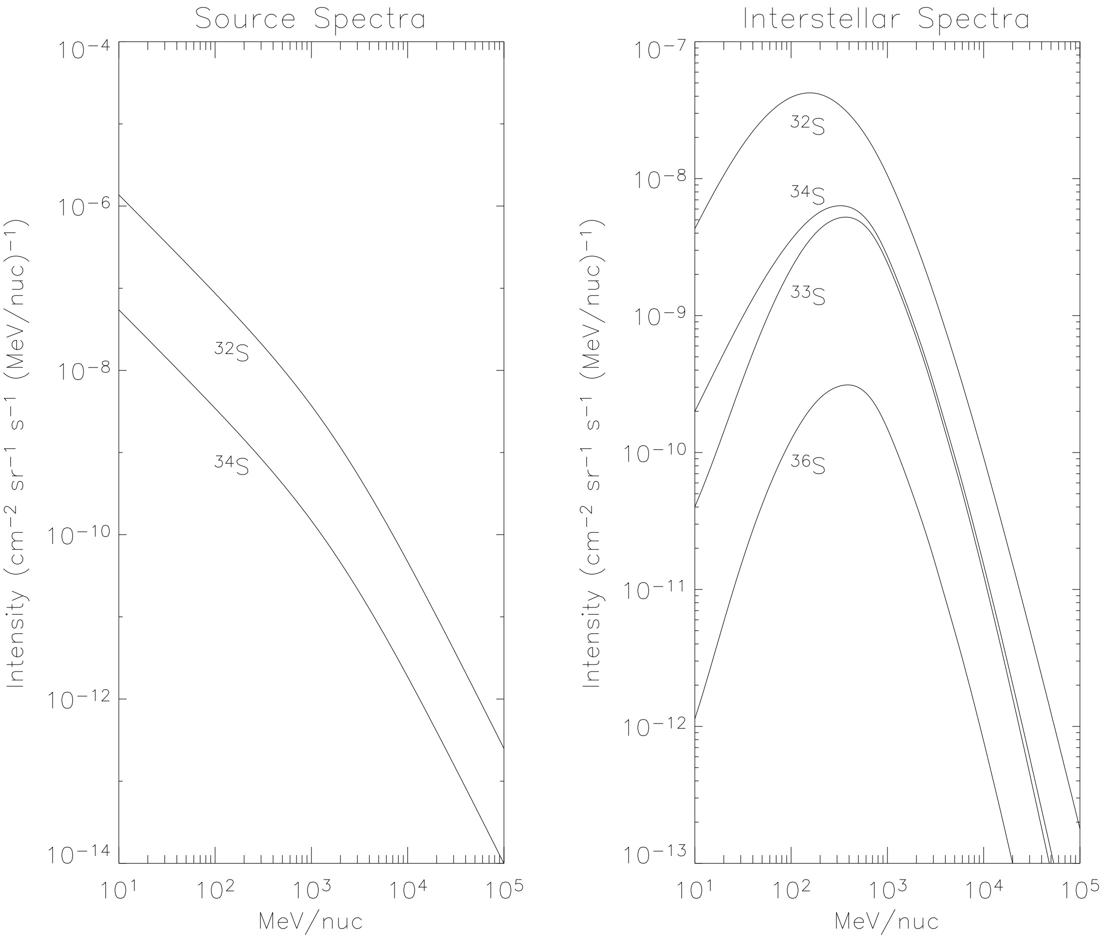

Figure 4.5: ^{34}S and ^{32}S model source spectra ($q_i f_i(\epsilon)$, Equation 4.1) for ^{34}S/^{32}S=0.0394 at the GCR source (left plot), and model interstellar spectra for ^{34}S, ^{32}S, and tracer isotopes ^{33}S, ^{36}S (right plot)

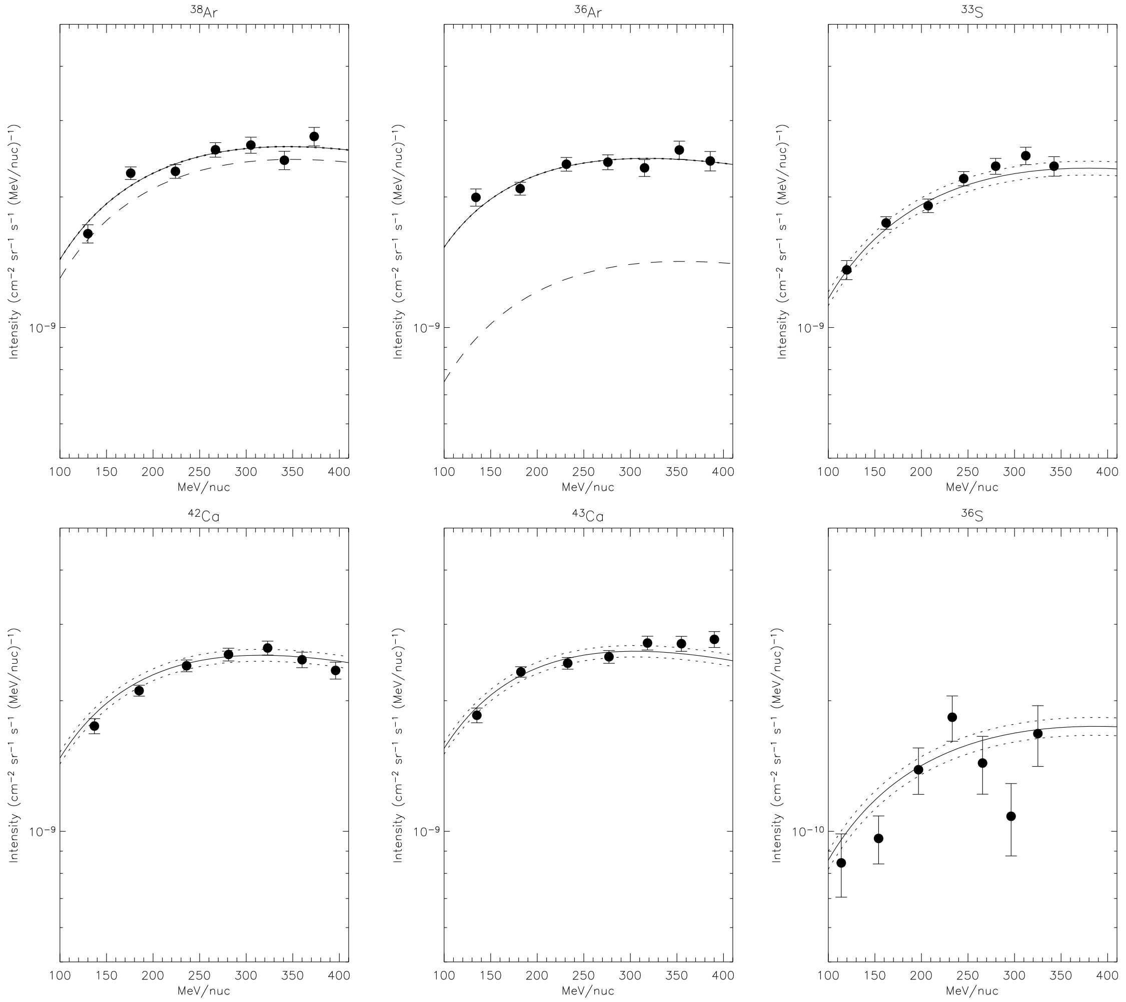

Figure 4.6: Model spectra and observations for ^{38}Ar/^{36}Ar=0.1570 at the GCR source. The dashed lines show secondary contributions to ^{38}Ar and ^{36}Ar, and dotted lines represent model uncertainties due to spallation cross-section uncertainties.

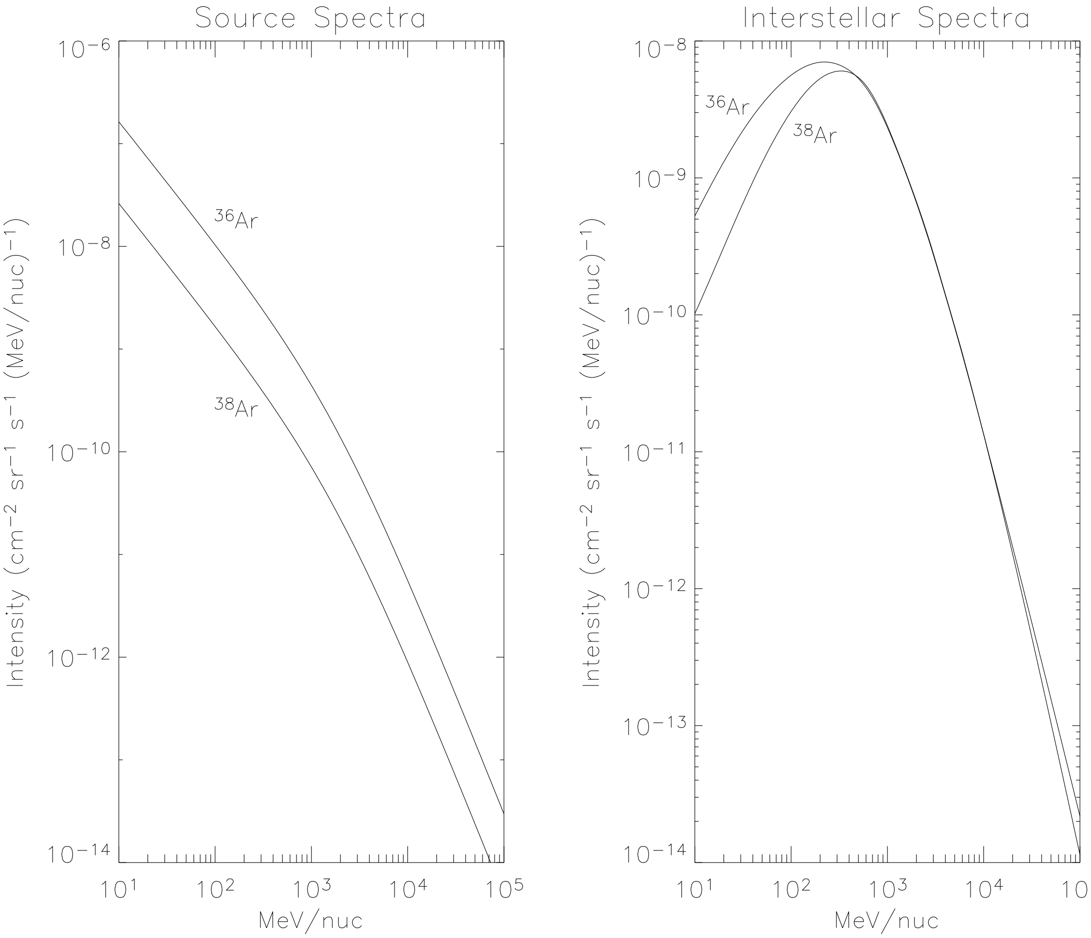

Figure 4.7: ^{38}Ar and ^{36}Ar model source spectra for ^{38}Ar/^{36}Ar=0.1570 at the GCR source (left plot), and model interstellar spectra (right plot)

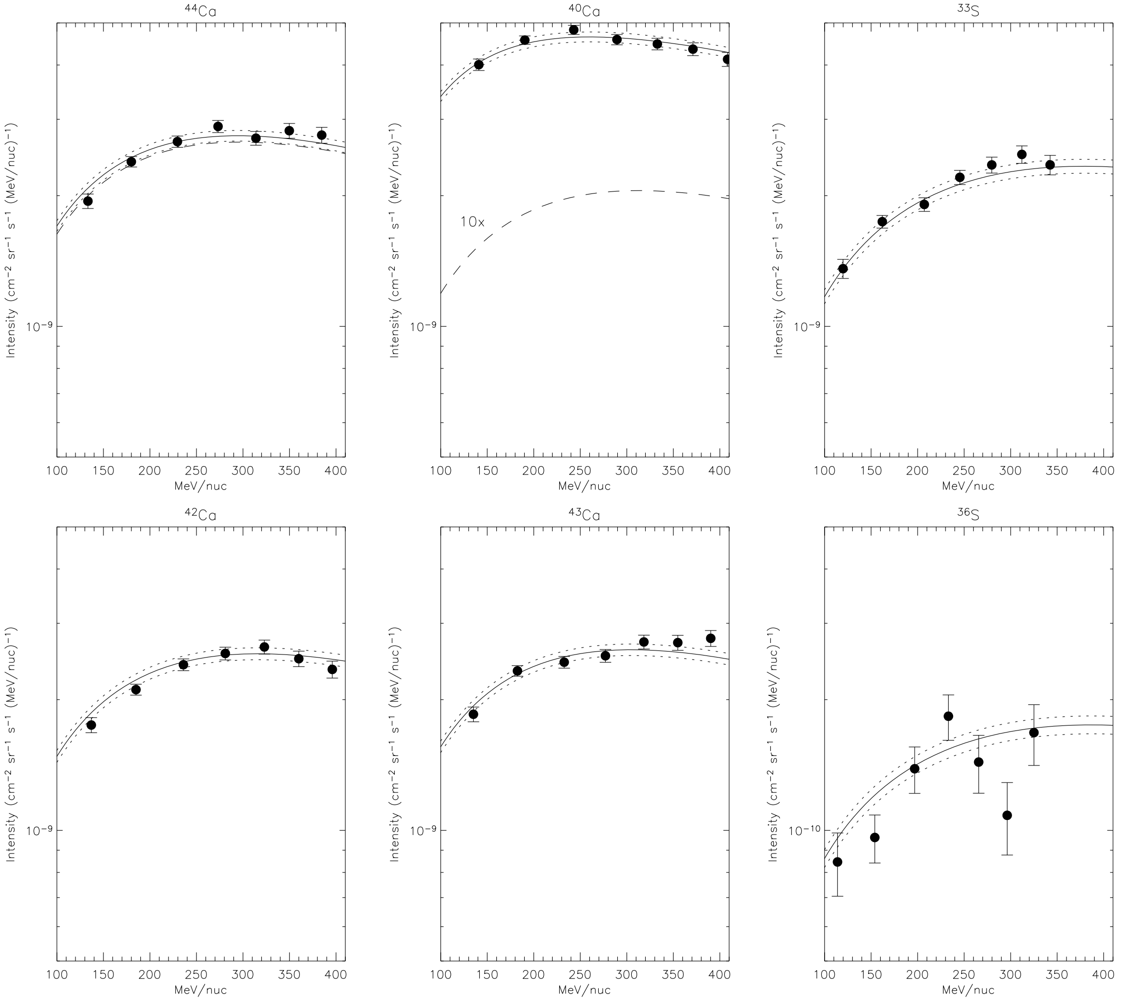

Figure 4.8: Model spectra and observations for ^{44}Ca/^{40}Ca=0.0195 at the GCR source. The dashed lines show secondary contributions to ^{44}Ca and ^{40}Ca (the ^{40}Ca curve is multiplied by ten as plotted), and dotted lines represent model uncertainties due to spallation cross-section uncertainties.

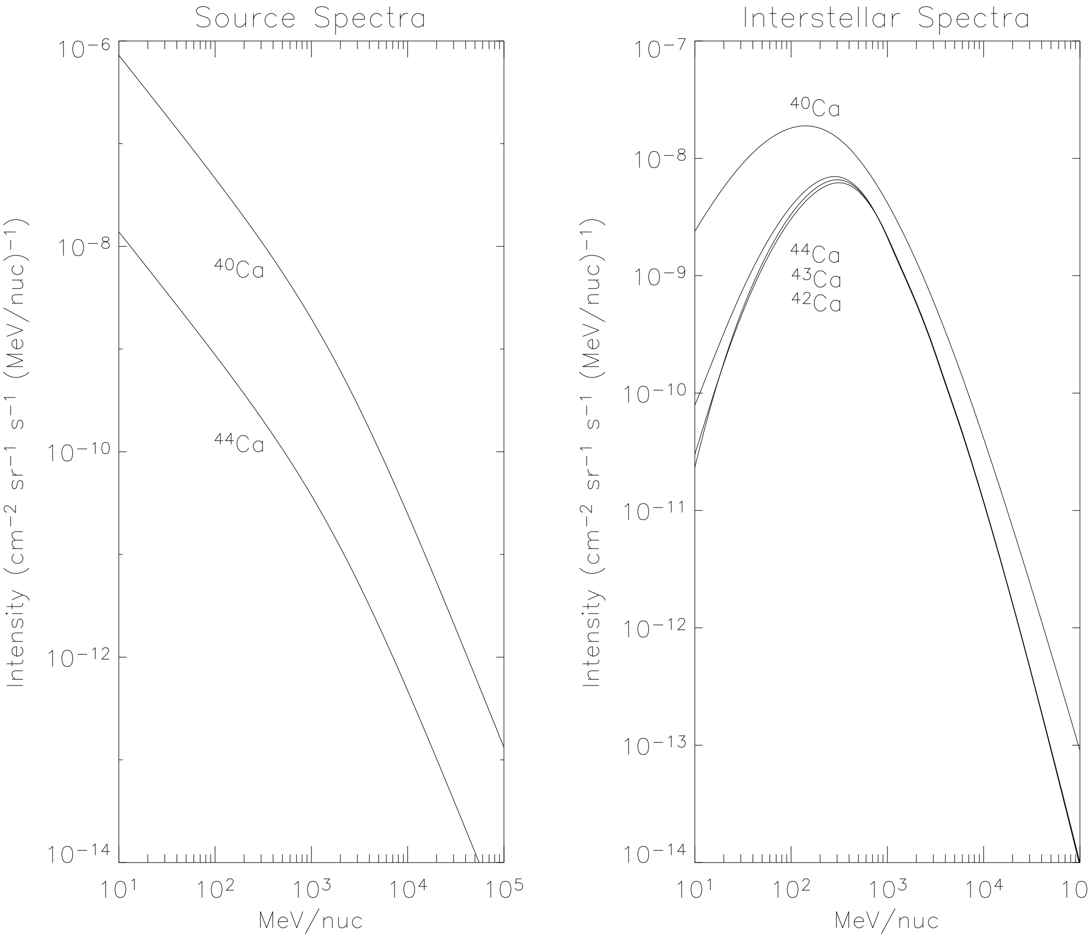

Figure 4.9: ^{44}Ca and ^{40}Ca model source spectra for ^{44}Ca/^{40}Ca=0.0195 at the GCR source (left plot), model interstellar spectra ^{44}Ca, ^{40}Ca and tracer isotopes ^{42}Ca, ^{43}Ca (right plot)

4.3.3 Source abundance uncertainty

4.3.3.1 Cross-section uncertainty

The cross-section uncertainties derived in Section 4.2.3 are based on estimates of semiemperical formulas, and the reported errors from many different experiments. As such, they may not reflect the actual uncertainties in the cross-section values used in the leaky-box model. Since these uncertainties are the primary source of error in the final derived source abundances, it is critical to have a reasonable estimation of them. The uncertainties on the derived source abundances will be dependent on the assumed cross-section uncertainties, though the actual abundance values (Table 4.1) are not sensitive to adjustments in these uncertainties.

The tracer isotopes used in the calculation can serve as a measure of cross-section uncertainties. From the leaky-box equation for a tracer isotope (Equation 4.8), it is evident that the abundance of isotope k varies with the loss and production mean free paths (ignoring energy loss, which won't change interstellar abundances):

$$\phi_k = \Lambda_k \sum_{j \geq k} \frac{\varphi_j}{\Lambda_{jk}}. \tag{4.10}$$

The loss mean free path is determined by the purely secondary tracer isotopes of ^{33}S, ^{36}S, ^{42}Ca, and ^{43}Ca. Since the loss balances the production, the uncertainty in the derived mean Λ_k for the ensemble of tracers reflects the variation of the production of individual tracers. This provides a check on the cross-section uncertainties derived in Section 4.2.3.

A quadratic curve is fit to χ^2 as a function of Λ_k (Figure 4.10). The minimum of this curve corresponds to the best-fit Λ_k, as determined by the purely secondary tracer isotopes of ^{33}S, ^{36}S, ^{42}Ca, and ^{43}Ca. The two values of Λ_k where $\chi^2 = \chi^2_{min} + 1$ define the 1σ

uncertainties on Λ_k (Bevington *et al.*, 1993).

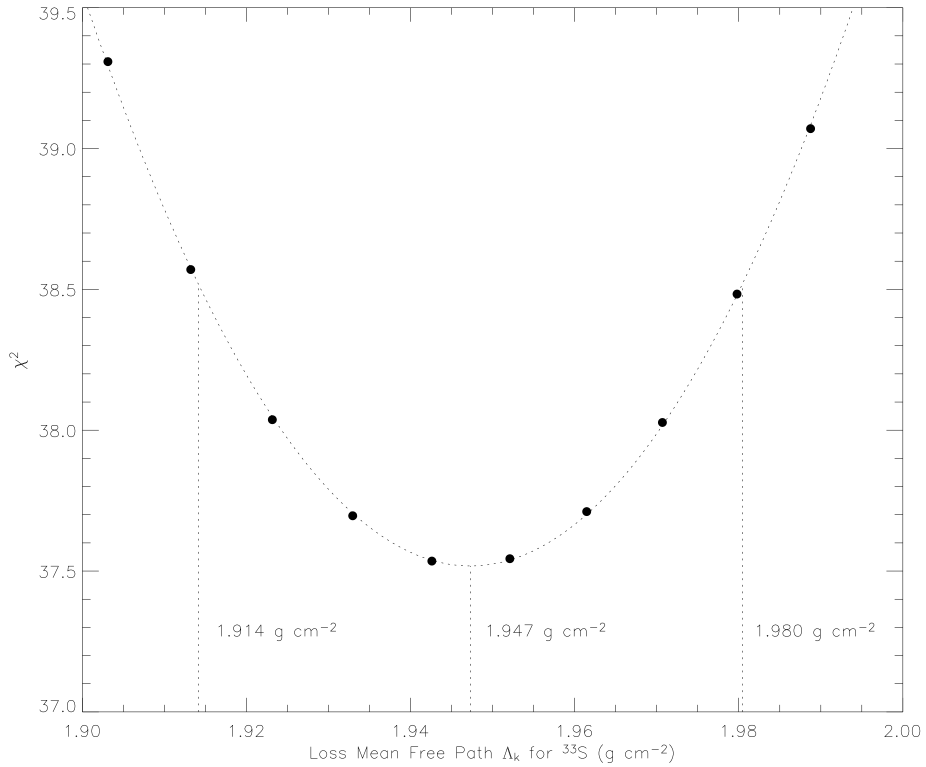

Figure 4.10: χ^2 vs. ^{33}S Λ_k derived from the leaky-box calculation. The uncertainity on the mean Λ_k deduced from the four tracers corresponds to a ~3% uncertainty in the secondary production, consistent with what was assumed for production cross-section uncertainties.

From Figure 4.10, the Λ_k for ^{33}S is 1.947 ± 0.033, an uncertainty of ~1.7%. The derived Λ_ks for the other tracer isotopes (Table 4.2) have different values due to different destruction cross-sections but yield a similar relative uncertainty. The average variance of this ensemble is $\sqrt{N_{\mathrm{tracers}}}$ times the uncertainty on the mean (~1.7%), which is ~3.4%. As discussed above, this value should be about the same as the cross-section uncertainty. Table 4.1 gives the cross-section uncertainties for the isotopes of interest. They range from ~3% to ~5%, so indeed these cross-section uncertainties, derived in an independent manner, are appropriate values to use.

Tracer Isotope	Global Λ_k (g/cm^2)	Individual Λ_k (g/cm^2)
^{33}S	1.95	2.01
^{36}S	1.92	–
^{42}Ca	1.77	1.71
^{43}Ca	1.76	1.78

Table 4.2: The globally and individually derived loss mean free path Λ_k for the four tracer isotopes. The global value is a fit to the ensemble (though Λ_i differs across isotopes, see Equation 4.3) while the individual value is a fit only to that isotope. The difference between the individual and global values varies from ~1% to ~3%, implying that the measured cross-sections have approximately this much uncertainty and that the derived values shown in Table 4.1 are valid. The tracer isotope ^{36}S has insufficient statistics to accurately calculate the individual Λ_k.

4.3.3.2 Uncertainty in source ratios

The fit parameters Λ_0, q_i, and q_j are not uncorrelated: if Λ_0 is changed, the amount of secondary nuclei is changed, which necessitates a change in the source abundances q_i and q_j needed to match the observed intensities. The χ^2 value varies quadratically near its minimum in terms of any of the three parameters, so assuming a $q\Lambda_0$ cross term, χ^2 can be expressed as:

$$\chi^2 = a_1\Lambda_0^2 + a_2\Lambda_0 + a_3 q_i^2 + a_4 q_i + a_5 q_j^2 + a_6 q_j + a_7 q_i \Lambda_0 + a_8 q_j \Lambda_0 + a_9. \tag{4.11}$$

Values for a_{1-9} can be derived by evaluating the χ^2 of many (q_i, q_j, Λ_0) points near the optimal values, as calculated earlier, and fitting a surface to the points. Setting χ^2=χ^2_{min}+1, and q_i to its optimal value, Equation 4.11 is solved for values of q_j and Λ_0 corresponding to χ^2_{min}+1. These values form an ellipse, as shown in Figures 4.11 – 4.16. The projection of the ellipse onto the q_j axis gives the total error in q_j, including correlated errors due to uncertainty in Λ_0. There is assumed to be no correlation between the qs because the uncertainty in the abundance of a single spallation parent will have only a small effect on the abundance of a lighter nuclei.

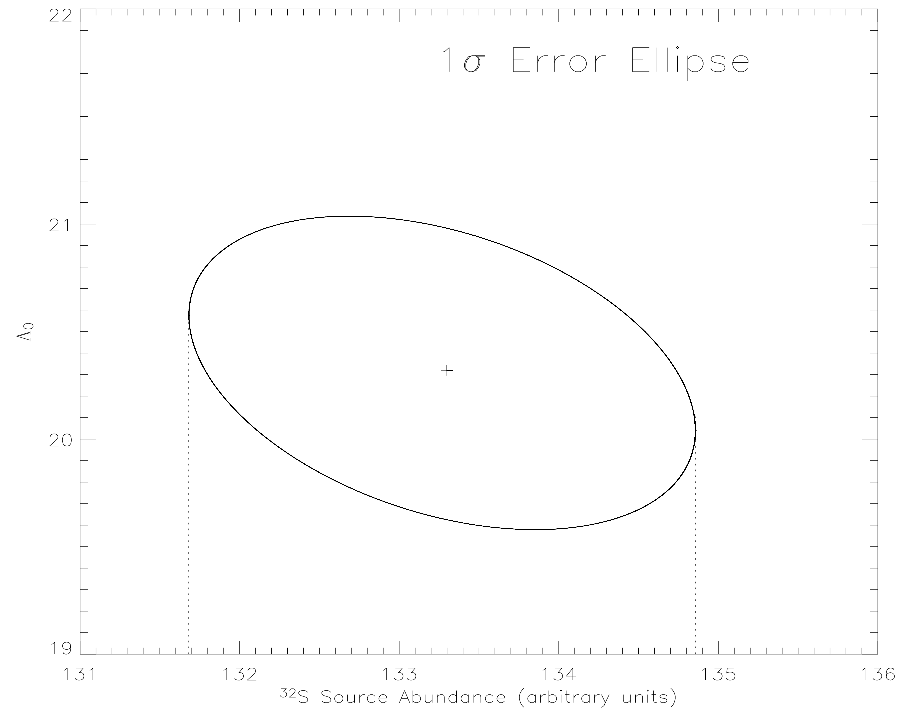

Figure 4.11: ^{32}S 1σ error ellipse showing the correlated uncertainty between the Λ_0 and q parameters in the leaky-box calculation. The projection of the ellipse onto the x-axis is the uncertainty assigned to the ^{32}S source abundance, to be combined with the ^{34}S uncertainty when the error on the ratio ^{34}S/^{32}S is calculated. The optimal (q,Λ_0) is given by the '+.'

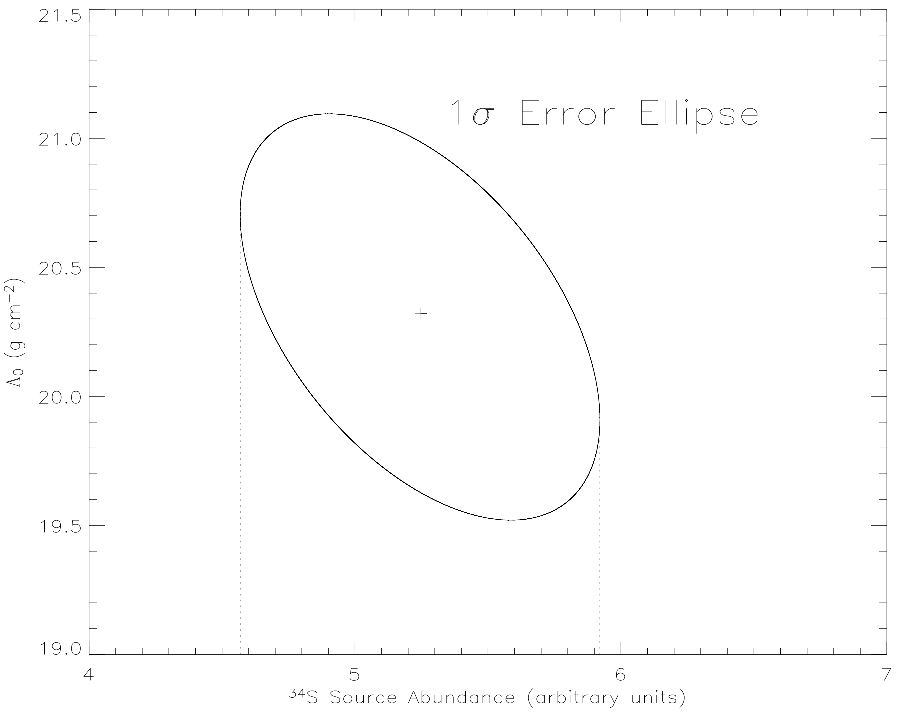

Figure 4.12: ^{34}S 1σ error ellipse. The total error on the ^{34}S is shown by dotted lines.

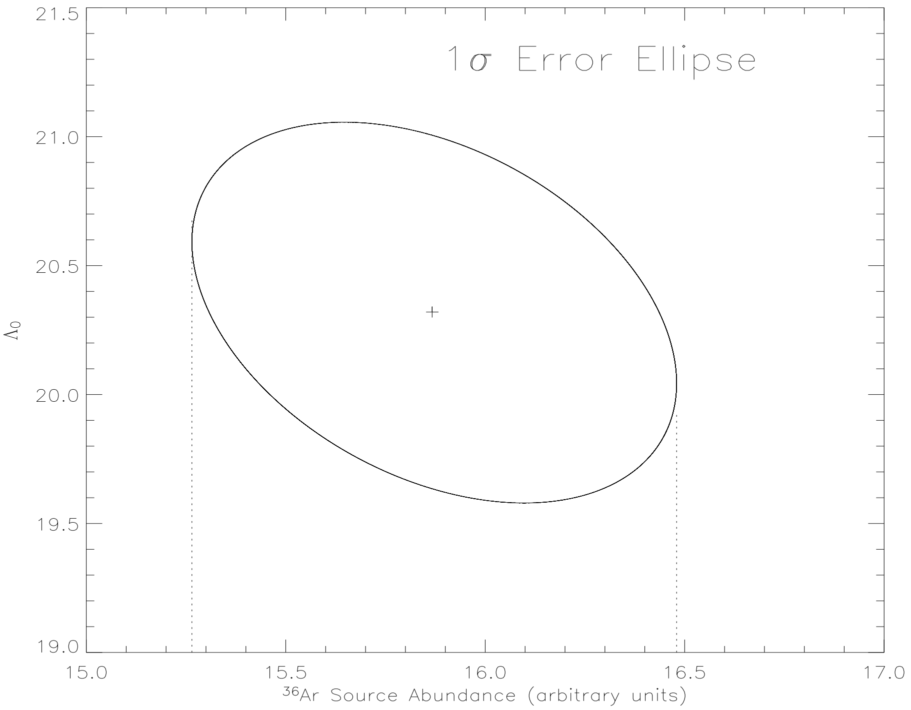

Figure 4.13: ^{36}Ar 1σ error ellipse. The total error on the ^{36}Ar is shown by dotted lines.

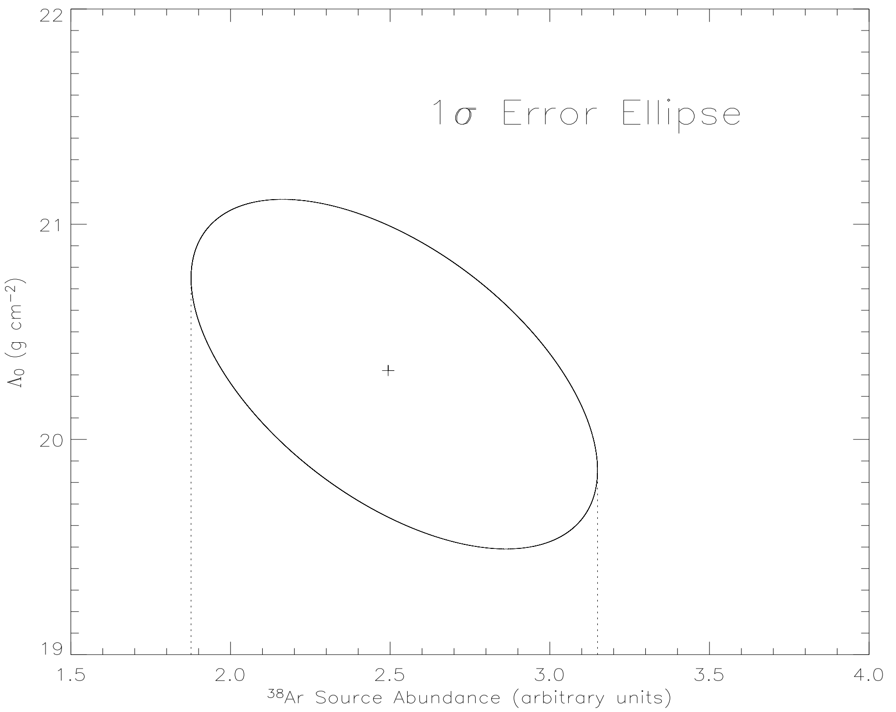

Figure 4.14: ^{38}Ar 1σ error ellipse. The total error on the ^{38}Ar is shown by dotted lines.

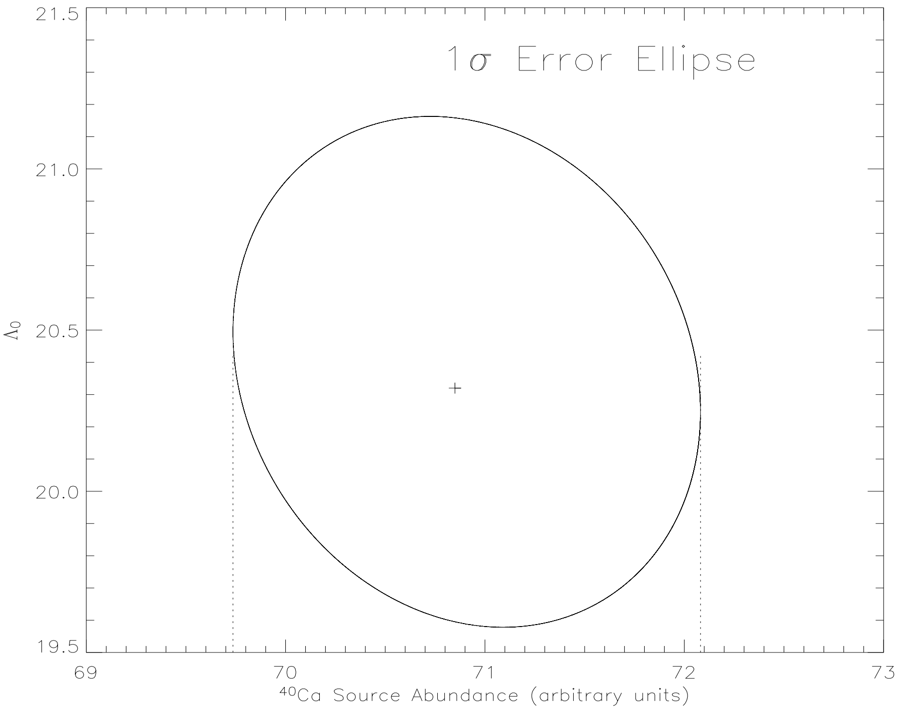

Figure 4.15: ^{40}Ca 1σ error ellipse. The total error on the ^{40}Ca is shown by dotted lines.

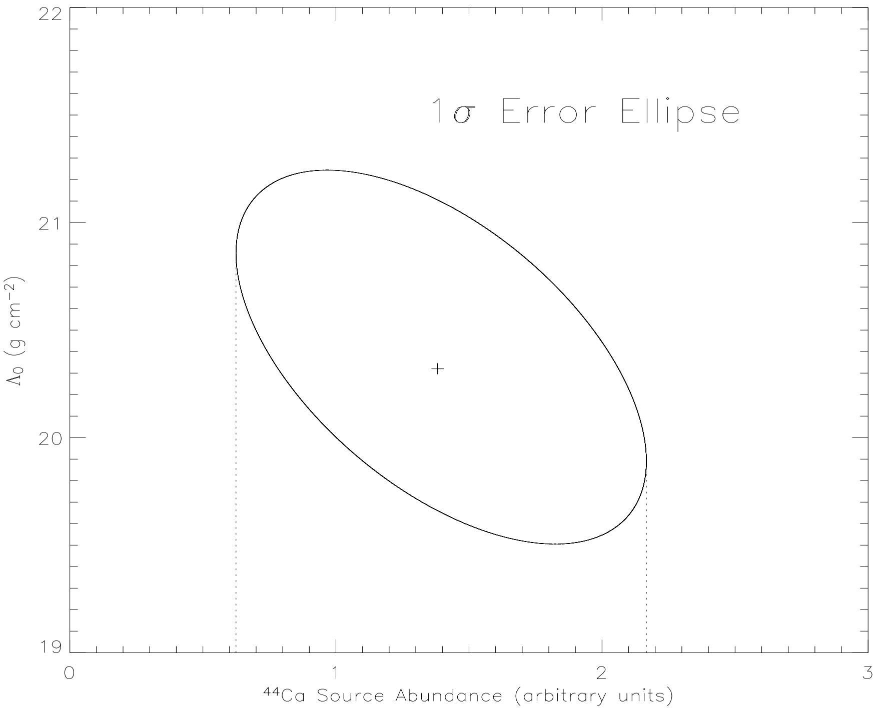

Figure 4.16: ^{44}Ca 1σ error ellipse. The total error on the ^{44}Ca is shown by dotted lines.

The uncertainties on q_i and q_j shown in Figures 4.11 – 4.16 are combined to find the uncertainty on the source ratio q_i/q_j. The source ratios and their derived uncertainties are given in Table 4.3. The three calculated ratios are consistent with solar system composition (also given in Table 4.3).

Isotope Ratios: GCR source and Solar System		
Ratio	GCR Source	Solar System
^{34}S/^{32}S	3.94%±0.54%	4.44%
^{38}Ar/^{36}Ar	15.70%±4.20%	18.18%
^{44}Ca/^{40}Ca	1.95%±1.12%	2.15%

Table 4.3: Derived isotope ratios at the GCR source and in the solar system as given by Lodders (2003)

The source composition of these isotopes can be explained by a cosmic ray source material that is similar to the solar system in its isotopic makeup. It can be logically assumed that all cosmic ray isotopes are accelerated out of the same sample of matter. Therefore, if a solar-like source is assumed to explain the abundances of the isotopes of sulfur, argon, and calcium, all GCR isotope abundances must reflect solar composition. The isotopes of neon violate this assumption, as explained in Section 1.1: the observed ^{22}Ne/^{20}Ne in the GCRs requires a non-solar contribution to the source of cosmic rays. The same source material that explains the neon isotopic anomaly must explain the solar-like abundances of the sulfur, argon, and calcium isotopes. The nature of this source is investigated in Chapter 5.

4.3.4 Uncertainty in the modulation parameter

The solar modulation parameter ϕ is not completely constrained, but can vary from 460 MV to 528 MV as shown in Figure 4.3. Therefore, the total uncertainty on the derived source ratios must take into account the uncertainty in ϕ. The uncertainty in the source abundances q_i and q_j have been calculated for ϕ=494 MV (Figures 4.11 – 4.16), and the uncertainty in ϕ was calculated in Section 4.3.1. Similar to what was done in Section 4.3.3.1, one can construct a 1σ contour in the ϕ-q plane using these data points, if the q values associated with the $\pm 1\sigma$ ϕ values from Figure 4.3 are known. Fortunately, q smoothly varies with ϕ, so the needed q values can be interpolated with reasonable accuracy. Another leaky-box minimization calculation (as in Section 4.3.2) was run with ϕ=470 MV to further constrain the contour. An ellipse was fit to the (q,ϕ) pairs, corresponding to 1σ uncertainties.

The total uncertainty on the source ratios, including the modulation uncertainty, did not differ from what was derived assuming ϕ=494 MV. Though the effect of modulation on interstellar spectra is not known with certainty, the derived source ratios do not vary significantly over a broad range of ϕs at solar minimum. This gives the calculated ratios robustness at solar minimum, though this is not the case for solar maximum, as will be seen in the next section.

4.3.5 Solar maximum

The GCR source abundances were derived using CRIS observations during the solar minimum time period, August 28, 1997, through August 17, 1999. The calculated ϕ parameter for the solar maximum time period, shown in Figure 3.5, is not smoothly varying, as it is for solar minimum. The solar maximum period has a larger total variation in ϕ, $\sim$400 MV, compared to solar minimum, $\sim$150 MV. Also, the calculated ϕ for different elements has a wider spread during solar maximum than it does during solar minimum. The modulation of interstellar spectra is more severe during solar maximum, so inaccuracies in the solar modulation model employed in this work will have a larger effect on the derived spectra at 1 AU (and consequently, the derived source abundances). Therefore, the source abundances were derived using CRIS observations for the solar minimum time period. The solar maximum time period could possibly be used as a consistency check, as described below.

The propagation of cosmic rays through the Galaxy does not depend on the state of the heliosphere, so the modeled propagation is the same for both time periods up until solar modulation. Therefore, the derivation of source abundances for the two different modulation levels should yield the same results if the modulation is being handled correctly. The scaling of parent nuclei (Section 4.2.4.1) is done using solar minimum observations for both time periods, as the demodulating of 1 AU spectra to interstellar spectra is more accurate for the lower modulation levels during solar minimum. Also, the magnitude of the escape mean free path, Λ_0, should not depend on the solar modulation level. The solar minimum calculations for the three source ratios yielded a Λ_0 value of 20.3 ± 0.8 g/cm^2 (in agreement with $\Lambda_0=20.5\pm2.7$ g/cm^2 as derived by Binns *et al.* (2005)).. For solar maximum, Λ_0 is held fixed at this value. The leaky-box model calculations are performed as for solar minimum, but the modulation modeled spectral shapes do not fit the observations as well as solar minimum, as shown in Figures 4.17 and 4.18. Past work using a similar Fisk model for solar modulation have also shown difficulties in fitting solar maximum observations, even though the solar minimum data fit nicely (Davis *et al.*, 2001).

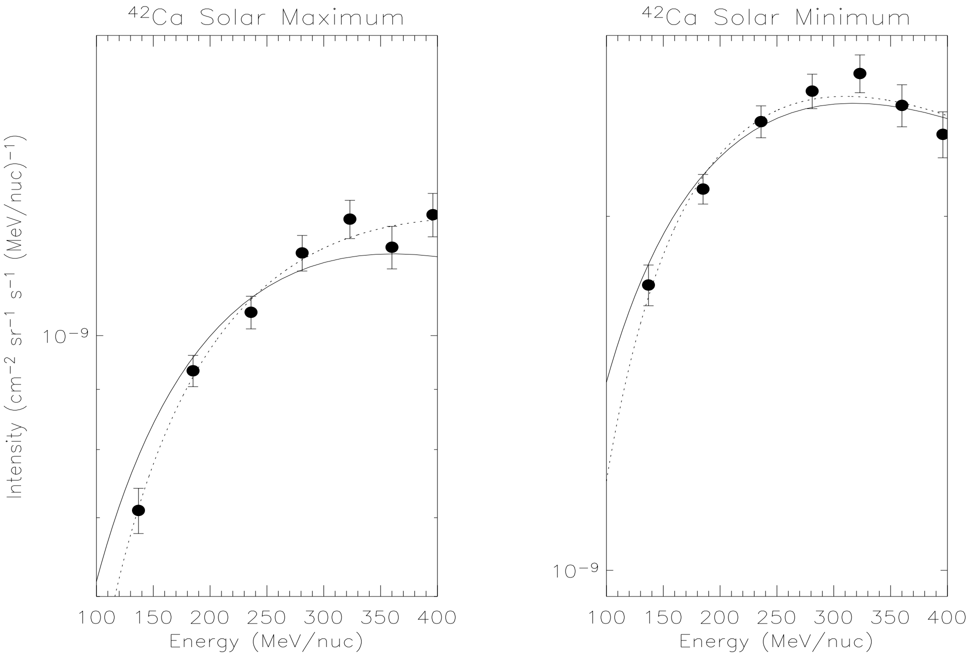

Figure 4.17: The solar maximum and minimum spectra for ^{42}Ca, a tracer isotope used in the leaky-box calculation. The solid line is the Fisk solar-modulated, leaky-box spectrum and the dotted line is a parabolic fit to the data in ln(E/M), as used to fit elemental spectra in Equation 3.23. The solid line does not fit the shape of the spectrum well at solar maximum (χ^2=16.0), but it is closer at solar minimum (χ^2=5.9).

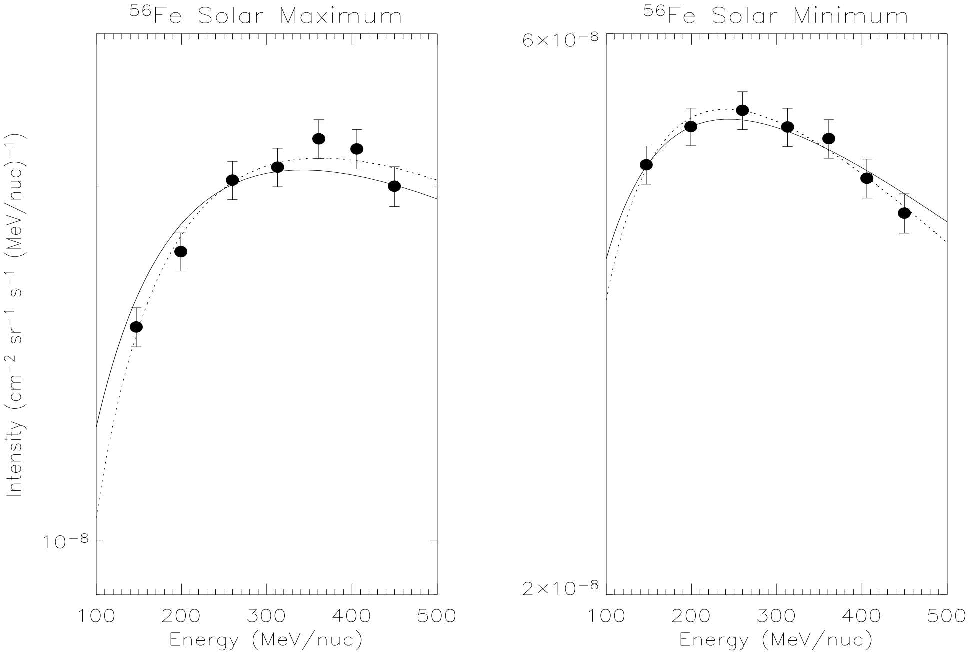

Figure 4.18: The solar maximum and minimum spectra for ^{56}Fe. As is the case for ^{42}Ca, the model calculated spectrum (solid line) over-predicts the intensity for low energies and under-predicts the intensity at high energies for solar maximum (χ^2=8.7). The model is much closer to the shape of the data for solar minimum (χ^2=1.8).

The leaky-box model calculations for solar maximum are very sensitive to ϕ. Varying the ϕ parameter by only a few MV results in a large change (nearly a factor of two) in the derived source abundance ratio. A source of this problem could be that modulation during solar maximum is making a large correction to the interstellar spectra. The derivation of source abundances of ^{34}S and ^{44}Ca is a task in finding subtle changes to the spectra as a very small source abundance is varied. The uncertainty in the large energy loss of interstellar nuclei could be drowning out the small changes the algorithm is looking for. The modulation model used here assumes that the diffusion coefficient (Equation 4.6) has the same linear dependence on rigidity during solar minimum and solar maximum. This simplifying assumption is contradicted by observations by the Voyager spacecraft in the outer heliosphere (Cummings, 1999). Modification of the modulation code to account for changes in the diffusion coefficient with ϕ would be an important step to facilitate the modeling of solar maximum, but is beyond the scope of this work.

4.4 Comparison to previous work

The Galactic cosmic ray source ratio ^{34}S/^{32}S was calculated using data from the *Ulysses* High Energy Telescope (Thayer, 1997). The propagation calculation was done using a leaky-box model, and solar modulation was handled using similar assumptions as this work. The observed ^{34}S/^{32}S is quoted as 24.2%±2.7% over the range of ∼100-300 MeV/nuc, consistent with the CRIS solar minimum ratio shown in Figure 3.26. The derived source ratio is 6.2%±2.6%±≤2.9%, where the first error is statistical and the second is due to uncertainty in the propagation calculation, due mainly to cross-section uncertainties. The Thayer value is consistent with the ratio derived here, 3.94%±0.54%. The source ratio uncertainty derived in this work is lower than in previous isotopic studies of the cosmic ray source, due to the high mass resolution of the CRIS instrument, combined with good statistics, an extensive set of cross-section measurements, and the use of multiple tracers to monitor secondary production.

The other cosmic ray isotopes in the element range 15≤Z≤20 are not well characterized (Mewaldt, 1989; Shapiro *et al.*, 1991). The ratios derived in this work are the first derived source ratios for the isotopes of argon and calcium.

Chapter 5

Constraints on the Origin of Galactic Cosmic Rays

The Galactic cosmic ray source ratios derived in Section 4.3 give clues to the nature of the environment where the cosmic rays were accelerated, as described in Section 1.1. Cosmic rays are thought to be accelerated in the cores of superbubbles formed by OB associations (Higdon *et al.*, 1998). The ejecta from supernova explosions and winds from Wolf-Rayet stars mixes with the interstellar medium to form the material out of which cosmic rays are accelerated. The mixing fraction of ejecta material to the accumulated gas and dust inside the superbubble core, denoted f_{ej}, is not known with certainty. A value of the mixing fraction f_{ej}=18%±5% was derived to explain the high ratio of ^{22}Ne/^{20}Ne observed in the cosmic rays, compared to the solar wind (Binns *et al.*, 2005; Higdon & Lingenfelter, 2003b). This f_{ej} was also shown to be consistent with cosmic ray observations of ^{12}C/^{16}O and ^{58}Fe/^{56}Fe.

The amount of mixing in the superbubble can be further constrained by the source ratios of other isotopes in the cosmic rays. Wolf-Rayet wind material is the dominant contributor to the ^{22}Ne, ^{12}C, and ^{58}Fe excess in superbubbles, so the f_{ej} derived from cosmic ray source abundances of those isotopes only constrains the contribution of Wolf-Rayet stars to the superbubble core composition. The supernova contribution to these isotopes is small compared to the Wolf-Rayet wind contribution. To sensitively probe this other ingredient in the mix of superbubble core material, the superbubble source composition of isotopes that are dominated by supernova ejecta must be calculated. The isotopes of sulfur, argon, and calcium are mostly created by core-collapse supernovae inside superbubbles, as will be shown later in this chapter. Comparing this composition with the cosmic ray isotopic composition will constrain the value of f_{ej}. The mixing fraction computed with these isotopes can be compared with the mixing fraction determined by the other isotopes. The level of agreement between these values will yield insight into the robustness of the superbubble origin of cosmic rays.

The isotopic composition of the superbubble core depends on the composition of the interstellar medium along with the supernova ejecta and Wolf-Rayet winds. The isotope abundances for sulfur, argon, and calcium are calculated for the ejecta in Sections 5.1 – 5.5 and for the ISM in Section 5.6.

5.1 Ejecta from Supernova Type II

Supernova Type II (SNII) are distinguished from Type I (SNI) by the presence of hydrogen lines in their spectra. A star larger than about eight solar masses ($8M_\odot$) will undergo a catastrophic collapse of its iron core at the end of its lifetime. The collapse of the core is eventually stopped by the degeneracy pressure of neutrons, and the infalling stellar matter rebounds, creating a shock wave which ejects the star's envelope. The supernova explosion creates much higher temperatures than were ever present during the star's main sequence lifetime. Nucleosynthesis occurs in the explosion, creating nuclides that are not produced, or only produced in low quantities, during quiescent burning of the star. The material created by supernova nucleosynthesis, as well as the star's envelope, which consists of material synthesized during the star's main sequence lifetime, is ejected by the explosion. A neutron star (or for heavier stars, a black hole) is left behind.

The isotopic ejecta yields for SNII are calculated for a range of initial stellar masses and metallicities by Woosley & Weaver (1995). Observations of OB associations by Daflon & Cunha (2004) show that the metallicity of stars in a typical nearby superbubble is within 50% of the solar system value (further discussed in Section 5.8). The Woosley & Weaver (1995) SNII models calculate ejecta yields for stars of solar metallicity and orders of magnitude larger and smaller. The calculations for solar metallicity will be used in this work.

5.2 Ejecta from Supernova Type Ibc

Type I supernovae do not have hydrogen lines in their spectra. Type Ib show evidence for neutral helium whereas Type Ic do not. Supernovae of Type I are core-collapse explosions like Type II, but the progenitor star of an SNIbc no longer has a hydrogen-rich outer envelope. This can happen due to intense stellar winds ejecting the stellar atmosphere as happens in the Wolf-Rayet phase of very massive stars.

This work uses yields for SNIbc as calculated by Woosley *et al.* (1995). These yields are calculated as a function of the progenitor star's helium core mass (the star's mass after it has ejected its hydrogen envelope). Results from Arnett (1978) are used to relate the helium core mass to the star's initial main sequence mass.

5.3 Wolf-Rayet winds

During the Wolf-Rayet (WR) phase of massive stars, a large amount of material is ejected from the star in the form of stellar winds that blow off the outer envelope (Maeder & Conti, 1994; Nugis & Lamers, 2000). The massive star models of Meynet *et al.* (2001) were used to calculate abundances in the Wolf-Rayet winds ejected between the star's birth and the end of the WR phase for stars of mass 40M$_\odot$, 60M$_\odot$, 85M$_\odot$, and 125M$_\odot$ by Goriely (2005) (see also, Binns *et al.* (2005); Arnould *et al.* (2006)). Uncertainties in the mass loss rates of massive stars makes it difficult to model the properties of WR stars. The yields used here do not take into account clumping in WR wind ejecta which could significantly change the amount of material the WR star loses in its winds (Hamann & Koesterke, 1998). The effect of this uncertainty is discussed in Section 5.11.

5.4 Superbubble ejecta abundances

Stars with initial masses greater than ~8M$_\odot$ and less than some limiting mass will explode as Type II supernova. The limiting mass, M_L, denotes where the star is large enough to enter the Wolf-Rayet phase, resulting in the loss of its outer envelope and the absence of hydrogen lines in the spectrum of its supernova. Therefore, above M_L the star will explode as a Type Ibc supernova (Filippenko, 1997). Recent work by Meynet & Maeder (2005) shows that the minimum initial mass for a star to enter the Wolf-Rayet phase is ~25M$_\odot$ ±4M$_\odot$, depending on the different evolutionary scenarios (metallicity, rotational velocity) of the star. This work will use an M_L value of 25M$_\odot$ ±4M$_\odot$.

Stars with very large initial masses will collapse into a black hole. In this case, the black hole accretes the material that otherwise would be expelled in a supernova, and no explosion occurs. No material is ejected into the surrounding environment for stars larger than M_{BH}. Estimates for M_{BH}, taking wind losses into account, are around 40M$_\odot$ (Fryer, 1999; Wellstein & Langer, 1999). This will be the value adopted for this work.

Stars are formed when the dense core of a molecular cloud becomes gravitationally unstable, fragments, and then collapses. Generally, this process creates more low-mass stars than high-mass stars. The distribution of stellar masses is called the initial mass function (IMF). The OB association that forms a superbubble is assumed for this study to have the Salpeter IMF (Salpeter, 1955): $dN/dM \propto M^{\gamma}$ where $\gamma = -2.35$. Observational evidence for the IMF in nearby OB associations varies over a range of γ values, from -1.7 to -3.1 (Massey *et al.*, 1995; Brown *et al.*, 1994; Claudius & Grosbol, 1980). For this work, γ is assumed to be the Salpeter value, -2.35. The variation in the IMF over the range $-1.7 \leq \gamma \leq -3.1$ is explored in Section 5.11.

The isotopic composition of the ejecta will have contributions from the three ingredients described above for stars of various mass, weighted by the Salpeter IMF (normalized to unity at $8M_{\odot}$). As seen in Figures 5.1 – 5.3, SNII are responsible for the majority of the ejecta isotope abundances (though Wolf-Rayet winds make up a sizable fraction of the total ^{44}Ca ejecta).

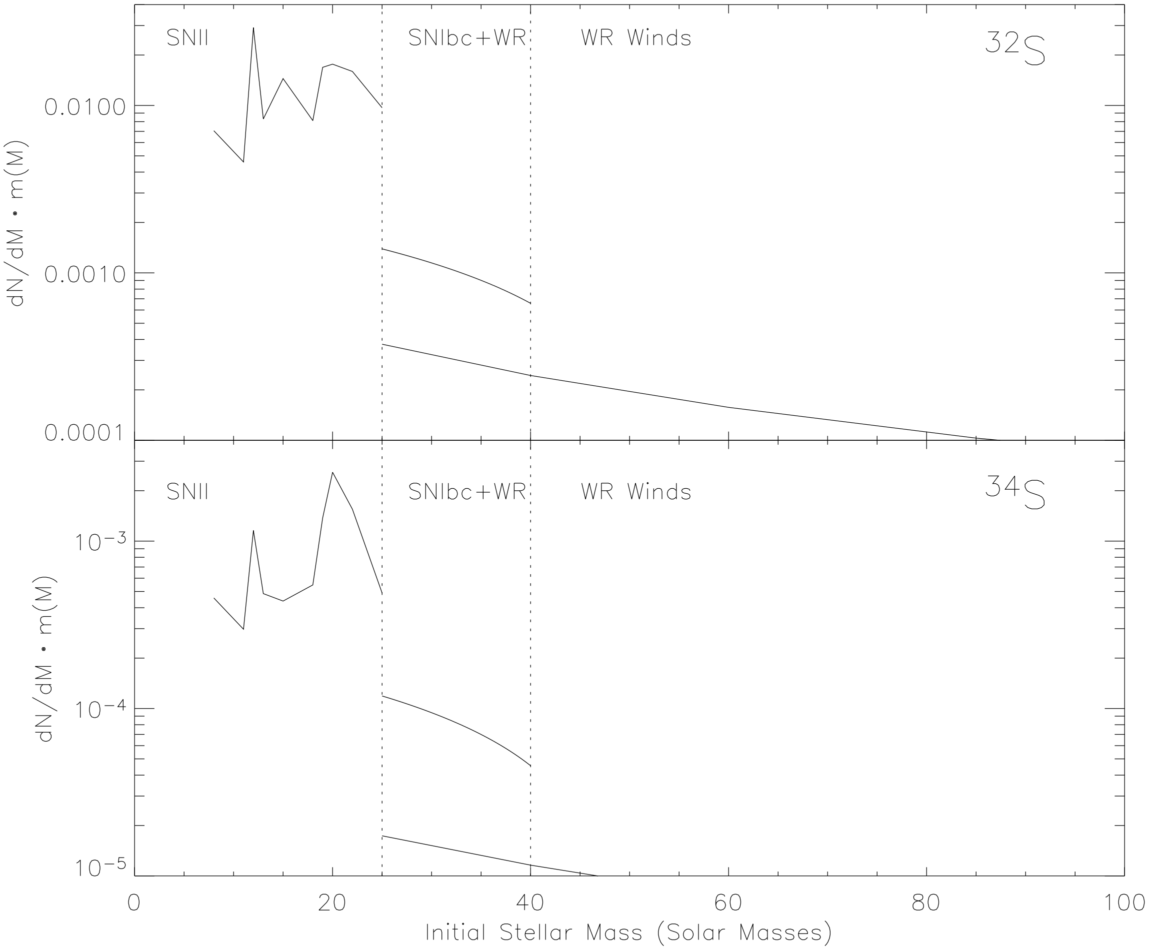

Figure 5.1: The ejected mass of ^{32}S and ^{34}S per star, weighted by the Salpeter IMF as a function of the star's initial mass. Type II Supernova contribute ejecta below 25M$_\odot$, SNI between 25M$_\odot$ and 40M$_\odot$, and stars heavier than 25M$_\odot$ eject material into the superbubble in the form of Wolf-Rayet winds

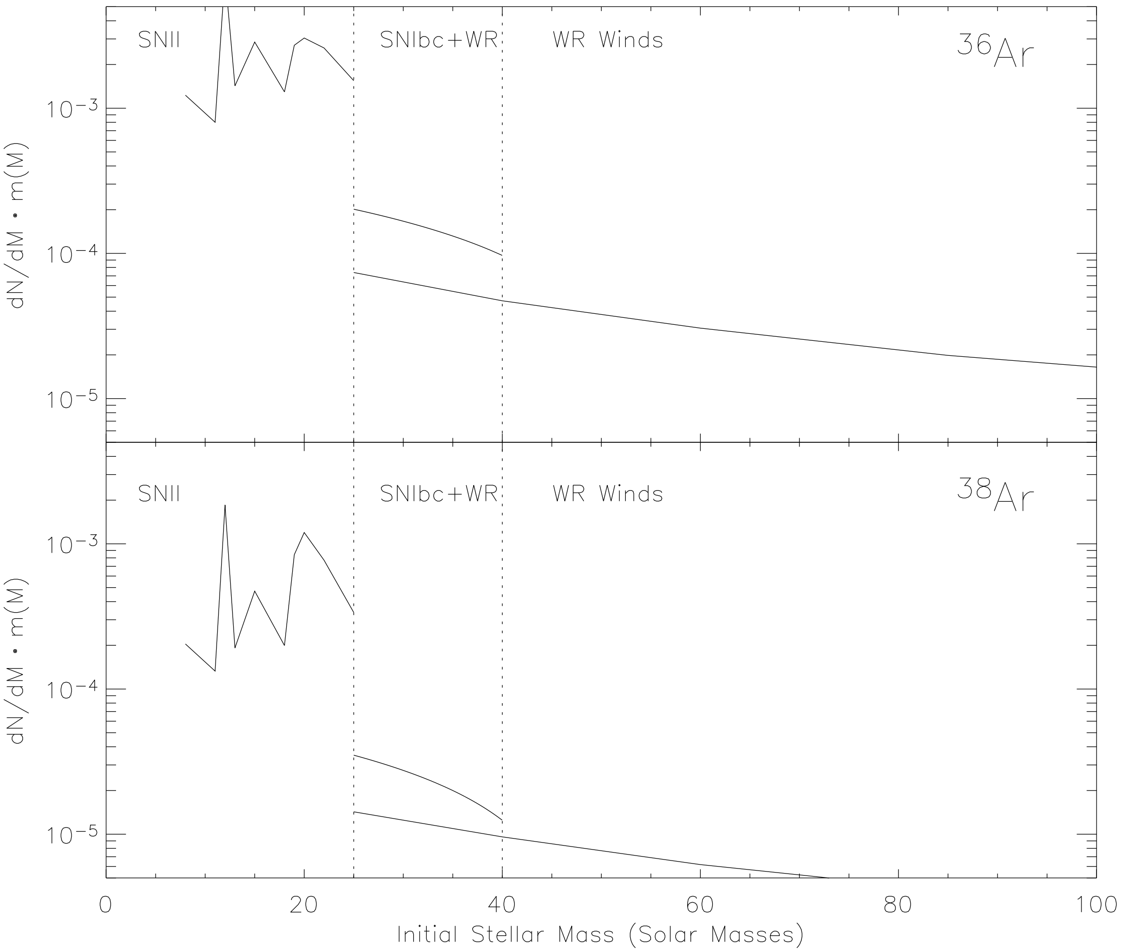

Figure 5.2: The ejected mass of ^{36}Ar and ^{38}Ar per star, weighted by the Salpeter IMF as a function of the star's initial mass.

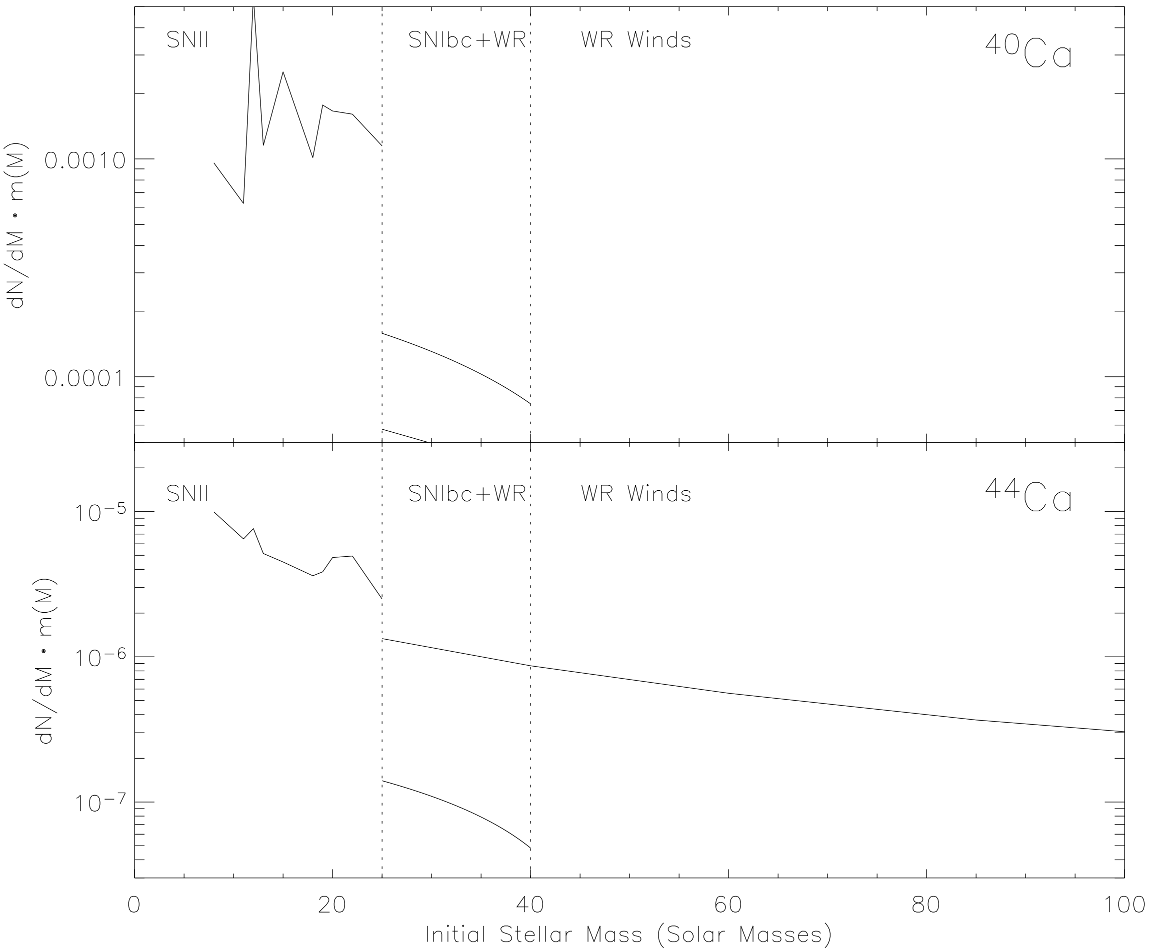

Figure 5.3: The ejected mass of ^{40}Ca and ^{44}Ca per star, weighted by the Salpeter IMF as a function of the star's initial mass

5.5 Time variation of ejecta

The lifetimes of stars in the superbubble will vary from 3 Myr for a $120\mathrm{M}_\odot$ star to 37 Myr for an $8\mathrm{M}_\odot$ star (Schaller *et al.*, 1992). Therefore, the composition of the superbubble interior will evolve over time. The cosmic rays observed at Earth come from many supernovae from many superbubbles of various ages (Higdon & Lingenfelter, 2003a). The observed isotope abundances in the cosmic rays should, therefore, be reflective of the time-averaged superbubble composition. If the initial mass function of the OB association is known, the time-dependent ejecta composition depends on the stellar mass-lifetime relationship, which is taken to be a quartic, as derived by Higdon & Lingenfelter (2003b) using models from Schaller *et al.* (1992):

$$\ln t_\star(M) = C_5 + C_4 \ln M + C_3(\ln M)^2 + C_2(\ln M)^3 + C_1(\ln M)^4, \tag{5.1}$$

with $C_{1-5} = [0.0119914, -0.218395, 2.69502, -6.6851, 11.9115]$. The relative supernova rate in the superbubble, dN/dt, can be deduced simply from Equation 5.1 and the Salpeter IMF: $dN/dt = (dN/dM)(dM/dt)$. This rate and the stellar mass-lifetime relation are plotted in Figure 5.4.

Using these relationships, and the wind and ejecta yields, the accumulated isotope mass in the superbubble as a function of time can be calculated. Initially, only Wolf-Rayet winds and the supernova ejecta from very massive stars contribute to the accumulated mass of isotope x, μ_x. Stars larger than $\sim 25\mathrm{M}_\odot$ will have the shortest lifetimes and explode as SNIbc. They will also contribute wind material to the superbubble during their Wolf-Rayet

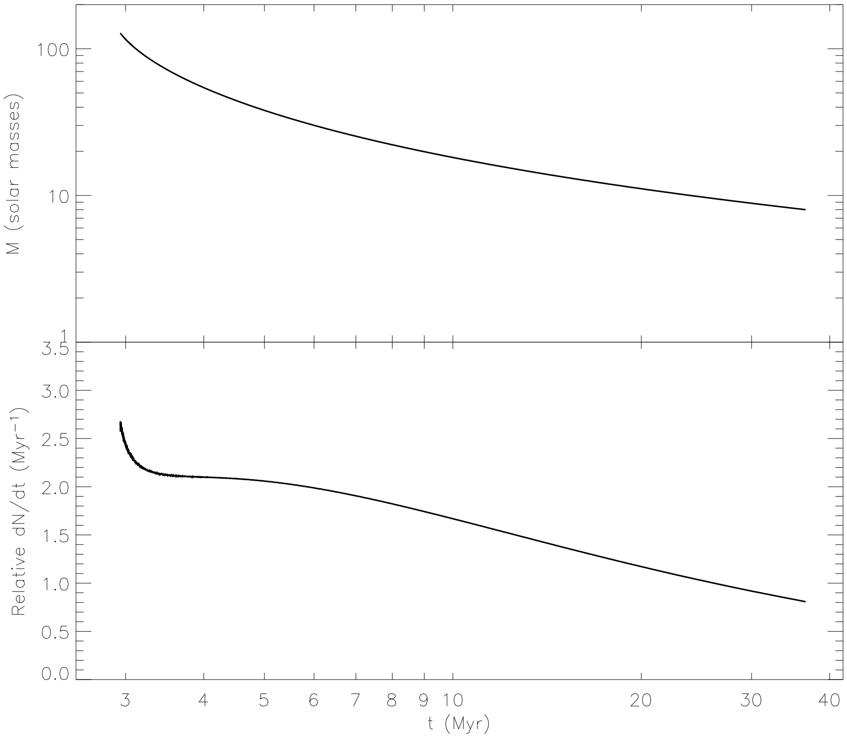

Figure 5.4: Initial stellar mass is plotted against the star's lifetime in the top plot. The bottom plot shows the supernova rate as a function of time after star formation in the superbubble.

phase. The accumulated ejecta of isotope x for 3 Myr$< t < t_\star(25\mathrm{M}_\odot)$:

$$\mu_x(t) = \int_{3\ \mathrm{Myr}}^{t} {}_{\mathrm{WR}}m_x(t') \left(\frac{dN}{dt'}\right) dt' + \int_{t_\star(M_{BH})}^{t} {}_{\mathrm{SNIbc}}m_x(t') \left(\frac{dN}{dt'}\right) dt'. \tag{5.2}$$

For later times, SNII will contribute to the accumulated mass, with SNIbc and Wolf-Rayet winds no longer adding material to the superbubble interior. For $t_\star(25\mathrm{M}_\odot) < t < t_\star(8\mathrm{M}_\odot)$:

$$\begin{aligned}\mu_x(t) = {} & \int_{3\ \mathrm{Myr}}^{t_\star(M_L)} {}_{\mathrm{WR}}m_x(t') \left(\frac{dN}{dt'}\right) dt' + \int_{t_\star(M_{BH})}^{t_\star(M_L)} {}_{\mathrm{SNIbc}}m_x(t') \left(\frac{dN}{dt'}\right) dt' \\ & + \int_{t_\star(M_L)}^{t} {}_{\mathrm{SNII}}m_x(t') \left(\frac{dN}{dt'}\right) dt'.\end{aligned} \tag{5.3}$$

The accumulated masses μ_x are plotted for the isotopes of sulfur, argon, and calcium in Figures 5.5 – 5.7.

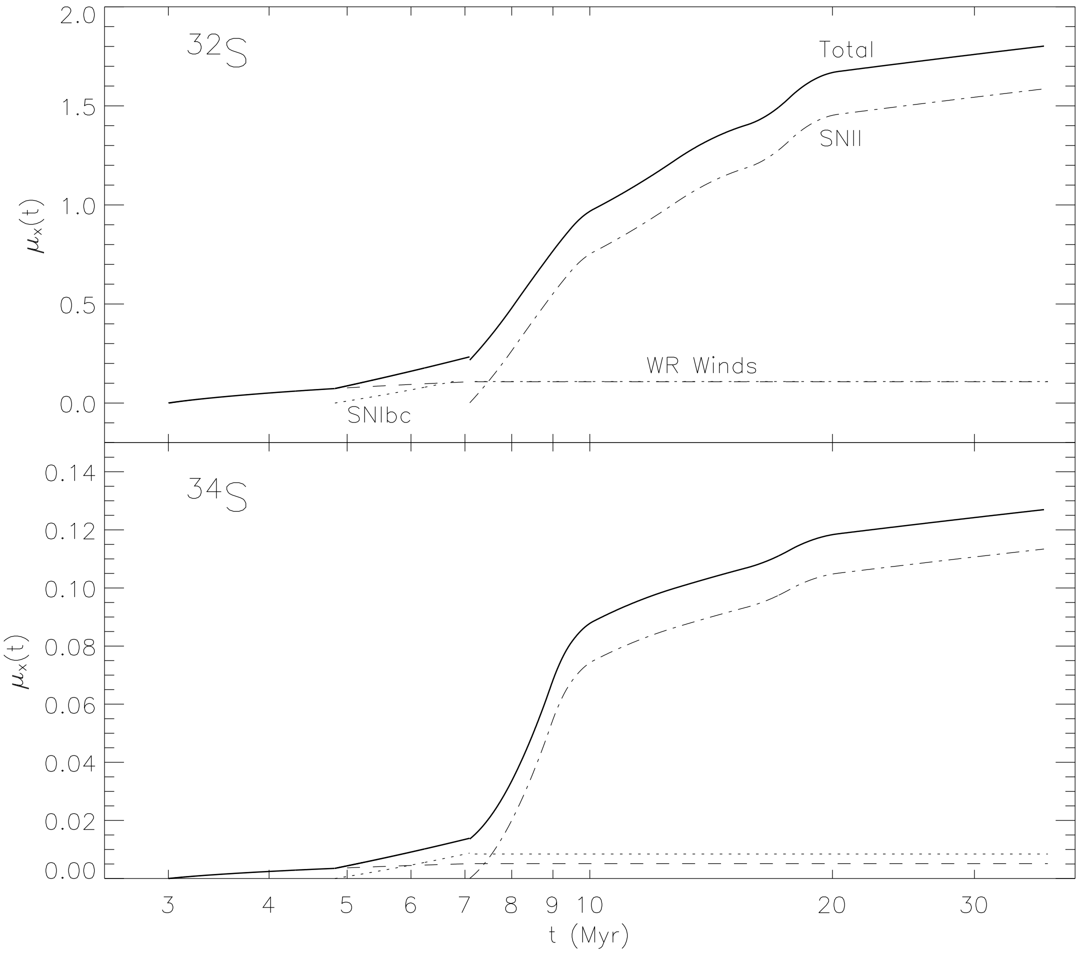

Figure 5.5: Accumulated mass (arbitrary units) of ^{32}S and ^{34}S as a function of the superbubble age

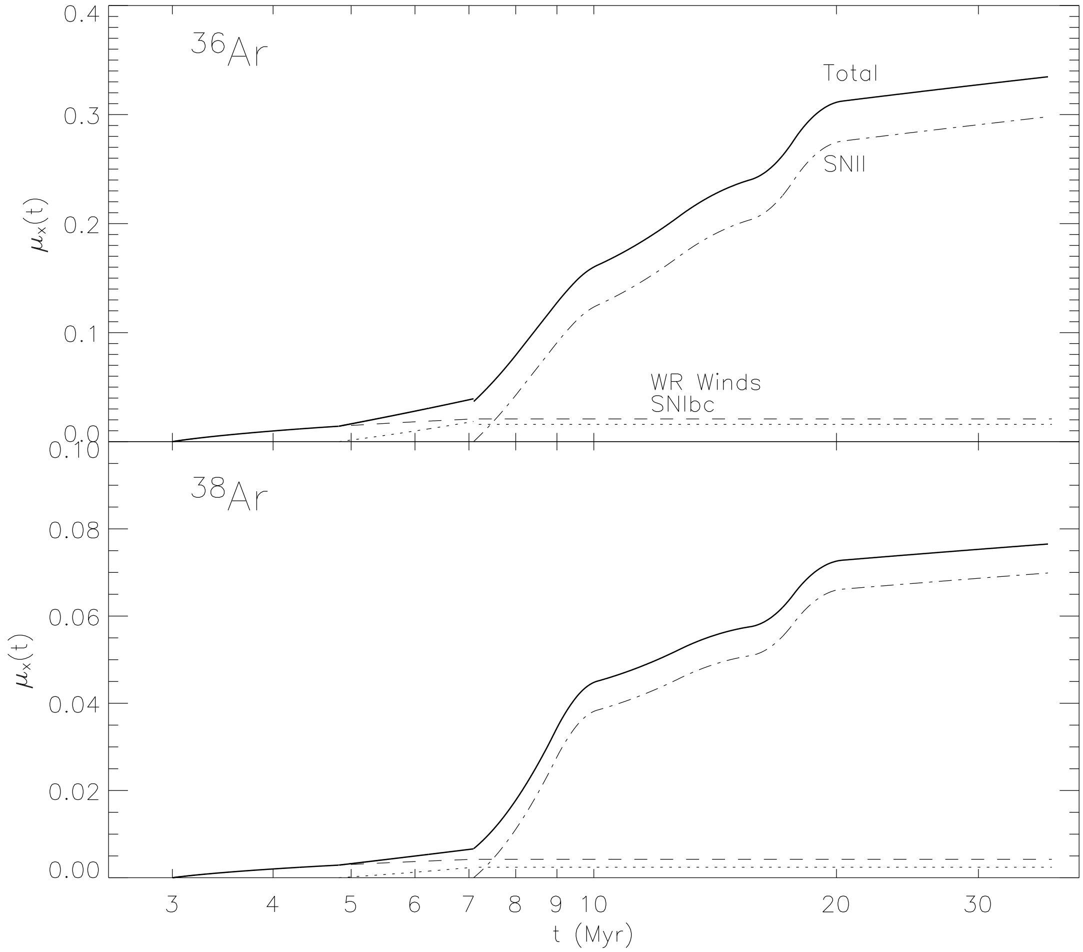

Figure 5.6: Accumulated mass of ^{36}Ar and ^{38}Ar as a function of the superbubble age

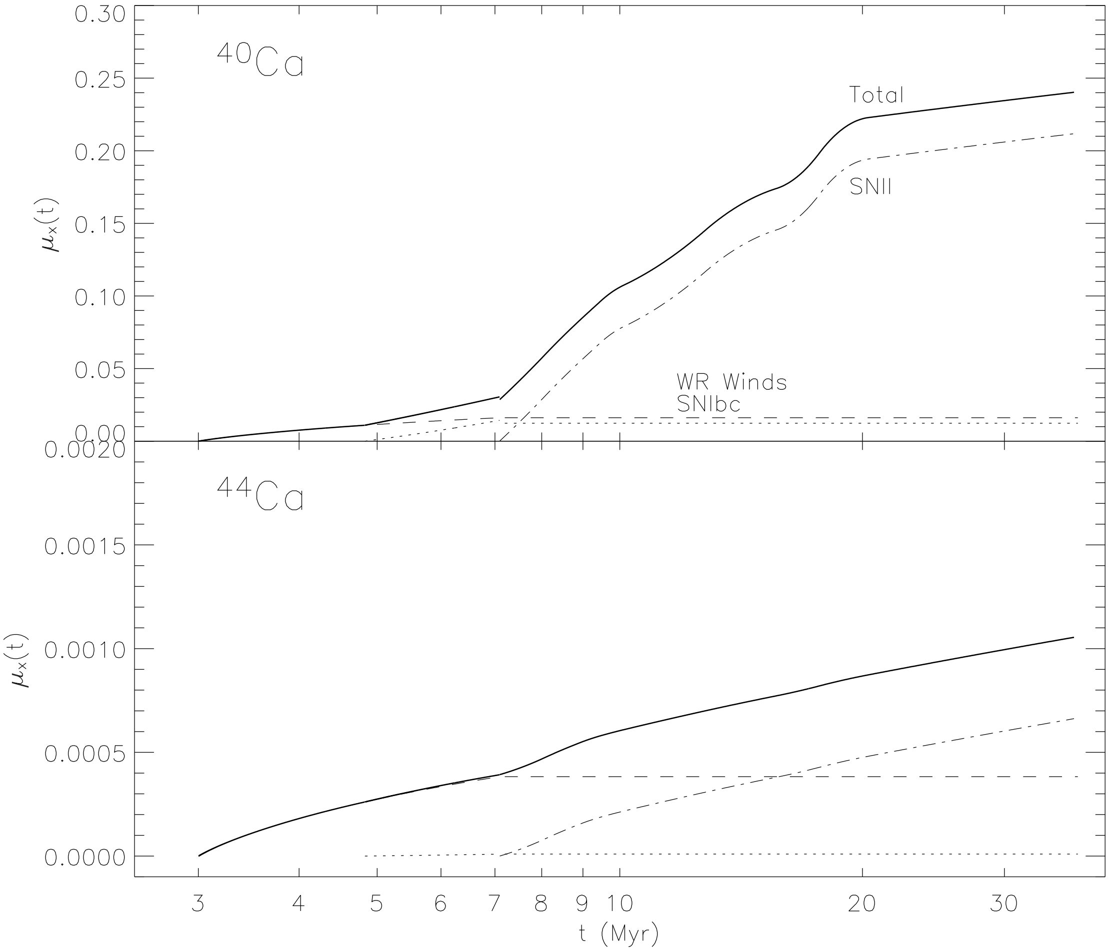

Figure 5.7: Accumulated mass of ^{40}Ca and ^{44}Ca as a function of the superbubble age

Cosmic rays are accelerated in the superbubble by supernova shocks. The timescale to accelerate GCRs by the shocks is about 100,000 years (Higdon, 1999). The relative supernova rate, dN/dt, varies by less than a factor of two, over an order of magnitude in age. A supernova will occur in an OB association of 100 stars every ~3 Myr, so the timescale to accelerate cosmic rays is short compared to the supernova rate. Therefore, the rate of cosmic ray acceleration in the superbubble is proportional to the supernova rate.

The accumulated mass of isotope x ejecta in the superbubble, weighted by the time-dependent cosmic ray acceleration rate, and time-averaged over the duration of cosmic ray-accelerating supernova activity in the superbubble, is:

$$\langle \mu_x \rangle = \int_{t_\star(M_{BH})}^{t_\star(8\mathrm{M}_\odot)} \mu_x(t') \left(\frac{dN}{dt'} \right) dt'. \tag{5.4}$$

Similarly, the weighted and time-averaged total ejecta is calculated: $\langle \mu_{\text{ejecta}} \rangle$. The mean mass fraction of isotope x in the superbubble ejecta material over the duration of cosmic ray acceleration is:

$$(f_x)_{\text{ejecta}} = \frac{\langle \mu_x \rangle}{\langle \mu_{\text{ejecta}} \rangle}. \tag{5.5}$$

The calculation of the time-averaged accumulated mass in Equation 5.4 is weighted by the supernova rate, dN/dt, which is a factor of two higher during the first few million years of the superbubble's lifetime (Figure 5.4). The accumulated mass from which the cosmic rays are accelerated in the superbubble, however, is larger by an order of magnitude from 7 Myr to 37 Myr (Figures 5.5 – 5.7). Most cosmic rays originating in the superbubble will be accelerated out of the material later in its lifetime. Therefore, cosmic rays accelerated in superbubbles are representative of the mature superbubble composition.

5.6 Interstellar medium abundances

The material from Wolf-Rayet winds and supernova ejecta is diluted in the superbubble by the gas evaporated from molecular clouds and the interstellar medium that is swept up by the bubble's expansion. The ISM mass fraction $(f_x)_{\text{ISM}}$ of an isotope of sulfur, argon, or calcium will be taken from the solar system values given by Lodders (2003). The ISM abundances of the isotopes of a given element relative to each other are set to be the same as solar, as has been assumed in the past for elements in this charge range (Wilson & Matteucci, 1992). In Section 5.9, ISM isotopic abundances will be adjusted in light of more recent observations (Chin *et al.*, 1996).

5.7 Sulfur, argon, and calcium isotopes in superbubbles

The abundance of isotope x in the superbubble will consist of a fraction f_{ej} of ejecta material and $1 - f_{ej}$ ISM material. The superbubble mass fraction of x is:

$$(f_x)_{\text{sb}} = (1 - f_{ej})\,(f_x)_{\text{ISM}} + f_{ej}\,(f_x)_{\text{ejecta}}\,. \tag{5.6}$$

The sulfur, argon, and calcium isotope ratios in the superbubble are simply:

$$\left(\frac{^{34}\text{S}}{^{32}\text{S}}\right)_{\text{sb}} = \frac{32}{34}\frac{(f_{^{34}\text{S}})_{\text{sb}}}{(f_{^{32}\text{S}})_{\text{sb}}} \tag{5.7}$$

$$\left(\frac{^{38}\text{Ar}}{^{36}\text{Ar}}\right)_{\text{sb}} = \frac{36}{38}\frac{(f_{^{38}\text{Ar}})_{\text{sb}}}{(f_{^{36}\text{Ar}})_{\text{sb}}} \tag{5.8}$$

$$\left(\frac{^{44}\text{Ca}}{^{40}\text{Ca}}\right)_{\text{sb}} = \frac{40}{44}\frac{(f_{^{44}\text{Ca}})_{\text{sb}}}{(f_{^{40}\text{Ca}})_{\text{sb}}}. \tag{5.9}$$

This ratio, as a function of f_{ej}, can be calculated and compared to the derived source abundance ratios from Section 4.3. The 1σ (68% confidence) range was calculated earlier.

As mentioned earlier, the mass at which a star will eventually evolve into a Wolf-Rayet star, and explode as SNIbc, is taken to be $M_L = 25\mathrm{M}_\odot \pm 4\mathrm{M}_\odot$. The calculations done in Section 5.1 – 5.6 are repeated for $M_L = 21\mathrm{M}_\odot$ and $M_L = 29\mathrm{M}_\odot$. The superbubble isotope ratios for all three M_Ls as a function of f_{ej} are plotted compared to the derived cosmic ray source ratios, with associated 68% confidence interval, in Figures 5.8 – 5.10

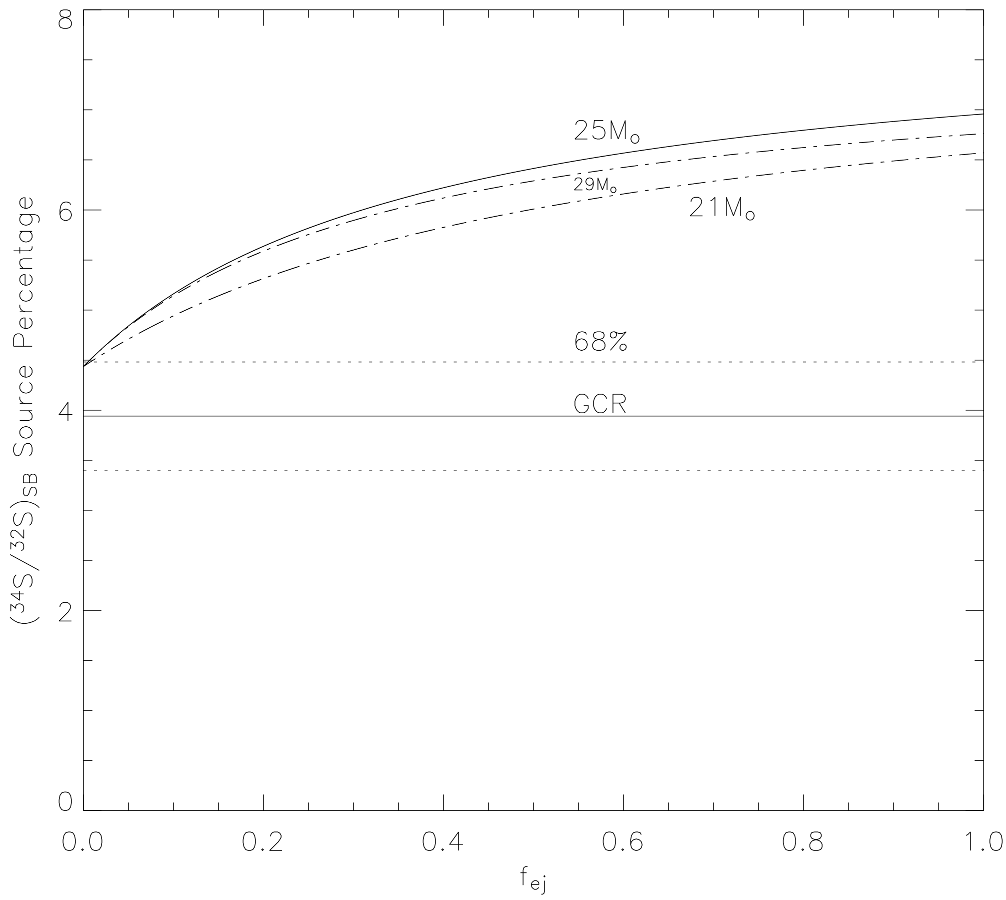

Figure 5.8: The sulfur isotope ratio inside a superbubble as a function of the ejecta mixing fraction, f_{ej}. The solid line is the cosmic ray source ratio derived earlier; dotted lines are the 1σ (68%) uncertainties.

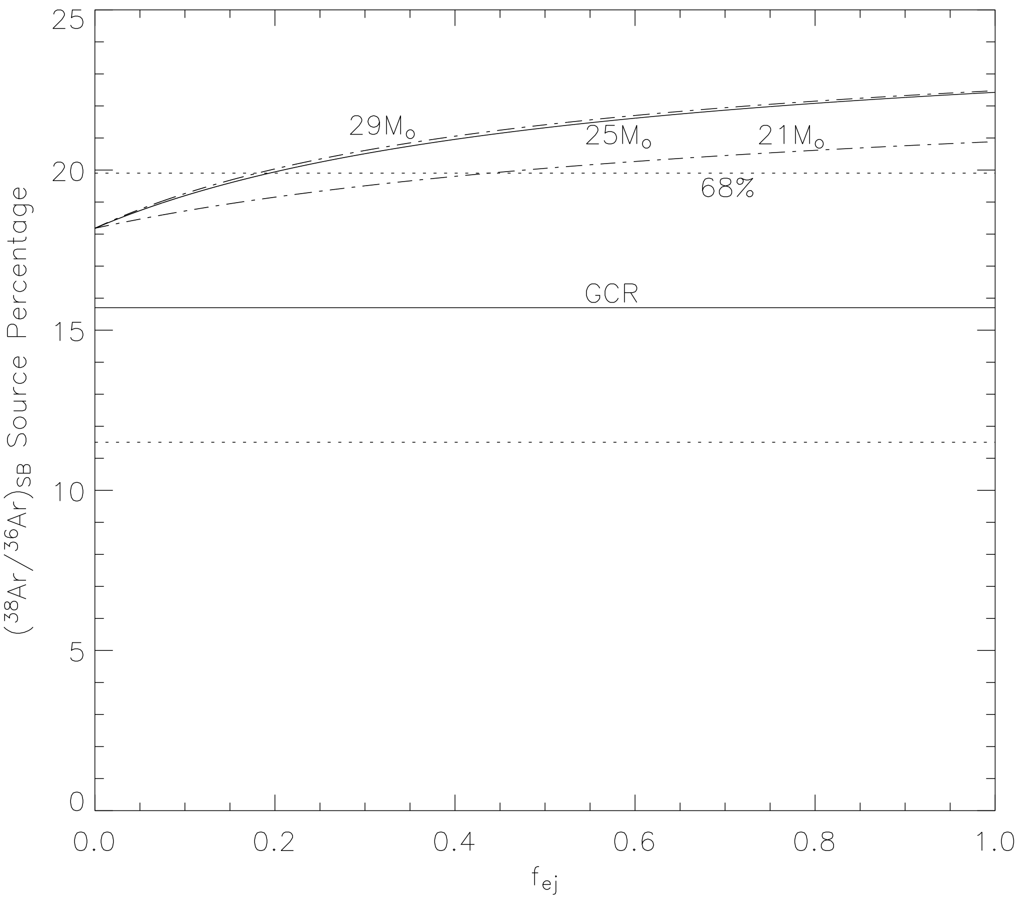

Figure 5.9: The argon isotope ratio inside a superbubble as a function of the ejecta mixing fraction, f_{ej}

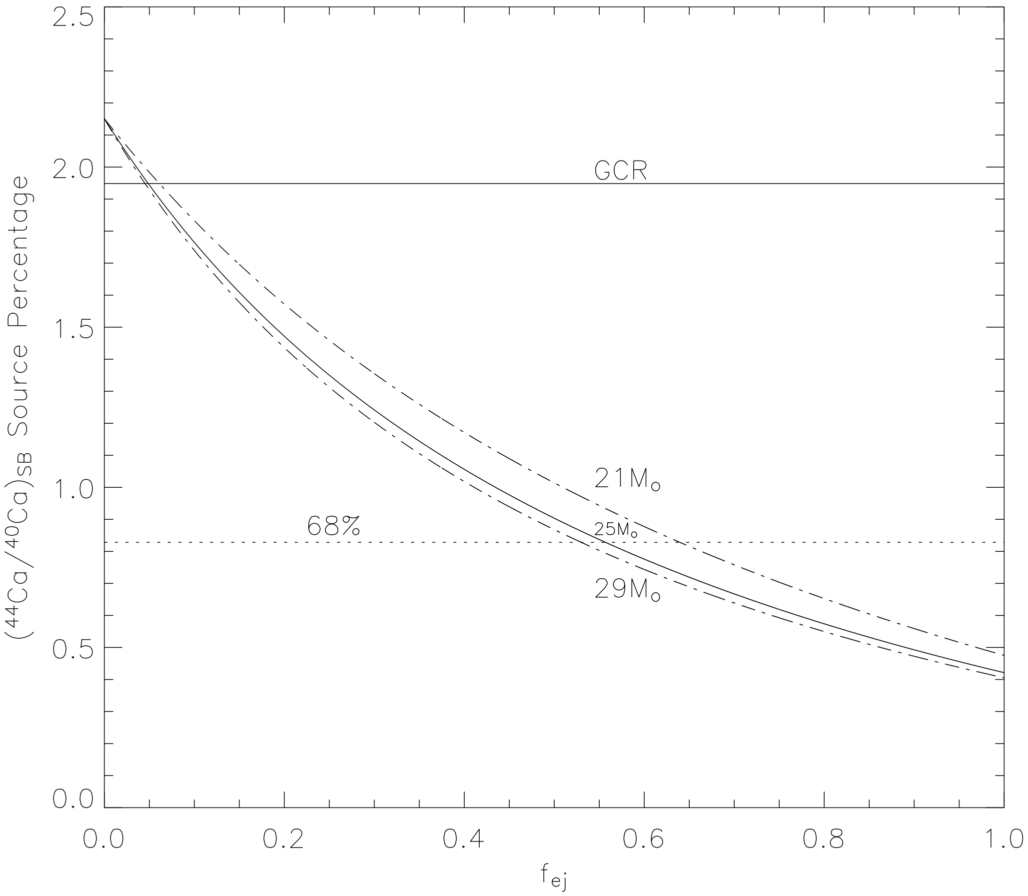

Figure 5.10: The calcium isotope ratio inside a superbubble as a function of the ejecta mixing fraction, f_{ej}

Figures 5.8 – 5.9 show that the supernova ejecta and Wolf-Rayet winds (f_{ej}=1) contain an excess of ^{34}S relative to ^{32}S compared to the solar system (f_{ej}=0). The same is true for ^{38}Ar relative to ^{36}Ar, but ^{44}Ca relative to ^{40}Ca shows a depletion with respect to the solar system. The ^{44}Ca is not produced directly during quiescent burning or explosive nucleosynthesis. Rather, it is created almost entirely out of the radioactive decay of ^{44}Ti (Woosley & Weaver, 1995). This is an α-like nuclide (equal number of protons and neutrons) that is not overproduced relative to ^{40}Ca in the ejecta material. The isotopes of sulfur and argon are produced in small amounts during quiescent oxygen and explosive silicon burning, but are mostly synthesized during explosive oxygen burning (Woosley *et al.*, 2002). It is obvious from Figures 5.8 – 5.9 that the ejecta yields for isotopes in this study are enhanced in α+2 nuclides, compared to the solar system values. However, the cosmic ray source abundances of α+2 to α nuclides are slightly depleted, compared to what is seen in the solar system. The derived GCR source ratios are inconsistent with mixing of these two samples of matter. Clearly, previous assumptions made concerning the nucleosynthesis conditions of OB stars producing the ejecta, or isotopic abundances in the interstellar medium, or both, are inaccurate. The disagreement between model and observations requires a more detailed look at parameters of the model. Constraining superbubble model parameters by observations will increase the accuracy of predictions, similar to what was done in the implementation of the leaky-box model in Section 4.2.4. In particular, observational results will be used for the metallicity of nearby OB associations (Section 5.8) and the isotopic composition of the interstellar medium (Section 5.9).

5.8 The metallicity of nearby OB associations

The creation of sulfur and argon in explosive oxygen burning is sensitive to the nucleosynthesis environment. In particular, the relative isotopic abundances are sensitive to the star's metallicity Z, and the number of excess neutrons per nucleon (compared to an α particle), called the neutron excess, η. A factor of two increase in η will result in a factor of two increase in $^{34}S/^{32}S$ and $^{38}Ar/^{36}Ar$ (Woosley *et al.*, 1973), as can be seen in Figure 5.11.

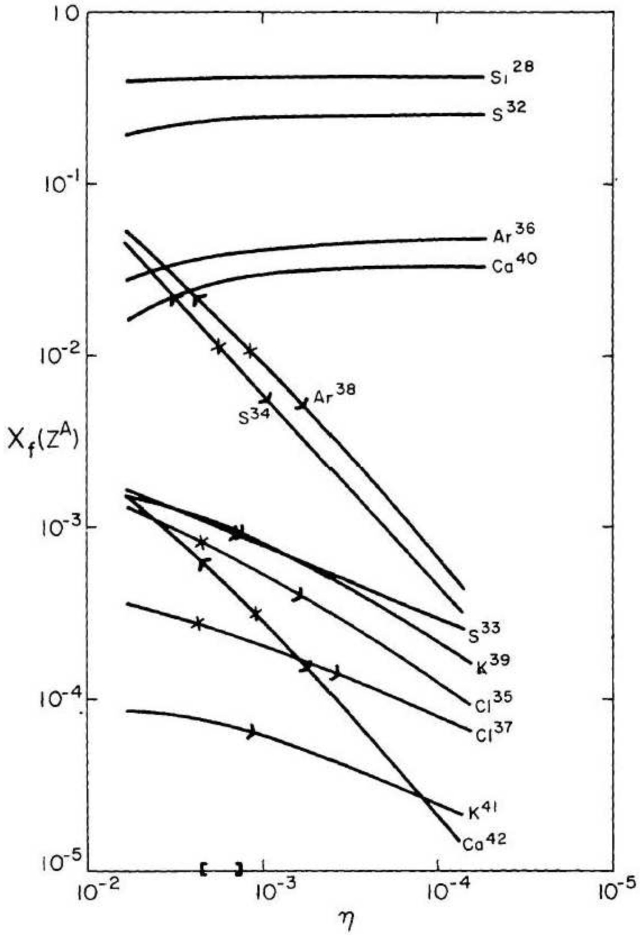

Figure 5.11: Isotope abundances (relative to ^{28}Si) as a function of the neutron excess η, reproduced from Woosley *et al.* (1973). The x corresponds to the η value that yields solar system abundance, the brackets denote solar abundance; within a factor of two. The $^{34}S/^{32}S$ and $^{38}Ar/^{36}Ar$ ratios are highly dependent on η.

During helium burning, α-capture upon ^{14}N creates ^{22}Ne by the reaction:

$$^{14}\mathrm{N}(\alpha,\gamma)^{18}\mathrm{F}(e^{+}\nu)^{18}\mathrm{O}(\alpha,\gamma)^{22}\mathrm{Ne}. \tag{5.10}$$

The abundance of ^{14}N is proportional to the star's initial metallicity, so the abundances of ^{22}Ne and ^{18}O also scale linearly with metallicity. The isotopes ^{22}Ne and ^{18}O have excess neutrons. It is their abundance which determines the neutron excess for all future stages of the star, including explosive oxygen burning. The neutron excess is proportional to the star's initial metallicity (Woosley & Weaver, 1981). Therefore, the initial metallicity of the star will determine its neutron excess, which will then affect the ratio of ^{34}S/^{32}S and ^{38}Ar/^{36}Ar. As stated in Section 5.1, observations of nearby OB associations have been made by Daflon & Cunha (2004). They deduced the abundances of various elements in OB associations as a function of Galactocentric radius; their results are shown in Figure 5.12.

Metallicity is defined to be the relative fraction of elements heavier than helium, so the depletion in metallicity relative to solar can be calculated from these data for OB associations at a given Galactocentric radius. The flux of primary cosmic rays observed at Earth is dominated by sources within a few kpc of the Sun (Taillet & Maurin, 2003). From Figure 5.12, it is evident that the metallicity of OB associations in the superbubbles that are accelerating cosmic rays is lower than solar metallicity. The OB association metallicity is 2/3 of solar metallicity as calculated from the high abundance elements C, N, and O in Figure 5.12.

The neutron excess during explosive oxygen burning is proportional to the star's metallicity, as stated earlier. Therefore, an OB association of many stars with 2/3 solar metallicity will also have 2/3 of the solar neutron excess. From Figure 5.11, this depletion results in 2/3 the values for both the ^{34}S/^{32}S and ^{38}Ar/^{36}Ar ratios produced in the supernova and present in its ejecta material. Since the ejecta of these isotopes is dominated by SNII (Figures 5.1 – 5.2), the calculated superbubble-accelerated ejecta should actually be 2/3 of the previously derived value to be consistent with the observations by Daflon & Cunha (2004).

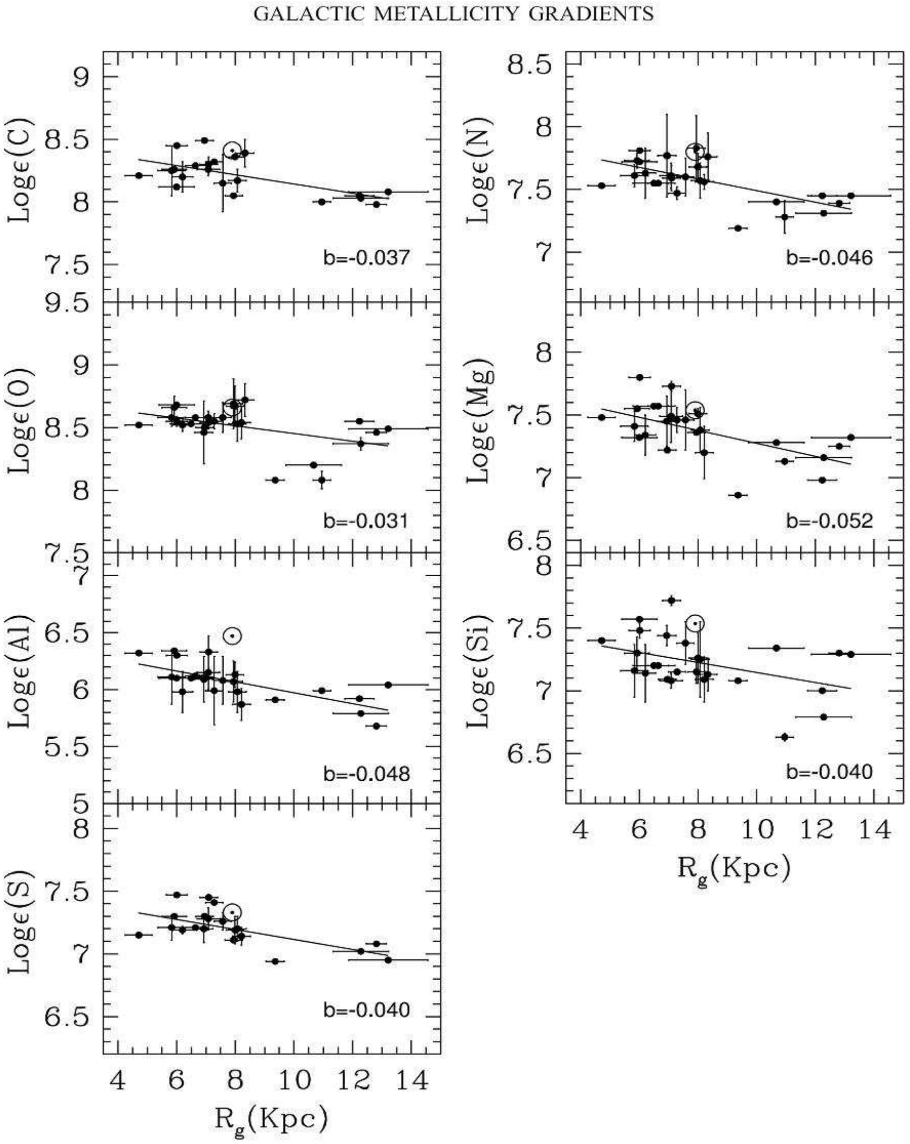

Figure 5.12: The abundance of various elements in OB associations is plotted as a function of Galactocentric radius by Daflon & Cunha (2004). The solar system ($\odot$) is more abundant in these elements than OB associations nearby, where cosmic rays originate. These abundances show that OB associations within a couple kpc of the Sun have lower than solar metallicity.

5.9 Sulfur and argon isotopes in the interstellar medium

The relative ISM abundances of sulfur, argon, and calcium isotopes were assumed to be the same as solar system in Section 5.6. A spectroscopic line survey of carbon monosulfides $^{12}C^{32}S$,$^{13}C^{32}S$, $^{12}C^{34}S$, and $^{12}C^{33}S$ was done by Chin *et al.* (1996) to study the interstellar $^{34}S/^{32}S$ ratio. They deduced this ratio as a function of Galactocentric radius, shown in Figure 5.13.

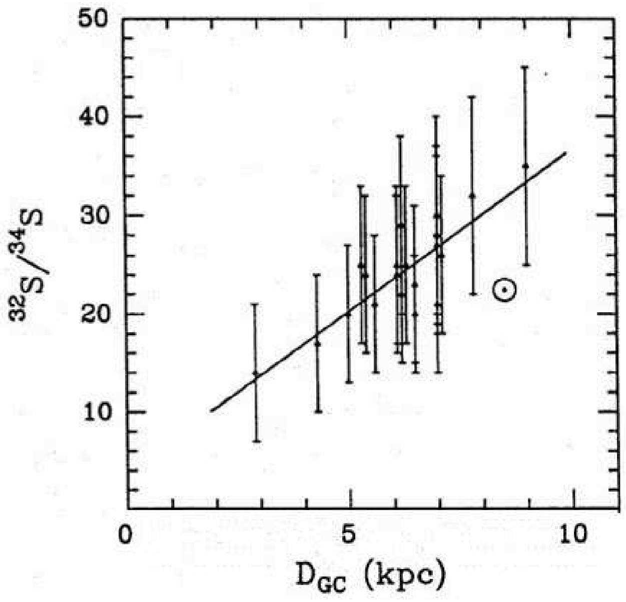

Figure 5.13: The $^{32}S/^{34}S$ ratio as a function of Galactocentric distance, from Chin *et al.* (1996). The data points are the twenty star-forming regions that were studied; the large error bars are due to uncertainties in the carbon ratios necessary to study sulfur isotopes from observations of carbon monosulfides. A least-squares fit to the data is plotted as a solid line. The solar value (⊙) is plotted at a Galactic radius of 8.5kpc. The ISM (line) is overabundant in $^{32}S/^{34}S$ compared to the Sun, meaning that the ISM in the vicinity of the Sun is underabundant in $^{34}S/^{32}S$, by a factor of 0.7 relative to the solar system.

The interstellar $^{34}S/^{32}S$ ratio at the Sun's Galactocentric radius is 70% of the solar system ratio. The argon isotopes are produced by the same mechanism as sulfur, mainly explosive oxygen burning in supernovae, and are similarly sensitive to the neutron excess in the environment at the time of nucleosynthesis. Therefore, it can be assumed that the $^{38}Ar/^{36}Ar$ ratio is also 70% of the previously derived value in the ISM, though no measurements have been made of the argon interstellar isotopic abundance. The argon and sulfur ratios in the interstellar material are now assumed to be 70% of their solar system values. The calcium isotope ratio ^{44}Ca/^{40}Ca is not sensitive to the neutron excess of the synthesis environment (^{44}Ca is produced primarily from the decay of ^{44}Ti), and since no measurements of this ratio in the interstellar medium have been made, the ^{44}Ca/^{40}Ca ratio is assumed to be the same as solar.

5.10 The superbubble composition with observational constraints

In light of these observations, the calculations of the superbubble accelerated composition from Section 5.7 are modified. The ISM ratio (f_{ej}=0) is multiplied by a factor of 0.7 and the accelerated ejecta and wind material (f_{ej}=1) is multiplied by a factor of 0.67. The superbubble composition of ^{34}S/^{32}S and ^{38}Ar/^{36}Ar as a function of f_{ej}, with the observational constraints of Sections 5.9 and 5.8, is plotted compared to the GCR source ratio and 1σ uncertainties in Figures 5.14 – 5.15.

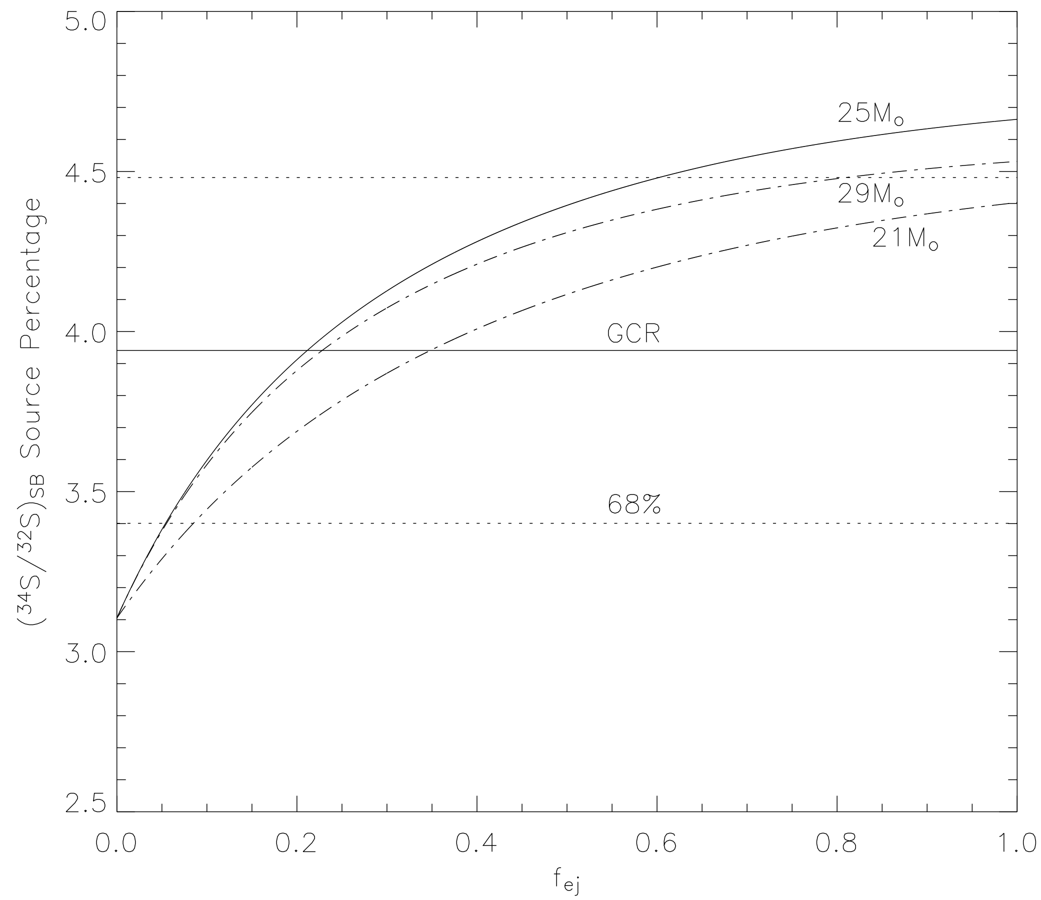

Figure 5.14: The sulfur isotope ratio inside a superbubble as a function of the ejecta mixing fraction, f_{ej}, recalculated to account for observations of the metallicity of nearby OB associations and the sulfur isotopic ratio in the interstellar medium. The GCR source ratio is shown as a solid line with 1σ uncertainties shown by dotted lines. The solid superbubble isotope ratio is calculated for various values of M_L, the mass at which a star can eventually enter the Wolf-Rayet phase.

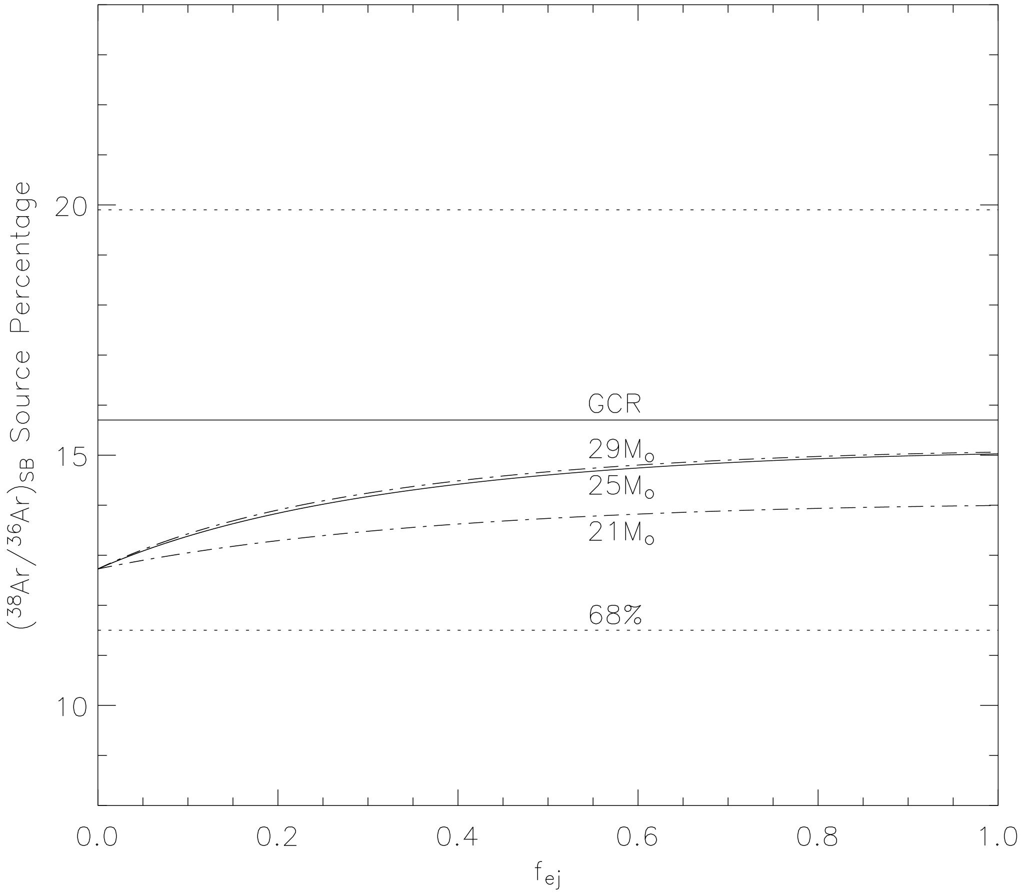

Figure 5.15: The argon isotope ratio inside a superbubble as a function of the ejecta mixing fraction, f_{ej}, recalculated to account for observations of the metallicity of OB associations and the sulfur isotopic ratio in the interstellar medium

The ^{44}Ca/^{40}Ca ratio is not affected by ~30% changes in metallicity during its synthesis, since ^{44}Ca is the decay product of an α nuclide, as discussed in Section 5.7. This ratio is also unchanged by the Chin *et al.* (1996) observations. Therefore, Figure 5.10 still reflects the superbubble-accelerated composition of ^{44}Ca/^{40}Ca, taking into account these new observations.

5.11 Model uncertainties

Possible errors in the mass-loss rate of Wolf-Rayet stars, as discussed in Section 5.3, will not significantly affect the derived results for sulfur and argon, as these isotopes receive little contribution from Wolf-Rayet stars (see Figures 5.5 and 5.6). Clumping in the Wolf-Rayet wind ejecta would decrease the ^{44}Ca mass fraction in the superbubble, causing f_{ej} corresponding to the 1σ GCR source uncertainties to decrease. In the worst case scenario, the derived upper limit of 57% would fall to ~45%. This possible source of error will not dramatically change the derived results and will be ignored for the rest of the analysis.

The initial mass function for the OB association is observed to vary from the assumed Salpeter IMF (γ=-2.35), as discussed in Section 5.4. The isotopic composition of the superbubble core was calculated using γ=-1.7 and -3.1. As mentioned earlier, the cosmic rays observed at Earth are likely produced by a number of OB associations (~30, Binns (2006)). The initial mass function of all the OB associations sampled will be an average of many IMFs with γs falling between -1.7 and -3.1. The Salpeter γ value of -2.35 is a reasonable average γ for this range. The ranges of f_{ej} corresponding to $\pm 1\sigma$ over different γ and M_L values for the three isotope ratios (Figures 5.10, 5.14, and 5.15) are shown in Tables 5.1 – 5.3.

1σ allowable f_{ej}, Sulfur			
	M_L=21	M_L=25	M_L=29
γ=-3.1	0.08-1.0	0.05-1.0	0.05-1.0
γ=-2.35	0.09-1.0	0.05-0.60	0.06-0.81
γ=-1.7	0.12-1.0	0.08-0.70	0.08-0.90

Table 5.1: The allowable range of f_{ej}, due to 1σ uncertainties on the GCR source ratio ^{34}S/^{32}S

1σ allowable f_{ej}, Argon			
	M_L=21	M_L=25	M_L=29
γ=-3.1	0.0-1.0	0.0-1.0	0.0-1.0
γ=-2.35	0.0-1.0	0.0-1.0	0.0-1.0
γ=-1.7	0.0-1.0	0.0-1.0	0.0-1.0

Table 5.2: The allowable range of f_{ej}, due to 1σ uncertainties on the GCR source ratio ^{38}Ar/^{36}Ar

1σ allowable f_{ej}, Calcium			
	M_L=21	M_L=25	M_L=29
γ=-3.1	0.48-1.0	0.42-1.0	0.41-1.0
γ=-2.35	0.64-1.0	0.56-1.0	0.53-1.0
γ=-1.7	0.90-1.0	0.78-1.0	0.74-1.0

Table 5.3: The allowable range of f_{ej}, due to 1σ uncertainties on the GCR source ratio ^{44}Ca/^{40}Ca

5.12 Optimal superbubble mixing fraction

A Salpeter IMF (γ=-2.35) and a limiting mass M_L of 25$M_\odot$ are assumed in the determination of the optimal superbubble mixing fraction. A χ^2 between the GCR source and superbubble ratio as a function of f_{ej} is calculated from Figures 5.10, 5.14, and 5.15, using the 1σ uncertainties on the derived GCR source ratios. Figure 5.16 shows the three-isotope summed χ^2 vs. f_{ej} plot. The f_{ej} corresponding to a minimum total χ^2 is the optimal f_{ej} for these three isotopes, with an uncertainty given by the f_{ej} at one plus the minimum total χ^2. As seen in Table 4.3, the relative uncertainty on the GCR source ^{34}S/^{32}S ratio is much smaller than ^{38}Ar/^{36}Ar or ^{44}Ca/^{40}Ca. Consequently, the optimal f_{ej} calculated as a sum of the χ^2 contributions of all the ratios will be determined mostly by the sulfur results.

The mixing fraction of supernova ejecta and Wolf-Rayet winds to the accumulated material inside a superbubble, f_{ej}, is derived to be $18\%^{+26\%}_{-14\%}$. The mixing fraction derived in previous work (Binns *et al.*, 2005; Higdon & Lingenfelter, 2003b) using GCR neon isotopes is 18%±5%.

5.12.1 Superbubble metallicity

The mixture of material available to be accelerated to GCR energies in a superbubble core contains two components of different metallicity. The newly synthesized Wolf-Rayet wind material and supernova ejecta are enriched in elements heavier than helium, whereas the metallicity of the older ISM is closer to solar, $Z_\odot$. Higdon & Lingenfelter (2003b) calculate the metallicity of the Wolf-Rayet wind and supernova ejecta to be 9±1 times solar. The metallicity of the ISM is taken to be 1.32$Z_\odot$ (Twarog, 1980; Rana, 1991; Timmes *et al.*, 1995; Dwek, 1998). The metallicity of the material in the superbubble core $Z_{\rm sb}$ can be deduced from the metallicity of the ISM, $Z_{\rm ISM}$, the metallicity of the ejecta, Z_{ej}, and the

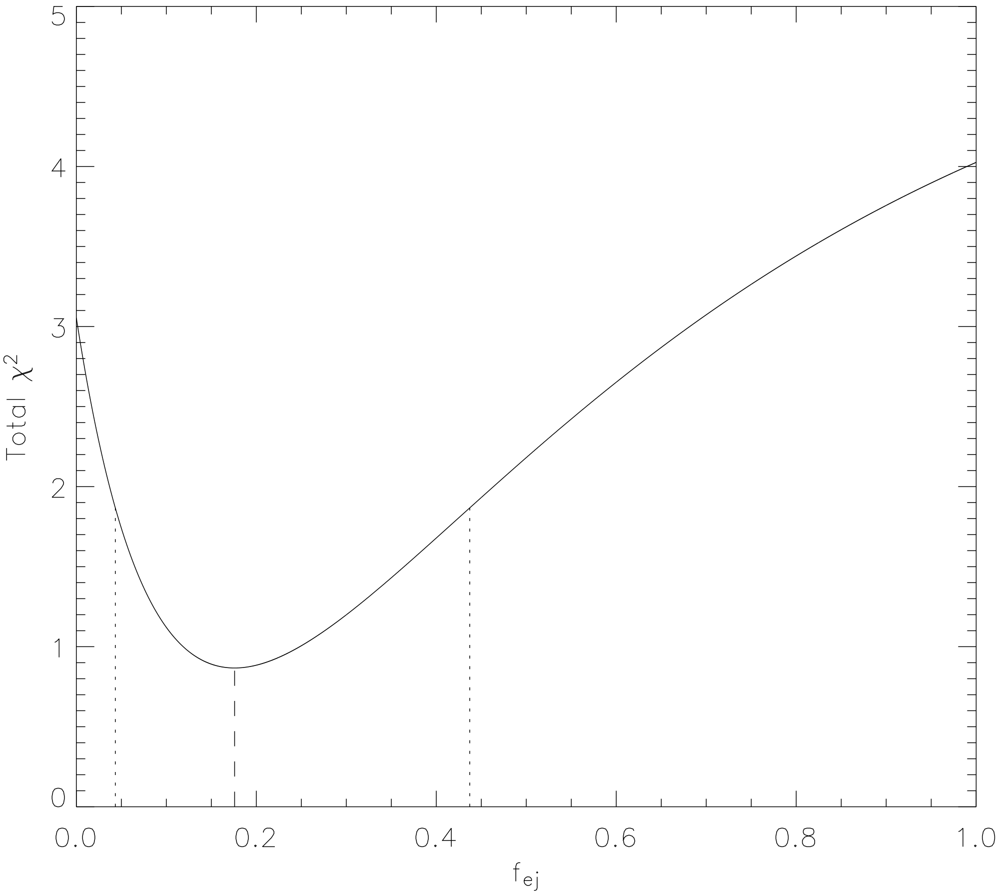

Figure 5.16: Total χ^2 vs. f_{ej}. The optimal f_{ej} value for the ensemble of isotope ratios, $^{34}S/^{32}S$, $^{38}Ar/^{36}Ar$, and $^{44}Ca/^{40}Ca$, is located at the minimum of this curve: 18%. The 1σ uncertainties, corresponding to one plus the minimum of total χ^2, are 4% and 44%

mixing fraction, f_{ej}, simply:

$$Z_{\rm sb} = Z_{\rm ISM}(1 - f_{ej}) + f_{ej} Z_{ej}. \tag{5.11}$$

Assuming $Z_{\rm ISM}$=1.32Z$_\odot$ and Z_{ej}=9Z$_\odot$ ±1Z$_\odot$, this reduces to:

$$Z_{\rm sb} = 1.3 + (7.7 \pm 1.0) f_{ej}. \tag{5.12}$$

The mixing fraction f_{ej} was calculated to be $18\%^{+26\%}_{-14\%}$, which corresponds to a metallicity of cosmic ray seed material inside the superbubble core: $Z_{\mathrm{sb}} = 2.7^{+3.9}_{-2.1}\mathrm{Z}_{\odot}$. The superbubble core metallicity derived from the neon isotopes is $2.7\mathrm{Z}_{\odot} \pm 0.4\mathrm{Z}_{\odot}$ (Higdon & Lingenfelter, 2003b).

5.12.2 Comparison to previous work

The superbubble mixing fraction and metallicity derived in this thesis are consistent with the values derived previously by Higdon & Lingenfelter (2003b) and Binns *et al.* (2005). This agreement provides an important consistency check on the superbubble origin of cosmic rays. The isotopes of sulfur, argon, and calcium are primarily produced in supernova explosions, whereas ^{22}Ne is produced by Wolf-Rayet stars. The results derived here indicate that both supernovae and Wolf-Rayet stars must contribute material to the cosmic ray source composition. The superbubble environment, with ~82% ISM material mixed with ~18% ejecta material from Wolf-Rayet stars and supernovae, is the likely origin of Galactic cosmic rays.

Chapter 6

Conclusions

This thesis has investigated the isotopes of sulfur, argon, and calcium in the Galactic cosmic rays. Isotope ratios at Earth are reported, and a leaky-box model was employed to deduce the abundances of these nuclides at their source in the Galaxy. To examine the nature of the Galactic cosmic ray source, the isotopic abundances of sulfur, argon, and calcium in the material accelerated within a superbubble were derived. The matter ejected from supernovae and massive Wolf-Rayet stars was assumed to be mixed with the surrounding interstellar medium. Comparing the derived superbubble abundances with the cosmic ray source abundance of the sulfur, argon, and calcium isotopes constrained the amount of ejecta to be $18\%^{+26\%}_{-14\%}$ of the total superbubble material, with the rest being interstellar medium. This amount of mixing of metal-rich ejecta and older ISM material corresponds to a metallicity of $2.7^{+3.9}_{-2.1}\mathrm{Z}_{\odot}$ for the material present in the superbubble core that can be accelerated to Galactic cosmic ray energies.

6.1 Improvements in the derivation of cosmic ray source abundances

The measurement of Galactic cosmic rays, the analysis of the data, and the derivation of source abundances has been happening for many years in cosmic ray astrophysics. Improvements in the statistical accuracy and mass resolution of cosmic ray instruments have made it possible to study this unique sample of cosmic material in more detail. High-quality data calls for high-quality data analysis. This thesis has contributed to the data analysis of cosmic rays in several ways.

This work has investigated the effect different $\Delta E \cdot E'$ combinations have on mass resolution (Appendix A). A particle telescope consisting of stacked detectors can calculate a particle's charge and mass many different ways. Mass resolution of the telescope is degraded by fluctuations in the particle's energy loss, and scattering in the detector. These effects vary depending on which $\Delta E \cdot E'$ combination is chosen. Some of the details of this critical issue, relevant to all silicon stack particle detectors, have been illuminated by work done in this thesis.

To accurately calculate abundances of isotopes measured by a cosmic ray detector at Earth, a sophisticated peak-fitting algorithm is required. This thesis has presented a maximum-likelihood technique that avoids the binning of data, thereby improving the accuracy of calculating abundances of rare particles. The fitting algorithm presented here also takes into account the variation in mass resolution due to a particle's incident angle into the telescope. High-angle data, which is usually cut from the data set, can be incorporated with this technique to improve statistics.

The leaky-box model has been used for many years to calculate source abundances.

Improved measurements of cosmic rays at Earth make it necessary to improve on the simple leaky-box model used in the past. An expanded cross-section data set was compiled for this work, as well as an updated set of decay reactions. The source abundances were derived using the tracer approach, constrained by observations as used previously. But in this thesis multiple tracers were analyzed simultaneously to constrain the cosmic ray secondary production, and minimize errors due to uncertainties in spallation cross sections. This improved the accuracy of the calculation, and also made it possible to reasonably assign uncertainties to the derived source abundance.

6.2 Insight into the cosmic ray source

The superbubble ejecta mixing fraction of $18\%^{+26\%}_{-14\%}$ and core material metallicity $2.7^{+3.9}_{-2.1}Z_{\odot}$ derived in this work is consistent with the mixing ratio calculated for the isotopes of cosmic ray neon ($18\% \pm 5\%$ and $2.7Z_{\odot} \pm 0.4Z_{\odot}$). The sulfur, argon, and calcium isotopes are generated by supernova explosions, whereas the neon results are constrained by Wolf-Rayet ejecta. Other GCR isotopes have been shown to be consistent with a mixing of Wolf-Rayet wind material and ISM, but the presence of the supernovae material, required to be a part of the accelerated matter by the nature of the superbubble, had not been sensitively investigated by cosmic ray isotope studies. This dissertation investigated the mostly supernovae-produced isotopes of sulfur, argon, and calcium, and showed the source abundances were consistent with the mixing ratio and metallicity derived from the Wolf-Rayet isotopes. Taken together, these results verify two major ingredients of the material predicted to be accelerated inside superbubbles. This thesis, in the context of previous studies of cosmic ray source abundances, provides support for the superbubble origin of Galactic cosmic rays.

Bibliography

Aharonian, F., Akhperjanian, A. G., Aye, K.-M., Bazer-Bachi, A. R., Beilicke, M., Benbow, W., Berge, D., Berghaus, P., Bernlöhr, K., Boisson, C., Bolz, O., Borgmeier, C., Braun, I., Breitling, F., Brown, A. M., Gordo, J. B., Chadwick, P. M., Chounet, L.-M., Cornils, R., Costamante, L., Degrange, B., Djannati-Ataï, A., Drury, L. O., Dubus, G., Ergin, T., Espigat, P., Feinstein, F., Fleury, P., Fontaine, G., Funk, S., Gallant, Y. A., Giebels, B., Gillessen, S., Goret, P., Hadjichristidis, C., Hauser, M., Heinzelmann, G., Henri, G., Hermann, G., Hinton, J. A., Hofmann, W., Holleran, M., Horns, D., de Jager, O. C., Jung, I., Khélifi, B., Komin, N., Konopelko, A., Latham, I. J., Le Gallou, R., Lemière, A., Lemoine, M., Leroy, N., Lohse, T., Marcowith, A., Masterson, C., McComb, T. J. L., de Naurois, M., Nolan, S. J., Noutsos, A., Orford, K. J., Osborne, J. L., Ouchrif, M., Panter, M., Pelletier, G., Pita, S., Pühlhofer, G., Punch, M., Raubenheimer, B. C., Raue, M., Raux, J., Rayner, S. M., Redondo, I., Reimer, A., Reimer, O., Ripken, J., Rob, L., Rolland, L., Rowell, G., Sahakian, V., Saugé, L., Schlenker, S., Schlickeiser, R., Schuster, C., Schwanke, U., Siewert, M., Sol, H., Steenkamp, R., Stegmann, C., Tavernet, J.-P., Terrier, R., Théoret, C. G., Tluczykont, M., van der Walt, D. J., Vasileiadis, G., Venter, C., Vincent, P., Visser, B., Völk, H. J., & Wagner, S. J. 2005a. A New Population of Very High Energy Gamma-Ray Sources in the Milky Way. *Science*, **307**(Mar.), 1938–1942.

Aharonian, F., Akhperjanian, A. G., Aye, K.-M., Bazer-Bachi, A. R., Beilicke, M., Benbow, W., Berge, D., Berghaus, P., Bernlöhr, K., Boisson, C., Bolz, O., Braun, I., Breitling, F., Brown, A. M., Bussons Gordo, J., Chadwick, P. M., Chounet, L.-M., Cornils, R., Costamante, L., Degrange, B., Djannati-Ataï, A., O'C. Drury, L., Dubus, G., Emmanoulopoulos, D., Espigat, P., Feinstein, F., Fleury, P., Fontaine, G., Fuchs, Y., Funk, S., Gallant, Y. A., Giebels, B., Gillessen, S., Glicenstein, J. F., Goret, P., Hadjichristidis, C., Hauser, M., Heinzelmann, G., Henri, G., Hermann, G., Hinton, J. A., Hofmann, W., Holleran, M., Horns, D., de Jager, O. C., Khélifi, B., Komin, N., Konopelko, A., Latham, I. J., Le Gallou, R., Lemière, A., Lemoine-Goumard, M., Leroy, N., Lohse, T., Martineau-Huynh, O., Marcowith, A., Masterson, C., McComb, T. J. L., de Naurois, M., Nolan, S. J., Noutsos, A., Orford, K. J., Osborne, J. L., Ouchrif, M., Panter, M., Pelletier, G., Pita, S., Pühlhofer, G., Punch, M., Raubenheimer, B. C., Raue, M., Raux, J., Rayner, S. M., Redondo, I., Reimer, A., Reimer, O., Ripken, J., Rob, L., Rolland, L., Rowell, G., Sahakian, V., Saugé, L., Schlenker, S., Schlickeiser, R., Schuster, C., Schwanke, U., Siewert, M., Sol, H., Steenkamp, R., Stegmann, C., Tavernet, J.-P., Terrier, R., Théoret, C. G., Tluczykont, M., van der Walt, D. J., Vasileiadis, G., Venter, C., Vincent, P., Völk, H. J., & Wagner, S. J. 2005b. Serendipitous discovery of the unidentified extended TeV γ-ray source HESS J1303-631. *Astron. & Astrophys.*, **439**(Sept.), 1013–1021.

Allbritton, G. L., Andersen, H., Barnes, A., Christian, E. R., Cummings, A. C., Dougherty, B. L., Jensen, L., Lee, J., Leske, R. A., Madden, M. P., Mewaldt, R., Milliken, B., Nahory, B. W., O'Donnell, R., Schmidt, P., Sears, B. R., von Rosenvinge, T. T., Walton, J. T., Wiedenbeck, M. E., & Wong, Y. K. 1996. Large diameter lithium compensated silicon detectors for the NASA Advanced Composition Explorer (ACE) mission. *IEEE Trans. Nucl. Sci.*, **43**(June), 1505–1509.

Anderson, H. H., & Ziegler, J. F. 1977. *Hydrogen: Stopping Powers and Ranges in All Elements.* New York, N. Y.: Pergamon Press.

Arnett, W. D. 1978. On the bulk yields of nucleosynthesis from massive stars. *Pages 161–+ of:* Basinska-Grzesik, E., & Mayor, M. (eds), *IAU Colloq. 45: Chemical and Dynamical Evolution of our Galaxy.*

Arnould, M., Goriely, S., & Meynet, G. 2006. The production of short-lived radionuclides by new non-rotating and rotating Wolf-Rayet model stars. *Astron. & Astrophys.*, **453**(July), 653–659.

Axford, W. I. 1981. The acceleration of cosmic rays by shock waves. *New York Academy Sciences Annals*, **375**(Dec.), 297–313.

Bevington, P. R., Robinson, D. K., & Bunce, G. 1993. Data Reduction and Error Analysis for the Physical Sciences, 2nd ed. *American Journal of Physics*, **61**(Aug.), 766–767.

Binns, W. R. 2006. *OB Associations within 2kpc of the Sun.* private communication.

Binns, W. R., Wiedenbeck, M. E., Arnould, M., Cummings, A. C., George, J. S., Goriely, S., Israel, M. H., Leske, R. A., Mewaldt, R. A., Meynet, G., Scott, L. M., Stone, E. C., & von Rosenvinge, T. T. 2005. Cosmic-Ray Neon, Wolf-Rayet Stars, and the Superbubble Origin of Galactic Cosmic Rays. *Astrophys. J.*, **634**(Nov.), 351–364.

Blandford, R. D., & Ostriker, J. P. 1980. Supernova shock acceleration of cosmic rays in the Galaxy. *Astrophys. J.*, **237**(May), 793–808.

Bradt, H. L., & Peters, B. 1950. The Heavy Nuclei of the Primary Cosmic Radiation. *Physical Review*, **77**(Jan.), 54–70.

Brown, A. G. A., de Geus, E. J., & de Zeeuw, P. T. 1994. The Orion OB1 association. 1: Stellar content. *Astron. & Astrophys.*, **289**(Sept.), 101–120.

Casse, M., & Paul, J. A. 1982. On the stellar origin of the Ne-22 excess in cosmic rays. *Astrophys. J.*, **258**(July), 860–863.

Chin, Y.-N., Henkel, C., Whiteoak, J. B., Langer, N., & Churchwell, E. B. 1996. Interstellar sulfur isotopes and stellar oxygen burning. *Astron. & Astrophys.*, **305**(Jan.), 960–+.

Claudius, M., & Grosbol, P. J. 1980. On the initial mass function – The mass spectrum of young OB associations. *Astron. & Astrophys.*, **87**(July), 339–342.

Connell, J. J. 1998. Galactic Cosmic-Ray Confinement Time: ULYSSES High Energy Telescope Measurements of the Secondary Radionuclide ^{10}Be. *Astrophys. J.*, **501**(July), L59+.

Cowsik, R., Pal, Yash, Tandon, S. N., & Verma, R. P. 1967. Steady State of Cosmic-Ray Nuclei: Their Spectral Shape and Path Length at Low Energies. *Phys. Rev.*, **158**(5), 1238–1242.

Cummings, A. C. 1999. Radial Interplanetary Mean Free Paths Inferred from Anomalous Cosmic Ray Observations in the Outer Heliosphere. *Pages 496–+ of: International Cosmic Ray Conference.*

Daflon, S., & Cunha, K. 2004. Galactic Metallicity Gradients Derived from a Sample of OB Stars. *Astrophys. J.*, **617**(Dec.), 1115–1126.

Davis, A. J., Mewaldt, R. A., Binns, W. R., Christian, E. R., Cummings, A. C., George, J. S., Hink, P. L., Leske, R. A., von Rosenvinge, T. T., Wiedenbeck, M. E., & Yanasak, N. E. 2000. On the Low Energy Decrease in Galactic Cosmic Ray Secondary/Primary

Ratios. *Pages 421–+ of:* Mewaldt, R. A., Jokipii, J. R., Lee, M. A., Möbius, E., & Zurbuchen, T. H. (eds), *AIP Conf. Proc. 528: Acceleration and Transport of Energetic Particles Observed in the Heliosphere.*

Davis, A. J., Mewaldt, R. A., Cohen, C. M. S., Cummings, A. C., George, J. S., Leske, R. A., Stone, E. C., Wiedenbeck, M. E., Yanasak, N. E., Christian, E. R., von Rosenvinge, T. T., Binns, W. R., & Hink, P. L. 2001 (Aug.). The Evolution of Galactic Cosmic Ray Element Spectra from Solar Minimum to Solar Maximum. *Pages 3971–+ of: International Cosmic Ray Conference.*

Dermer, C. D. 1986. Binary collision rates of relativistic thermal plasmas. II – Spectra. *Astrophys. J.*, **307**(Aug.), 47–59.

Dwek, E. 1998. The Evolution of the Elemental Abundances in the Gas and Dust Phases of the Galaxy. *Astrophys. J.*, **501**(July), 643–+.

Engelmann, J. J., Ferrando, P., Soutoul, A., Goret, P., & Juliusson, E. 1990. Charge composition and energy spectra of cosmic-ray nuclei for elements from Be to NI - Results from HEAO-3-C2. *Astron. & Astrophys.*, **233**(July), 96–111.

Filippenko, A. V. 1997. Optical Spectra of Supernovae. *Annu. Rev. Astron. Astrophys.*, **35**, 309–355.

Firestone, R. B., & Shirley, V. S. 1998. *Table of Isotopes, 2 Volume Set, 8th Edition.* Wiley-VCH.

Fisk, L. A., Ramaty, R., & Goldstein, M. L. 1971. Energy Loss of Cosmic Rays in the Interplanetary Medium. (Abstract). *Pages 799–+ of: International Cosmic Ray Conference.*

Fryer, C. L. 1999. Mass Limits For Black Hole Formation. *Astrophys. J.*, **522**(Sept.), 413–418.

Garmany, C. D. 1994. OB associations: Massive stars in context. *Proc. Astron. Soc. Pacific*, **106**(Jan.), 25–37.

Garrard, T. L., Davis, A. J., Hammond, J. S., & Sears, S. R. 1998. The ACE Science Center. *Space Science Reviews*, **86**, 649–663.

George, J. S., Binns, W. R., Christian, E. R., Cummings, A. C., Davis, A. J., de Nolfo, G. A., Hink, P. L., Israel, M. H., Leske, R. A., Lijowski, M., Mewaldt, R. A., Scott, L. M., Stone, E. C., von Rosenvinge, T. T., Wiedenbeck, M. E., & Yanasak, N. E. 2006. in progress.

Gleeson, L. J., & Axford, W. I. 1968. Solar Modulation of Galactic Cosmic Rays. *Astrophys. J.*, **154**(Dec.), 1011–+.

Goriely, S. 2005. *Calculated Wolf-Rayet Wind Ejecta Yields.* private communication.

Hamann, W.-R., & Koesterke, L. 1998. Spectrum formation in clumped stellar winds: consequences for the analyses of Wolf-Rayet spectra. *Astron. & Astrophys.*, **335**(July), 1003–1008.

HEGRA Collaboration: F. Aharonian. 2005. The unidentified TeV source (TeVJ2032+4130) and surrounding field: Final HEGRA IACT-System results. *ArXiv Astrophysics e-prints*, Jan.

Higdon, J. C. 1999 (Aug.). The Source of Cosmic Rays: 2. Superbubble Composition. *Pages 144–+ of: International Cosmic Ray Conference.*

Higdon, J. C., & Lingenfelter, R. E. 2003a. The Myriad-Source Model of Cosmic Rays. I. Steady State Age and Path Length Distributions. *Astrophys. J.*, **582**(Jan.), 330–341.

Higdon, J. C., & Lingenfelter, R. E. 2003b. The Superbubble Origin of ^{22}Ne in Cosmic Rays. *Astrophys. J.*, **590**(June), 822–832.

Higdon, J. C., Lingenfelter, R. E., & Ramaty, R. 1998. Cosmic-Ray Acceleration from Supernova Ejecta in Superbubbles. *Astrophys. J.*, **509**(Dec.), L33–L36.

Kapteyn, J. C. 1914. On the individual parallaxes of the brighter galactic helium stars in the southern hemisphere, together with considerations on the parallax of stars in general. *Astrophys. J.*, **40**(July), 43–126.

Klarmann, J., Binns, W. R., Hink, P. L., Israel, M. H., Fishman, G. J., Parnell, T. A., & Pendleton, G. N. 1998. Scintillating Optical Fibers in Astrophysics Research. *Nuclear Physics B Proceedings Supplements*, **61**(Feb.), 378–383.

Lada, C. J., & Kylafis, N. D. (eds). 1991. *The Physics of Star Formation and Early Stellar Evolution*. Springer.

Lal, D., & Elliot, H. 1975. Long-Term Variations in the Cosmic-Ray Flux [and Discussion]. *Philosophical Transactions of the Royal Society of London. Series A, Mathematical and Physical Sciences*, **277**(1270), 395–411.

Letaw, J. R., Silberberg, R., & Tsao, C. H. 1983. Proton-nucleus total inelastic cross sections - an empirical formula for E greater than 10 MeV. *Astrophys. J. Suppl.*, **51**(Mar.), 271–275.

Lodders, K. 2003. Solar System Abundances and Condensation Temperatures of the Elements. *Astrophys. J.*, **591**(July), 1220–1247.

Maeder, A., & Conti, P. S. 1994. Massive Star Populations in Nearby Galaxies. *Annu. Rev. Astron. Astrophys.*, **32**, 227–275.

Maehl, R., Hagen, F. A., Fisher, A. J., Ormes, J. F., & Simon, M. 1975. Astrophysical implications of the isotopic composition of cosmic rays. *Pages 367–372 of: International Cosmic Ray Conference.*

Maran, S. P. (ed). 1991. *The Astronomy and Astrophysics Encyclopedia.* Wiley-VCH.

Markwardt, C. B. 2006. *Markwardt Interactive Data Language (IDL) Library.* `http://cow.physics.wisc.edu/~craigm/idl/`.

Massey, P., Johnson, K. E., & Degioia-Eastwood, K. 1995. The Initial Mass Function and Massive Star Evolution in the OB Associations of the Northern Milky Way. *Astrophys. J.*, **454**(Nov.), 151–+.

McCray, R., & Snow, Jr., T. P. 1979. The violent interstellar medium. *Annu. Rev. Astron. Astrophys.*, **17**, 213–240.

Mewaldt, R. A. 1989. The abundances of isotopes in the cosmic radiation. *Pages 124–146 of:* Waddington, C. J. (ed), *AIP Conf. Proc. 183: Cosmic Abundances of Matter.*

Mewaldt, R. A., Wiedenbeck, M. E., Scott, L. M., Binns, W. R., Cummings, A. C., Davis, A. J., Israel, M. H., Leske, R. A., Stone, E. C., & von Rosenvinge, T. T. 2004 (Sept.). Cosmic-Ray Spectra in Interstellar Space. *Pages 127–132 of:* Florinski, V., Pogorelov, N. V., & Zank, G. P. (eds), *AIP Conf. Proc. 719: Physics of the Outer Heliosphere.*

Meyer, J.-P., Drury, L. O., & Ellison, D. C. 1997. Galactic Cosmic Rays from Supernova Remnants. I. A Cosmic-Ray Composition Controlled by Volatility and Mass-to-Charge Ratio. *Astrophys. J.*, **487**(Sept.), 182–+.

Meynet, G., & Maeder, A. 2005. Stellar evolution with rotation. XI. Wolf-Rayet star populations at different metallicities. *Astron. & Astrophys.*, **429**(Jan.), 581–598.

Meynet, G., Arnould, M., Paulus, G., & Maeder, A. 2001. Wolf-Rayet star nucleosynthesis and the isotopic composition of the Galactic Cosmic Rays. *Space Science Reviews*, **99**(Oct.), 73–84.

Niebur, S. M., Scott, L. M., Wiedenbeck, M. E., Binns, W. R., Christian, E. R., Cummings, A. C., Davis, A. J., George, J. S., Hink, P. L., Israel, M. H., Leske, R. A., Mewaldt, R. A., Stone, E. C., von Rosenvinge, T. T., & Yanasak, N. E. 2003. Cosmic ray energy loss in the heliosphere: Direct evidence from electron-capture-decay secondary isotopes. *Journal of Geophysical Research (Space Physics)*, **108**(Aug.), 8–1.

Nomoto, K., Iwamoto, K., Nakasato, N., Thielemann, F.-K., Brachwitz, F., Tsujimoto, T., Kubo, Y., & Kishimoto, N. 1997. Nucleosynthesis in type Ia supernovae. *Nuclear Physics A*, **621**(Feb.), 467–476.

Nugis, T., & Lamers, H. J. G. L. M. 2000. Mass-loss rates of Wolf-Rayet stars as a function of stellar parameters. *Astron. & Astrophys.*, **360**(Aug.), 227–244.

Ogliore, R. C., Mewaldt, R. A., Leske, R. A., Stone, E. C., & von Rosenvinge, T. T. 2001 (Aug.). A direct measurement of the geomagnetic cutoff for cosmic rays at space station latitudes. *Pages 4112–+ of: International Cosmic Ray Conference.*

Orear, J. 1982. *Notes on Statistics for Physicists, Revised.* Ithaca, N. Y.: Cornell University.

Orth, C. D., & Buffington, A. 1976. Secondary cosmic-ray electrons and positrons from 1 to 100 GeV in the upper atmosphere and interstellar space, and interpretation of a recent positron flux measurement. *Astrophys. J.*, **206**(May), 312–332.

Parker, E. N. 1965. The passage of energetic charged particles through interplanetary space. *Planet. Space Sci.*, **13**(Jan.), 9–+.

Parker, E. N. 1966. The effect of adiabatic deceleration on the cosmic ray spectrum in the solar system. *Planet. Space Sci.*, **14**(Apr.), 371–+.

Payne, M. G. 1969. Energy Straggling of Heavy Charged Particles in Thick Absorbers. *Physical Review*, **185**(Sept.), 611–623.

Potgieter, M. S., & Ferreira, S. E. S. 2001. Modulation of cosmic rays in the heliosphere: theory and models. *Pages I217+ of:* Gladysheva, O. G., Kocharov, G. E., Kovaltsov, G. A., & Usoskin, I. G. (eds), *International Cosmic Ray Conference.*

Ptuskin, V. S. 2001. Propagation, Confinement Models, and Large-Scale Dynamical Effects of Galactic Cosmic Rays. *Space Science Reviews*, **99**(Oct.), 281–293.

Raisbeck, G. M. 1979. International Cosmic Ray Conference v14. *Pages 146–+ of: International Cosmic Ray Conference.*

Rana, N. C. 1991. Chemical evolution of the Galaxy. *Annu. Rev. Astron. Astrophys.*, **29**, 129–162.

Reames, D. V. 1974. The Abundances of Nuclei in the Cosmic Radiation. *Pages 54–+ of:* McDonald, F. B., & Fichtel, C. E. (eds), *High Energy Particles and Quanta in Astrophysics.*

Rossi, B. 1952. *High Energy Particles.* Englewood Cliffs, N. J.: Prentice-Hall, Inc.

Rudstam, G. 1966. Systematics of Spallation Yields. *Zeitschrift fur Naturforschung Section C, Biosciences*, **21.7**, 1027–.

Salpeter, E. E. 1955. The Luminosity Function and Stellar Evolution. *Astrophys. J.*, **121**(Jan.), 161–+.

Schaller, G., Schaerer, D., Meynet, G., & Maeder, A. 1992. New grids of stellar models from 0.8 to 120 solar masses at Z = 0.020 and Z = 0.001. *Astron. & Astrophys., Supplement*, **96**(Dec.), 269–331.

Scott, Lauren M. 2005. *Cosmic-Ray Energy Loss in the Heliosphere and Interstellar Reacceleration.* Ph.D. thesis, Washington University.

Shapiro, M. M., Silberberg, R., & Wefel, J. P. (eds). 1991. *Cosmic Rays, Supernovae and the Interstellar Medium.* Kluwer.

Silberberg, R., Tsao, C. H., & Shapiro, M. M. 1976. *Semiempirical cross sections, and applications to nuclear interactions of cosmic rays.* ASSL Vol. 59: Spallation Nuclear Reactions and their Applications. Pages 49–81.

Silberberg, R., Tsao, C. H., & Barghouty, A. F. 1998. Updated Partial Cross Sections of Proton-Nucleus Reactions. *Astrophys. J.*, **501**(July), 911–+.

Simpson, J. A. 1983. Elemental and Isotopic Composition of the Galactic Cosmic Rays. *Annual Review of Nuclear and Particle Science*, **33**, 323–382.

Soutoul, A. 1999. Energy Dependent Abundance of Secondary Nuclei in Cosmic Rays: An Indication of Altitude Dependent Convection above the Galactic Plane? *Pages 184–+ of: International Cosmic Ray Conference.*

Soutoul, A., Casse, M., & Juliusson, E. 1978. Time delay between the nucleosynthesis of cosmic rays and their acceleration to relativistic energies. *Astrophys. J.*, **219**(Jan.), 753–755.

Stone, E. C., & Wiedenbeck, M. E. 1979. A secondary tracer approach to the derivation of galactic cosmic-ray source isotopic abundances. *Astrophys. J.*, **231**(July), 606–623.

Stone, E. C., Cohen, C. M. S., Cook, W. R., Cummings, A. C., Gauld, B., Kecman, B., Leske, R. A., Mewaldt, R. A., Thayer, M. R., Dougherty, B. L., Grumm, R. L., Milliken, B. D., Radocinski, R. G., Wiedenbeck, M. E., Christian, E. R., Shuman, S., Trexel, H., von Rosenvinge, T. T., Binns, W. R., Crary, D. J., Dowkontt, P., Epstein, J., Hink, P. L., Klarmann, J., Lijowski, M., & Olevitch, M. A. 1998. The Cosmic-Ray Isotope Spectrometer for the Advanced Composition Explorer. *Space Science Reviews*, **86**, 285–356.

Strong, A. W., & Moskalenko, I. V. 2001 (Aug.). New developments in the GALPROP CR propagation model. *Pages 1942–1945 of: International Cosmic Ray Conference.*

Taillet, R., & Maurin, D. 2003. Spatial origin of Galactic cosmic rays in diffusion models. I. Standard sources in the Galactic disk. *Astron. & Astrophys.*, **402**(May), 971–983.

Tanimori, T., Hayami, Y., Kamei, S., Dazeley, S. A., Edwards, P. G., Gunji, S., Hara, S., Hara, T., Holder, J., Kawachi, A., Kifune, T., Kita, R., Konishi, T., Masaike, A., Matsubara, Y., Matsuoka, T., Mizumoto, Y., Mori, M., Moriya, M., Muraishi, H., Muraki, Y., Naito, T., Nishijima, K., Oda, S., Ogio, S., Patterson, J. R., Roberts, M. D., Rowell, G. P., Sakurazawa, K., Sako, T., Sato, Y., Susukita, R., Suzuki, A., Suzuki, R., Tamura, T., Thornton, G. J., Yanagita, S., Yoshida, T., & Yoshikoshi, T. 1998. Discovery of TeV Gamma Rays from SN 1006: Further Evidence for the Supernova Remnant Origin of Cosmic Rays. *Astrophys. J.*, **497**(Apr.), L25+.

Tenorio-Tagle, G., & Bodenheimer, P. 1988. Large-scale expanding superstructures in galaxies. *Annu. Rev. Astron. Astrophys.*, **26**, 145–197.

Thayer, M. R. 1997. An Investigation into Sulfur Isotopes in the Galactic Cosmic Rays. *Astrophys. J.*, **482**(June), 792–+.

Timmes, F. X., Woosley, S. E., & Weaver, T. A. 1995. Galactic chemical evolution: Hygrogen through zinc. *Astrophys. J. Suppl.*, **98**(June), 617–658.

Tripathi, R. K., Cucinotta, F. A., & Wilson, J. W. 1997 (Jan.). *Universal Parameterization of Absorption Cross Sections.* Tech. rept.

Tsao, C. H., Silberberg, R., Barghouty, A. F., Sihver, L., & Kanai, T. 1993. Scaling algorithm to calculate heavy-ion spallation cross sections. *Phys. Rev. C*, **47**(Mar.), 1257–1262.

Twarog, B. A. 1980. The chemical evolution of the solar neighborhood. II - The age-metallicity relation and the history of star formation in the galactic disk. *Astrophys. J.*, **242**(Nov.), 242–259.

van den Bergh, S., & McClure, R. D. 1994. Rediscussion of extragalactic supernova rates derived from Evans's 1980-1988 observations. *Astrophys. J.*, **425**(Apr.), 205–209.

Villagrasa-Canton, Carmen. 2003. *Etude de la production des noyaux re'siduels dans la re'action de spallation Fe + p a' 5 e'nergies (300-1500 MeV/A) et application au calcul de dommage sur une fene'tre de syste'me hybride.* Ph.D. thesis, Universite de Paris XI.

Webber, W. R., Kish, J. C., & Schrier, D. A. 1990. Formula for calculating partial cross sections for nuclear reactions of nuclei with E>~200 MeV/nucleon in hydrogen targets. *Phys. Rev. C*, **41**(2), 566–571.

Webber, W. R., Kish, J. C., & Schrier, D. A. 1990a. Individual charge changing fragmentation cross sections of relativistic nuclei in hydrogen, helium, and carbon targets. *Phys. Rev. C*, **41**(Feb.), 533–546.

Webber, W. R., Kish, J. C., & Schrier, D. A. 1990b. Individual isotopic fragmentation cross sections of relativistic nuclei in hydrogen, helium, and carbon targets. *Phys. Rev. C*, **41**(Feb.), 547–565.

Webber, W. R., Kish, J. C., & Schrier, D. A. 1990c. Total charge and mass changing cross sections of relativistic nuclei in hydrogen, helium, and carbon targets. *Phys. Rev. C*, **41**(Feb.), 520–532.

Wellstein, S., & Langer, N. 1999. Implications of massive close binaries for black hole formation and supernovae. *Astron. & Astrophys.*, **350**(Oct.), 148–162.

Westfall, G. D., Wilson, L. W., Lindstrom, P. J., Crawford, H. J., Greiner, D. E., & Heckman, H. H. 1979. Fragmentation of relativistic ^{56}Fe. *Phys. Rev. C*, **19**(Apr.), 1309–1323.

Wiedenbeck, M. E. 2005. The Level of Solar Modulation of Galactic Cosmic Rays from 1997 to 2005 as Derived from ACE Measurements of Elemental Energy Spectra. *Pages 277–+ of: International Cosmic Ray Conference.*

Wiedenbeck, M. E. 2006. *Solar modulation parameter ϕ inferred from spectra of C, O, Mg, Si, and Fe.* private communication.

Wiedenbeck, M. E., Binns, W. R., Christian, E. R., Cummings, A. C., Dougherty, B. L., Hink, P. L., Klarmann, J., Leske, R. A., Lijowski, M., Mewaldt, R. A., Stone, E. C., Thayer, M. R., von Rosenvinge, T. T., & Yanasak, N. E. 1999. Constraints on the Time

Delay between Nucleosynthesis and Cosmic-Ray Acceleration from Observations of ^{59}Ni and ^{59}Co. *Astrophys. J.*, **523**(Sept.), L61–L64.

Wiedenbeck, M. E., Yanasak, N. E., Cummings, A. C., Davis, A. J., George, J. S., Leske, R. A., Mewaldt, R. A., Stone, E. C., Hink, P. L., Israel, M. H., Lijowski, M., Christian, E. R., & von Rosenvinge, T. T. 2001. The Origin of Primary Cosmic Rays: Constraints from ACE Elemental and Isotopic Composition Observations. *Space Science Reviews*, **99**(Oct.), 15–26.

Wilson, T. L., & Matteucci, F. 1992. Abundances in the interstellar medium. *Astron. Astrophys. Rev.*, **4**(June), 1–33.

Woosley, S. E., & Weaver, T. A. 1981. Anomalous isotopic composition of cosmic rays. *Astrophys. J.*, **243**(Jan.), 651–659.

Woosley, S. E., & Weaver, T. A. 1995. The Evolution and Explosion of Massive Stars. II. Explosive Hydrodynamics and Nucleosynthesis. *Astrophys. J. Suppl.*, **101**(Nov.), 181–+.

Woosley, S. E., Arnett, W. D., & Clayton, D. D. 1973. The Explosive Burning of Oxygen and Silicon. *Astrophys. J. Suppl.*, **26**(Nov.), 231–+.

Woosley, S. E., Langer, N., & Weaver, T. A. 1995. The Presupernova Evolution and Explosion of Helium Stars That Experience Mass Loss. *Astrophys. J.*, **448**(July), 315–+.

Woosley, S. E., Heger, A., & Weaver, T. A. 2002. The evolution and explosion of massive stars. *Reviews of Modern Physics*, **74**(Nov.), 1015–1071.

Yanasak, N. E., Wiedenbeck, M. E., Mewaldt, R. A., Davis, A. J., Cummings, A. C., George, J. S., Leske, R. A., Stone, E. C., Christian, E. R., von Rosenvinge, T. T., Binns, W. R., Hink, P. L., & Israel, M. H. 2001. Measurement of the Secondary Radionuclides ^{10}Be,

^{26}Al, ^{36}Cl, ^{54}Mn, and ^{14}C and Implications for the Galactic Cosmic-Ray Age. *Astrophys. J.*, **563**(Dec.), 768–792.

Appendix A

Effects of $\Delta E \cdot E'$ combination on mass resolution

As described in Section 3.1.1, the dominant contributors to mass resolution are Landau fluctuations and multiple Coulomb scattering. The charge and mass of a particle detected in the CRIS stack can be calculated by different $\Delta E \cdot E'$ combinations, so it is critical to understand how these contributions vary using different ΔE and E' detectors, and how best to combine multiple measurements to achieve the smallest total mass resolution, $\sigma_{M_{total}}$, for the particle's calculated mass.

Making the ΔE detector thin and E' thick will reduce the amount of multiple scattering (fewer scattering nuclei in the ΔE detector for the incident particle to scatter off of), but will cause an increase in the Landau fluctuations (relative amount of statistical energy fluctuation in the ΔE detector, $\Delta E/E$, goes as $\sqrt{N}/N = 1/\sqrt{N}$, where N is the number of energy loss interactions). The converse situation, with a very thick ΔE and thin E', will have Landau fluctuations in the E' detector, and more severe multiple scattering due to the thicker ΔE. Modeling mass resolution for the thin, moderate, and thick ΔE situations using equations 3.3 – 3.8 will yield insight into which $\Delta E \cdot E'$ combination gives the optimal $\sigma_{M_{total}}$.

The E' detector sum must contain the range the particle stopped in, and the ΔE sum

$\Delta E \cdot E'$ Combinations for Range 8			
Mass Calculation	Minimum ΔE	Moderate ΔE	Minimum E'
1	[1]·[2+3+4+5+6+7+8]	[1]·[2+3+4+5+6+7+8]	[1+2+3+4+5+6+7]·[8]
2	[2]·[3+4+5+6+7+8]	[1+2]·[3+4+5+6+7+8]	[2+3+4+5+6+7]·[8]
3	[3]·[4+5+6+7+8]	[1+2+3]·[4+5+6+7+8]	[3+4+5+6+7]·[8]
4	[4]·[5+6+7+8]	[1+2+3+4]·[5+6+7+8]	[4+5+6+7]·[8]
5	[5]·[6+7+8]	[1+2+3+4+5]·[6+7+8]	[5+6+7]·[8]
6	[6]·[7+8]	[1+2+3+4+5+6]·[7+8]	[6+7]·[8]
7	[7]·[8]	[1+2+3+4+5+6+7]·[8]	[7]·[8]

Table A.1: Three different methods for calculating a set of seven masses for a range 8 particle

must directly precede E'. For a particle stopping in range R, there can be at most R-1 ways to calculate mass using a specified method. Table A.1 describes the three methods for calculating mass R-1 different ways for a range 8 particle.

Using Equations 3.3 – 3.8, the mass resolution is calculated as the quadrature sum of the Landau fluctuations and multiple scattering contributions. Figure A.1 shows the results for the minimum, moderate, and maximum ΔE calculations for range 8 sulfur.

Since the final mass estimate will be a weighted average of the R-1 mass calculations, correlations between the calculations will have an effect on the overall mass resolution. The minimum ΔE method will have less correlation between calculations because a single, different ΔE detector is used in each calculation. The moderate ΔE and minimum E' methods will have larger correlations because the ΔE detector contains the same range in all the calculations. Figure A.2 shows the strong correlations in the sulfur mass calculations for moderate ΔE, and the less correlated data for the minimum ΔE method.

The correlations between different mass measurements shown in Figure A.2 worsen the overall mass resolution $\sigma_{M_{total}}$. The moderate ΔE and minimum E' have better individual mass resolution (as shown in Figure A.1), but the weighted average of the R-1 calculations could be worse than the minimum ΔE method, because the latter method uses independent

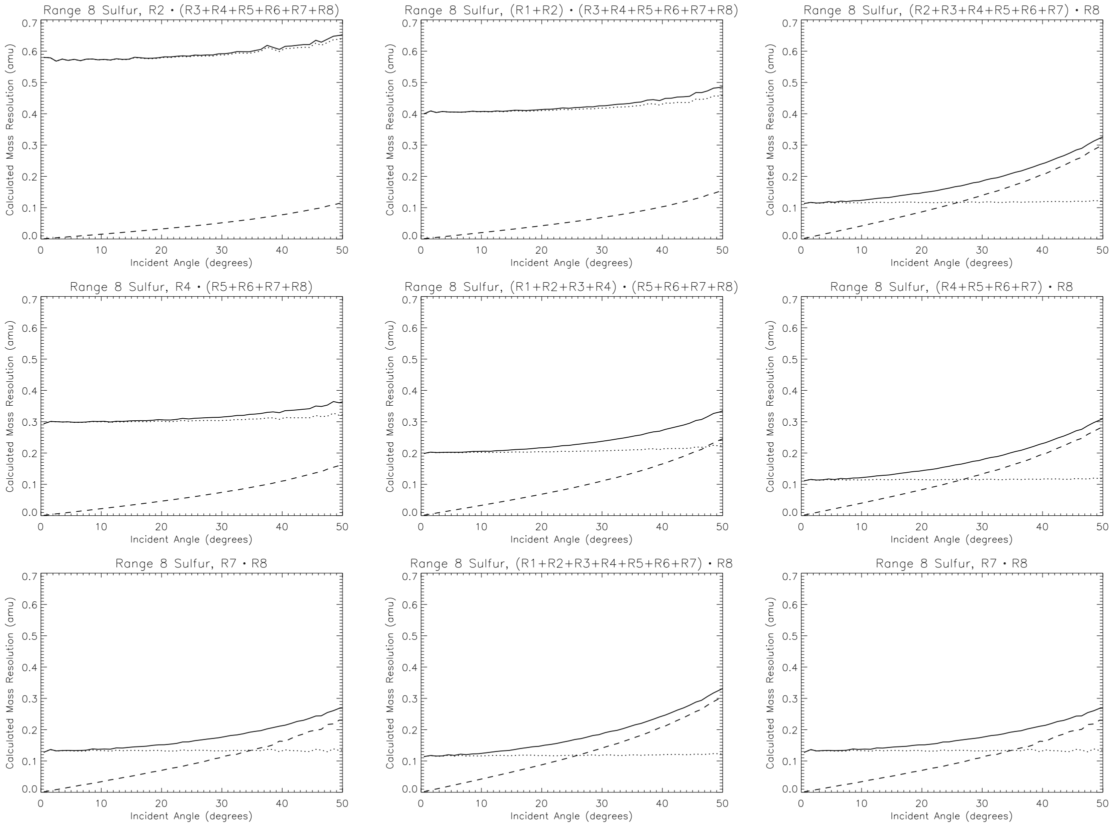

Figure A.1: Mass resolution as a function of incident angle for range 8 sulfur for various $\Delta E \cdot E'$ combinations. “Minimum ΔE” calculations are in the left column, and the corresponding “Moderate ΔE” and “Maximum ΔE” are in the center and right columns, respectively. The dashed line is the multiple scattering contribution, the dotted line represents Landau fluctuations, and the solid line is their quadrature sum.

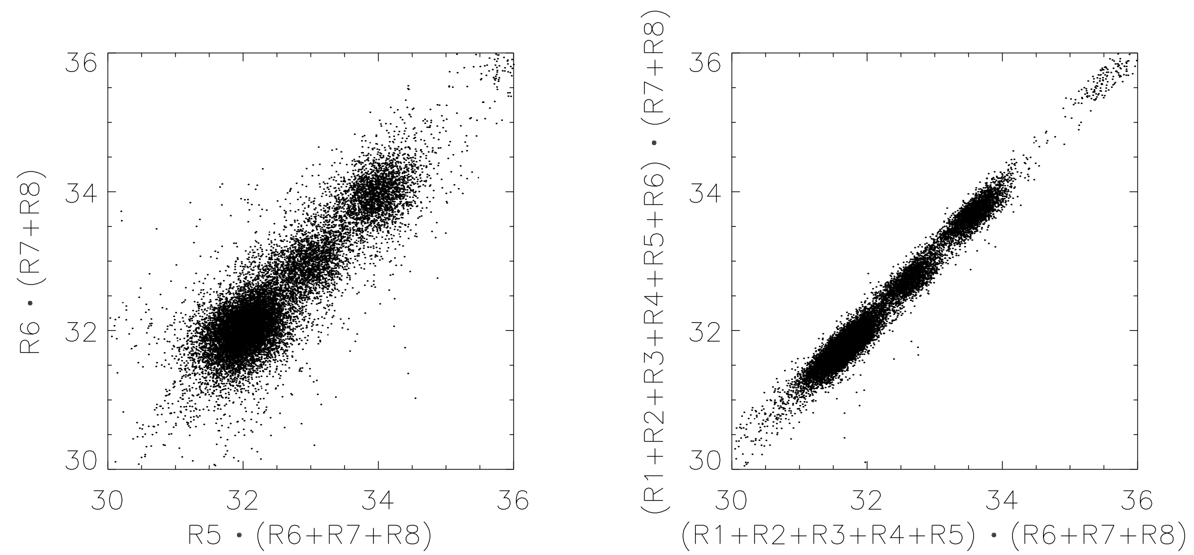

Figure A.2: Mass calculation #6 vs. #5 is shown for minimum ΔE in the left panel, and for moderate ΔE in the right panel.

measurements for ΔE. The histogrammed data will show which method is optimal.

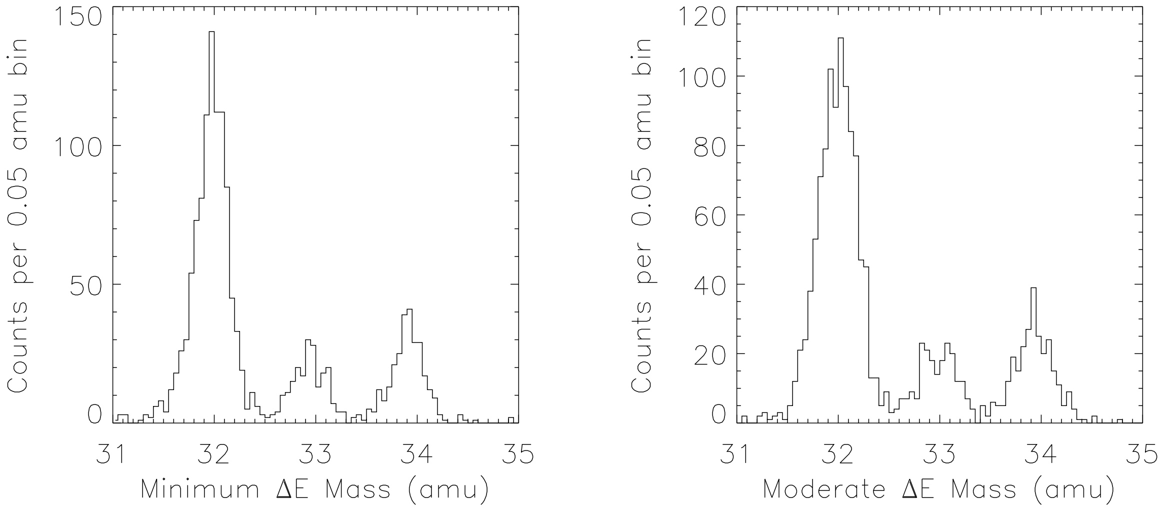

Figure A.3: Mass histograms for two mass calculation methods

As seen in Figure A.3, the minimum ΔE method shows narrower peaks than the moderate ΔE method. The correlated mass calculations worsen the mass resolution beyond what is gained from the better resolution in the individual calculations. The minimum ΔE method is used to calculate mass in this analysis.

Appendix B

Isotope Tables

B.1 Phosphorus

^{31}P Solar Minimum, $0° < \theta < 25°$

Range	Fit Abundance	Spallation Correction	SOFT Efficiency	Corrected Abundance
2	228.99±15.13	1.127±0.034	1.009±0.020	260.42±19.59
3	492.00±22.18	1.173±0.035	1.009±0.020	582.47±33.59
4	400.02±20.00	1.238±0.037	1.010±0.020	500.11±30.80
5	337.99±18.38	1.307±0.039	1.009±0.020	445.80±29.07
6	304.97±17.46	1.380±0.041	1.010±0.020	425.02±28.73
7	234.01±15.30	1.456±0.044	1.010±0.020	344.26±25.68
8	238.00±15.43	1.541±0.046	1.010±0.020	370.41±27.45

^{31}P Solar Minimum, $25° < \theta < 50°$

Range	Fit Abundance	Spallation Correction	SOFT Efficiency	Corrected Abundance
2	410.98±20.27	1.155±0.035	1.009±0.020	478.88±29.23
3	787.05±28.06	1.211±0.036	1.009±0.020	961.72±48.69
4	543.07±23.31	1.290±0.039	1.010±0.020	707.62±39.61
5	395.05±19.88	1.371±0.041	1.009±0.020	546.45±33.79
6	260.01±16.13	1.458±0.044	1.010±0.020	383.02±27.46
7	217.02±14.73	1.550±0.046	1.010±0.020	339.74±26.10
8	204.01±14.28	1.644±0.049	1.010±0.020	338.86±26.67

^{31}P Solar Maximum, 0° < θ < 25°

Range	Fit Abundance	Spallation Correction	SOFT Efficiency	Corrected Abundance
2	192.00±13.86	1.127±0.034	1.009±0.020	218.35±17.61
3	403.99±20.10	1.173±0.035	1.009±0.020	478.28±29.36
4	358.01±18.92	1.238±0.037	1.010±0.020	447.59±28.61
5	309.01±17.58	1.307±0.039	1.009±0.020	407.58±27.43
6	292.99±17.12	1.380±0.041	1.010±0.020	408.32±28.01
7	282.01±16.79	1.456±0.044	1.010±0.020	414.87±28.86
8	275.99±16.61	1.541±0.046	1.010±0.020	429.55±30.11

^{31}P Solar Maximum, 25° < θ < 50°

Range	Fit Abundance	Spallation Correction	SOFT Efficiency	Corrected Abundance
2	365.00±19.10	1.155±0.035	1.009±0.020	425.30±27.01
3	667.99±25.85	1.211±0.036	1.009±0.020	816.23±43.11
4	519.02±22.78	1.290±0.039	1.010±0.020	676.28±38.37
5	402.98±20.07	1.371±0.041	1.009±0.020	557.42±34.24
6	309.01±17.58	1.458±0.044	1.010±0.020	455.20±30.63
7	240.98±15.52	1.550±0.046	1.010±0.020	377.25±27.83
8	203.01±14.25	1.644±0.049	1.010±0.020	337.20±26.59

Table B.1: Measured and corrected counts of phosphorus for solar minimum and solar maximum, separated into low-angle and high-angle data sets

B.2 Sulfur

^{32}S Solar Minimum, $0^\circ < \theta < 25^\circ$

Range	Fit Abundance	Spallation Correction	SOFT Efficiency	Corrected Abundance
2	1214.5±34.94	1.129±0.034	1.009±0.020	1384.2±63.74
3	2109.9±46.01	1.176±0.035	1.009±0.020	2503.9±105.3
4	1833.6±42.86	1.242±0.037	1.009±0.020	2297.8±98.55
5	1464.8±38.34	1.312±0.039	1.009±0.020	1939.7±86.26
6	1245.5±35.36	1.387±0.042	1.009±0.020	1743.2±79.86
7	1080.2±32.92	1.464±0.044	1.010±0.020	1597.2±75.27
8	980.70±31.36	1.550±0.047	1.010±0.020	1535.7±73.88

^{33}S Solar Minimum, $0^\circ < \theta < 25^\circ$

Range	Fit Abundance	Spallation Correction	SOFT Efficiency	Corrected Abundance
2	168.91±13.31	1.132±0.034	1.009±0.020	192.90±16.71
3	385.38±19.92	1.178±0.035	1.009±0.020	458.27±28.85
4	292.06±17.25	1.248±0.037	1.009±0.020	367.92±25.44
5	281.36±16.99	1.317±0.040	1.009±0.020	373.87±26.27
6	243.44±15.80	1.394±0.042	1.009±0.020	342.52±25.41
7	229.30±15.30	1.474±0.044	1.010±0.020	341.33±25.86
8	209.52±14.61	1.559±0.047	1.010±0.020	329.99±25.88

^{34}S Solar Minimum, $0^\circ < \theta < 25^\circ$

Range	Fit Abundance	Spallation Correction	SOFT Efficiency	Corrected Abundance
2	235.45±15.44	1.136±0.034	1.009±0.020	269.86±20.18
3	428.72±20.82	1.183±0.036	1.009±0.020	511.99±30.94
4	330.38±18.23	1.250±0.038	1.009±0.020	416.87±27.46
5	346.84±18.70	1.322±0.040	1.009±0.020	462.82±29.99
6	294.02±17.20	1.400±0.042	1.009±0.020	415.41±28.52
7	244.50±15.68	1.481±0.044	1.010±0.020	365.74±26.89
8	275.83±16.66	1.567±0.047	1.010±0.020	436.71±30.69

^{36}S Solar Minimum, 0° < θ < 25°

Range	Fit Abundance	Spallation Correction	SOFT Efficiency	Corrected Abundance
2	7.1042±2.691	1.131±0.034	1.009±0.020	8.1062±3.084
3	24.005±4.900	1.184±0.036	1.009±0.020	28.691±5.947
4	23.000±4.796	1.264±0.038	1.009±0.020	29.337±6.208
5	20.000±4.472	1.336±0.040	1.009±0.020	26.969±6.108
6	20.000±4.472	1.412±0.042	1.009±0.020	28.495±6.454
7	7.0000±2.646	1.497±0.045	1.010±0.020	10.583±4.018
8	15.948±4.000	1.589±0.048	1.010±0.020	25.602±6.488

^{32}S Solar Minimum, 25° < θ < 50°

Range	Fit Abundance	Spallation Correction	SOFT Efficiency	Corrected Abundance
2	2195.0±47.32	1.158±0.035	1.009±0.020	2564.0±107.5
3	3357.3±58.47	1.215±0.036	1.009±0.020	4115.3±164.4
4	2375.5±49.06	1.294±0.039	1.009±0.020	3102.4±128.6
5	1678.3±41.36	1.379±0.041	1.009±0.020	2335.8±101.8
6	1115.7±33.78	1.468±0.044	1.009±0.020	1652.6±77.69
7	816.88±28.90	1.559±0.047	1.010±0.020	1286.7±64.89
8	676.65±26.50	1.658±0.050	1.010±0.020	1133.0±60.23

^{33}S Solar Minimum, 25° < θ < 50°

Range	Fit Abundance	Spallation Correction	SOFT Efficiency	Corrected Abundance
2	336.74±19.87	1.161±0.035	1.009±0.020	394.46±27.26
3	538.94±24.70	1.221±0.037	1.009±0.020	664.02±38.68
4	416.47±21.60	1.301±0.039	1.009±0.020	546.91±34.51
5	337.95±19.60	1.384±0.042	1.009±0.020	472.11±32.21
6	248.33±16.80	1.477±0.044	1.009±0.020	370.15±28.36
7	190.18±14.65	1.578±0.047	1.010±0.020	303.19±25.78
8	138.96±12.89	1.677±0.050	1.010±0.020	235.40±23.41

^{34}S Solar Minimum, 25° < θ < 50°

Range	Fit Abundance	Spallation Correction	SOFT Efficiency	Corrected Abundance
2	425.12±21.23	1.165±0.035	1.009±0.020	499.67±30.75
3	725.95±27.36	1.224±0.037	1.009±0.020	896.92±46.72
4	492.38±22.85	1.305±0.039	1.009±0.020	648.56±38.07
5	384.60±20.18	1.392±0.042	1.009±0.020	540.19±34.36
6	274.82±17.03	1.484±0.045	1.009±0.020	411.43±29.48
7	233.90±15.61	1.580±0.047	1.010±0.020	373.40±28.31
8	164.68±13.16	1.688±0.051	1.010±0.020	280.74±24.60

^{36}S Solar Minimum, $25^\circ < \theta < 50^\circ$

Range	Fit Abundance	Spallation Correction	SOFT Efficiency	Corrected Abundance
2	25.099±5.020	1.167±0.035	1.009±0.020	29.569±6.009
3	27.795±5.329	1.236±0.037	1.009±0.020	34.670±6.763
4	28.696±5.400	1.315±0.039	1.009±0.020	38.086±7.297
5	31.176±5.607	1.400±0.042	1.009±0.020	44.029±8.076
6	10.106±3.195	1.496±0.045	1.009±0.020	15.257±4.855
7	11.037±3.328	1.574±0.047	1.010±0.020	17.547±5.328
8	8.7055±2.999	1.676±0.050	1.010±0.020	14.742±5.106

^{32}S Solar Maximum, $0^\circ < \theta < 25^\circ$

Range	Fit Abundance	Spallation Correction	SOFT Efficiency	Corrected Abundance
2	805.07±28.45	1.129±0.034	1.009±0.020	917.55±46.25
3	1572.9±39.74	1.176±0.035	1.009±0.020	1866.6±82.03
4	1425.0±37.81	1.242±0.037	1.009±0.020	1785.8±79.80
5	1248.2±35.39	1.312±0.039	1.009±0.020	1652.9±75.69
6	1017.6±31.95	1.387±0.042	1.009±0.020	1424.1±67.98
7	937.87±30.65	1.464±0.044	1.010±0.020	1386.7±67.37
8	895.65±30.01	1.550±0.047	1.010±0.020	1402.5±68.92

^{33}S Solar Maximum, $0^\circ < \theta < 25^\circ$

Range	Fit Abundance	Spallation Correction	SOFT Efficiency	Corrected Abundance
2	180.13±13.62	1.132±0.034	1.009±0.020	205.72±17.22
3	365.14±19.40	1.178±0.035	1.009±0.020	434.21±27.85
4	311.52±17.88	1.248±0.037	1.009±0.020	392.43±26.58
5	272.65±16.76	1.317±0.040	1.009±0.020	362.29±25.80
6	268.79±16.54	1.394±0.042	1.009±0.020	378.20±26.96
7	230.57±15.27	1.474±0.044	1.010±0.020	343.22±25.87
8	221.11±15.08	1.559±0.047	1.010±0.020	348.23±26.85

^{34}S Solar Maximum, $0^\circ < \theta < 25^\circ$

Range	Fit Abundance	Spallation Correction	SOFT Efficiency	Corrected Abundance
2	194.63±14.02	1.136±0.034	1.009±0.020	223.08±17.95
3	416.98±20.55	1.183±0.036	1.009±0.020	497.97±30.38
4	394.49±19.96	1.250±0.038	1.009±0.020	497.77±30.90
5	335.13±18.43	1.322±0.040	1.009±0.020	447.18±29.38
6	287.64±17.01	1.400±0.042	1.009±0.020	406.39±28.12
7	252.56±15.92	1.481±0.044	1.010±0.020	377.78±27.41
8	248.35±15.81	1.567±0.047	1.010±0.020	393.20±28.75

^{36}S Solar Maximum, $0^\circ < \theta < 25^\circ$

Range	Fit Abundance	Spallation Correction	SOFT Efficiency	Corrected Abundance
2	12.170±3.517	1.131±0.034	1.009±0.020	13.886±4.044
3	26.015±5.102	1.184±0.036	1.009±0.020	31.094±6.200
4	20.002±4.472	1.264±0.038	1.009±0.020	25.513±5.778
5	30.000±5.477	1.336±0.040	1.009±0.020	40.453±7.528
6	19.000±4.359	1.412±0.042	1.009±0.020	27.070±6.286
7	21.000±4.583	1.497±0.045	1.010±0.020	31.749±7.022
8	19.889±4.473	1.589±0.048	1.010±0.020	31.928±7.273

^{32}S Solar Maximum, $25^\circ < \theta < 50^\circ$

Range	Fit Abundance	Spallation Correction	SOFT Efficiency	Corrected Abundance
2	1494.7±39.24	1.158±0.035	1.009±0.020	1746.0±77.74
3	2494.7±50.46	1.215±0.036	1.009±0.020	3058.0±126.2
4	1846.8±43.31	1.294±0.039	1.009±0.020	2412.0±103.5
5	1400.0±37.92	1.379±0.041	1.009±0.020	1948.4±87.71
6	992.29±32.07	1.468±0.044	1.009±0.020	1469.8±71.06
7	808.36±28.72	1.559±0.047	1.010±0.020	1273.3±64.36
8	614.62±25.26	1.658±0.050	1.010±0.020	1029.1±56.19

^{33}S Solar Maximum, $25^\circ < \theta < 50^\circ$

Range	Fit Abundance	Spallation Correction	SOFT Efficiency	Corrected Abundance
2	332.34±19.79	1.161±0.035	1.009±0.020	389.31±27.08
3	499.71±23.82	1.221±0.037	1.009±0.020	615.69±36.76
4	450.84±22.29	1.301±0.039	1.009±0.020	592.06±36.19
5	333.48±19.54	1.384±0.042	1.009±0.020	465.87±32.03
6	239.95±16.75	1.477±0.044	1.009±0.020	357.65±28.09
7	178.45±14.31	1.578±0.047	1.010±0.020	284.49±25.00
8	192.96±14.86	1.677±0.050	1.010±0.020	326.88±27.78

^{34}S Solar Maximum, $25^\circ < \theta < 50^\circ$

Range	Fit Abundance	Spallation Correction	SOFT Efficiency	Corrected Abundance
2	343.76±19.24	1.165±0.035	1.009±0.020	404.04±26.87
3	674.64±26.57	1.224±0.037	1.009±0.020	833.53±44.45
4	499.28±22.92	1.305±0.039	1.009±0.020	657.64±38.35
5	398.10±20.39	1.392±0.042	1.009±0.020	559.14±34.99
6	305.76±17.88	1.484±0.045	1.009±0.020	457.74±31.42
7	248.13±16.21	1.580±0.047	1.010±0.020	396.12±29.53
8	187.44±14.04	1.688±0.051	1.010±0.020	319.54±26.55

^{36}S Solar Maximum, 25° < θ < 50°

Range	Fit Abundance	Spallation Correction	SOFT Efficiency	Corrected Abundance
2	22.147±4.720	1.167±0.035	1.009±0.020	26.091±5.639
3	54.916±7.416	1.236±0.037	1.009±0.020	68.499±9.573
4	33.044±5.753	1.315±0.039	1.009±0.020	43.856±7.796
5	22.475±4.784	1.400±0.042	1.009±0.020	31.740±6.852
6	18.998±4.359	1.496±0.045	1.009±0.020	28.680±6.661
7	14.057±3.760	1.574±0.047	1.010±0.020	22.348±6.031
8	11.973±3.465	1.676±0.050	1.010±0.020	20.275±5.912

Table B.2: Measured and corrected counts of the four isotopes of sulfur for solar minimum and solar maximum, separated into low-angle and high-angle data sets.

B.3 Argon

^{36}Ar Solar Minimum, $0° < \theta < 25°$

Range	Fit Abundance	Spallation Correction	SOFT Efficiency	Corrected Abundance
2	272.57±16.61	1.140±0.034	1.009±0.020	313.58±22.19
3	475.83±21.98	1.188±0.036	1.009±0.020	570.40±33.39
4	385.73±19.75	1.260±0.038	1.009±0.020	490.59±30.69
5	326.52±18.19	1.335±0.040	1.009±0.020	439.96±29.17
6	279.05±16.74	1.414±0.042	1.009±0.020	398.26±27.86
7	243.32±15.66	1.497±0.045	1.009±0.020	367.65±27.10
8	222.00±14.94	1.587±0.048	1.009±0.020	355.47±27.13

^{37}Ar Solar Minimum, $0° < \theta < 25°$

Range	Fit Abundance	Spallation Correction	SOFT Efficiency	Corrected Abundance
2	128.97±11.63	1.142±0.034	1.009±0.020	148.69±14.44
3	228.67±15.56	1.194±0.036	1.009±0.020	275.44±21.19
4	225.56±15.27	1.265±0.038	1.009±0.020	287.95±22.08
5	177.80±13.62	1.339±0.040	1.009±0.020	240.27±20.33
6	174.13±13.41	1.419±0.043	1.009±0.020	249.28±21.18
7	141.97±12.10	1.505±0.045	1.009±0.020	215.58±19.94
8	128.93±11.50	1.598±0.048	1.009±0.020	207.91±19.99

^{38}Ar Solar Minimum, $0° < \theta < 25°$

Range	Fit Abundance	Spallation Correction	SOFT Efficiency	Corrected Abundance
2	216.35±14.84	1.146±0.034	1.009±0.020	250.11±19.37
3	489.54±22.31	1.197±0.036	1.009±0.020	591.25±34.32
4	385.63±19.74	1.268±0.038	1.009±0.020	493.38±30.87
5	357.65±19.02	1.344±0.040	1.009±0.020	484.92±31.13
6	273.88±16.69	1.426±0.043	1.009±0.020	394.15±27.89
7	216.74±14.83	1.513±0.045	1.009±0.020	330.80±25.57
8	255.05±16.04	1.608±0.048	1.009±0.020	413.85±29.98

^{40}Ar Solar Minimum, $0^\circ < \theta < 25^\circ$

Range	Fit Abundance	Spallation Correction	SOFT Efficiency	Corrected Abundance
2	31.123±5.590	1.152±0.035	1.009±0.020	36.178±6.627
3	51.029±7.146	1.203±0.036	1.009±0.020	61.966±8.959
4	46.066±6.792	1.272±0.038	1.009±0.020	59.112±8.971
5	46.009±6.784	1.355±0.041	1.009±0.020	62.888±9.544
6	42.883±6.558	1.439±0.043	1.009±0.020	62.265±9.782
7	25.996±5.098	1.526±0.046	1.009±0.020	40.020±7.979
8	28.998±5.385	1.628±0.049	1.009±0.020	47.633±9.010

^{36}Ar Solar Minimum, $25^\circ < \theta < 50^\circ$

Range	Fit Abundance	Spallation Correction	SOFT Efficiency	Corrected Abundance
2	488.01±22.43	1.170±0.035	1.009±0.020	576.36±33.63
3	709.36±27.31	1.232±0.037	1.009±0.020	881.64±46.45
4	526.71±23.37	1.318±0.040	1.009±0.020	700.39±40.00
5	392.88±20.28	1.405±0.042	1.009±0.020	557.13±35.05
6	251.91±16.15	1.504±0.045	1.009±0.020	382.39±28.10
7	214.34±15.00	1.597±0.048	1.009±0.020	345.43±27.18
8	160.17±13.00	1.706±0.051	1.009±0.020	275.66±24.47

^{37}Ar Solar Minimum, $25^\circ < \theta < 50^\circ$

Range	Fit Abundance	Spallation Correction	SOFT Efficiency	Corrected Abundance
2	234.60±16.23	1.175±0.035	1.009±0.020	278.21±21.69
3	388.94±21.50	1.239±0.037	1.009±0.020	486.39±32.07
4	281.47±18.07	1.325±0.040	1.009±0.020	376.23±27.68
5	209.24±15.65	1.419±0.043	1.009±0.020	299.50±24.86
6	158.58±13.39	1.514±0.045	1.009±0.020	242.21±22.23
7	126.90±12.18	1.611±0.048	1.009±0.020	206.34±21.15
8	91.794±10.48	1.723±0.052	1.009±0.020	159.60±19.10

^{38}Ar Solar Minimum, $25^\circ < \theta < 50^\circ$

Range	Fit Abundance	Spallation Correction	SOFT Efficiency	Corrected Abundance
2	419.75±20.99	1.178±0.035	1.009±0.020	498.94±30.73
3	806.12±29.38	1.240±0.037	1.009±0.020	1008.5±51.64
4	496.81±23.09	1.327±0.040	1.009±0.020	665.38±39.10
5	409.74±20.83	1.421±0.043	1.009±0.020	587.58±36.59
6	321.92±18.38	1.512±0.045	1.009±0.020	491.21±33.14
7	212.51±15.16	1.615±0.048	1.009±0.020	346.22±27.66
8	175.03±13.82	1.730±0.052	1.009±0.020	305.56±26.52

^{40}Ar Solar Minimum, $25^\circ < \theta < 50^\circ$

Range	Fit Abundance	Spallation Correction	SOFT Efficiency	Corrected Abundance
2	55.616±7.495	1.193±0.036	1.009±0.020	66.952±9.339
3	90.545±9.546	1.252±0.038	1.009±0.020	114.35±12.74
4	63.006±7.939	1.345±0.040	1.009±0.020	85.490±11.20
5	47.179±6.889	1.439±0.043	1.009±0.020	68.493±10.30
6	28.590±5.395	1.544±0.046	1.009±0.020	44.531±8.554
7	30.228±5.516	1.670±0.050	1.009±0.020	50.933±9.473
8	15.010±3.876	1.750±0.053	1.009±0.020	26.511±6.912

^{36}Ar Solar Maximum, $0^\circ < \theta < 25^\circ$

Range	Fit Abundance	Spallation Correction	SOFT Efficiency	Corrected Abundance
2	168.90±13.09	1.140±0.034	1.009±0.020	194.32±16.60
3	398.04±20.09	1.188±0.036	1.009±0.020	477.15±29.57
4	382.75±19.66	1.260±0.038	1.009±0.020	486.80±30.53
5	309.03±17.70	1.335±0.040	1.009±0.020	416.39±28.16
6	302.55±17.50	1.414±0.042	1.009±0.020	431.79±29.41
7	235.85±15.41	1.497±0.045	1.009±0.020	356.37±26.58
8	214.44±14.71	1.587±0.048	1.009±0.020	343.35±26.59

^{37}Ar Solar Maximum, $0^\circ < \theta < 25^\circ$

Range	Fit Abundance	Spallation Correction	SOFT Efficiency	Corrected Abundance
2	118.80±11.10	1.142±0.034	1.009±0.020	136.96±13.71
3	197.17±14.39	1.194±0.036	1.009±0.020	237.50±19.32
4	198.31±14.31	1.265±0.038	1.009±0.020	253.17±20.41
5	204.87±14.57	1.339±0.040	1.009±0.020	276.85±22.06
6	155.59±12.68	1.419±0.043	1.009±0.020	222.73±19.84
7	133.07±11.68	1.505±0.045	1.009±0.020	202.07±19.16
8	119.82±11.09	1.598±0.048	1.009±0.020	193.22±19.18

^{38}Ar Solar Maximum, $0^\circ < \theta < 25^\circ$

Range	Fit Abundance	Spallation Correction	SOFT Efficiency	Corrected Abundance
2	240.64±15.60	1.146±0.034	1.009±0.020	278.18±20.62
3	412.52±20.46	1.197±0.036	1.009±0.020	498.23±30.52
4	366.94±19.24	1.268±0.038	1.009±0.020	469.47±29.85
5	371.54±19.39	1.344±0.040	1.009±0.020	503.74±31.92
6	300.78±17.40	1.426±0.043	1.009±0.020	432.86±29.49
7	277.95±16.74	1.513±0.045	1.009±0.020	424.22±29.76
8	225.75±15.07	1.608±0.048	1.009±0.020	366.30±27.77

^{40}Ar Solar Maximum, $0^\circ < \theta < 25^\circ$

Range	Fit Abundance	Spallation Correction	SOFT Efficiency	Corrected Abundance
2	32.647±5.751	1.152±0.035	1.009±0.020	37.951±6.823
3	54.337±7.409	1.203±0.036	1.009±0.020	65.982±9.305
4	58.014±7.618	1.272±0.038	1.009±0.020	74.445±10.14
5	40.586±6.418	1.355±0.041	1.009±0.020	55.475±8.996
6	42.103±6.496	1.439±0.043	1.009±0.020	61.132±9.685
7	37.162±6.129	1.526±0.046	1.009±0.020	57.209±9.657
8	34.999±5.916	1.628±0.049	1.009±0.020	57.490±9.935

^{36}Ar Solar Maximum, $25^\circ < \theta < 50^\circ$

Range	Fit Abundance	Spallation Correction	SOFT Efficiency	Corrected Abundance
2	343.95±18.92	1.170±0.035	1.009±0.020	406.22±26.70
3	651.22±26.22	1.232±0.037	1.009±0.020	809.37±43.69
4	495.12±22.82	1.318±0.040	1.009±0.020	658.39±38.48
5	368.29±19.87	1.405±0.042	1.009±0.020	522.27±33.86
6	241.39±15.95	1.504±0.045	1.009±0.020	366.42±27.57
7	212.86±15.12	1.597±0.048	1.009±0.020	343.04±27.31
8	166.59±13.19	1.706±0.051	1.009±0.020	286.71±24.94

^{37}Ar Solar Maximum, $25^\circ < \theta < 50^\circ$

Range	Fit Abundance	Spallation Correction	SOFT Efficiency	Corrected Abundance
2	204.55±15.12	1.175±0.035	1.009±0.020	242.57±19.94
3	373.97±20.80	1.239±0.037	1.009±0.020	467.66±30.98
4	274.42±17.86	1.325±0.040	1.009±0.020	366.80±27.27
5	198.54±15.38	1.419±0.043	1.009±0.020	284.18±24.27
6	141.98±12.87	1.514±0.045	1.009±0.020	216.85±21.14
7	135.62±12.62	1.611±0.048	1.009±0.020	220.51±22.01
8	110.41±11.12	1.723±0.052	1.009±0.020	191.95±20.53

^{38}Ar Solar Maximum, $25^\circ < \theta < 50^\circ$

Range	Fit Abundance	Spallation Correction	SOFT Efficiency	Corrected Abundance
2	405.23±20.50	1.178±0.035	1.009±0.020	481.68±29.90
3	675.87±26.66	1.240±0.037	1.009±0.020	845.58±45.13
4	533.60±23.74	1.327±0.040	1.009±0.020	714.64±40.88
5	385.09±20.22	1.421±0.043	1.009±0.020	552.24±35.14
6	267.18±16.85	1.512±0.045	1.009±0.020	407.69±29.59
7	214.21±15.16	1.615±0.048	1.009±0.020	348.99±27.71
8	193.42±14.21	1.730±0.052	1.009±0.020	337.67±27.61

^{40}Ar Solar Maximum, $25^\circ < \theta < 50^\circ$

Range	Fit Abundance	Spallation Correction	SOFT Efficiency	Corrected Abundance
2	40.256±6.429	1.193±0.036	1.009±0.020	48.461±7.933
3	96.962±9.880	1.252±0.038	1.009±0.020	122.46±13.23
4	75.879±8.720	1.345±0.040	1.009±0.020	102.96±12.40
5	50.078±7.082	1.439±0.043	1.009±0.020	72.703±10.61
6	38.442±6.229	1.544±0.046	1.009±0.020	59.876±9.938
7	24.326±4.964	1.670±0.050	1.009±0.020	40.990±8.493
8	30.586±5.562	1.750±0.053	1.009±0.020	54.022±10.01

Table B.3: Measured and corrected counts of the four isotopes of argon for solar minimum and solar maximum, separated into low-angle and high-angle data sets.

B.4 Calcium

^{40}Ca Solar Minimum, $0° < \theta < 25°$

Range	Fit Abundance	Spallation Correction	SOFT Efficiency	Corrected Abundance
2	585.86±24.43	1.150±0.035	1.009±0.020	679.98±37.44
3	1095.5±33.41	1.202±0.036	1.009±0.020	1329.0±62.66
4	882.15±29.68	1.278±0.038	1.009±0.020	1137.7±56.02
5	693.06±26.87	1.356±0.041	1.009±0.020	948.21±50.14
6	570.57±24.02	1.441±0.043	1.009±0.020	829.51±45.93
7	454.24±21.36	1.530±0.046	1.009±0.020	701.50±41.53
8	398.53±20.11	1.629±0.049	1.009±0.020	655.14±40.59

^{41}Ca Solar Minimum, $0° < \theta < 25°$

Range	Fit Abundance	Spallation Correction	SOFT Efficiency	Corrected Abundance
2	114.18±11.31	1.152±0.035	1.009±0.020	132.74±13.99
3	234.71±16.10	1.208±0.036	1.009±0.020	286.08±22.15
4	197.41±14.61	1.282±0.038	1.009±0.020	255.39±21.02
5	183.41±14.31	1.363±0.041	1.009±0.020	252.17±21.66
6	150.10±12.65	1.448±0.043	1.009±0.020	219.36±20.10
7	135.70±11.97	1.541±0.046	1.009±0.020	211.00±20.10
8	112.84±11.05	1.636±0.049	1.009±0.020	186.23±19.43

^{42}Ca Solar Minimum, $0° < \theta < 25°$

Range	Fit Abundance	Spallation Correction	SOFT Efficiency	Corrected Abundance
2	251.25±16.23	1.156±0.035	1.009±0.020	293.06±21.66
3	514.53±23.19	1.208±0.036	1.009±0.020	627.36±36.17
4	420.69±20.93	1.285±0.039	1.009±0.020	545.29±33.47
5	350.46±19.14	1.366±0.041	1.009±0.020	483.17±31.60
6	308.52±17.88	1.453±0.044	1.009±0.020	452.43±30.86
7	261.27±16.63	1.548±0.046	1.009±0.020	408.02±29.82
8	227.72±15.38	1.647±0.049	1.009±0.020	378.46±28.96

^{43}Ca Solar Minimum, $0^\circ < \theta < 25^\circ$

Range	Fit Abundance	Spallation Correction	SOFT Efficiency	Corrected Abundance
2	273.31±16.95	1.159±0.035	1.009±0.020	319.59±22.91
3	544.67±24.04	1.213±0.036	1.009±0.020	666.59±37.95
4	416.47±21.02	1.289±0.039	1.009±0.020	541.75±33.57
5	362.66±19.33	1.372±0.041	1.009±0.020	502.18±32.28
6	331.08±18.61	1.459±0.044	1.009±0.020	487.28±32.51
7	276.96±17.03	1.550±0.046	1.009±0.020	433.11±30.85
8	259.55±16.43	1.658±0.050	1.009±0.020	434.19±31.60

^{44}Ca Solar Minimum, $0^\circ < \theta < 25^\circ$

Range	Fit Abundance	Spallation Correction	SOFT Efficiency	Corrected Abundance
2	291.63±17.36	1.161±0.035	1.009±0.020	341.53±23.75
3	584.35±24.61	1.216±0.036	1.009±0.020	716.88±39.70
4	462.50±21.97	1.291±0.039	1.009±0.020	602.63±35.90
5	426.61±21.03	1.374±0.041	1.009±0.020	591.59±36.10
6	333.78±18.54	1.465±0.044	1.009±0.020	493.32±32.64
7	284.51±17.12	1.560±0.047	1.009±0.020	447.74±31.39
8	255.49±16.18	1.665±0.050	1.009±0.020	429.23±31.25

^{46}Ca Solar Minimum, $0^\circ < \theta < 25^\circ$

Range	Fit Abundance	Spallation Correction	SOFT Efficiency	Corrected Abundance
2	4.7430±2.664	1.168±0.035	1.009±0.020	5.5921±3.147
3	13.017±3.611	1.223±0.037	1.009±0.020	16.067±4.494
4	2.8942±2.046	1.299±0.039	1.009±0.020	3.7932±2.686
5	8.8548±3.615	1.376±0.041	1.009±0.020	12.291±5.037
6	2.0306±1.438	1.470±0.044	1.009±0.020	3.0117±2.136
7	9.9560±3.520	1.579±0.047	1.009±0.020	15.862±5.637
8	6.0203±2.458	1.686±0.051	1.009±0.020	10.241±4.197

^{40}Ca Solar Minimum, $25^\circ < \theta < 50^\circ$

Range	Fit Abundance	Spallation Correction	SOFT Efficiency	Corrected Abundance
2	1053.2±33.25	1.183±0.036	1.009±0.020	1257.7±60.18
3	1662.0±42.00	1.247±0.037	1.009±0.020	2092.1±91.94
4	1069.0±33.44	1.338±0.040	1.009±0.020	1442.9±68.76
5	726.69±27.80	1.435±0.043	1.009±0.020	1051.9±55.23
6	505.35±23.70	1.536±0.046	1.009±0.020	783.30±46.29
7	402.09±20.82	1.634±0.049	1.009±0.020	663.03±41.80
8	283.46±17.51	1.743±0.052	1.009±0.020	498.50±35.63

^{41}Ca Solar Minimum, 25° $< \theta <$ 50°

Range	Fit Abundance	Spallation Correction	SOFT Efficiency	Corrected Abundance
2	230.40±17.13	1.187±0.036	1.009±0.020	276.05±22.80
3	366.49±21.42	1.254±0.038	1.009±0.020	463.71±31.82
4	255.07±17.96	1.348±0.040	1.009±0.020	346.85±27.42
5	192.10±15.72	1.442±0.043	1.009±0.020	279.44±24.98
6	142.26±13.84	1.547±0.046	1.009±0.020	222.03±23.03
7	94.963±11.43	1.649±0.049	1.009±0.020	157.98±19.85
8	92.440±11.07	1.777±0.053	1.009±0.020	165.78±20.73

^{42}Ca Solar Minimum, 25° $< \theta <$ 50°

Range	Fit Abundance	Spallation Correction	SOFT Efficiency	Corrected Abundance
2	474.23±23.43	1.191±0.036	1.009±0.020	569.84±34.82
3	768.04±29.75	1.256±0.038	1.009±0.020	973.71±51.46
4	552.39±25.52	1.348±0.040	1.009±0.020	751.51±44.00
5	433.97±22.88	1.450±0.044	1.009±0.020	635.01±40.53
6	318.46±19.32	1.553±0.047	1.009±0.020	499.05±35.20
7	219.35±15.79	1.657±0.050	1.009±0.020	366.84±29.52
8	151.33±13.84	1.788±0.054	1.009±0.020	273.00±26.83

^{43}Ca Solar Minimum, 25° $< \theta <$ 50°

Range	Fit Abundance	Spallation Correction	SOFT Efficiency	Corrected Abundance
2	499.67±24.84	1.197±0.036	1.009±0.020	603.40±37.02
3	874.54±32.90	1.261±0.038	1.009±0.020	1113.2±57.93
4	569.78±26.17	1.351±0.041	1.009±0.020	776.71±45.31
5	410.99±22.77	1.455±0.044	1.009±0.020	603.42±39.85
6	310.47±19.64	1.560±0.047	1.009±0.020	488.81±35.57
7	242.27±17.01	1.672±0.050	1.009±0.020	408.74±32.25
8	182.09±14.97	1.802±0.054	1.009±0.020	331.15±29.72

^{44}Ca Solar Minimum, 25° $< \theta <$ 50°

Range	Fit Abundance	Spallation Correction	SOFT Efficiency	Corrected Abundance
2	526.65±24.76	1.199±0.036	1.009±0.020	637.10±37.71
3	880.30±31.66	1.265±0.038	1.009±0.020	1123.9±57.15
4	614.37±26.11	1.358±0.041	1.009±0.020	842.00±46.87
5	458.14±22.94	1.459±0.044	1.009±0.020	674.47±41.57
6	304.22±19.00	1.566±0.047	1.009±0.020	480.87±34.65
7	253.20±17.04	1.676±0.050	1.009±0.020	428.33±32.69
8	181.87±14.17	1.800±0.054	1.009±0.020	330.32±28.35

^{46}Ca Solar Minimum, $25° < \theta < 50°$

Range	Fit Abundance	Spallation Correction	SOFT Efficiency	Corrected Abundance
2	7.9344±2.863	1.203±0.036	1.009±0.020	9.6312±3.492
3	10.723±4.020	1.247±0.037	1.009±0.020	13.494±5.082
4	10.420±3.650	1.354±0.041	1.009±0.020	14.231±5.011
5	7.1244±2.693	1.497±0.045	1.009±0.020	10.765±4.087
6	3.4559±2.035	1.559±0.047	1.009±0.020	5.4360±3.207
7	2.2974±1.680	1.655±0.050	1.009±0.020	3.8364±2.808
8	4.0673±2.034	1.834±0.055	1.009±0.020	7.5286±3.774

^{40}Ca Solar Maximum, $0° < \theta < 25°$

Range	Fit Abundance	Spallation Correction	SOFT Efficiency	Corrected Abundance
2	372.58±19.44	1.150±0.035	1.009±0.020	432.44±27.40
3	767.71±28.39	1.202±0.036	1.009±0.020	931.36±48.04
4	658.72±25.75	1.278±0.038	1.009±0.020	849.57±45.12
5	528.46±23.15	1.356±0.041	1.009±0.020	723.02±40.97
6	480.04±21.94	1.441±0.043	1.009±0.020	697.90±40.58
7	422.66±20.62	1.530±0.046	1.009±0.020	652.73±39.56
8	414.34±20.48	1.629±0.049	1.009±0.020	681.12±41.63

^{41}Ca Solar Maximum, $0° < \theta < 25°$

Range	Fit Abundance	Spallation Correction	SOFT Efficiency	Corrected Abundance
2	111.08±10.86	1.152±0.035	1.009±0.020	129.14±13.45
3	211.65±15.06	1.208±0.036	1.009±0.020	257.97±20.56
4	159.22±12.98	1.282±0.038	1.009±0.020	205.99±18.36
5	155.26±13.46	1.363±0.041	1.009±0.020	213.47±20.04
6	142.84±12.18	1.448±0.043	1.009±0.020	208.75±19.32
7	132.26±11.69	1.541±0.046	1.009±0.020	205.65±19.62
8	115.07±11.13	1.636±0.049	1.009±0.020	189.92±19.60

^{42}Ca Solar Maximum, $0° < \theta < 25°$

Range	Fit Abundance	Spallation Correction	SOFT Efficiency	Corrected Abundance
2	230.60±15.48	1.156±0.035	1.009±0.020	268.97±20.48
3	465.74±22.47	1.208±0.036	1.009±0.020	567.88±34.17
4	399.59±20.35	1.285±0.039	1.009±0.020	517.95±32.29
5	343.95±18.86	1.366±0.041	1.009±0.020	474.21±31.09
6	319.22±18.25	1.453±0.044	1.009±0.020	468.12±31.62
7	253.09±16.12	1.548±0.046	1.009±0.020	395.25±28.91
8	265.47±16.52	1.647±0.049	1.009±0.020	441.19±31.72

^{43}Ca Solar Maximum, $0^\circ < \theta < 25^\circ$

Range	Fit Abundance	Spallation Correction	SOFT Efficiency	Corrected Abundance
2	238.60±15.87	1.159±0.035	1.009±0.020	279.01±21.10
3	442.68±21.65	1.213±0.036	1.009±0.020	541.77±32.89
4	429.19±21.23	1.289±0.039	1.009±0.020	558.31±34.14
5	367.38±19.74	1.372±0.041	1.009±0.020	508.72±32.89
6	309.19±18.08	1.459±0.044	1.009±0.020	455.07±31.24
7	294.41±17.49	1.550±0.046	1.009±0.020	460.40±31.97
8	282.41±17.22	1.658±0.050	1.009±0.020	472.43±33.45

^{44}Ca Solar Maximum, $0^\circ < \theta < 25^\circ$

Range	Fit Abundance	Spallation Correction	SOFT Efficiency	Corrected Abundance
2	269.21±16.67	1.161±0.035	1.009±0.020	315.28±22.58
3	575.44±24.34	1.216±0.036	1.009±0.020	705.95±39.19
4	412.53±20.64	1.291±0.039	1.009±0.020	537.53±33.12
5	352.77±18.97	1.374±0.041	1.009±0.020	489.19±31.65
6	319.75±18.19	1.465±0.044	1.009±0.020	472.58±31.80
7	312.79±17.90	1.560±0.047	1.009±0.020	492.24±33.27
8	269.08±16.63	1.665±0.050	1.009±0.020	452.06±32.32

^{46}Ca Solar Maximum, $0^\circ < \theta < 25^\circ$

Range	Fit Abundance	Spallation Correction	SOFT Efficiency	Corrected Abundance
2	4.0282±2.014	1.168±0.035	1.009±0.020	4.7493±2.381
3	16.506±5.608	1.223±0.037	1.009±0.020	20.373±6.960
4	10.025±3.171	1.299±0.039	1.009±0.020	13.139±4.183
5	3.1954±1.598	1.376±0.041	1.009±0.020	4.4355±2.223
6	4.8247±2.414	1.470±0.044	1.009±0.020	7.1557±3.590
7	2.0038±1.417	1.579±0.047	1.009±0.020	3.1925±2.260
8	3.8083±2.199	1.686±0.051	1.009±0.020	6.4782±3.747

^{40}Ca Solar Maximum, $25^\circ < \theta < 50^\circ$

Range	Fit Abundance	Spallation Correction	SOFT Efficiency	Corrected Abundance
2	675.06±26.63	1.183±0.036	1.009±0.020	806.11±43.03
3	1100.6±34.38	1.247±0.037	1.009±0.020	1385.4±65.98
4	927.93±31.56	1.338±0.040	1.009±0.020	1252.5±61.99
5	609.94±25.48	1.435±0.043	1.009±0.020	882.92±48.66
6	429.92±21.52	1.536±0.046	1.009±0.020	666.39±41.07
7	314.75±18.49	1.634±0.049	1.009±0.020	519.00±35.74
8	260.95±17.02	1.743±0.052	1.009±0.020	458.93±34.18

^{41}Ca Solar Maximum, 25° $< \theta <$ 50°

Range	Fit Abundance	Spallation Correction	SOFT Efficiency	Corrected Abundance
2	182.95±15.05	1.187±0.036	1.009±0.020	219.21±19.68
3	349.06±21.07	1.254±0.038	1.009±0.020	441.66±31.03
4	256.62±17.95	1.348±0.040	1.009±0.020	348.95±27.45
5	179.63±15.20	1.442±0.043	1.009±0.020	261.30±24.03
6	138.62±13.32	1.547±0.046	1.009±0.020	216.36±22.19
7	112.85±12.00	1.649±0.049	1.009±0.020	187.73±21.07
8	87.954±10.99	1.777±0.053	1.009±0.020	157.74±20.51

^{42}Ca Solar Maximum, 25° $< \theta <$ 50°

Range	Fit Abundance	Spallation Correction	SOFT Efficiency	Corrected Abundance
2	388.85±21.36	1.191±0.036	1.009±0.020	467.26±30.68
3	758.28±29.80	1.256±0.038	1.009±0.020	961.34±51.21
4	560.25±25.53	1.348±0.040	1.009±0.020	762.21±44.24
5	417.21±21.83	1.450±0.044	1.009±0.020	610.48±38.76
6	314.89±19.22	1.553±0.047	1.009±0.020	493.44±34.96
7	232.55±16.62	1.657±0.050	1.009±0.020	388.91±31.11
8	192.02±15.39	1.788±0.054	1.009±0.020	346.41±30.42

^{43}Ca Solar Maximum, 25° $< \theta <$ 50°

Range	Fit Abundance	Spallation Correction	SOFT Efficiency	Corrected Abundance
2	455.47±23.46	1.197±0.036	1.009±0.020	550.03±34.55
3	783.94±30.52	1.261±0.038	1.009±0.020	997.85±52.88
4	593.84±27.50	1.351±0.041	1.009±0.020	809.50±47.46
5	384.42±21.98	1.455±0.044	1.009±0.020	564.41±38.13
6	271.89±18.61	1.560±0.047	1.009±0.020	428.07±33.10
7	231.27±16.81	1.672±0.050	1.009±0.020	390.18±31.65
8	188.53±15.19	1.802±0.054	1.009±0.020	342.86±30.25

^{44}Ca Solar Maximum, 25° $< \theta <$ 50°

Range	Fit Abundance	Spallation Correction	SOFT Efficiency	Corrected Abundance
2	443.79±22.47	1.199±0.036	1.009±0.020	536.86±33.34
3	808.80±30.27	1.265±0.038	1.009±0.020	1032.6±53.59
4	576.50±26.09	1.358±0.041	1.009±0.020	790.09±45.67
5	425.02±22.57	1.459±0.044	1.009±0.020	625.71±40.13
6	324.81±19.39	1.566±0.047	1.009±0.020	513.41±35.78
7	230.58±16.09	1.676±0.050	1.009±0.020	390.06±30.62
8	188.14±14.50	1.800±0.054	1.009±0.020	341.72±29.06

^{46}Ca Solar Maximum, $25° < \theta < 50°$

Range	Fit Abundance	Spallation Correction	SOFT Efficiency	Corrected Abundance
2	12.317±4.038	1.203±0.036	1.009±0.020	14.951±4.930
3	6.5876±2.899	1.247±0.037	1.009±0.020	8.2900±3.660
4	10.634±3.559	1.354±0.041	1.009±0.020	14.525±4.889
5	11.518±3.455	1.497±0.045	1.009±0.020	17.403±5.258
6	8.0665±2.852	1.559±0.047	1.009±0.020	12.689±4.510
7	1.0133±1.013	1.655±0.050	1.009±0.020	1.6921±1.693
8	5.9350±2.631	1.834±0.055	1.009±0.020	10.986±4.887

Table B.4: Measured and corrected counts of six isotopes of calcium for solar minimum and solar maximum, separated into low-angle and high-angle data sets.

Appendix C

Ratio Tables

C.1 Phosphorus ratios

^{31}P/^{32}S Solar Minimum

Range	Angles	Spectral Correction	Ratio	Ratio: $0° < \theta < 50°$
2	$0° < \theta < 25°$	1.119	0.211±0.019	0.209±0.012
2	$25° < \theta < 50°$	1.115	0.208±0.015	
3	$0° < \theta < 25°$	1.100	0.256±0.018	0.256±0.012
3	$25° < \theta < 50°$	1.095	0.256±0.017	
4	$0° < \theta < 25°$	1.084	0.236±0.018	0.242±0.012
4	$25° < \theta < 50°$	1.079	0.246±0.017	
5	$0° < \theta < 25°$	1.072	0.246±0.019	0.248±0.014
5	$25° < \theta < 50°$	1.067	0.250±0.019	
6	$0° < \theta < 25°$	1.063	0.259±0.021	0.252±0.015
6	$25° < \theta < 50°$	1.058	0.245±0.021	
7	$0° < \theta < 25°$	1.055	0.227±0.020	0.250±0.016
7	$25° < \theta < 50°$	1.050	0.277±0.025	
8	$0° < \theta < 25°$	1.049	0.253±0.022	0.278±0.018
8	$25° < \theta < 50°$	1.044	0.312±0.030	

^{31}P/^{32}S Solar Maximum

Range	Angles	Spectral Correction	Ratio	Ratio: $0° < \theta < 50°$
2	$0° < \theta < 25°$	1.110	0.264±0.025	0.268±0.016
2	$25° < \theta < 50°$	1.109	0.270±0.021	
3	$0° < \theta < 25°$	1.105	0.283±0.021	0.290±0.015
3	$25° < \theta < 50°$	1.104	0.295±0.020	
4	$0° < \theta < 25°$	1.101	0.276±0.022	0.295±0.016
4	$25° < \theta < 50°$	1.100	0.308±0.022	
5	$0° < \theta < 25°$	1.099	0.271±0.022	0.294±0.016
5	$25° < \theta < 50°$	1.097	0.314±0.024	
6	$0° < \theta < 25°$	1.096	0.314±0.026	0.327±0.019
6	$25° < \theta < 50°$	1.095	0.339±0.028	
7	$0° < \theta < 25°$	1.095	0.327±0.028	0.326±0.020
7	$25° < \theta < 50°$	1.093	0.324±0.029	
8	$0° < \theta < 25°$	1.093	0.335±0.029	0.344±0.022
8	$25° < \theta < 50°$	1.092	0.358±0.034	

^{31}P/^{36}Ar Solar Minimum

Range	Angles	Spectral Correction	Ratio	Ratio: $0° < \theta < 50°$
2	$0° < \theta < 25°$	1.280	1.063±0.110	1.057±0.069
2	$25° < \theta < 50°$	1.269	1.054±0.089	
3	$0° < \theta < 25°$	1.232	1.259±0.103	1.302±0.072
3	$25° < \theta < 50°$	1.220	1.331±0.097	
4	$0° < \theta < 25°$	1.192	1.215±0.107	1.201±0.071
4	$25° < \theta < 50°$	1.179	1.191±0.095	
5	$0° < \theta < 25°$	1.163	1.178±0.110	1.150±0.074
5	$25° < \theta < 50°$	1.150	1.128±0.099	
6	$0° < \theta < 25°$	1.141	1.218±0.118	1.175±0.083
6	$25° < \theta < 50°$	1.128	1.130±0.116	
7	$0° < \theta < 25°$	1.123	1.052±0.110	1.072±0.081
7	$25° < \theta < 50°$	1.111	1.093±0.120	
8	$0° < \theta < 25°$	1.108	1.154±0.123	1.239±0.098
8	$25° < \theta < 50°$	1.096	1.348±0.160	

^{31}P/^{36}Ar Solar Maximum

Range	Angles	Spectral Correction	Ratio	Ratio: $0^\circ < \theta < 50^\circ$
2	$0^\circ < \theta < 25^\circ$	1.260	1.416±0.166	1.348±0.098
2	$25^\circ < \theta < 50^\circ$	1.257	1.316±0.120	
3	$0^\circ < \theta < 25^\circ$	1.249	1.252±0.109	1.255±0.072
3	$25^\circ < \theta < 50^\circ$	1.246	1.257±0.095	
4	$0^\circ < \theta < 25^\circ$	1.240	1.140±0.102	1.215±0.073
4	$25^\circ < \theta < 50^\circ$	1.237	1.270±0.103	
5	$0^\circ < \theta < 25^\circ$	1.233	1.207±0.115	1.266±0.083
5	$25^\circ < \theta < 50^\circ$	1.230	1.312±0.117	
6	$0^\circ < \theta < 25^\circ$	1.227	1.161±0.112	1.326±0.092
6	$25^\circ < \theta < 50^\circ$	1.224	1.521±0.154	
7	$0^\circ < \theta < 25^\circ$	1.223	1.424±0.145	1.383±0.103
7	$25^\circ < \theta < 50^\circ$	1.220	1.341±0.146	
8	$0^\circ < \theta < 25^\circ$	1.219	1.525±0.159	1.482±0.116
8	$25^\circ < \theta < 50^\circ$	1.216	1.430±0.168	

^{31}P/^{40}Ca Solar Minimum

Range	Angles	Spectral Correction	Ratio	Ratio: $0^\circ < \theta < 50^\circ$
2	$0^\circ < \theta < 25^\circ$	1.431	0.548±0.051	0.541±0.032
2	$25^\circ < \theta < 50^\circ$	1.413	0.538±0.042	
3	$0^\circ < \theta < 25^\circ$	1.354	0.593±0.044	0.605±0.030
3	$25^\circ < \theta < 50^\circ$	1.333	0.613±0.041	
4	$0^\circ < \theta < 25^\circ$	1.288	0.566±0.045	0.597±0.032
4	$25^\circ < \theta < 50^\circ$	1.267	0.621±0.046	
5	$0^\circ < \theta < 25^\circ$	1.242	0.584±0.049	0.611±0.036
5	$25^\circ < \theta < 50^\circ$	1.222	0.635±0.051	
6	$0^\circ < \theta < 25^\circ$	1.207	0.619±0.054	0.600±0.038
6	$25^\circ < \theta < 50^\circ$	1.188	0.581±0.054	
7	$0^\circ < \theta < 25^\circ$	1.179	0.579±0.055	0.587±0.040
7	$25^\circ < \theta < 50^\circ$	1.161	0.595±0.059	
8	$0^\circ < \theta < 25^\circ$	1.156	0.654±0.063	0.705±0.050
8	$25^\circ < \theta < 50^\circ$	1.138	0.774±0.082	

$^{31}P/^{40}Ca$ Solar Maximum

Range	Angles	Spectral Correction	Ratio	Ratio: $0° < \theta < 50°$
2	$0° < \theta < 25°$	1.404	0.709±0.073	0.728±0.047
2	$25° < \theta < 50°$	1.400	0.738±0.061	
3	$0° < \theta < 25°$	1.387	0.712±0.057	0.773±0.041
3	$25° < \theta < 50°$	1.382	0.814±0.058	
4	$0° < \theta < 25°$	1.371	0.723±0.060	0.732±0.041
4	$25° < \theta < 50°$	1.366	0.738±0.056	
5	$0° < \theta < 25°$	1.360	0.767±0.067	0.816±0.049
5	$25° < \theta < 50°$	1.355	0.856±0.071	
6	$0° < \theta < 25°$	1.352	0.791±0.071	0.854±0.055
6	$25° < \theta < 50°$	1.346	0.920±0.084	
7	$0° < \theta < 25°$	1.344	0.854±0.079	0.907±0.062
7	$25° < \theta < 50°$	1.339	0.973±0.098	
8	$0° < \theta < 25°$	1.338	0.844±0.078	0.898±0.063
8	$25° < \theta < 50°$	1.333	0.980±0.106	

Table C.1: Phosophorus ratios after spectral corrections

C.2 Sulfur ratios

^{33}S/^{40}Ca Solar Minimum

Range	Angles	Spectral Correction	Ratio	Ratio: $0° < \theta < 50°$
2	$0° < \theta < 25°$	1.299	0.368±0.038	0.393±0.026
2	$25° < \theta < 50°$	1.294	0.406±0.034	
3	$0° < \theta < 25°$	1.278	0.441±0.035	0.418±0.023
3	$25° < \theta < 50°$	1.272	0.404±0.029	
4	$0° < \theta < 25°$	1.259	0.407±0.035	0.445±0.026
4	$25° < \theta < 50°$	1.253	0.475±0.038	
5	$0° < \theta < 25°$	1.246	0.491±0.043	0.526±0.032
5	$25° < \theta < 50°$	1.240	0.556±0.048	
6	$0° < \theta < 25°$	1.236	0.510±0.047	0.545±0.036
6	$25° < \theta < 50°$	1.230	0.581±0.056	
7	$0° < \theta < 25°$	1.227	0.597±0.057	0.578±0.041
7	$25° < \theta < 50°$	1.221	0.558±0.059	
8	$0° < \theta < 25°$	1.220	0.614±0.061	0.597±0.046
8	$25° < \theta < 50°$	1.214	0.573±0.070	

^{33}S/^{40}Ca Solar Maximum

Range	Angles	Spectral Correction	Ratio	Ratio: $0° < \theta < 50°$
2	$0° < \theta < 25°$	1.332	0.634±0.067	0.638±0.043
2	$25° < \theta < 50°$	1.325	0.640±0.056	
3	$0° < \theta < 25°$	1.304	0.608±0.050	0.589±0.033
3	$25° < \theta < 50°$	1.296	0.576±0.044	
4	$0° < \theta < 25°$	1.279	0.591±0.051	0.597±0.035
4	$25° < \theta < 50°$	1.272	0.601±0.047	
5	$0° < \theta < 25°$	1.262	0.632±0.058	0.648±0.041
5	$25° < \theta < 50°$	1.254	0.662±0.058	
6	$0° < \theta < 25°$	1.248	0.676±0.062	0.671±0.045
6	$25° < \theta < 50°$	1.240	0.666±0.066	
7	$0° < \theta < 25°$	1.237	0.650±0.063	0.661±0.048
7	$25° < \theta < 50°$	1.229	0.674±0.075	
8	$0° < \theta < 25°$	1.227	0.627±0.062	0.725±0.054
8	$25° < \theta < 50°$	1.220	0.869±0.098	

^{33}S/^{32}S Solar Minimum

Range	Angles	Spectral Correction	Ratio	Ratio: $0^\circ < \theta < 50^\circ$
2	$0^\circ < \theta < 25^\circ$	1.028	0.143±0.014	0.153±0.010
2	$25^\circ < \theta < 50^\circ$	1.028	0.158±0.013	
3	$0^\circ < \theta < 25^\circ$	1.026	0.188±0.014	0.174±0.009
3	$25^\circ < \theta < 50^\circ$	1.026	0.166±0.012	
4	$0^\circ < \theta < 25^\circ$	1.025	0.164±0.013	0.173±0.010
4	$25^\circ < \theta < 50^\circ$	1.024	0.181±0.014	
5	$0^\circ < \theta < 25^\circ$	1.023	0.197±0.016	0.202±0.012
5	$25^\circ < \theta < 50^\circ$	1.023	0.207±0.017	
6	$0^\circ < \theta < 25^\circ$	1.022	0.201±0.018	0.214±0.013
6	$25^\circ < \theta < 50^\circ$	1.022	0.229±0.021	
7	$0^\circ < \theta < 25^\circ$	1.021	0.218±0.019	0.228±0.015
7	$25^\circ < \theta < 50^\circ$	1.021	0.241±0.024	
8	$0^\circ < \theta < 25^\circ$	1.021	0.219±0.020	0.216±0.015
8	$25^\circ < \theta < 50^\circ$	1.020	0.212±0.024	

^{33}S/^{32}S Solar Maximum

Range	Angles	Spectral Correction	Ratio	Ratio: $0^\circ < \theta < 50^\circ$
2	$0^\circ < \theta < 25^\circ$	1.031	0.231±0.023	0.230±0.015
2	$25^\circ < \theta < 50^\circ$	1.031	0.230±0.019	
3	$0^\circ < \theta < 25^\circ$	1.029	0.239±0.019	0.219±0.012
3	$25^\circ < \theta < 50^\circ$	1.028	0.207±0.015	
4	$0^\circ < \theta < 25^\circ$	1.026	0.226±0.018	0.241±0.013
4	$25^\circ < \theta < 50^\circ$	1.026	0.252±0.019	
5	$0^\circ < \theta < 25^\circ$	1.025	0.225±0.019	0.236±0.014
5	$25^\circ < \theta < 50^\circ$	1.024	0.245±0.020	
6	$0^\circ < \theta < 25^\circ$	1.023	0.272±0.023	0.260±0.016
6	$25^\circ < \theta < 50^\circ$	1.023	0.249±0.023	
7	$0^\circ < \theta < 25^\circ$	1.022	0.253±0.023	0.241±0.016
7	$25^\circ < \theta < 50^\circ$	1.022	0.228±0.023	
8	$0^\circ < \theta < 25^\circ$	1.021	0.254±0.023	0.283±0.019
8	$25^\circ < \theta < 50^\circ$	1.021	0.324±0.033	

^{33}S/^{36}Ar Solar Minimum

Range	Angles	Spectral Correction	Ratio	Ratio: $0° < \theta < 50°$
2	$0° < \theta < 25°$	1.167	0.718±0.080	0.769±0.054
2	$25° < \theta < 50°$	1.164	0.797±0.072	
3	$0° < \theta < 25°$	1.156	0.928±0.080	0.892±0.052
3	$25° < \theta < 50°$	1.152	0.868±0.068	
4	$0° < \theta < 25°$	1.146	0.859±0.080	0.878±0.055
4	$25° < \theta < 50°$	1.142	0.892±0.076	
5	$0° < \theta < 25°$	1.138	0.967±0.093	0.964±0.065
5	$25° < \theta < 50°$	1.135	0.962±0.089	
6	$0° < \theta < 25°$	1.133	0.974±0.099	1.033±0.076
6	$25° < \theta < 50°$	1.130	1.093±0.116	
7	$0° < \theta < 25°$	1.128	1.047±0.111	1.018±0.080
7	$25° < \theta < 50°$	1.125	0.987±0.114	
8	$0° < \theta < 25°$	1.124	1.044±0.114	1.006±0.085
8	$25° < \theta < 50°$	1.121	0.957±0.128	

^{33}S/^{36}Ar Solar Maximum

Range	Angles	Spectral Correction	Ratio	Ratio: $0° < \theta < 50°$
2	$0° < \theta < 25°$	1.185	1.254±0.150	1.172±0.088
2	$25° < \theta < 50°$	1.181	1.132±0.108	
3	$0° < \theta < 25°$	1.170	1.065±0.095	0.953±0.057
3	$25° < \theta < 50°$	1.166	0.887±0.071	
4	$0° < \theta < 25°$	1.157	0.932±0.086	0.992±0.062
4	$25° < \theta < 50°$	1.152	1.036±0.088	
5	$0° < \theta < 25°$	1.147	0.998±0.098	1.010±0.069
5	$25° < \theta < 50°$	1.143	1.019±0.096	
6	$0° < \theta < 25°$	1.140	0.998±0.098	1.049±0.077
6	$25° < \theta < 50°$	1.136	1.109±0.121	
7	$0° < \theta < 25°$	1.134	1.092±0.116	1.016±0.080
7	$25° < \theta < 50°$	1.130	0.937±0.111	
8	$0° < \theta < 25°$	1.129	1.145±0.125	1.207±0.098
8	$25° < \theta < 50°$	1.125	1.282±0.156	

^{34}S/^{32}S Solar Minimum

Range	Angles	Spectral Correction	Ratio	Ratio: $0^\circ < \theta < 50^\circ$
2	$0^\circ < \theta < 25^\circ$	1.054	0.206±0.018	0.205±0.012
2	$25^\circ < \theta < 50^\circ$	1.054	0.205±0.015	
3	$0^\circ < \theta < 25^\circ$	1.054	0.215±0.016	0.224±0.011
3	$25^\circ < \theta < 50^\circ$	1.053	0.230±0.015	
4	$0^\circ < \theta < 25^\circ$	1.053	0.191±0.015	0.208±0.011
4	$25^\circ < \theta < 50^\circ$	1.053	0.220±0.016	
5	$0^\circ < \theta < 25^\circ$	1.053	0.251±0.020	0.247±0.014
5	$25^\circ < \theta < 50^\circ$	1.052	0.243±0.019	
6	$0^\circ < \theta < 25^\circ$	1.052	0.251±0.021	0.256±0.015
6	$25^\circ < \theta < 50^\circ$	1.052	0.262±0.022	
7	$0^\circ < \theta < 25^\circ$	1.052	0.241±0.021	0.270±0.017
7	$25^\circ < \theta < 50^\circ$	1.052	0.305±0.028	
8	$0^\circ < \theta < 25^\circ$	1.052	0.299±0.025	0.283±0.018
8	$25^\circ < \theta < 50^\circ$	1.052	0.261±0.027	

^{34}S/^{32}S Solar Maximum

Range	Angles	Spectral Correction	Ratio	Ratio: $0^\circ < \theta < 50^\circ$
2	$0^\circ < \theta < 25^\circ$	1.078	0.262±0.025	0.253±0.016
2	$25^\circ < \theta < 50^\circ$	1.075	0.249±0.020	
3	$0^\circ < \theta < 25^\circ$	1.067	0.285±0.021	0.288±0.015
3	$25^\circ < \theta < 50^\circ$	1.065	0.290±0.020	
4	$0^\circ < \theta < 25^\circ$	1.058	0.295±0.023	0.291±0.015
4	$25^\circ < \theta < 50^\circ$	1.055	0.288±0.021	
5	$0^\circ < \theta < 25^\circ$	1.052	0.285±0.023	0.293±0.016
5	$25^\circ < \theta < 50^\circ$	1.049	0.301±0.023	
6	$0^\circ < \theta < 25^\circ$	1.047	0.299±0.025	0.312±0.019
6	$25^\circ < \theta < 50^\circ$	1.044	0.325±0.027	
7	$0^\circ < \theta < 25^\circ$	1.043	0.284±0.025	0.303±0.019
7	$25^\circ < \theta < 50^\circ$	1.040	0.324±0.029	
8	$0^\circ < \theta < 25^\circ$	1.039	0.291±0.026	0.304±0.020
8	$25^\circ < \theta < 50^\circ$	1.037	0.322±0.032	

Table C.2: Sulfur ratios after spectral corrections

C.3 Argon ratios

^{37}Ar/^{36}Ar Solar Minimum

Range	Angles	Spectral Correction	Ratio	Ratio: $0° < \theta < 50°$
2	$0° < \theta < 25°$	1.028	0.488±0.059	0.493±0.037
2	$25° < \theta < 50°$	1.028	0.496±0.048	
3	$0° < \theta < 25°$	1.025	0.495±0.048	0.538±0.034
3	$25° < \theta < 50°$	1.024	0.565±0.048	
4	$0° < \theta < 25°$	1.023	0.600±0.059	0.570±0.039
4	$25° < \theta < 50°$	1.022	0.549±0.051	
5	$0° < \theta < 25°$	1.021	0.557±0.060	0.552±0.041
5	$25° < \theta < 50°$	1.020	0.548±0.057	
6	$0° < \theta < 25°$	1.019	0.638±0.070	0.641±0.052
6	$25° < \theta < 50°$	1.018	0.645±0.076	
7	$0° < \theta < 25°$	1.018	0.597±0.071	0.602±0.053
7	$25° < \theta < 50°$	1.017	0.608±0.079	
8	$0° < \theta < 25°$	1.017	0.595±0.073	0.592±0.056
8	$25° < \theta < 50°$	1.016	0.588±0.088	

^{37}Ar/^{36}Ar Solar Maximum

Range	Angles	Spectral Correction	Ratio	Ratio: $0° < \theta < 50°$
2	$0° < \theta < 25°$	1.032	0.727±0.096	0.652±0.054
2	$25° < \theta < 50°$	1.031	0.616±0.065	
3	$0° < \theta < 25°$	1.028	0.512±0.052	0.563±0.037
3	$25° < \theta < 50°$	1.027	0.594±0.051	
4	$0° < \theta < 25°$	1.025	0.533±0.054	0.555±0.039
4	$25° < \theta < 50°$	1.024	0.571±0.054	
5	$0° < \theta < 25°$	1.023	0.680±0.071	0.611±0.046
5	$25° < \theta < 50°$	1.022	0.556±0.060	
6	$0° < \theta < 25°$	1.021	0.527±0.059	0.562±0.047
6	$25° < \theta < 50°$	1.020	0.604±0.074	
7	$0° < \theta < 25°$	1.020	0.578±0.070	0.616±0.054
7	$25° < \theta < 50°$	1.019	0.655±0.084	
8	$0° < \theta < 25°$	1.018	0.573±0.072	0.622±0.058
8	$25° < \theta < 50°$	1.018	0.681±0.094	

^{37}Ar/^{40}Ca Solar Minimum

Range	Angles	Spectral Correction	Ratio	Ratio: $0^\circ < \theta < 50^\circ$
2	$0^\circ < \theta < 25^\circ$	1.147	0.251±0.028	0.252±0.018
2	$25^\circ < \theta < 50^\circ$	1.144	0.253±0.023	
3	$0^\circ < \theta < 25^\circ$	1.132	0.235±0.021	0.252±0.015
3	$25^\circ < \theta < 50^\circ$	1.128	0.262±0.021	
4	$0^\circ < \theta < 25^\circ$	1.119	0.283±0.026	0.287±0.018
4	$25^\circ < \theta < 50^\circ$	1.115	0.291±0.025	
5	$0^\circ < \theta < 25^\circ$	1.109	0.281±0.028	0.299±0.021
5	$25^\circ < \theta < 50^\circ$	1.105	0.315±0.031	
6	$0^\circ < \theta < 25^\circ$	1.102	0.331±0.034	0.335±0.025
6	$25^\circ < \theta < 50^\circ$	1.098	0.339±0.037	
7	$0^\circ < \theta < 25^\circ$	1.096	0.337±0.037	0.338±0.027
7	$25^\circ < \theta < 50^\circ$	1.092	0.340±0.041	
8	$0^\circ < \theta < 25^\circ$	1.090	0.346±0.040	0.347±0.031
8	$25^\circ < \theta < 50^\circ$	1.086	0.348±0.048	

^{37}Ar/^{40}Ca Solar Maximum

Range	Angles	Spectral Correction	Ratio	Ratio: $0^\circ < \theta < 50^\circ$
2	$0^\circ < \theta < 25^\circ$	1.167	0.370±0.044	0.357±0.027
2	$25^\circ < \theta < 50^\circ$	1.163	0.350±0.034	
3	$0^\circ < \theta < 25^\circ$	1.149	0.293±0.028	0.349±0.022
3	$25^\circ < \theta < 50^\circ$	1.144	0.386±0.031	
4	$0^\circ < \theta < 25^\circ$	1.133	0.337±0.033	0.333±0.022
4	$25^\circ < \theta < 50^\circ$	1.127	0.330±0.029	
5	$0^\circ < \theta < 25^\circ$	1.121	0.429±0.042	0.391±0.028
5	$25^\circ < \theta < 50^\circ$	1.116	0.359±0.037	
6	$0^\circ < \theta < 25^\circ$	1.112	0.355±0.038	0.357±0.028
6	$25^\circ < \theta < 50^\circ$	1.107	0.360±0.042	
7	$0^\circ < \theta < 25^\circ$	1.105	0.342±0.038	0.397±0.033
7	$25^\circ < \theta < 50^\circ$	1.100	0.467±0.057	
8	$0^\circ < \theta < 25^\circ$	1.098	0.312±0.036	0.370±0.032
8	$25^\circ < \theta < 50^\circ$	1.093	0.457±0.060	

^{37}Ar/^{32}S Solar Minimum

Range	Angles	Spectral Correction	Ratio	Ratio: $0^\circ < \theta < 50^\circ$
2	$0^\circ < \theta < 25^\circ$	0.903	0.097±0.010	0.098±0.007
2	$25^\circ < \theta < 50^\circ$	0.905	0.098±0.009	
3	$0^\circ < \theta < 25^\circ$	0.911	0.100±0.009	0.105±0.006
3	$25^\circ < \theta < 50^\circ$	0.913	0.108±0.008	
4	$0^\circ < \theta < 25^\circ$	0.919	0.115±0.010	0.113±0.007
4	$25^\circ < \theta < 50^\circ$	0.921	0.112±0.009	
5	$0^\circ < \theta < 25^\circ$	0.924	0.114±0.011	0.117±0.008
5	$25^\circ < \theta < 50^\circ$	0.927	0.119±0.011	
6	$0^\circ < \theta < 25^\circ$	0.928	0.133±0.013	0.135±0.009
6	$25^\circ < \theta < 50^\circ$	0.931	0.136±0.014	
7	$0^\circ < \theta < 25^\circ$	0.932	0.126±0.013	0.137±0.011
7	$25^\circ < \theta < 50^\circ$	0.934	0.150±0.017	
8	$0^\circ < \theta < 25^\circ$	0.935	0.127±0.014	0.129±0.011
8	$25^\circ < \theta < 50^\circ$	0.938	0.132±0.017	

^{37}Ar/^{32}S Solar Maximum

Range	Angles	Spectral Correction	Ratio	Ratio: $0^\circ < \theta < 50^\circ$
2	$0^\circ < \theta < 25^\circ$	0.892	0.133±0.015	0.127±0.009
2	$25^\circ < \theta < 50^\circ$	0.894	0.124±0.012	
3	$0^\circ < \theta < 25^\circ$	0.901	0.115±0.011	0.129±0.008
3	$25^\circ < \theta < 50^\circ$	0.904	0.138±0.011	
4	$0^\circ < \theta < 25^\circ$	0.910	0.129±0.012	0.135±0.009
4	$25^\circ < \theta < 50^\circ$	0.913	0.139±0.012	
5	$0^\circ < \theta < 25^\circ$	0.917	0.154±0.014	0.143±0.010
5	$25^\circ < \theta < 50^\circ$	0.920	0.134±0.013	
6	$0^\circ < \theta < 25^\circ$	0.922	0.144±0.015	0.140±0.010
6	$25^\circ < \theta < 50^\circ$	0.925	0.136±0.015	
7	$0^\circ < \theta < 25^\circ$	0.926	0.135±0.014	0.147±0.011
7	$25^\circ < \theta < 50^\circ$	0.929	0.161±0.018	
8	$0^\circ < \theta < 25^\circ$	0.930	0.128±0.014	0.148±0.012
8	$25^\circ < \theta < 50^\circ$	0.933	0.174±0.021	

^{38}Ar/^{36}Ar Solar Minimum

Range	Angles	Spectral Correction	Ratio	Ratio: $0° < \theta < 50°$
2	$0° < \theta < 25°$	1.065	0.850±0.089	0.895±0.059
2	$25° < \theta < 50°$	1.063	0.920±0.078	
3	$0° < \theta < 25°$	1.056	1.094±0.090	1.161±0.064
3	$25° < \theta < 50°$	1.053	1.204±0.088	
4	$0° < \theta < 25°$	1.047	1.053±0.093	1.017±0.061
4	$25° < \theta < 50°$	1.044	0.992±0.081	
5	$0° < \theta < 25°$	1.041	1.147±0.106	1.118±0.072
5	$25° < \theta < 50°$	1.038	1.095±0.097	
6	$0° < \theta < 25°$	1.036	1.025±0.102	1.173±0.083
6	$25° < \theta < 50°$	1.033	1.328±0.132	
7	$0° < \theta < 25°$	1.032	0.929±0.099	0.979±0.076
7	$25° < \theta < 50°$	1.030	1.032±0.116	
8	$0° < \theta < 25°$	1.029	1.198±0.126	1.172±0.094
8	$25° < \theta < 50°$	1.026	1.138±0.141	

^{38}Ar/^{36}Ar Solar Maximum

Range	Angles	Spectral Correction	Ratio	Ratio: $0° < \theta < 50°$
2	$0° < \theta < 25°$	1.065	1.524±0.172	1.346±0.095
2	$25° < \theta < 50°$	1.063	1.261±0.114	
3	$0° < \theta < 25°$	1.058	1.105±0.096	1.104±0.064
3	$25° < \theta < 50°$	1.056	1.103±0.084	
4	$0° < \theta < 25°$	1.052	1.014±0.091	1.086±0.066
4	$25° < \theta < 50°$	1.050	1.140±0.093	
5	$0° < \theta < 25°$	1.048	1.267±0.117	1.177±0.077
5	$25° < \theta < 50°$	1.046	1.106±0.100	
6	$0° < \theta < 25°$	1.044	1.047±0.101	1.099±0.078
6	$25° < \theta < 50°$	1.042	1.160±0.121	
7	$0° < \theta < 25°$	1.041	1.240±0.127	1.150±0.087
7	$25° < \theta < 50°$	1.040	1.058±0.119	
8	$0° < \theta < 25°$	1.039	1.109±0.120	1.160±0.093
8	$25° < \theta < 50°$	1.037	1.222±0.146	

Table C.3: Argon ratios after spectral corrections

C.4 Calcium ratios

^{41}Ca/^{36}Ar Solar Minimum

Range	Angles	Spectral Correction	Ratio	Ratio: $0° < \theta < 50°$
2	$0° < \theta < 25°$	0.918	0.389±0.049	0.422±0.034
2	$25° < \theta < 50°$	0.920	0.440±0.045	
3	$0° < \theta < 25°$	0.925	0.464±0.045	0.478±0.031
3	$25° < \theta < 50°$	0.926	0.487±0.042	
4	$0° < \theta < 25°$	0.930	0.484±0.050	0.471±0.034
4	$25° < \theta < 50°$	0.932	0.462±0.045	
5	$0° < \theta < 25°$	0.935	0.536±0.058	0.499±0.039
5	$25° < \theta < 50°$	0.937	0.470±0.051	
6	$0° < \theta < 25°$	0.938	0.517±0.060	0.531±0.046
6	$25° < \theta < 50°$	0.940	0.546±0.069	
7	$0° < \theta < 25°$	0.941	0.540±0.065	0.487±0.046
7	$25° < \theta < 50°$	0.943	0.431±0.064	
8	$0° < \theta < 25°$	0.943	0.494±0.064	0.527±0.052
8	$25° < \theta < 50°$	0.945	0.568±0.087	

^{41}Ca/^{36}Ar Solar Maximum

Range	Angles	Spectral Correction	Ratio	Ratio: $0° < \theta < 50°$
2	$0° < \theta < 25°$	0.937	0.623±0.084	0.543±0.047
2	$25° < \theta < 50°$	0.936	0.505±0.056	
3	$0° < \theta < 25°$	0.932	0.504±0.051	0.506±0.034
3	$25° < \theta < 50°$	0.931	0.508±0.045	
4	$0° < \theta < 25°$	0.928	0.393±0.043	0.449±0.033
4	$25° < \theta < 50°$	0.927	0.491±0.048	
5	$0° < \theta < 25°$	0.925	0.474±0.055	0.467±0.038
5	$25° < \theta < 50°$	0.924	0.462±0.052	
6	$0° < \theta < 25°$	0.923	0.446±0.051	0.491±0.042
6	$25° < \theta < 50°$	0.921	0.544±0.069	
7	$0° < \theta < 25°$	0.921	0.531±0.064	0.518±0.047
7	$25° < \theta < 50°$	0.920	0.503±0.069	
8	$0° < \theta < 25°$	0.919	0.508±0.066	0.507±0.051
8	$25° < \theta < 50°$	0.918	0.505±0.079	

^{41}Ca/^{32}S Solar Minimum

Range	Angles	Spectral Correction	Ratio	Ratio: $0^\circ < \theta < 50^\circ$
2	$0^\circ < \theta < 25^\circ$	0.809	0.078±0.009	0.084±0.006
2	$25^\circ < \theta < 50^\circ$	0.812	0.087±0.008	
3	$0^\circ < \theta < 25^\circ$	0.823	0.094±0.008	0.093±0.006
3	$25^\circ < \theta < 50^\circ$	0.827	0.093±0.007	
4	$0^\circ < \theta < 25^\circ$	0.836	0.093±0.009	0.093±0.006
4	$25^\circ < \theta < 50^\circ$	0.840	0.094±0.008	
5	$0^\circ < \theta < 25^\circ$	0.845	0.110±0.011	0.105±0.007
5	$25^\circ < \theta < 50^\circ$	0.850	0.102±0.010	
6	$0^\circ < \theta < 25^\circ$	0.853	0.107±0.011	0.111±0.009
6	$25^\circ < \theta < 50^\circ$	0.857	0.115±0.013	
7	$0^\circ < \theta < 25^\circ$	0.859	0.114±0.012	0.110±0.009
7	$25^\circ < \theta < 50^\circ$	0.864	0.106±0.014	
8	$0^\circ < \theta < 25^\circ$	0.865	0.105±0.012	0.114±0.010
8	$25^\circ < \theta < 50^\circ$	0.869	0.127±0.017	

^{41}Ca/^{32}S Solar Maximum

Range	Angles	Spectral Correction	Ratio	Ratio: $0^\circ < \theta < 50^\circ$
2	$0^\circ < \theta < 25^\circ$	0.852	0.120±0.014	0.111±0.009
2	$25^\circ < \theta < 50^\circ$	0.850	0.107±0.011	
3	$0^\circ < \theta < 25^\circ$	0.842	0.116±0.011	0.119±0.007
3	$25^\circ < \theta < 50^\circ$	0.840	0.121±0.010	
4	$0^\circ < \theta < 25^\circ$	0.833	0.096±0.010	0.110±0.007
4	$25^\circ < \theta < 50^\circ$	0.831	0.120±0.011	
5	$0^\circ < \theta < 25^\circ$	0.827	0.107±0.011	0.109±0.008
5	$25^\circ < \theta < 50^\circ$	0.824	0.111±0.011	
6	$0^\circ < \theta < 25^\circ$	0.822	0.121±0.013	0.121±0.009
6	$25^\circ < \theta < 50^\circ$	0.820	0.121±0.014	
7	$0^\circ < \theta < 25^\circ$	0.818	0.121±0.013	0.121±0.010
7	$25^\circ < \theta < 50^\circ$	0.816	0.120±0.015	
8	$0^\circ < \theta < 25^\circ$	0.815	0.110±0.013	0.116±0.010
8	$25^\circ < \theta < 50^\circ$	0.813	0.125±0.018	

^{41}Ca/^{40}Ca Solar Minimum

Range	Angles	Spectral Correction	Ratio	Ratio: $0° < \theta < 50°$
2	$0° < \theta < 25°$	1.023	0.200±0.024	0.216±0.016
2	$25° < \theta < 50°$	1.022	0.224±0.021	
3	$0° < \theta < 25°$	1.020	0.220±0.020	0.224±0.014
3	$25° < \theta < 50°$	1.020	0.226±0.018	
4	$0° < \theta < 25°$	1.018	0.229±0.022	0.238±0.016
4	$25° < \theta < 50°$	1.018	0.245±0.023	
5	$0° < \theta < 25°$	1.017	0.270±0.027	0.270±0.020
5	$25° < \theta < 50°$	1.016	0.270±0.028	
6	$0° < \theta < 25°$	1.016	0.269±0.029	0.278±0.022
6	$25° < \theta < 50°$	1.015	0.288±0.034	
7	$0° < \theta < 25°$	1.015	0.305±0.034	0.274±0.024
7	$25° < \theta < 50°$	1.014	0.242±0.034	
8	$0° < \theta < 25°$	1.014	0.288±0.035	0.309±0.029
8	$25° < \theta < 50°$	1.014	0.337±0.049	

^{41}Ca/^{40}Ca Solar Maximum

Range	Angles	Spectral Correction	Ratio	Ratio: $0° < \theta < 50°$
2	$0° < \theta < 25°$	1.017	0.304±0.037	0.286±0.023
2	$25° < \theta < 50°$	1.018	0.277±0.029	
3	$0° < \theta < 25°$	1.018	0.282±0.027	0.308±0.020
3	$25° < \theta < 50°$	1.019	0.325±0.028	
4	$0° < \theta < 25°$	1.019	0.247±0.026	0.269±0.019
4	$25° < \theta < 50°$	1.020	0.284±0.026	
5	$0° < \theta < 25°$	1.020	0.301±0.033	0.302±0.023
5	$25° < \theta < 50°$	1.020	0.302±0.032	
6	$0° < \theta < 25°$	1.021	0.305±0.033	0.318±0.026
6	$25° < \theta < 50°$	1.021	0.331±0.040	
7	$0° < \theta < 25°$	1.021	0.322±0.036	0.343±0.030
7	$25° < \theta < 50°$	1.021	0.369±0.049	
8	$0° < \theta < 25°$	1.021	0.285±0.034	0.311±0.029
8	$25° < \theta < 50°$	1.022	0.351±0.053	

^{42}Ca/^{40}Ca Solar Minimum

Range	Angles	Spectral Correction	Ratio	Ratio: $0^\circ < \theta < 50^\circ$
2	$0^\circ < \theta < 25^\circ$	1.053	0.454±0.042	0.468±0.028
2	$25^\circ < \theta < 50^\circ$	1.051	0.476±0.037	
3	$0^\circ < \theta < 25^\circ$	1.045	0.493±0.037	0.488±0.025
3	$25^\circ < \theta < 50^\circ$	1.042	0.485±0.033	
4	$0^\circ < \theta < 25^\circ$	1.037	0.497±0.039	0.521±0.029
4	$25^\circ < \theta < 50^\circ$	1.035	0.539±0.041	
5	$0^\circ < \theta < 25^\circ$	1.032	0.526±0.044	0.576±0.034
5	$25^\circ < \theta < 50^\circ$	1.030	0.621±0.051	
6	$0^\circ < \theta < 25^\circ$	1.028	0.561±0.049	0.606±0.039
6	$25^\circ < \theta < 50^\circ$	1.025	0.653±0.060	
7	$0^\circ < \theta < 25^\circ$	1.024	0.596±0.056	0.581±0.040
7	$25^\circ < \theta < 50^\circ$	1.022	0.566±0.058	
8	$0^\circ < \theta < 25^\circ$	1.022	0.590±0.058	0.576±0.044
8	$25^\circ < \theta < 50^\circ$	1.019	0.558±0.068	

^{42}Ca/^{40}Ca Solar Maximum

Range	Angles	Spectral Correction	Ratio	Ratio: $0^\circ < \theta < 50^\circ$
2	$0^\circ < \theta < 25^\circ$	1.050	0.653±0.065	0.624±0.040
2	$25^\circ < \theta < 50^\circ$	1.049	0.608±0.051	
3	$0^\circ < \theta < 25^\circ$	1.046	0.638±0.051	0.690±0.037
3	$25^\circ < \theta < 50^\circ$	1.045	0.725±0.052	
4	$0^\circ < \theta < 25^\circ$	1.043	0.636±0.052	0.635±0.036
4	$25^\circ < \theta < 50^\circ$	1.042	0.634±0.048	
5	$0^\circ < \theta < 25^\circ$	1.041	0.683±0.059	0.703±0.043
5	$25^\circ < \theta < 50^\circ$	1.040	0.719±0.060	
6	$0^\circ < \theta < 25^\circ$	1.040	0.697±0.062	0.732±0.047
6	$25^\circ < \theta < 50^\circ$	1.039	0.769±0.072	
7	$0^\circ < \theta < 25^\circ$	1.038	0.629±0.060	0.695±0.049
7	$25^\circ < \theta < 50^\circ$	1.037	0.777±0.082	
8	$0^\circ < \theta < 25^\circ$	1.037	0.672±0.063	0.716±0.052
8	$25^\circ < \theta < 50^\circ$	1.036	0.782±0.090	

^{43}Ca/^{36}Ar Solar Minimum

Range	Angles	Spectral Correction	Ratio	Ratio: $0^\circ < \theta < 50^\circ$
2	$0^\circ < \theta < 25^\circ$	0.967	0.985±0.099	1.003±0.066
2	$25^\circ < \theta < 50^\circ$	0.967	1.013±0.086	
3	$0^\circ < \theta < 25^\circ$	0.970	1.133±0.093	1.189±0.066
3	$25^\circ < \theta < 50^\circ$	0.971	1.225±0.091	
4	$0^\circ < \theta < 25^\circ$	0.972	1.074±0.095	1.077±0.065
4	$25^\circ < \theta < 50^\circ$	0.973	1.079±0.088	
5	$0^\circ < \theta < 25^\circ$	0.974	1.112±0.103	1.081±0.070
5	$25^\circ < \theta < 50^\circ$	0.975	1.056±0.096	
6	$0^\circ < \theta < 25^\circ$	0.976	1.194±0.115	1.221±0.086
6	$25^\circ < \theta < 50^\circ$	0.977	1.249±0.129	
7	$0^\circ < \theta < 25^\circ$	0.977	1.151±0.118	1.155±0.087
7	$25^\circ < \theta < 50^\circ$	0.978	1.158±0.129	
8	$0^\circ < \theta < 25^\circ$	0.979	1.195±0.126	1.187±0.096
8	$25^\circ < \theta < 50^\circ$	0.980	1.177±0.149	

^{43}Ca/^{36}Ar Solar Maximum

Range	Angles	Spectral Correction	Ratio	Ratio: $0^\circ < \theta < 50^\circ$
2	$0^\circ < \theta < 25^\circ$	0.963	1.383±0.158	1.330±0.095
2	$25^\circ < \theta < 50^\circ$	0.964	1.305±0.119	
3	$0^\circ < \theta < 25^\circ$	0.967	1.098±0.095	1.158±0.067
3	$25^\circ < \theta < 50^\circ$	0.968	1.193±0.090	
4	$0^\circ < \theta < 25^\circ$	0.970	1.112±0.097	1.159±0.070
4	$25^\circ < \theta < 50^\circ$	0.971	1.194±0.099	
5	$0^\circ < \theta < 25^\circ$	0.972	1.188±0.111	1.112±0.074
5	$25^\circ < \theta < 50^\circ$	0.973	1.052±0.098	
6	$0^\circ < \theta < 25^\circ$	0.974	1.027±0.099	1.078±0.078
6	$25^\circ < \theta < 50^\circ$	0.975	1.139±0.123	
7	$0^\circ < \theta < 25^\circ$	0.976	1.261±0.128	1.187±0.090
7	$25^\circ < \theta < 50^\circ$	0.977	1.111±0.126	
8	$0^\circ < \theta < 25^\circ$	0.977	1.345±0.141	1.265±0.101
8	$25^\circ < \theta < 50^\circ$	0.978	1.170±0.145	

^{43}Ca/^{32}S Solar Minimum

Range	Angles	Spectral Correction	Ratio	Ratio: $0^\circ < \theta < 50^\circ$
2	$0^\circ < \theta < 25^\circ$	0.850	0.196±0.017	0.199±0.011
2	$25^\circ < \theta < 50^\circ$	0.854	0.201±0.015	
3	$0^\circ < \theta < 25^\circ$	0.864	0.230±0.016	0.233±0.011
3	$25^\circ < \theta < 50^\circ$	0.868	0.235±0.015	
4	$0^\circ < \theta < 25^\circ$	0.876	0.207±0.016	0.215±0.011
4	$25^\circ < \theta < 50^\circ$	0.881	0.220±0.016	
5	$0^\circ < \theta < 25^\circ$	0.886	0.229±0.018	0.230±0.013
5	$25^\circ < \theta < 50^\circ$	0.890	0.230±0.018	
6	$0^\circ < \theta < 25^\circ$	0.893	0.250±0.020	0.257±0.015
6	$25^\circ < \theta < 50^\circ$	0.897	0.265±0.023	
7	$0^\circ < \theta < 25^\circ$	0.899	0.244±0.021	0.263±0.017
7	$25^\circ < \theta < 50^\circ$	0.903	0.287±0.027	
8	$0^\circ < \theta < 25^\circ$	0.904	0.256±0.022	0.260±0.017
8	$25^\circ < \theta < 50^\circ$	0.909	0.266±0.028	

^{43}Ca/^{32}S Solar Maximum

Range	Angles	Spectral Correction	Ratio	Ratio: $0^\circ < \theta < 50^\circ$
2	$0^\circ < \theta < 25^\circ$	0.835	0.254±0.023	0.261±0.016
2	$25^\circ < \theta < 50^\circ$	0.838	0.264±0.020	
3	$0^\circ < \theta < 25^\circ$	0.851	0.247±0.019	0.267±0.014
3	$25^\circ < \theta < 50^\circ$	0.855	0.279±0.019	
4	$0^\circ < \theta < 25^\circ$	0.865	0.270±0.020	0.283±0.015
4	$25^\circ < \theta < 50^\circ$	0.870	0.292±0.021	
5	$0^\circ < \theta < 25^\circ$	0.876	0.270±0.021	0.262±0.015
5	$25^\circ < \theta < 50^\circ$	0.881	0.255±0.021	
6	$0^\circ < \theta < 25^\circ$	0.885	0.283±0.024	0.271±0.017
6	$25^\circ < \theta < 50^\circ$	0.890	0.259±0.024	
7	$0^\circ < \theta < 25^\circ$	0.892	0.296±0.025	0.286±0.018
7	$25^\circ < \theta < 50^\circ$	0.897	0.275±0.026	
8	$0^\circ < \theta < 25^\circ$	0.898	0.303±0.026	0.302±0.020
8	$25^\circ < \theta < 50^\circ$	0.903	0.301±0.031	

^{43}Ca/^{40}Ca Solar Minimum

Range	Angles	Spectral Correction	Ratio	Ratio: $0^\circ < \theta < 50^\circ$
2	$0^\circ < \theta < 25^\circ$	1.077	0.506±0.046	0.512±0.031
2	$25^\circ < \theta < 50^\circ$	1.075	0.516±0.040	
3	$0^\circ < \theta < 25^\circ$	1.068	0.536±0.040	0.555±0.028
3	$25^\circ < \theta < 50^\circ$	1.066	0.567±0.039	
4	$0^\circ < \theta < 25^\circ$	1.061	0.505±0.040	0.541±0.030
4	$25^\circ < \theta < 50^\circ$	1.058	0.570±0.043	
5	$0^\circ < \theta < 25^\circ$	1.055	0.559±0.047	0.583±0.035
5	$25^\circ < \theta < 50^\circ$	1.053	0.604±0.051	
6	$0^\circ < \theta < 25^\circ$	1.051	0.617±0.054	0.635±0.041
6	$25^\circ < \theta < 50^\circ$	1.049	0.654±0.061	
7	$0^\circ < \theta < 25^\circ$	1.048	0.647±0.060	0.646±0.044
7	$25^\circ < \theta < 50^\circ$	1.045	0.644±0.065	
8	$0^\circ < \theta < 25^\circ$	1.044	0.692±0.066	0.692±0.051
8	$25^\circ < \theta < 50^\circ$	1.042	0.692±0.079	

^{43}Ca/^{40}Ca Solar Maximum

Range	Angles	Spectral Correction	Ratio	Ratio: $0^\circ < \theta < 50^\circ$
2	$0^\circ < \theta < 25^\circ$	1.086	0.701±0.069	0.726±0.046
2	$25^\circ < \theta < 50^\circ$	1.084	0.740±0.061	
3	$0^\circ < \theta < 25^\circ$	1.076	0.626±0.050	0.714±0.038
3	$25^\circ < \theta < 50^\circ$	1.073	0.773±0.055	
4	$0^\circ < \theta < 25^\circ$	1.067	0.701±0.057	0.693±0.039
4	$25^\circ < \theta < 50^\circ$	1.064	0.688±0.053	
5	$0^\circ < \theta < 25^\circ$	1.060	0.746±0.064	0.707±0.043
5	$25^\circ < \theta < 50^\circ$	1.057	0.676±0.059	
6	$0^\circ < \theta < 25^\circ$	1.055	0.688±0.062	0.682±0.045
6	$25^\circ < \theta < 50^\circ$	1.052	0.676±0.067	
7	$0^\circ < \theta < 25^\circ$	1.051	0.741±0.068	0.762±0.053
7	$25^\circ < \theta < 50^\circ$	1.048	0.788±0.084	
8	$0^\circ < \theta < 25^\circ$	1.047	0.727±0.068	0.748±0.054
8	$25^\circ < \theta < 50^\circ$	1.045	0.780±0.090	

^{44}Ca/^{40}Ca Solar Minimum

Range	Angles	Spectral Correction	Ratio	Ratio: $0^\circ < \theta < 50^\circ$
2	$0^\circ < \theta < 25^\circ$	1.112	0.558±0.050	0.560±0.033
2	$25^\circ < \theta < 50^\circ$	1.107	0.561±0.043	
3	$0^\circ < \theta < 25^\circ$	1.093	0.590±0.043	0.587±0.029
3	$25^\circ < \theta < 50^\circ$	1.088	0.585±0.039	
4	$0^\circ < \theta < 25^\circ$	1.077	0.571±0.044	0.601±0.032
4	$25^\circ < \theta < 50^\circ$	1.072	0.626±0.046	
5	$0^\circ < \theta < 25^\circ$	1.066	0.665±0.054	0.673±0.039
5	$25^\circ < \theta < 50^\circ$	1.061	0.680±0.055	
6	$0^\circ < \theta < 25^\circ$	1.057	0.629±0.054	0.637±0.040
6	$25^\circ < \theta < 50^\circ$	1.053	0.646±0.060	
7	$0^\circ < \theta < 25^\circ$	1.050	0.670±0.062	0.673±0.045
7	$25^\circ < \theta < 50^\circ$	1.045	0.675±0.067	
8	$0^\circ < \theta < 25^\circ$	1.044	0.684±0.065	0.686±0.050
8	$25^\circ < \theta < 50^\circ$	1.040	0.689±0.077	

^{44}Ca/^{40}Ca Solar Maximum

Range	Angles	Spectral Correction	Ratio	Ratio: $0^\circ < \theta < 50^\circ$
2	$0^\circ < \theta < 25^\circ$	1.098	0.801±0.077	0.755±0.047
2	$25^\circ < \theta < 50^\circ$	1.096	0.730±0.060	
3	$0^\circ < \theta < 25^\circ$	1.091	0.827±0.063	0.818±0.042
3	$25^\circ < \theta < 50^\circ$	1.089	0.811±0.057	
4	$0^\circ < \theta < 25^\circ$	1.084	0.686±0.056	0.684±0.038
4	$25^\circ < \theta < 50^\circ$	1.082	0.683±0.052	
5	$0^\circ < \theta < 25^\circ$	1.080	0.730±0.063	0.749±0.045
5	$25^\circ < \theta < 50^\circ$	1.077	0.764±0.065	
6	$0^\circ < \theta < 25^\circ$	1.076	0.729±0.065	0.777±0.050
6	$25^\circ < \theta < 50^\circ$	1.074	0.827±0.077	
7	$0^\circ < \theta < 25^\circ$	1.073	0.809±0.073	0.807±0.055
7	$25^\circ < \theta < 50^\circ$	1.071	0.805±0.084	
8	$0^\circ < \theta < 25^\circ$	1.070	0.710±0.067	0.745±0.054
8	$25^\circ < \theta < 50^\circ$	1.068	0.796±0.090	

Table C.4: Calcium ratios after spectral corrections

Appendix D

The Webber semi-empirical spallation cross-section formula

Formulae for calculating the cross-sections for producing secondary fragments due to collisions with hydrogen nuclei have been derived by Silberberg *et al.* (1998), Webber *et al.* (1990), and others. As discussed in Section 4.2.3, the Webber formula will be used for this work.

The Webber formula is based on the systematics of Rudstam (1966), with modifications due to measurements by Webber *et al.* (1990c,a,b), resulting in a simplification over previous cross-section formulations. The general form of the cross-section formula for producing a fragment of charge Z_f and mass A_f from an incident nuclei of charge Z_i and mass A_i given by Webber is:

$$\sigma(Z_f, A_f, E) = \sigma_0(Z_f, Z_i) f_1(Z_f, A_f, Z_i, A_i) f_2(E, Z_f, Z_i). \tag{D.1}$$

The first term, σ_0, is essentially the charge-changing cross section. It depends only on the charge of the incident particle Z_i and the charge of the fragment Z_f (Webber *et al.*, 1990a).

This term takes the form:

$$\sigma_0(Z_f, Z_i) = \sigma_{Zf} \exp\left(\frac{-(Z_i - Z_f)}{\Delta_{Zf}}\right) \exp\left(\frac{-|N_{Zi} - N_{Zf}|}{8.5}\right), \tag{D.2}$$

where σ_{Zf} is 142.5 mb for S, 144.5 mb for Ar, and 160.2 mb for Ca. The Δ_{Zf} parameter is 5.6 for S, 4.9 for Ar, and 5.9 for Ca. The neutron-excess N is defined to be $A - 2Z$, and the second exponential illustrates that the production of (Z_f, A_f) from (Z_i, A_i) is maximal when the primary and secondary nuclei both have masses near the stability line.

The second term describes the distribution of isotopic cross-sections for a given element and is written as:

$$f_1(Z_f, A_f, Z_i, A_i) = \frac{1}{\delta_{Zf}\sqrt{2\pi}} \exp\left(\frac{-(N_{Zi} - N_{Zf})^2}{2\delta_{Zf}}\right), \tag{D.3}$$

where $\delta_{Zf} = 0.32 Z_f^{0.39}$ for $Z_f > 4$ as derived in Webber *et al.* (1990b). The isotopic cross-sections represented here are assumed to be independent of energy, an assumption that is not strictly true for isotopes far from the β-decay stability line, or at very low energy compared to GCR energies (Webber *et al.*, 1990b).

The energy dependence of the cross-sections may be separated from the other terms (Webber *et al.*, 1990a,b), and is described by the third term in Equation D.1, f_2. This function depends on the charge of the incident nuclei Z_i and $\Delta Z = Z_i - Z_f$:

$$f_2(E, Z_i, Z_i - Z_f) = \left[1 + m(\Delta Z) g(Z_i) \exp\left(\frac{-(E - E_m)^2}{\Delta E_m}\right) + ...\right], \tag{D.4}$$

where $g(Z_i)$ describes the magnitude of the energy dependence, which is a strong function of Z_i (Webber *et al.*, 1990a), and takes the form:

$$g(Z_i) = (Z_i/26)^p. \tag{D.5}$$

The power p is taken to be equal to 2.5 for energies between 600 and 2000 MeV/nucleon, 1.4 for 200-600 MeV/nucleon, and 0.4 for less than 200 MeV/nucleon. The values for $m(\Delta Z)$, E_m, and ΔE_m in Equation D.4 are derived from fitting cross-section data (Webber *et al.*, 1990c,a,b).

This thesis uses a `Fortran` implementation of the cross-section formula described here and in Webber *et al.* (1990).